POLITECNICO DI TORINO

Master’s Degree

in Automotive Engineering

Master’s degree Thesis

Finite Element Analysis of Surface Hardening Treatments of Steels for Automotive Powertrain Applications

Advisors:

Prof. Daniele Botto

Prof. Roberto Doglione

Candidate:

Filippo Jones

Anno Accademico 2020/2021

ABSTRACT

Surface hardening is a procedure that is usually performed on steel components, in order to impart in these the strength and surface hardness that are necessary for their correct operation, whilst maintaining a reasonable value of ductility in the overall component.

The latter is usually composed of a sequence of heat treatments: carburizing, quenching and tempering. Each of these have different effects that, if correctly combined, can lead to the desired final mechanical properties in the component.

Carburizing is a process that increases the amount of carbon concentration at the component surface. Quenching is a quick decrease in temperature that causes in the component different phase transformations and an increase in the surface hardness, causing however also a decrease in toughness. Lastly, tempering is the reheat of the component to a prescribed temperature for a certain amount of time, which leads to an increase in toughness with consequent decrease in hardness.

All of these processes involve complex phenomena that are difficult to study and predict. However, the prediction of the mechanical properties of heat-treated components is very useful and important for large automotive companies.

A simulation tool is therefore created to predict the mechanical properties in automotive powertrain components after the carburizing-quenching-tempering sequence. This tool is designed in ABAQUS, with the addition of user-defined subroutines to include in the FEA software all of the metallurgy-related-effects that are not already present.

The outputs of this simulation are microhardness and steel phase composition. They are then compared to experimental microhardness measurements and to microstructure images obtained from the real automotive components. The results from such a comparison show that the simulation tool is able to predict qualitatively the different steel phases that are present in the component at different locations, and their general trend as a function of depth. Furthermore, the simulation software is also able to predict the general trend of the microhardness profile found at the surface of the components at the end of the heat treatment sequence.

DEDICATION

To my family that always helped and supported me, and to my dearest friends.

ACKNOWLEDGEMENTS

This thesis document represents the peak of my university career. During this difficult but exciting academic path, that started in September 2016 in Politecnico di Torino with the start of a BSc course in automotive engineering, I had the opportunity to learn a lot of important concepts, meet many motivated and interesting people, and grow and develop my knowledge and personality. In this last year, in particular, I had the opportunity to participate in this very special project between the University of Windsor, Politecnico di Torino, and Stellantis. This project allowed me to travel to Canada and grow from both a personal and academic point of view. For this reason, I would like to thank all parties involved for the great opportunity and help that they provided to me, in order to make the best of the project even through all of the difficulties created by the COVID-19 pandemic situation.

At first, I would like to thank immensely all of my Stellantis advisors from CRF in Italy and from Stellantis north America, that provided me with their expertise and their very deep-rooted knowledge in metallurgy. I particularly would like to thank each advisor for their involvement, interest, availability, and passion that they demonstrated towards the thesis project, motivating me to work harder and strive for the best.

I would then like express my enormous gratitude to my academic advisors from both the University of Windsor: Dr. A. Edrisy, and from Politecnico di Torino: Dr. D. Botto and Dr. R. Doglione, that provided their knowledge and guidance throughout the thesis project, and allowed me to work with method, and perform in the best way possible. This help becomes even more valuable considering the distance and absence of any in-person meeting due to the pandemic situation.

I would also like to give a special thank to Dr. G. Belingardi and Dr. M. P. Cavatorta from Politecnico di Torino, that shared their contagious passion for this project and that constantly assisted me throughout the duration of it. They provided their help and experience during the first part of the project when, due to travel restrictions, I could not travel to Canada. This same help and interest also continued during my travel to Canada when the restrictions were lifted, and finally also during my stay in Canada, despite the distance.

Special thanks to Dr. J. Johrendt from the University of Windsor and Marie Mills from Stellantis, for the great opportunity provided to me and for the guidance during the project.

I would like to enormously thank my family, Bryn, Grazia and Gilberto that always supported me and helped me not only during the length of this project, but throughout my entire life. Thank also to my grandparents, that are not with us anymore, but would be very proud and cheering for me in this moment.

I would like to give a special thank to my roommates and colleagues in this project: S. Da Col and G. Rosso, that shared with me many happy moments and allowed me to live in a better way this very difficult pandemic situation filled with lockdowns.

Finally, I would like to thank my closest friends from Italy: Alessandro, Andrea and Lorenzo, that always kept in touch and supported me during my academic career.

TABLE OF CONTENTS

CHAPTER 4: RESULTS AND DISCUSSION 111

LIST OF ABBREVIATIONS AND SYMBOLS

FEA	Finite Element Analysis
OEM	Original Equipment Manufacturer
TRIP	Transformation Induced Plasticity
J	Flux of carbon atoms
β	Mass transfer coefficient
C_p	Carbon potential of the carbon-rich gas atmosphere
C_s	Carbon percentage at the component surface
D	Diffusivity of the steel
C	Carbon concentration within the component
Cr	Concentration of chromium within the component
Mn	Concentration of Manganese within the component
Si	Concentration of Silicon within the component
Ni	Concentration of Nickel within the component
Mo	Concentration of Molybdenum within the component
Al	Concentration of Aluminium within the component
V	Concentration of Vanadium within the component
Cu	Concentration of Copper within the component
As	Concentration of Arsenic within the component
W	Concentration of Tungsten within the component
Ti	Concentration of Titanium within the component
R	Gas Constant
t	Time
T	Temperature
x	Depth within the component
$f(x)$	Carbon concentration as a function of the depth
t_b	Total vacuum carburization boost time
t_c	Time duration of the carburizing operation
Δm	Mass increment during a certain period of carburization
S	Surface of the component exposed to the carburizing gas
φ	Carburizing capacity of the atmosphere, that varies as a function of the time of the process τ
J_v	Carbon flux during vacuum carburizing
S_{re}	Dimensionless reaction efficiency
m_c	Mass of carbon per one mole of vacuum carburizing gas
I_z	Number of molecules of vacuum carburizing gas reaching the steel surface
ρ_m	Density of the steel
p	Pressure of the vacuum carburizing gas
M_g	Molar mass of the carburizing gas
T_c	Carburizing temperature
t_C	Time during carburization
d	Austenite grain size in micrometer
n	Time exponent in Arrhenius type equation

A_a	Constant in Arrhenius type equation
Q	Activation energy in Arrhenius type equation
$norm$	Norm between point defined in ".dat" file and point being analyzed in the quenching simulation
x_{actual}	X coordinate is that of the node that is currently being analyzed in the quenching simulation
$x_{\text{".dat" file}}$	X coordinate as found in the ".dat" file
y_{actual}	Y coordinate is that of the node that is currently being analyzed in the quenching simulation.
$y_{\text{".dat" file}}$	Y coordinate as found in the ".dat" file
z_{actual}	Z coordinate is that of the node that is currently being analyzed in the quenching simulation.
$z_{\text{".dat" file}}$	Z coordinate as found in the ".dat" file
E	Young's modulus
σ	Stress evaluated in the experimental test
ε	Strain evaluated in the experimental test
λ	Thermal conductivity
ρc	Volumetric heat capacity
i	Index used to indicate different steel phases: • "i" is equal to "m" to symbolize martensite • "i" is equal to "b" to symbolize bainite • "i" is equal to "f" to symbolize ferrite • "i" is equal to "a" to symbolize austenite • "i" is equal to "p" to symbolize perlite
ξ_i	Phase fraction of different steel phases "i"
A	Material related parameter in Johnson–Mehl–Avrami–Kolmogorov equation
B	Material related parameter in Johnson–Mehl–Avrami–Kolmogorov equation
θ	Time required to have a F_θ phase fraction
F_θ	Starting phase fraction of the diffusion phase
$\emptyset$	Time required to have a $F_\emptyset$ phase fraction
$F_\emptyset$	Ending phase fraction of the diffusion phase
t_j	Time value to be used in Johnson–Mehl–Avrami–Kolmogorov equation at the jth iteration
Δt_j	Time increment in the jth iteration in the simulation
F_{j-1}	Phase fraction of diffusive phase at the $(j-1)$th iteration
X	Normalized diffusive steel phase fraction
τ_F	Amount of time that is necessary for ferrite to achieve a certain value X of normalized phase fraction
G	Austenite grain size diameter expressed in ASTM
Ae_3	Austenite-ferrite transformation temperature
$I(X)$	Integration terms for ferrite and perlite in Kirkaldy's formulations

τ_P	Amount of time that is necessary for perlite to achieve a certain value X of normalized phase fraction
Ae_1	Temperature below which ferrite starts to form
τ_B	Amount of time that is necessary for bainite to achieve a certain value X of normalized phase fraction
B_s	Temperature below which bainite starts to form
$I'(X)$	Integration term for bainite in Kirkaldy's formulations
D'	Effective diffusion coefficient
N	Number of austenite grains per square inch that can be counted in a 100X magnification image
$\tau_{F,1\%}$	Times necessary for ferrite to achieve a 1% of transformation
$\tau_{P,1\%}$	Times necessary for perlite to achieve a 1% of transformation
$\tau_{B,1\%}$	Times necessary for bainite to achieve a 1% of transformation
$\tau_{F,99\%}$	Times necessary for ferrite to achieve a 99% of transformation
$\tau_{P,99\%}$	Times necessary for perlite to achieve a 99% of transformation
$\tau_{B,99\%}$	Times necessary for bainite to achieve a 99% of transformation
X_F	Normalized phase fraction of ferrite
X_P	Normalized phase fraction of perlite
X_B	Normalized phase fraction of bainite
$S(X)$	Integration terms for ferrite, perlite and bainite in Li et al.'s formulations
M_s	Martensite transformation starting temperature
ΔH	Latent heat of transformation
$\dot{Q}$	Heat generation rate due to the phase transformation
ε_{tot}	Total strain
ε_e	Elastic strain
ε_p	Plastic strain
ε_{th}	Thermal strain
ε_{tr}	Transformation strain
ε_{tp}	Transformation induced plasticity strain
α	Thermal expansion coefficient
σ_k	Kronecker delta
$\frac{\Delta V}{3V}$	Factor that is representing the volume differences between the different phases
s	Deviatoric stress
HV_M	Hardness of martensite
HV_B	Hardness of bainite
HV_{A-F-P}	Hardness of austenite, ferrite and perlite
HV	Overall hardness
HR_c	Hardness evaluated in Rockwell scale
V_r	Cooling rate at 700°C
TP	Jaffe-Holloman tempering parameter
T_t	Tempering temperature
t_t	Tempering time

c_t	Jaffe-Holloman constant
${HV_M}^T$	Hardness of tempered martensite
HV^T	Overall hardness after tempering
f	Ratio between the value of the hardness of the tempered martensite to the hardness of the as-quenched martensite
$SDV1$	User-defined-variable used to describe the phase fraction of Austenite
$SDV4$	User-defined-variable used to describe the phase fraction of Martensite
$SDV17$	User-defined-variable used to describe as-quenched hardness
$SDV18$	User-defined-variable used to describe the tempered hardness
$SDV35$	User-defined-variable used to describe the hardness of Austenite
$SDV36$	User-defined-variable used to describe the hardness of Bainite
$SDV37$	User-defined-variable used to describe the hardness of Martensite
$SDV43$	User-defined-variable used to describe M_s
$SDV45$	User-defined-variable used to describe the ASTM austenite grain size
$CONC$	ABAQUS defined variable to describe the carbon concentration

LIST OF EQUATIONS

$$CO_2 + C \leftrightarrow 2CO \tag{1}$$

$$J = \beta \cdot (C_p - C_s) \tag{2}$$

$$J = -D \cdot \frac{\partial c}{\partial x} \tag{3}$$

$$J = -D \cdot \nabla c \tag{4}$$

$$D = (0.146 - 0.036C \cdot (1 - 1.075Cr) - 0.0315Mn + 0.0509Si - 0.0085Ni + 0.3031Mo - 0.052Al) \cdot e^{-\frac{144300 - 15000C + 370C^2 - 4366.3Mn + 4050.7Si - 1240.7Ni + 7726Cr + 12126.6Mo - 6788.6Al}{R \cdot T}} \tag{5}$$

$$-D \cdot \nabla C = \beta \cdot (C_p - C_s) \tag{6}$$

$$J_v = \frac{\int_0^{C_0} f(x)}{S \cdot t_b} \tag{7}$$

$$J_v = \frac{\Delta m}{S \cdot t_c} \tag{8}$$

$$C_s = \varphi \tag{9}$$

$$J_v = -D \cdot \frac{\partial C}{\partial x} \tag{10}$$

$$-D \cdot \frac{\partial C}{\partial x} = J_v = \beta \cdot (C_p - C_s) \tag{11}$$

$$\beta = S_{re} \cdot m_c \cdot I_z \cdot \rho_m \tag{12}$$

$$I_z = \frac{p}{\sqrt{6 \cdot R \cdot T_c \cdot M_g}} \tag{13}$$

$$d = 766671 \cdot e^{\left(-\frac{89098 + 3581C + 1211Ni + 1443Cr + 4031Mo}{RT_c}\right)} \cdot {t_C}^{0.211} \tag{14}$$

$$d = A_a \cdot e^{\left(-\frac{Q}{RT_c}\right)} \cdot {t_C}^{n} \tag{15}$$

$$norm = \sqrt{(x_{actual} - x_{\text{".dat" file}})^2 + (y_{actual} - y_{\text{".dat" file}})^2 + (z_{actual} - z_{\text{".dat" file}})^2} \tag{16}$$

$$E = \frac{\sigma}{\varepsilon} \tag{17}$$

$$E = 1.985 \cdot 10^{11} - 4.462 \cdot 10^{7} \cdot T - 9.09 \cdot 10^{4} \cdot T^{2} - 2.059 \cdot T^{3} \tag{18}$$

$$E = 2.145 \cdot 10^{11} - 3.097 \cdot 10^{7} \cdot T - 9.208 \cdot 10^{-4} \cdot T^{2} - 2.797 \cdot T^{3} \tag{19}$$

$$\lambda = 18 \tag{20}$$

$$\lambda = 10.41 + 2.51 \cdot 10^{-8} \cdot T^{2.5} + 4.653 \cdot 10^{-1} \cdot T^{0.5} \tag{21}$$

$$\lambda = 44.01 - 3.863 \cdot 10^{-5} \cdot T^{2} - 3.001 \cdot 10^{-7} \cdot T^{2.5} \tag{22}$$

$$\lambda = 44.04 - 4.871 \cdot 10^{-4} \cdot T^{1.5} - 1.794 \cdot 10^{-8} \cdot T^{3} \tag{23}$$

$$\lambda = 44.05 - 5.019 \cdot 10^{-4} \cdot T^{1.5} - 1.611 \cdot 10^{-8} \cdot T^{3} \tag{24}$$

$$\rho c = 4.29 \cdot 10^{6} \tag{25}$$

$$\rho c = 4.019 \cdot 10^{6} + 4.034 \cdot 10^{-1} \cdot T^{2} + 2.015 \cdot 10^{4} \cdot T^{0.5} \tag{26}$$

$$\rho c = 3.42 \cdot 10^{6} + 1.347 \cdot 10^{-1} \cdot T^{2.5} - 3.745 \cdot 10^{-3} \cdot T^{3} + 2.698 \cdot 10^{-2} \cdot T^{0.5} \tag{27}$$

$$\rho c = 3.487 \cdot 10^{6} + 1.404 \cdot 10^{3} \cdot T + 5.715 \cdot 10^{3} \cdot T^{0.5} \tag{28}$$

$$\rho c = 3.41 \cdot 10^{6} + 3.215 \cdot 10^{-3} \cdot T^{3} + 2.919 \cdot 10^{4} \cdot T^{0.5} \tag{29}$$

$$\xi_i = 1 - e^{-A \cdot t^{B}} \tag{30}$$

$$A = -\frac{\ln(1 - F_{\theta})}{\theta^{B}} \tag{31}$$

$$A = -\frac{\ln(1 - F_{\emptyset})}{\emptyset^{B}} \tag{32}$$

$$B = \frac{ln\left(\frac{\ln(1-F_{\theta})}{\ln(1-F_{\emptyset})}\right)}{ln\left(\frac{\theta}{\emptyset}\right)} \tag{33}$$

$$t_j = \Delta t_j + \left[-\frac{\ln\,(1-F_{j-1})}{A}\right]^{1/_B} \tag{34}$$

$$\sum_j \frac{\Delta t_j}{\tau_j} = 1 \tag{35}$$

$$\tau_F = \frac{59.6 \cdot Mn + 1.45 \cdot Ni + 67.7 \cdot Cr + 244 \cdot Mo}{0.3 \cdot 2^{\frac{G-1}{2}} \cdot (Ae_3 - T)^3 \cdot e^{-\frac{23500}{R \cdot T}}} \cdot I(X) \tag{36}$$

$$\tau_P = \frac{1.79 + 5.42 \cdot (Cr + Mo + 4 \cdot Mo \cdot Ni)}{2^{\frac{G-1}{2}} \cdot (Ae_1 - T)^3 \cdot D'} \cdot I(X) \tag{37}$$

$$\tau_B = \frac{(2.34 + 10.1 \cdot C + 3.8 \cdot Cr + 19 \cdot Mo) \cdot 10^{-4}}{2^{\frac{G-1}{2}} \cdot (B_s - T)^3 \cdot e^{-\frac{27500}{R \cdot T}}} \cdot I'(X) \tag{38}$$

$$\frac{1}{D'} = \frac{1}{e^{-\frac{27500}{R \cdot T}}} + \frac{0.01 \cdot Cr + 0.52 \cdot Mo}{e^{-\frac{37000}{R \cdot T}}} \tag{39}$$

$$I(X) = \int_0^x \frac{1}{X^{0.66 \cdot (1-X)} \cdot (1-X)^{0.66 \cdot X}}\, dX \tag{40}$$

$$I'^{(X)} = \int_0^x \frac{e^{X^2 \cdot (1.9 \cdot C + 2.5 \cdot Mn + 0.9 \cdot Ni + 1.7 \cdot Cr + 4 \cdot Mo - 2.6)}}{X^{0.66 \cdot (1-X)} \cdot (1-X)^{0.66 \cdot X}}\, dX \tag{41}$$

$$N = 2^{G-1} \tag{42}$$

$$Ae_3 = 910 - 203 \cdot \sqrt{C} - 15.2 \cdot Ni + 44.7 \cdot Si + 104 \cdot V + 31.5 \cdot Mo + 13.1 \cdot W - 30 \cdot Mn - 11 \cdot Cr - 20 \cdot Cu + 700 \cdot P + 400 \cdot Al + 120 \cdot As + 400 \cdot Ti \tag{43}$$

$$Ae_1 = 723 - 10.7 \cdot Mn - 16.9 \cdot Ni + 29 \cdot Si + 16.9 \cdot Cr + 290 \cdot As + 6.4 \cdot W \tag{44}$$

$$B_s = 656 - 58 \cdot C - 35 \cdot Mn - 75 \cdot Si - 15 \cdot Ni - 34 \cdot Cr - 41 \cdot Mo \tag{45}$$

$$\sum_j \frac{\Delta t_j}{\tau_{F,1\%}} = 1 \tag{46}$$

$$\sum_j \frac{\Delta t_j}{\tau_{P,1\%}} = 1 \tag{47}$$

$$\sum_j \frac{\Delta t_j}{\tau_{B,1\%}} = 1 \tag{48}$$

$$X_F = \sum_j \frac{\Delta t_j}{\tau_{F,99\%} - \tau_{F,1\%}} \tag{49}$$

$$X_P = \sum_j \frac{\Delta t_j}{\tau_{P,99\%} - \tau_{P,1\%}} \tag{50}$$

$$X_B = \sum_j \frac{\Delta t_j}{\tau_{B,99\%} - \tau_{B,1\%}} \tag{51}$$

$$\tau_F = \frac{e^{1+6.31C+1.78Mn+0.31Si+1.12Ni+2.70Cr+4.06Mo}}{2^{0.41G} \cdot (Ae_3 - T)^3 \cdot e^{-\frac{27500}{R \cdot T}}} \cdot S(X) \tag{52}$$

$$\tau_P = \frac{e^{-4.25+4.12C+4.36Mn+0.44Si+1.71Ni+3.33Cr+5.19Mo^{0.5}}}{2^{0.32G} \cdot (Ae_1 - T)^3 \cdot e^{-\frac{27500}{R \cdot T}}} \cdot S(X) \tag{53}$$

$$\tau_B = \frac{e^{-10.23+10.18C+0.85Mn+0.55Ni+0.90Cr+0.36Mo}}{2^{0.29G} \cdot (B_s - T)^2 \cdot e^{-\frac{27500}{R \cdot T}}} \cdot S(X) \tag{54}$$

$$S(X) = \int_0^x \frac{1}{X^{0.4 \cdot (1-X)} \cdot (1-X)^{0.4 \cdot X}} dX \tag{55}$$

$$\xi_m = 1 - e^{-0.011 \cdot (M_s - T)} \tag{56}$$

$$M_s = 550 - 360 \cdot C - 40 \cdot Mn - 20 \cdot Ni - 40 \cdot Cr - 30 \cdot Mo \tag{57}$$

$$\xi(j) = \begin{cases} \xi(j), & \xi(j) \geq \xi(j-1) \\ \xi(j-1), & \xi(j) < \xi(j-1) \end{cases} \tag{58}$$

$$\Delta H = 1.082 \cdot 10^2 - 0.162 \cdot T + 1.118 \cdot 10^{-4} \cdot T^2 - 3 \cdot 10^{-8} \cdot T^3 - 3.501 \cdot 10^4 \cdot T^{-1} \tag{59}$$

$$\Delta H = 1.56 \cdot 10^9 - 1.50 \cdot 10^6 \cdot T \tag{60}$$

$$\Delta H = 6.40 \cdot 10^8 \tag{61}$$

$$\dot{Q} = \frac{\Delta H_i \cdot \Delta \xi_i}{\Delta t} \tag{62}$$

$$\varepsilon_{tot} = \varepsilon_e + \varepsilon_p + \varepsilon_{th} + \varepsilon_{tr} + \varepsilon_{tp} \tag{63}$$

$$\varepsilon_{th} = \alpha \cdot \Delta T \tag{64}$$

$$\varepsilon_{th} = \Delta T \cdot \sigma_k \cdot \sum_i \alpha_i \cdot \xi_i \tag{65}$$

$$\varepsilon_{tr} = \sigma_k \cdot \sum_i \left(\frac{\Delta V}{3V}\right)_i \cdot \Delta \xi_i \tag{66}$$

$$\varepsilon_{tp} = \sum_i -\eta_i \cdot \Delta \xi_i \cdot (1 - \xi_i) \cdot s \tag{67}$$

$$HV_M = 127 + 949C + 27Si + 11Mn + 8Ni + 16Cr + 21 \log V_r \tag{68}$$

$$HV_B = 323 + 185C + 330Si + 153Mn + 65Ni + 144Cr + 191Mo + (89 + 53C - 55Si - 22Mn - 10Ni - 20Cr - 33Mo) \log V_r \tag{69}$$

$$HV_{A-F-P} = 42 + 223C + 53Si + 30Mn + 12.6Ni + 7Cr + 19Mo + (10 - 19Si + 4Ni + 8Cr + 130V) \log V_r \tag{70}$$

$$HV = \xi_m \cdot HV_M + \xi_b \cdot HV_B + \xi_f \cdot HV_{A-F-P} + \xi_p \cdot HV_{A-F-P} + \xi_a \cdot HV_{A-F-P} \tag{71}$$

$$HR_c = 193 \cdot \log HV - 21.41(\log HV)^2 - 316 \tag{72}$$

$$TP = T_t \cdot (\log(t_t) + c_t) \tag{73}$$

$$T_t = \frac{TP}{(\log(t_t) + c_t)} \tag{74}$$

$$f = \frac{{HV_M}^T}{HV_M} \tag{75}$$

$$f = \begin{cases} 1.304 \cdot (1 - 0.0013323 \cdot T_t) \cdot (1 - 0.3619482 \cdot C), & C < 0.45 \\ 1.102574 \cdot (1 - 0.0016554 \cdot T_t) \cdot (1 + 0.19088063 \cdot C), & C \geq 0.45 \end{cases} \tag{76}$$

$$HV^T = \xi_m \cdot {HV_M}^T + \xi_b \cdot HV_B + \xi_f \cdot HV_{A-F-P} + \xi_p \cdot HV_{A-F-P} + \xi_a \cdot HV_{A-F-P} \tag{77}$$

$$percentage\ of\ error = \frac{(simulated\ hardness - experimental\ hardness)}{experimental\ hardness} \tag{78}$$

CHAPTER 1:

INTRODUCTION

Surface hardening is a common procedure that is used in steel components in order to increase the strength at the surface of the steel object, whilst allowing the region underneath the surface to remain soft and ductile. It determines the formation of a thin harder metal layer at the component surface. The combination of a hard surface and a ductile interior is greatly appreciated as it allows for the component to be very tough whilst having both great surface hardness as well as scratch and corrosion resistance [1]. These traits are fundamental in powertrain and geartrain automotive components, which are the class of components on which this thesis research will focus on.

Surface hardening heat treatments involve complex thermo-metallurgical-mechanical phenomena. Numerous different studies have been made to better understand these phenomena and simulate the thermo-metallurgical-mechanical interactions. The simulation of the surface hardening procedure, in fact, leads to numerous advantages. [2] [3]

Firstly, a primary advantage, is that it allows the component designer to select the best process parameters, for example time and temperature for the different heat treatments, that lead to the desired properties within the component. To better explain this concept, a diagram showing the subsequent steps that are followed during the design of an automotive component is shown in Figure 1. 1.

Figure 1. 1: Process flow during an automotive component design.

As shown in Figure 1. 1, a first step when designing a component is to determine the working conditions at which the component is going to operate. Knowing these conditions and considering safety factors that are selected according to a company policy or the local law, allows the selection of the mechanical properties that the component must have in order to withstand the operating conditions. At this point, knowing the mechanical properties that are needed, and with some deep knowledge of metallurgy, the microstructure that determines the desired properties is predicted. As a final step, the best sequence of heat treatments and heat treatment parameters, that determine the desired microstructure, is identified.

This last step, in particular, is the one where a simulation tool, able to simulate the different heat treatments, has the greatest beneficial effects. The simulation tool can in fact be used to confirm if the predicted heat treatment sequence is producing in the component the expected properties. Furthermore, it can also be useful to understand if the same final properties could be obtained by another sequence that is less expensive or easier to apply, considering the particular situation of the Original Equipment Manufacturer (OEM).

Another benefit of the simulation tool is the possibility to optimize/adapt/modify existing heat treatments in order to obtain different mechanical properties in the component than those for which the heat treatment sequence was originally designed.

From a more economical point of view, the simulation tool would allow savings to the user. By providing results by means of numerical simulation, it would ideally save all costs associated with experimental tests. In fact, if a simulation tool has been validated, the results obtained by using that tool can be considered as good approximations of the real phenomenon, of course only in the fields where the latter has been validated and considering the limits of the simulation. By running the simulation tool, information that would otherwise be provided by costly experimental tests, can be obtained by inputting data in the software and running the simulation. This faster response is also a very important trait in the automotive industry.

Overall, it can be seen that a heat treatment simulation tool can be very useful when considering the point of view of large OEM's that design multiple steel components for their automotive products. These large manufacturers, in fact, need to find out the best heat treatment parameters for their manufactured components quickly and at low cost to be able to prepare and optimize the manufacturing process while remaining competitive in the market.

From the point of view of large OEM's, another important beneficial effect of having a simulation tool is the ability to reduce their reliance on the suppliers. In fact, the selection of the heat treatments is usually done by the steel suppliers, who have greater knowledge on the field of metallurgy. With the use of a simulation tool, however, this selection can be done by the OEM directly, without the need to rely completely on external suppliers.

Considering all of these advantages in creating a simulation tool, this thesis report will outline a methodology for the creation of a carburizing-quenching-tempering simulation tool used for the prediction of mechanical properties at the end of the processes, and will explain the different phenomena that must be considered when doing so. The simulation tool will focus on traditional and vacuum carburizing, quenching with an inert gas, and finally low-temperature tempering.

1.1 *Objective*

The objective of the present study, is to generate a simulation tool that is able to predict properties of components heat-treated by carburizing-quenching-tempering, and to display them to the user in a clear and understandable manner. These properties include the microhardness, and the phase fraction of the different steel phases present within the component. This last information, is particular important because many mechanical properties can be evaluated with a linear mixture, by knowing the value of the property for each steel phase, and the amount of each steel phase that is present.

1.2 *Scopes*

This thesis will answer the question: is it possible to simulate the effects of the surface hardening by carburizing-quenching -tempering on automotive steels? How close to reality are the results obtained with such a simulation, in terms of microhardness and microstructure?

The simulation of different heat treatments, due to its many benefits mentioned above, has been studied by many different researchers. However, many of these studies focused on only one or two of the three heat treatments that are considered in this study. The most relevant simulation that handled all three of them, furthermore, was considering the quenching process as a thermal exchange only and performed the simulations considering a traditional carburizing process. In this thesis, the methodology to simulate both vacuum and traditional carburizing will be covered. Furthermore, the simulation results will be compared to experimental measurements taken on real automotive components being treated with vacuum carburizing. Additionally, the effective simulation program along with its coding, to the best of my knowledge, is not available online for the previous simulation that handled all three of the carburizing-quenching-tempering heat treatments.

In the next chapter, the literature review will be shown. It presents the most relevant heat treatment simulations available in literature, a brief explanation of the different heat treatments that are analyzed in this thesis, and also a brief explanation of the different heat treatment simulation software that are available on the market.

CHAPTER 2:
LITERATURE REVIEW

In this chapter, to give a better understanding on the heat treatments that are simulated in this research and to briefly describe how their simulation has been tackled by previous researchers, the following topics will be covered:

1. A description of the different software available on the market, that are able to perform the heat treatment simulations. The advantages and drawbacks of different solutions are described.
2. A brief description of the heat treatments that are studied in this thesis: carburizing, quenching, and tempering.
3. A review of the studies considered to be more relevant during the development of the simulation tool.

The first of these issues to be covered is the software selection, that is discussed in the next paragraph. The other two topics will then be described in the paragraphs following the latter.

2.1 Software Selection

Over the years, because of the numerous advantages described in the introduction chapter, different studies to simulate the different phenomena that occur during heat treatments were carried out. Furthermore, different software packages were developed with the same aim.

At present, in fact, different simulation packages that allow the user to study different heat treatments are commercially available. In the work of Gur and Simsir [4], the history of heat treatment simulations from the 1970's to 2012, along with a very comprehensive study of the different simulation packages that are available, is presented. In that study, furthermore, the complexity of the simulation process is described, considering the different thermal, mechanical and metallurgical sectors. What can be understood from such a study is that different simulation packages, with different levels of complexity, are available on the market. Examples of these software are Dante, Deform-ht, Forge, Hearts, Musimap, Simufact, and Sysweld. These software, as mentioned in the paper, are easily useable and user friendly, and have other advantages as for example being currently updated, revised and having customer support. All of these software can perform different heat treatment simulations tasks. Figure 2. 1, taken from the [4] study, shows the diverse fields and heat treatments covered by the different simulation packages.

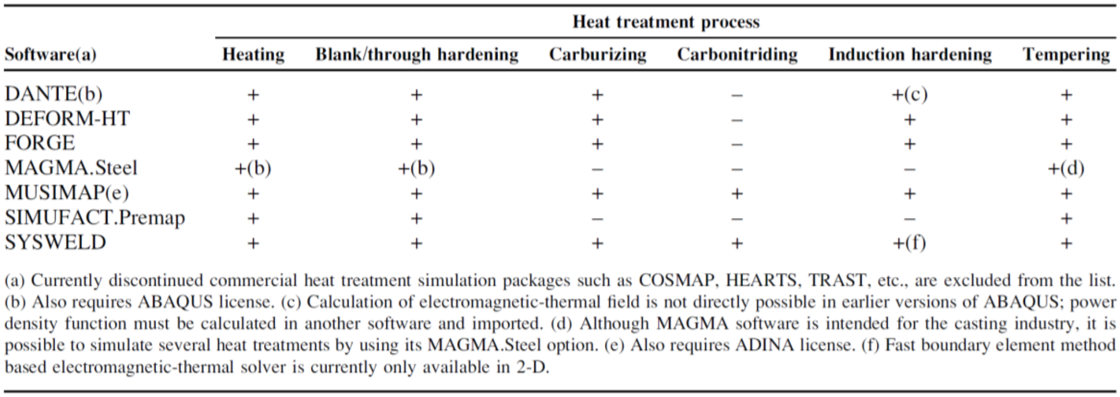

	Heat treatment process					
Software(a)	**Heating**	**Blank/through hardening**	**Carburizing**	**Carbonitriding**	**Induction hardening**	**Tempering**
DANTE(b)	+	+	+	–	+(c)	+
DEFORM-HT	+	+	+	–	+	+
FORGE	+	+	+	–	+	+
MAGMA.Steel	+(b)	+(b)	–	–	–	+(d)
MUSIMAP(e)	+	+	+	+	+	+
SIMUFACT.Premap	+	+	–	–	–	+
SYSWELD	+	+	+	+	+(f)	+

(a) Currently discontinued commercial heat treatment simulation packages such as COSMAP, HEARTS, TRAST, etc., are excluded from the list. (b) Also requires ABAQUS license. (c) Calculation of electromagnetic-thermal field is not directly possible in earlier versions of ABAQUS; power density function must be calculated in another software and imported. (d) Although MAGMA software is intended for the casting industry, it is possible to simulate several heat treatments by using its MAGMA.Steel option. (e) Also requires ADINA license. (f) Fast boundary element method based electromagnetic-thermal solver is currently only available in 2-D.

Figure 2. 1: Summary of heat treatment software packages. [4]

As it can be seen in the image above, different software are available, and each of these focuses on the simulation of some heat treatment. When using these software packages, the best solution would be to choose the software that manages to simulate all of the heat treatments that need to be simulated. [4]

On the other hand, the simulation process can also be performed with the use of powerful general purposes FEA packages such as ABAQUS, Adina, ANSYS, COMSOL, LS-DYNA, MSC. In this case, these general purposes do not have all of the metallurgical related information built in, and so these information are implemented into the simulation separately, with the use of external coding. This approach, as explained in [4], usually requires a lot of time and expertise. Furthermore, the simulation process developed is usually less tested and much less user friendly. However, as explained in [2], this simulation tool gives to the developer more freedom to modify and adapt the simulation to the process that is being simulated. In fact, as explained in [2], the commercial packages mentioned above, give the user no access to the source code, so the user cannot freely modify the simulation as wanted, to better fit the process that is being simulated.

The conclusion that can be drawn from the information provided above, is that different solutions are possible for what regards the software with which to perform the heat treatment simulations. Therefore, the selection of the software with which to create the simulation tool for this thesis research comes down to a tradeoff between using an already made software package, more user friendly and readily available, or using a general purpose FEA, to which user coding must be carefully created and added, but that leads to more freedom in performing the simulation.

As it will be discussed in greater detail in the methodology chapter, for the simulation tool that is being developed for this thesis research, the latter approach is followed. In fact, in order to have greater flexibility in the simulation, the combination of ABAQUS as general purpose FEA, and user subroutines as user codes, was selected for the creation of the simulation tool. The user subroutines, written in Fortran language, are accounting for the different metallurgical effects not already present in ABAQUS that will be described in greater detail in the following chapter. In order to utilize this method, ABAQUS must be connected to a Fortran compiler and to visual studio. The Fortran compiler used is Intel oneAPI.

This approach, as explained in [4], requires a lot of time as many different phenomena, that are not implemented in ABAQUS directly, must be comprehended and implemented as user coding in the simulation tool.

2.2 *Carburizing-Quenching-Tempering*

The heat treatment that is going to be analyzed in this thesis research is a sequence of carburizing, quenching and tempering. These heat treatments have the objective of increasing the hardness of the surface of a low carbon, ductile, steel component, with the objective of having a final product that is ductile enough to have good durability, and with a surface hard enough to withstand different impacts or wear that the component may be exposed to during its working life.

These three heat treatments all have different effects on the component. A brief introduction to the three treatments is provided below.

2.2.1 Carburizing

Carburizing is the heat treatment in which carbon atoms are diffused in the component's surface. This increase in the carbon content, is obtained by exposing the component to a carbon rich environment at a high temperature, for a certain amount of time. [5]

Temperature, along with the carburizing time, are two very important factors in the carburization process. For this reason, they are usually tuned in order to obtain the wanted amount of carbon and at the wanted depth. In fact, the high energy provided to the carbon atoms by the high temperature, determines a higher carbon diffusion, and the longer the component is exposed to the carbon rich environment, the higher will be the carbon concentration [6]. Carburizing temperatures are usually in the 850°C to 950°C range [5].

Carburizing is performed as the increase in carbon concentration makes the steel more hardenable. This means that the steel has greater ability to become harder in the following steps. In fact, the greatest effect of the presence of carbon atoms, is found when the component is cooled down from the high carburization temperature. This, because the carbon atoms, due to the high cooling temperature and the limited time to diffuse, do not diffuse during cooling and so remain trapped in the original austenite phase that is found at high temperatures. The phase structure of austenite is face-centered cubic (FCC), that is a structure that can accommodate some carbon atoms within it. During a very slow cooling, the FCC structure, would transform into another structure, that is body centered cubic (BCC). This structure, belonging to a steel phase called ferrite, is more compact and so less prone to contain carbon atoms within its structure. During slow cooling, however, the carbon atoms would have time to diffuse and so they would be able to move out of the FCC structure before the BCC structure formation. However, during a very quick cooling as that experienced during quenching, the carbon atoms do not have time to diffuse. This means that the interstitial carbon atoms present within the FCC structure remain trapped inside the structure and deform it. The structure that arises is called a body centered tetragonal structure and it is formed by the deformation of a BCC structure due to the presence of interstitial carbon atoms. This last structure belongs to martensite. This steel phase is very hard and wear resistant. For these reasons, it is the wanted steel phase at the surface. The carburizing and quenching sequence have in fact as aim, the formation of a martensite layer at the surface. Furthermore, carbon atoms, being interstitial in the steel, block the dislocations movements and therefore determine an increase in hardness, as seen with work hardening, and also determine a better corrosion resistance. Figure 2. 2, taken from [7], shows in part "a" the FCC crystal structure of austenite, where also the interstitial atom is depicted, and in part "b" the distorted BCC structure that is the body centered tetragonal structure of martensite. In part "b", it is also possible to see the interstitial atom that is creating the structure distortion. A more detailed explanation of these concepts is reported in [8] and [7].

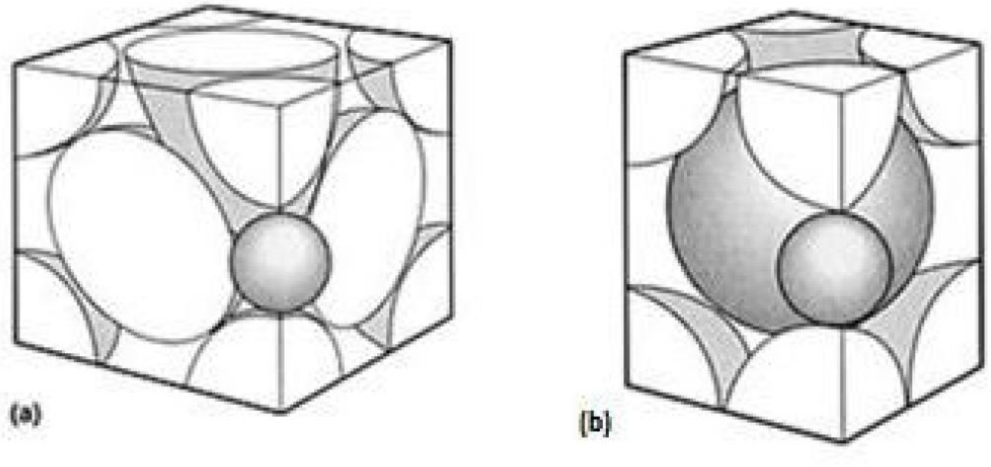

Figure 2. 2: FCC structure of austenite with interstitial carbon atom and deformed BCC structure of martensite, in (a) and (b) respectively. [7]

Surface hardening steels typically have a base carbon content that is quite low, for example around 0.2% [1]. This is done as, having low carbon content, means greater toughness, and so life expectancy. Low carbon content, however, also means lower hardness. So, by choosing a low carbon content as the starting steel, and then performing carburizing, the internal part of the component remains tough, whilst the hard and wear resistant surface is ensured by the carburizing and quenching sequence. With this strategy, the objective of obtaining a high-carbon martensitic surface with good wear resistance and hardness, covering a tough, low carbon steel interior, is met [1].

The carbon content at the surface, however, must not be too high. This because the excessive amount of carbon concentration at the surface leads to the formation of carbides and so to a very brittle microstructure [5]. Furthermore, as explained earlier, the carburizing process is followed by a quenching process, where there is a quick decrease in temperature that determines the formation of martensite. However, as it will be better explained in the following paragraph, the temperature at which martensite starts to form upon cooling is highly dependent on the alloying composition, in particular, on the amount of carbon present [8]. The rule of thumb is that the higher the carbon content, the lower is the temperature at which martensite starts to form. For this reason, if the carbon content at the surface is too high, the martensite starting temperature becomes too low and thus inhibits the formation of martensite [2] [8]. The output of such a scenario is a great amount of untransformed austenite at the surface [8]. However, since austenite is a soft phase, its presence at the surface does not lead to the "high hardness" desired results. For this reason, the amount of carbon content found at the surface after carburizing, must be carefully planned, not to obtain any unwanted results. Values between 0.8% and 1% are usually desired at the surface, as reported in [1]. Of course, the amount of carbon desired depends on the application the component is destined for, and so the properties that it must have.

The diffusion of carbon into steel is affected not only by temperature and carburizing time as mentioned above, but also by the other alloying elements present in the steel. Alloying elements in fact have effects on both the diffusivity and the solubility of carbon into austenite. [9]

The addition of carbon into austenite at the components surface occurs by means of different important processes [5]. These are:

- the reaction of the component surface with the carbon rich environment, that leads to the carbon absorption in the component.
- the diffusion of the carbon atoms inside the component: from the surface and towards the interior of the component.

Different methods for carburizing exist. The different methods differ in the type of medium used to "insert" the carbon atoms within the component. The most common methods are [1]:

- Gas, or Traditional, carburizing: this method uses as medium a gaseous atmosphere.
- Liquid carburizing: this method uses as medium liquid salt baths.
- Pack carburizing: this method uses as medium solid compounds.
- Vacuum carburizing: this method uses carbon-carrying gases as medium within a vacuum atmosphere.

These different methods all have advantages and disadvantages.

As reported in [1], the most used of these methods is the traditional carburizing. In that study, results from a very interesting survey are reported. The survey, comprising 800 commercial shops in the United States of America and Canada, of which only 70% offered carburizing processes, reported that 48% of the commercial shops offered gas atmosphere carburizing, 19% of the commercial shops offered pack carburizing, 12% of the commercial shops offered salt carburizing, 5% of the commercial shops offered carburizing in fluid beds and finally 2% of the commercial shops offered vacuum carburizing. This shows just how vastly more popular the traditional carburizing is with respect to the other methods. The paper [1], written by Seyed Reza Elmi Hosseini and Zhuguo Li was published in 2016.

Each of these methods will be briefly described in the following subsections.

2.2.1.1 Gas Carburizing (Traditional Carburizing)

In traditional gas carburizing, carbon is diffused in the surface by placing the component in contact with carbon carrying gases that, with chemical reactions, release the carbon to the component. A typical example of such a chemical reaction is shown below [10].

$$CO_2 + C \leftrightarrow 2CO \qquad (1)$$

Here, the gas that is inserted in the chamber with the component in order to perform the carburizing operation is CO. This gas, as shown in the reaction shown above in equation 1, reacts with the surface inserting the carbon atoms C inside the component and developing exhaust CO2.

CO is not the only gas with which gas carburization can be conducted, in fact, different other gases such as CO, CO2, CH4, H2, H2O, and N2 can be used [11]. These are generally produced by combustion of natural gas or other hydrocarbon gas.

This method of carburizing ensures good control of the case depth, that is the depth hat the carbon reaches within the component during carburizing. However, dealing with dangerous gases, this method requires the presence of good gas controls. [1]

2.2.1.2 Liquid Carburizing

In liquid carburizing, the task of adding carbon at the surface of the component is carried out by placing the component in contact with a carbon-carrying liquid medium. The process consists in inserting the component in a container where the liquid is present. The latter contains the carbon that must be inserted in the surface. The temperature of the liquid and container is than raised up to a level where the carbon becomes active and spreads withing the surface of the component. This process requires a certain temperature and time, that must be selected in order to obtain the desired carbon content and case depth. The liquid used in the process usually consists of salt solutions. Great care must be placed in selecting the correct salt bath composition, as this affects the final carbon distribution within the component. [12]

An advantage of this solution is the absence of soot related problems and the rapid rate of penetration of the carbon inside the component. Disadvantages of this method are concerning the disposal of the salt solution and the maintenance of the salt bath. An additional inconvenience of this method is the necessity to wash the component after the process. [1]

2.2.1.3 Pack Carburizing

As reported in [1], pack carburizing was once the most used method. It consists in placing the component in contact with coke and charcoal in a closed container at a high temperature. The high temperature provides the energy necessary for the diffusion of the carbon atoms, that are provided to the component from the coke and charcoal. This method is very simple and requires very little equipment. However, it offers limited control on the case depth. This inhibits its operation on all components where the case depth must be carefully controlled. This method, although labor intensive, is still used due to its low equipment cost, and is usually employed for components requiring a deeper case depth rather that a lighter one. [1]

Advantages of this method are the low investments necessary in carburizing equipment. Disadvantages of this method are the limited control on the case depth and carbon profile. [1]

2.2.1.4 Vacuum Carburizing

Vacuum carburizing is performed using gaseous carbon carriers in a low-pressure/vacuum environment. The carbon carriers are usually C2H2, C3H8, and C6H12 [5].

The gaseous carbon carrier in injected in the chamber where it reacts very quickly with the component surface, releasing a great amount of carbon. This injection period is called pulse phase. This pulse phase is then followed by a diffusion phase. During the diffusion period, the injection of the gaseous carbon carrier is stopped, and so also the carbon build-up at the surface is interrupted. Furthermore, during this period, the high temperature allows the carbon content that has formed at the surface during the "pulse phase" to diffuse towards the interior part of the component, therefore reducing the very high carbon concentration at the surface. The pulse and diffusion phases are alternated cyclically. Alternating the two phases is done in order to avoid, or at least bring to a minimum, the soot formation at the surface, by allowing the carbon to diffuse from the surface into the interior of the component and so avoiding excessive carbon build up at the surface. [13]

Advantages of this method are the exceptional control of the process and its good speed compared to the other methods [1]. Furthermore, this method is safe ecologically and saves power [13]. A very important drawback of this method is the high equipment cost [1].

2.2.2 Quenching

In the carburizing-quenching-tempering sequence, that is analyzed in this research, the step that comes immediately after carburizing is quenching. The latter is a quick drop in temperature that allows for non-diffusive phase transformation. During quenching, in fact, the component is placed in contact with a quenching fluid that cools down the component in a very rapid manner.

The quenching fluid can be a liquid or a gas. The different cooling fluids have different cooling properties, and also lead to different properties in the component at the end of the process. For this reason, the selection of the best quenching fluid for the process should be carried out with great caution. Different studies have been made in order to study the properties of the two types of cooling fluids, both of which are used in the manufacturing industries.

Over the years, quenching with inert gases has become more popular as it gives great advantages with very few drawbacks. In fact, as expressed in [14] and [15], although it generally determines lower cooling rates with respect to quenching with a liquid, it also reduces the onset of unwanted deformations in the steel due to too high temperature gradients. Furthermore, it utilizes a quenching medium that is much cleaner than the oils usually used when quenching with liquids, determining no toxic waste gases. Furthermore, whilst the gas-cooling heat transfer coefficients show very little temperature dependence and so a homogeneous heat transfer is guaranteed during the quenching process, most liquid quenching mediums such as water or oil have distinct boiling points, and thus different heat transfer mechanisms at various temperature stages, making the heat transfer nonhomogeneous and so more difficult to control. [14] [16]
The study presented in [17], also confirmed numerically that quenching with gases is more environmentally friendly with respect to quenching with liquids.

During quenching, the most important phenomena that occurs in the component, happens at the microstructure level, where different steel phase transformations occur. These phase transformations happen when the microstructure found during carburizing, that is austenite, transforms into various different microstructures, depending on the cooling rate. In particular, considering the high cooling rates experienced, the most likely microstructures that can be found at the end of quenching are bainite, martensite, and retained austenite, where the latter includes all of the austenite that did not transform into other phases during cooling.

In fact, the other steel phases that can generally be found in steels, that are perlite and ferrite, are stable phases that can be seen in the iron carbon-diagram and that are formed when much lower cooling rates with respect to those associated with quenching are experienced [18]. The iron-carbon diagram is a graph where the area of presence of different stable steel phases is plotted against the temperature for different mass percentages of carbon in the steel [19]. An iron-carbon diagram is shown in Figure 2. 3. A close-up of this graph, referring only to the steel portion, is shown in Figure 2. 4. Steel refers to iron-carbon mixtures where the carbon present in less than 2%. If more than 2% carbon is present, the mixture is called cast iron [20] [19].

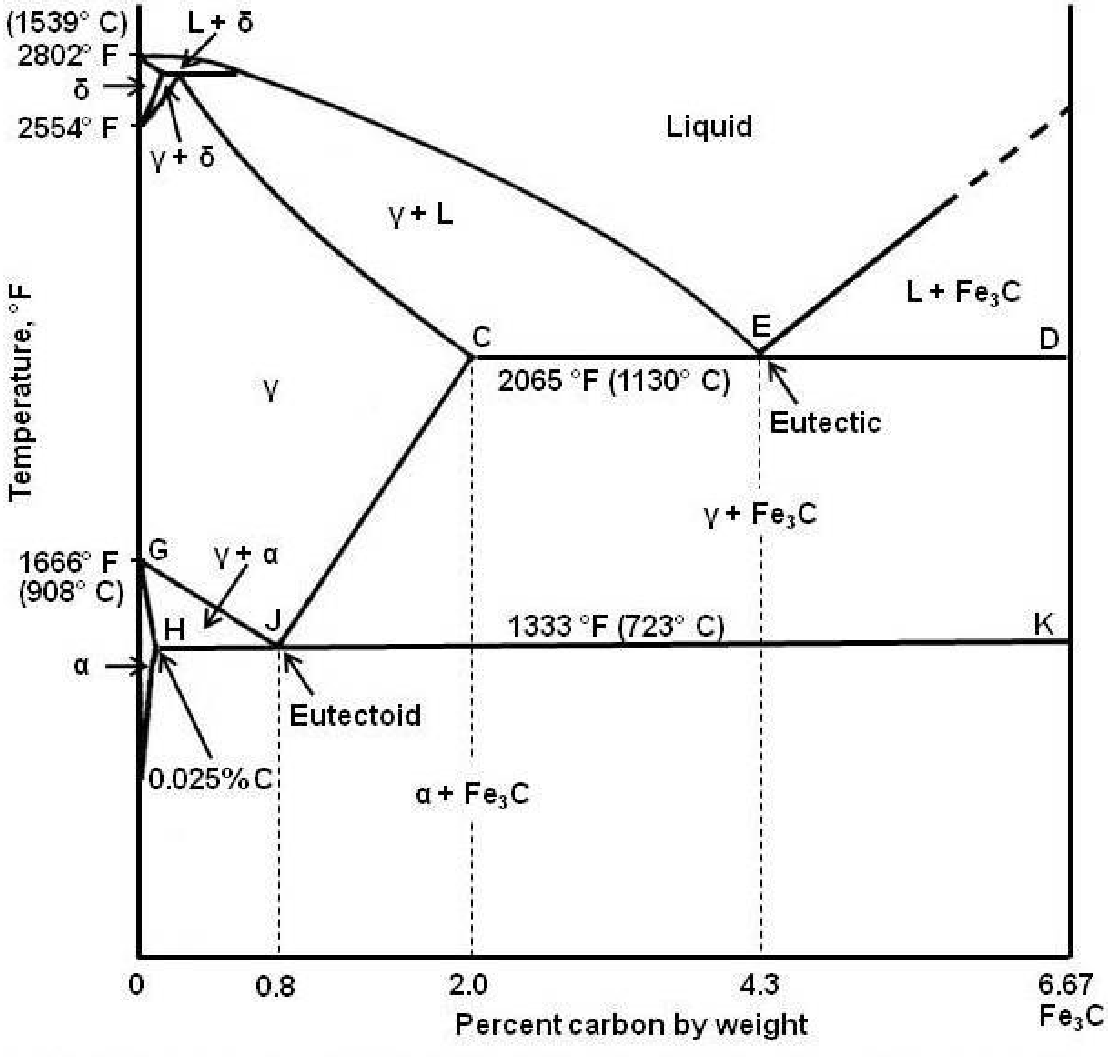

Figure 2. 3: Iron-Carbon diagram. [20]

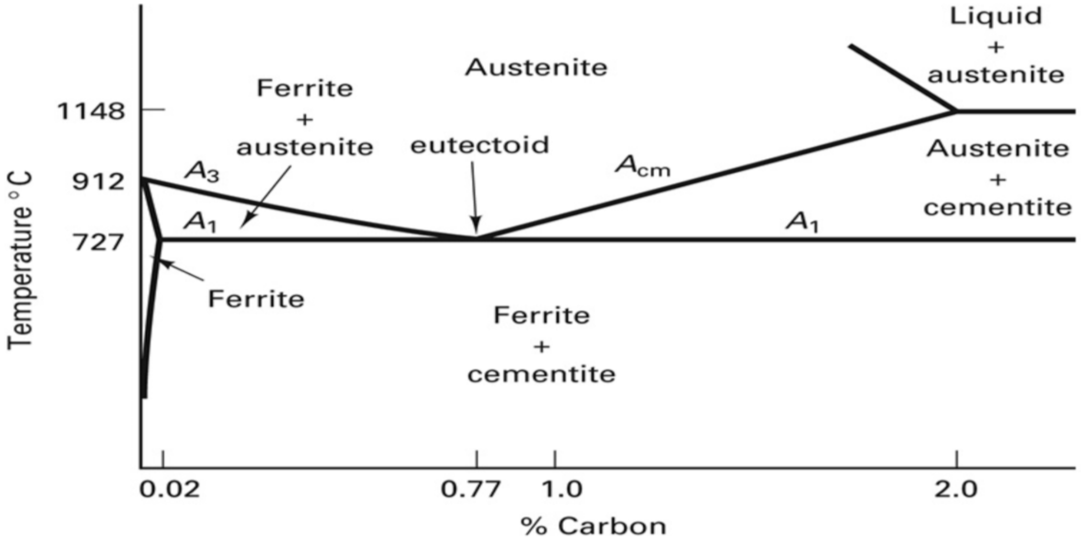

Figure 2. 4: Zoom-in at region below 2% of carbon in Iron-Carbon diagram. [21]

The iron-carbon diagram shows the area at which the different steel phases are stable [19]. However, due to the very high temperature gradient experienced during quenching, the phase transformations that will occur during quenching, will not follow what can be seen in the iron-carbon diagram, because they occur far from the equilibrium that the diagram is referring to.

A deeper look at the microstructures most likely to be found at the end of quenching: bainite, martensite and retained austenite, will be given in the following paragraphs.

2.2.2.1 Austenite

Austenite is a solid-state solution of iron and carbon that is found in steel. The space lattice of austenite is face-centered cubic, as shown previously in Figure 2. 2 part "a". In this structure, all three axes of the unit cell are of the same length and are mutually perpendicular. There are a total of four atoms per unit cell. [22]

Austenite is present in a stable form above the austenitization temperature. This temperature is, as shown in Figure 2. 4, of around 727°C. However, it must be noted that this temperature is dependent on the alloying composition. The relation between this temperature and the different alloying elements is known and formulations are available in literature for its prediction. This temperature forms, on the graph shown in Figure 2. 4, an horizontal line that is the eutectoid line. This line, represents the temperature above which the different phases present in the steel change their structure during heating, becoming austenite. [19]

Austenite has a fundamental role in the heat treatment of steels as, most of the phenomena related to steel processing, are based on the transformation of austenite to the other phases upon cooling. These transformations allow the formation of a great variety of different microstructures. Austenite can therefore be regarded as the parent phase for all the other phases upon cooling. [22]

Austenite is stable only at high temperatures. However, it can also be present at low temperature. This happens when, for some reasons, the austenite cannot manage to transform into the other phases upon cooling. In this scenario, the austenite is referred to as retained austenite. This happens for example in the case, also previously described in the carburizing paragraph, where the carbon content at the surface is very high, and so the transformation to martensite is hindered so much that the austenite, not being able to transform, is found at the surface also at low temperatures. [2] [8]

2.2.2.2 Bainite

Now that the "parent phase" has been described, the structure of bainite will be discussed. Bainite is a structure phase that is formed starting from austenite upon cooling. Bainite is formed with diffusive transformations and is created by ferrite and cementite, where ferrite is very ductile and soft, and cementite is hard and brittle. Two different types of bainite are generally encountered: upper and lower bainite. Upper bainite is formed at higher temperatures and presents a structure more similar to that of perlite, that is made up of alternating layers of ferrite and cementite. The properties of upper bainite are also similar to those of perlite and so it is tougher and less hard with respect to its lower counterpart. The concepts mentioned above for bainite were taken from [23], were bainite is very extensively discussed. Figure 2. 5, also taken from [23], shows the microstructure of upper bainite formed in a 4360 steel, isothermally transformed at 495 °C.

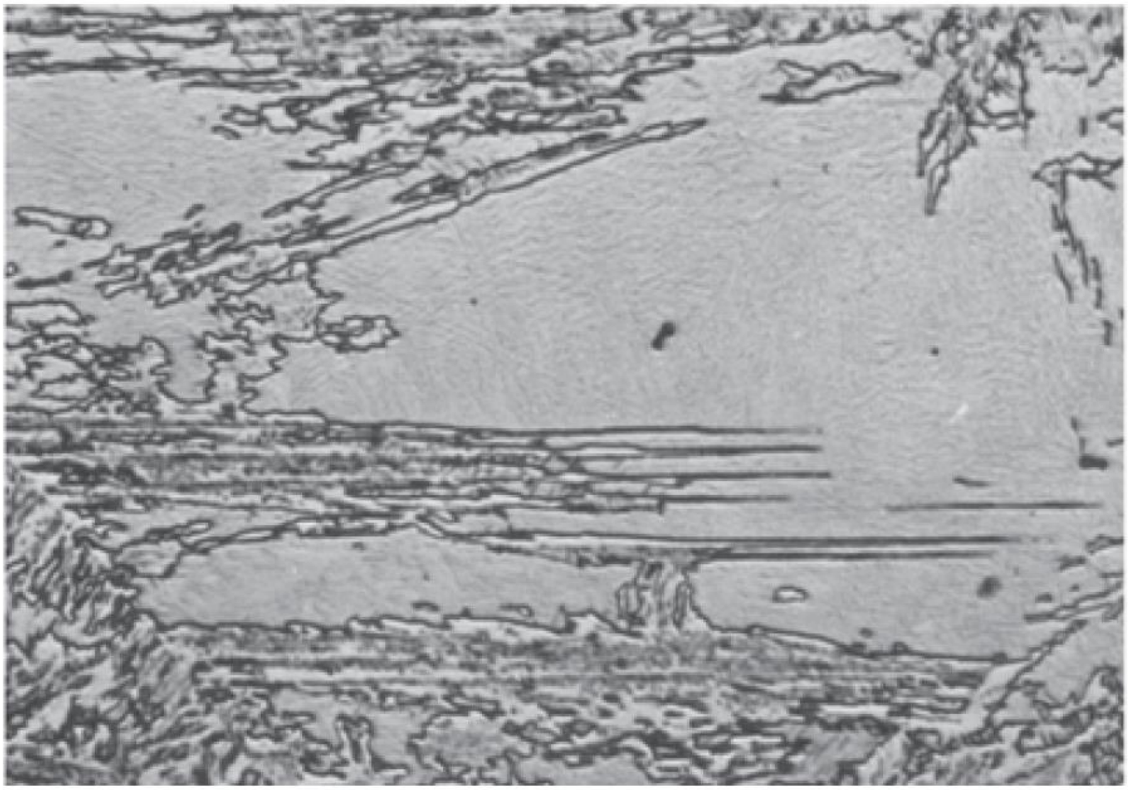

Figure 2. 5: Upper bainite microstructure formed in a 4360 steel, isothermally transformed at 495 °C. [23]

Lower bainite on the other hand is created at lower temperatures and has a structure and properties more similar to those found in martensite. The product is always quite tough, but also harder with respect to upper bainite. [23]

Figure 2. 6, also taken from [23], shown the microstructure of lower bainite found in 4360 steel, transformed at 300 °C.

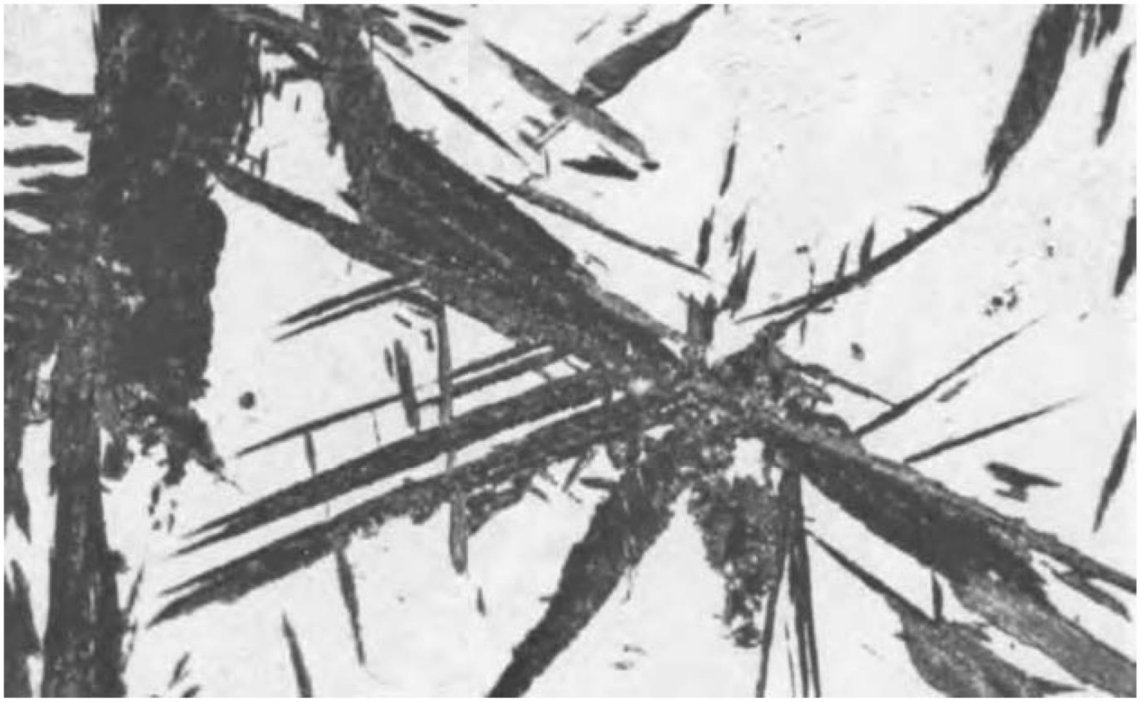

Figure 2. 6: Lower bainite microstructure found in 4360 steel, transformed at 300 °C. [23]

The transformation from the parent austenite into bainite can be studied by looking at the TTT diagrams. These diagrams illustrate the transformation from the parent phase austenite into perlite, bainite, and martensite upon cooling. This kind of diagram is displayed in Figure 2. 7, taken from [23].

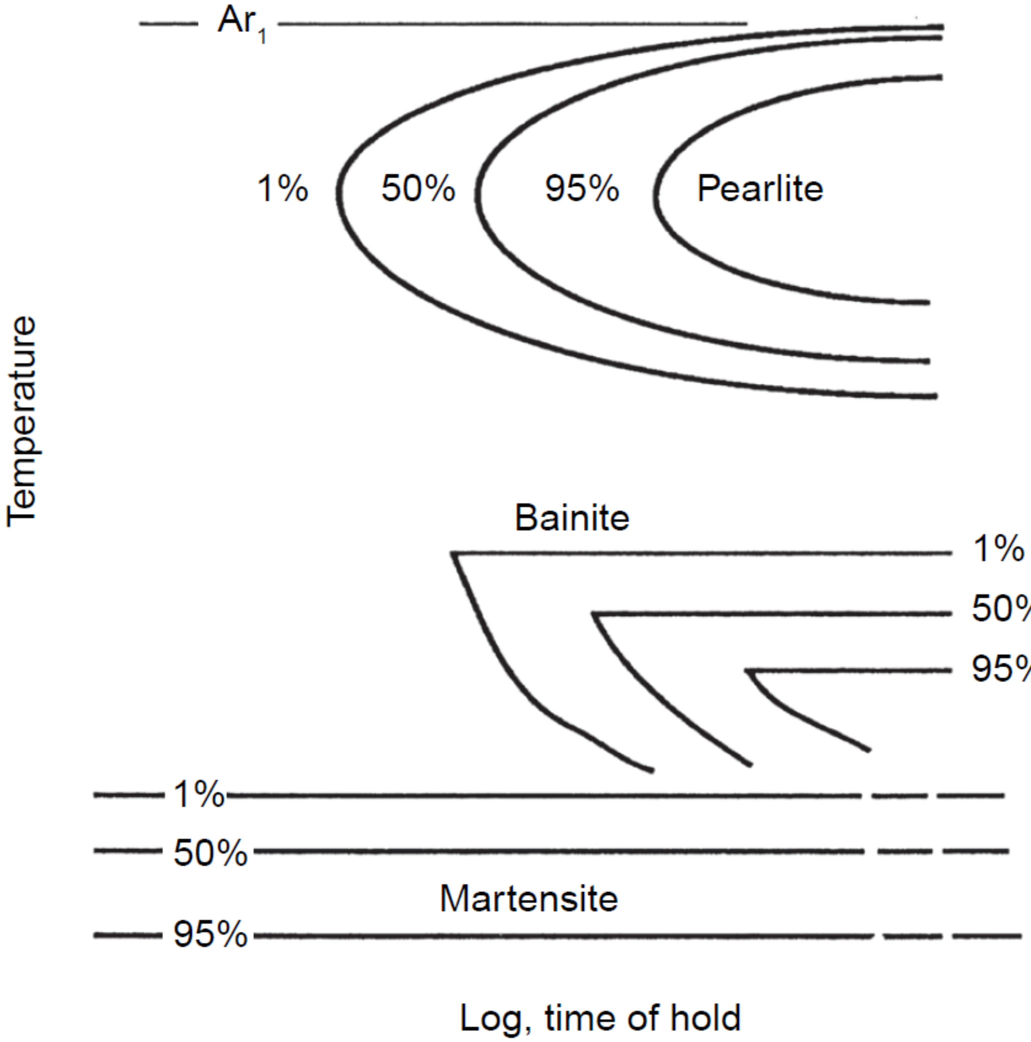

Figure 2. 7: Qualitative TTT diagram. [23]

In this graph, the abscissa indicates the time at which a certain temperature is kept constant, whilst the ordinate indicates the temperature value. On the graph, three different regions can be distinguished. The region where perlite is formed, that is at higher temperatures, the region in which bainite is formed, and finally the region in which martensite is formed. It is possible to see that for each of the regions, also an indicator of the percentage of completion of the phase transformation is displayed. This type of graph is much more relevant when studying quenching with respect to the iron-carbon diagram that was presented before. In fact, by using the TTT diagram, the transformations from austenite into the different steel phase during cooling can be predicted if the temperature profile that the component experiences during cooling is known. This means knowing the temperatures that the component will experience and for what amount of time. It must be noted, in fact, that the TTT diagram can predict the phases formed during cooling only for isothermal transformations. Therefore, in order to predict the steel phases transformations during cooling using TTT diagrams, the cooling curve must be known and divided into many isothermal segments, that hence allow the use of TTT diagram for phase prediction. This method, and the studies about it, will be explained in greater detail in the following methodology chapter when discussing the phase transformations. However, if the component has been previously carburized, the TTT diagram, as again it will be described in greater detail in the following methodology chapter, cannot be used for determining the amount of the different steel phases that form during quenching. This, because the temperatures in the TTT diagram at which the different steel phases start to form, are highly dependent on the alloying composition, particularly on the amount of carbon present [8] [23]. For this reason, in order to use the TTT diagrams to predict the different phase transformations, different TTT diagrams should be used for each location within the component where the alloying composition differs. This concept, and the studies about it, will be more extensively discussed in the methodology chapter when discussing the steel phase transformations.

The TTT diagram, also explains why perlite is not usually found after quenching. In fact, looking at Figure 2. 7, it is possible to see that perlite is formed when high temperatures, just below the Ar1 temperature at which austenite starts to transform, are kept for a very long amount of time. Clearly this is not the case with quenching, where the temperature decreases very quickly. Bainite formation is instead more likely during quenching, as this steel phase, as it is possible to see from Figure 2. 7, forms at much lower temperatures.

2.2.2.3 Martensite

From the TTT diagram shown in Figure 2. 7, it is possible to see that, unlike what seen for perlite and bainite, the transformation into martensite is independent on time. In fact, the transformation into martensite does not require a certain holding time but only the temperature to be below a certain threshold. This because the transformation into martensite, as discussed previously in the carburization paragraph, is not diffusive, and so does not require a certain amount of time for diffusion to occur, but it is rather an immediate transformation that occurs when the temperature goes below the martensite start transformation temperature, that is the threshold mentioned above [8]. This temperature threshold, as mentioned before, is highly dependent on the alloying concentration and, if too low, can lead to the formation of untransformed austenite. The non-diffusion transformation is the cause of the particular structure of martensite, that, as explained earlier and illustrated in the image taken from [7] and displayed in Figure 2. 2 part "b", is a deformation of the BCC structure due to the presence of an interstitial carbon atom. It is therefore evident that martensite is a metastable phase, that is present only due to the fact that, because of the very high cooling rate, the diffusion has been blocked [8].

Since no diffusion is present and so the transformation is dependent only on the temperature and not on the time, the evaluation methods to find out the amount of austenite transformed into martensite during cooling will reflect this situation. This is the case with the equation developed by Koistinen-Marburger [24], that describes the transformation of austenite into martensite. This formulation will be reported and discussed more in detail in the methodology chapter.

The deformed structure mentioned above, leads to martensite having a very high hardness and surface resistance. These properties are very important and are desired at the surface of components such as those used in the automotive powertrain systems. However, martensite is also very brittle. In order to reduce the brittleness and make the surface a little bit more tough, tempering is performed on the quenched components. [25]

2.2.3 Tempering

Tempering is an increase in temperature that is applied to the component after the quenching operation. The tempering temperature is kept below the austenitization temperature, that is that at which the different phases transform into austenite during heating. This increase in temperature, has the aim to allow the diffusion of carbon atoms that was inhibited during the quenching operation, due to the very fast cooling rate. The diffusion of carbon atoms, allow these to move from the oversaturated martensite. This diffusion determines a decrease in the strength and hardness, but also a much-wanted increase in toughness [8]. The temperature and time for the tempering must be carefully selected depending on the desired properties in the heat-treated component. As a general trend, tempering at higher temperatures and for longer times favor a faster diffusion of carbon atoms away from the martensite, and so a quicker decrease in hardness and strength of martensite. Overall, the increase in temperature for a prolonged time tends to approach to an equilibrium mixture of phases, more so with increasing tempering intensity. The concepts mentioned above for tempering were taken from [25], where tempering is very extensively discussed.

2.3 *Most Relevant Simulations*

After having briefly explained the principles of carburizing-quenching-tempering, the most relevant simulations found in the literature will be discussed. However, before doing so, the complex phenomena that occur during these heat treatments, are introduced. The phenomena and their interactions can be summarized as shown in the graph reported below in Figure 2. 8.

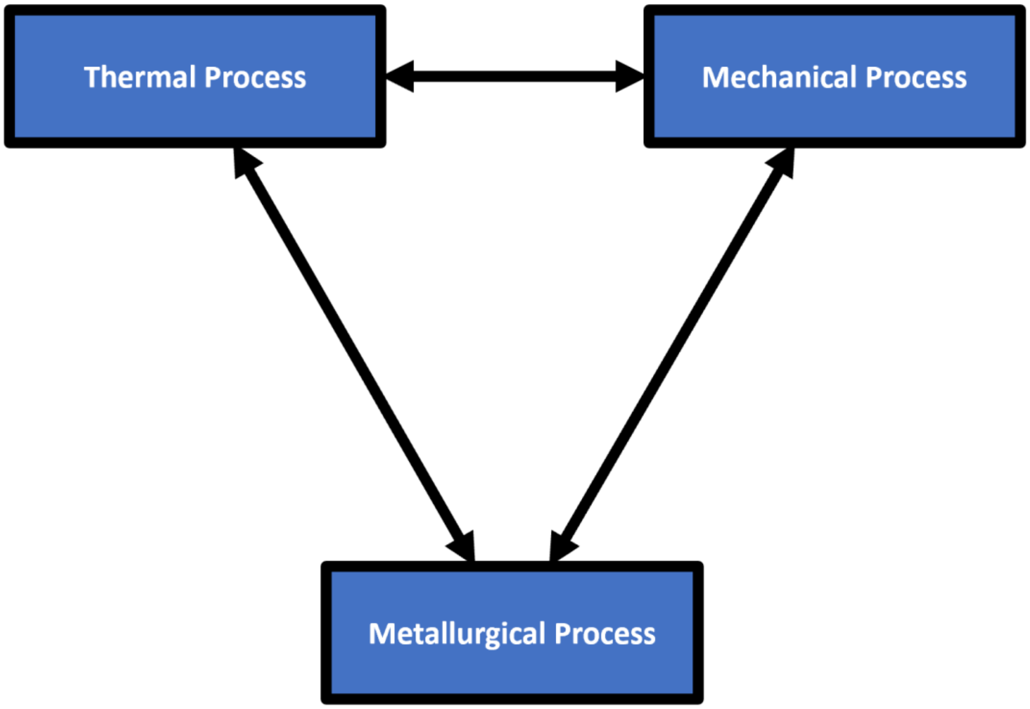

Figure 2. 8: Complex phenomena found in heat treatments.

As it is possible to see, there are three main areas that interact and influence each other. These areas represent three different types of phenomena: metallurgical, mechanical and thermal.

The thermal field interacts with the mechanical field, as the strong temperature decrease during quenching generates a great amount of strains and deformations in the component. The relation also goes in the other direction. For what regards the thermal-metallurgical relation, this can be seen when considering that the temperature field variations determine the different phase transformations. A consequence of the phase transformations, as it will be later explained in greater detail in the methodology chapter, is the release of different amounts of heat, dependent on the types of phase transformations that are encountered. This heat release therefore affects the temperature field. For what regards the relation between the mechanical and metallurgical fields, this can be found when considering that the phase transformations mentioned above cause strains that are due to the difference between the diverse crystalline structures of the steel phases. This effect and its implementation in the simulation tool will be better explained in the methodology chapter. All of these effects are important and must be considered for the simulation of heat treatments. The concepts regarding these interactions were taken from the studies [2] and [3]. In these two studies, similar graphs to that shown in Figure 2. 8 are also found.

During my literature review, many different studies were found that dealt with the “heat treatment simulation” topic. The simulation of heat treatments in fact, due to the great advantages seen in the introductory chapter, and due to the fundamental role of heat treatments in many different industries, was studied in great detail during the course of the past years. What resulted, was the creation of many different papers discussing different methodologies and using different software to perform the heat treatment simulations. In this chapter I will explain with greater detail the studies deemed more important for the thesis research.

The study performed in [2], regards the simulation of the laser surface hardening. In this heat treatment, laser is applied at the component’s surface. The laser determines a quick increase in temperature, eventually followed by a quick drop in temperature when the laser beam is ceased. This generates effects similar to those seen during quenching, so, although the heat treatment simulated is different from the carburizing-quenching-tempering sequence analyzed in this research, this study is very useful to analyze the method with which quenching can be simulated. In this study, ABAQUS with the addition of user subroutines is used. The solution that is adopted in this study can be summarized as shown in the scheme shown in Figure 2. 9, that was taken from [2].

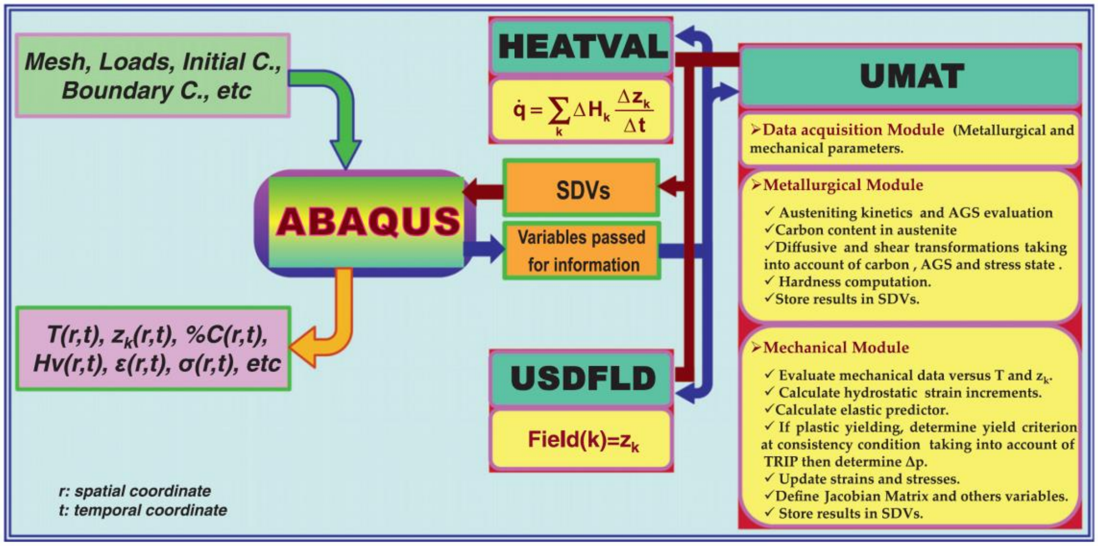

Figure 2. 9: Scheme to model the heat treatment simulation of steels in ABAQUS, as presented in [2].

In this scheme, the general working principle of the simulation tool is explained. The green arrow indicates the inputs to the simulation tool. These include the material properties and the component geometry, along with all of the boundary conditions necessary to correctly simulate the heat treatment problem. These inputs are provided to ABAQUS. The blue arrow in the scheme shows the flow of information from ABAQUS to the external codes, that are the user subroutines. In this study, three different user subroutines are considered. These are codes that are used to study different metallurgical related effects that are not already simulated in ABAQUS. All the different user subroutines, with different names, have different, specific purposes.

These codes, to be applied in the simulation, must be introduced in ABAQUS. This to advise the general purpose to look for, and apply, the user subroutines. An example of a message presented in ABAQUS, that appears when the use of a user subroutine is introduced, is presented in Figure 2. 10.

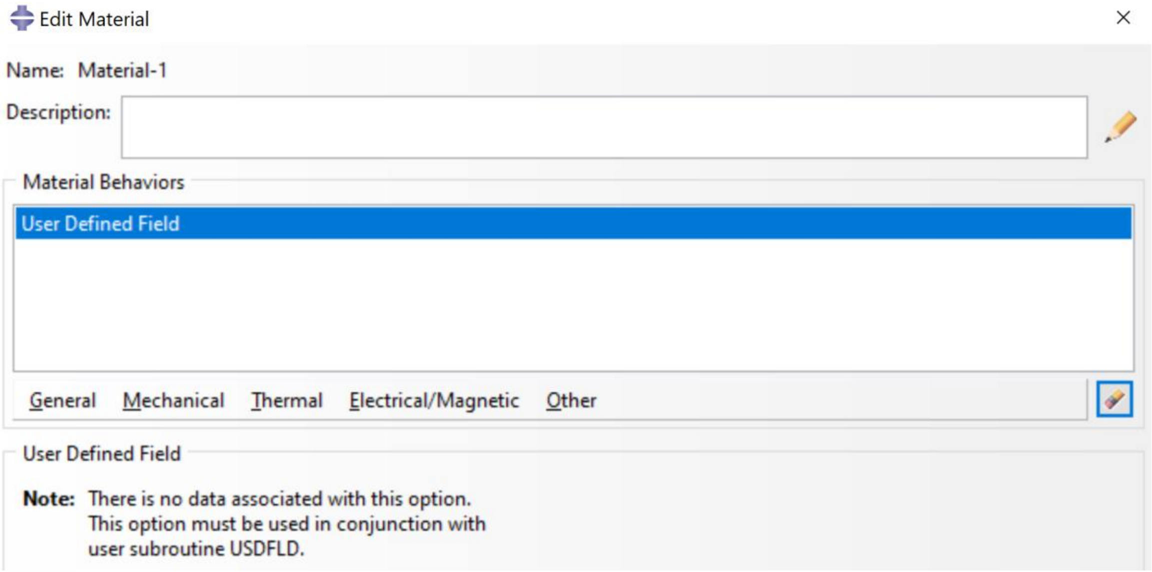

Name: Material-1

User Defined Field

User Defined Field

Note: There is no data associated with this option.
This option must be used in conjunction with
user subroutine USDFLD.

Figure 2. 10: User subroutine USDFLD introduction in the material property definition section in ABAQUS.

The text shown in Figure 2. 10, in particular, appears when the “User-defined field” property is selected. This is done in the ABAQUS section where the material properties are defined. It is possible to see from the image that the message: “There is no data associated with this option. This option must be used in conjunction with user subroutine USDFLD”, appears. This message, states that the user subroutine USDFLD must be given as input in the study. This stands to show that ABAQUS is aware on the presence of the subroutine in question and will be looking for it in order to apply it in the simulation. In the example shown in Figure 2. 10, the introduction of the user subroutine is done in the material property definition section of ABAQUS. This, because the user subroutine USDFLD is of vital role in the correct definition of material properties, as it will be described further on in the paragraph. However, the user subroutines can be used for other purposes rather than material properties definition. In fact, they can be used to define loads, interactions, and also boundary conditions. In these cases, the specific user subroutine for each phenomenon that is to be simulated must be introduced in ABAQUS in the correct section of the general purpose. For example, if the user subroutine FILM is to be used, this subroutine will be introduced in ABAQUS in the "Interaction" section, as the main purpose of this subroutine is to modify the heat transfer coefficient and temperature of a fluid interacting with the component. Documentation for the FILM subroutine is found in [26].

In the study shown in [2], three different user subroutines are used: UMAT, USDFLD and HETVAL. The first subroutine is the most complex of them all. It in fact requires the user to determine and define the mechanical constitutive behavior of a material. This, as also mentioned on the online guide [27], requires considerable expertise. It is also mentioned in the online guide that "the implementation of any realistic constitutive model requires extensive development and testing". This user subroutine is used in [2] to make up for most of the important effects related with the heat treatments, that are not already available in ABAQUS. In particular, in [2], this subroutine accounts for: the effects of the temperature on the phase transformations, the evolution of stresses and strains, the evaluation of the hardness profile, the evaluation of the deformations, and also the effects of the temperature on the carbon diffusion, that is caused by the high temperatures involved and affects the phase transformation temperatures. This user subroutine, as it can be seen, incorporates many different functions. A second subroutine that is used in [2] is HETVAL. This subroutine accounts for the effects of latent heat of transformation. This is a heat release that is associated to the phase transformations and has a magnitude that depends on the type of phase transformation analyzed and on the amount of phases transformed. Documentation for the HETVAL subroutine is found in [28]. The last subroutine used in [2], USDFLD, is also incredibly important as it allows the user to define field variables "FIELD(n)" that are used to relate the material properties at each location to the temperature and to the amount of different steel phases present. This subroutine is also very important as it allows to create some user-defined variables called SDV's, that are very important as they can be visualized in the ABAQUS post-processor. Documentation for the USDFLD subroutine is found in [29]. The blue arrows in Figure 2. 9, that show the interaction between the different subroutines, show that the subroutines also interact with each other and not exclusively with ABAQUS. The SDV's, that are defined in USDFLD, can in fact be updated in the other subroutines or can just be passed on for information. These are then then provided back to ABAQUS, where they are displayed in the ABAQUS post-processing, as shown by the red arrows. Finally, the orange arrows in Figure 2. 9, show the outputs of the ABAQUS-subroutines combination. These comprise the temperature field, deformations, carbon percentage, hardness profile, phase distribution and stresses. All of these results are then presented and validated in the study [2].

A second study that is considered to be very important for this research is that presented in [30]. Also in this study, the thermo-mechanical-metallurgical relations that are found when simulating heat treatments such as quenching and tempering, are implemented in ABAQUS with the use of subroutines. In this case, however, a different approach to that used in [2] is found. The difference between the two studies resides in the choice of user subroutines. A sketch, representing the ABAQUS-subroutines interactions as modelled in [30], is shown in Figure 2. 11.

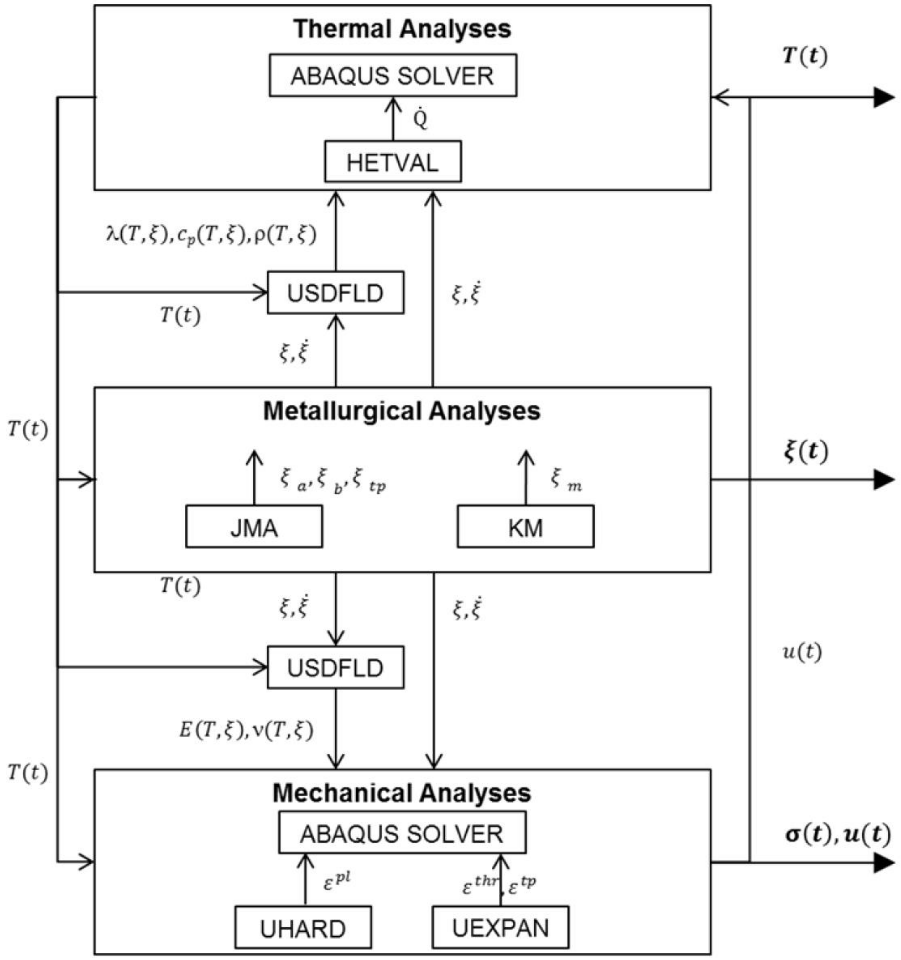

Figure 2. 11: Scheme to model the heat treatment simulation of steels in ABAQUS, as presented in [30].

In this study, as it is possible to see, many more user subroutines are implemented with respect to the previous study presented above. In fact, linked to the ABAQUS solver, there are six different subroutines: USDFLD, UHARD, UEXPAN, JMA, KM and HETVAL. The reason why so many different subroutines are used, is to avoid the usage of UMAT. This is done because, as previously mentioned, the UMAT subroutine is particularly hard to create and requires great expertise. In addition to this, as reported in [30], the UMAT subroutine is also very computationally expensive and not particularly efficient. For this reason, the main aim of the study presented in [30] was to develop a tool to simulate the complex interactions that occur during heat treatments without the use of the very challenging subroutine UMAT. Avoiding the use of the latter, the functions once performed by that subroutine are somehow redistributed between different other subroutines. The evaluation of the different phase transformations during quenching is performed in the two subroutines JMA and KM. In fact, the names of these subroutines, that were created by the authors, are the initials of "Johnson–Mehl–Avrami" and "Koistinen-Marburger". Koistinen and Marburger are the surnames of the developers of the Koistinen-Marburger equations, that are used to determine the amount of martensite formed. Johnson, Mehl and Avrami are the surnames of the developers of the formulations used to evaluate the amount of diffusive transformation phases that are formed upon cooling: ferrite, perlite and bainite. These two subroutines, as shown in the graph, connect and provide information to all other subroutines. The user subroutine USDFLD has the same function that was explained before. In fact, it obtains the information regarding the different phase fractions that are generated ξ, and the phase generation rates $\dot{\xi}$, from the two subroutines KM and JMA, and it uses this information to create field variables with which to select the most suitable values of the material properties according to the amount of different steel phases present. These material properties, as displayed in the scheme shown above, include the elastic constant E, the Poisson's Ratio v, the thermal conductivity λ, the density ρ, and the specific heat c_p. As mentioned before, this subroutine is also used to create some SDV's that can be displayed in the ABAQUS post processing and that can be updated or passed in as information to the other subroutines. This can be used, for example, to show the amount of a particular steel phase present in the component at any instant in time at a particular location. USDFLD then, as shown in Figure 2. 11, provides the steel phase fraction information to the last three remaining subroutines: HETVAL, UHARD and UEXPAN. The first one of the three was implemented also in the previous method used in [2] and has the same function of accounting for the latent heat of steel phase transformations. The subroutine UHARD is used in the simulation to evaluate the plastic strain that is found in the component due to the heat treatments. Documentation for the UHARD subroutine is found in [31]. Finally, the subroutine UEXPAN is used to introduce in the simulation all of the other strains that are experienced by the component. These are the strain due to thermal expansion, the strain due to the phase volume difference and finally the strain due to transformation induced plasticity (TRIP). Documentation for the UEXPAN subroutine is found in [32]. Again, as for the previous study, the methodology just presented was tested by the author and it was validated. The simulations performed were concerning a cylindrical workpiece on which a sequence of austenitizing, quenching and tempering were performed.

A third study, that conducted by Bortoleto et Al. in [3], also examined the simulation of the complex thermo-mechanical-metallurgical relations that are found when dealing with heat treatments. In that study a very similar approach to that just explained is found. In fact, the ABAQUS-subroutines combination is used and a scheme as that shown in Figure 2. 12 is followed.

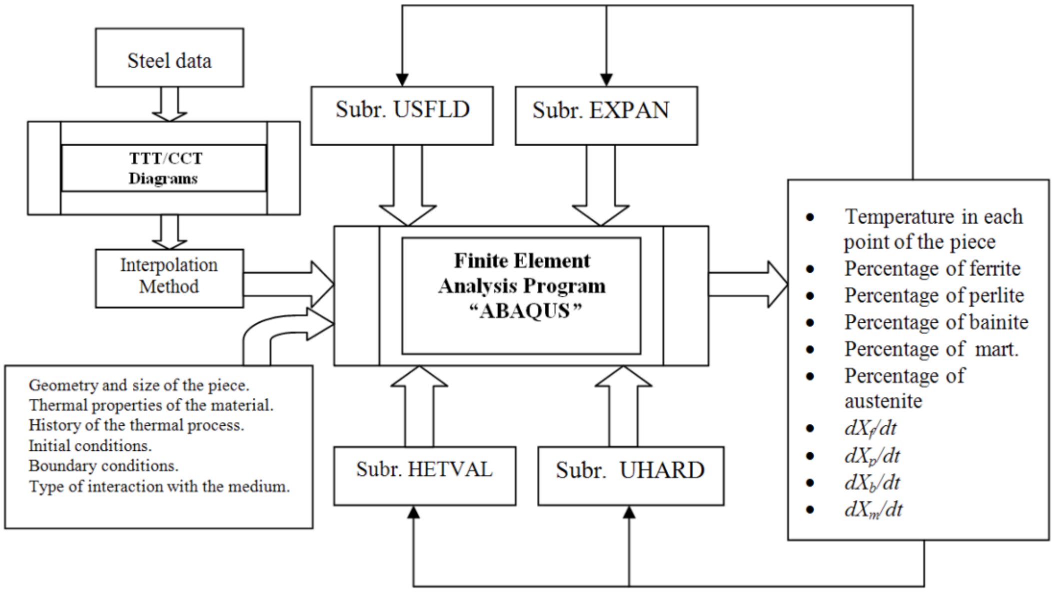

Figure 2. 12: Scheme to model the heat treatment simulation of steels in Abaqus, as presented in [3].

In Figure 2. 12, in fact, it is possible to see that, again, there are different subroutines that are used and, again, the subroutine UMAT is avoided due to its being very complicated. A certain number of inputs must be inserted into ABAQUS. These are regarding the properties of the material, the component design, the initial and boundary conditions, and also the type of interaction of the component being heat treated with the cooling medium. These inputs are given to ABAQUS that, with the use of some user-defined subroutines, provides some outputs such as the temperature field within the component, the amount of the different steel phases present, and the phase formation rate. In this study, four different subroutines are used: USDFLD, HETVAL, UHARD and UEXPAN. It is possible to see that the two subroutines KM and JMA, that were evaluating the phase transformations in the [30] study discussed previously and that were created by the authors, are not present in this study. This is because the phase fractions evaluations, in this study, have been integrated in the USDFLD subroutine. This being the case, the methodology of this study is actually the same as that seen in [30], with the only difference that in this study the subroutine USDFLD has also the additional function of evaluating the phase transformations. As for the two previous studies, also in this case the simulation tool is validated by performing simulations and then comparing the results with some available in previous literature. This validation was done considering three different components: a cylinder, a Navy-C ring and a gear.

It must be noted, however, that the three studies mentioned above, all evaluate the phase fractions with the combination of the Koistinen-Marburger equation for martensite, and the Johnson–Mehl–Avrami equations for ferrite, perlite and bainite. The implementation of the Johnson–Mehl–Avrami equation, however, requires as input information on the TTT diagram of the material used in component. This method is explained in detail in the methodology chapter. However, the TTT diagram, as explained in the previous paragraph, is greatly dependent on the alloying composition of the steel. For this reason, this method to study the steel phase generation, cannot be used to accurately predict the rate of formation of the different phases when a component having a varying alloying composition is considered.

This, however, is not a problem for the three studies mentioned above, because in these the carburizing process was not simulated, and so the alloying composition was considered to be uniform within the component. However, if the quenching process, where the phase transformations take place, is preceded by carburizing, the assumption of having uniform alloying composition within the component cannot be used due to the variations in carbon content at different depths. In fact, in order to use this phase transformation evaluation method when carburizing is considered, different TTT diagrams should be used for each location where a different alloying composition is found. This last concept would be extremely difficult to be applied as many different experimental TTT diagrams should be evaluated for the different alloying compositions.

Nevertheless, the rest of the methodology used in the previous papers is very interesting and instructive for the development of the simulation tool that is created in this thesis research.

Another very important and interesting study, is that reported in [33]. In this study, as for the previous three, ABAQUS, with the addition of user subroutines, is used to simulate heat treatment processes. In this case, however, also the carburizing process is considered, that was not included in the three previous studies. This study was in fact made as in the years many attempts were made to simulate the quenching and tempering problem, or the carburizing and quenching problem, but few were made to simulate the three processes (carburizing, quenching and tempering) together. In this study, the traditional carburizing is studied. In this simulation tool, a program is created where, when provided with the correct inputs, the simulations of the three heat treatments are performed in sequence and the wanted final results are returned to the user. A scheme of this integrated simulation tool is shown in Figure 2. 13, that was taken from [33].

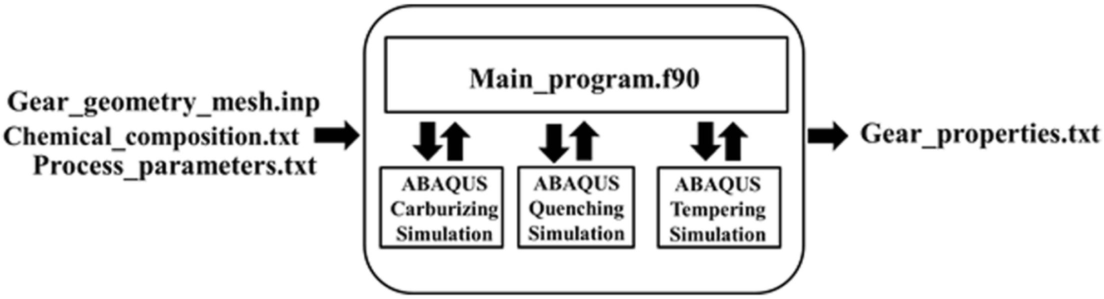

Figure 2. 13: Structure of steel heat treatment simulation tool created in [33]. [33]

It is possible to see that a set of inputs consisting of the component geometry and its mesh, a text file containing the chemical composition information of the material used, and a text file containing all information regarding the process parameters, are provided to the main program. The main program is written in Fortran language and performs the simulations of the three heat treatments in sequence. In fact, at first the carburizing simulation is done, then the quenching simulation is performed utilizing the results obtained from the carburization study, and finally the tempering simulation is conducted using information obtained from the quenching simulation. The program, at the end of the simulations, provides as output a text file containing all of the simulated properties.

A better understanding of the interaction between the three simulations and the flow of information from one another is obtained when looking at Figure 2. 14, also taken from [33].

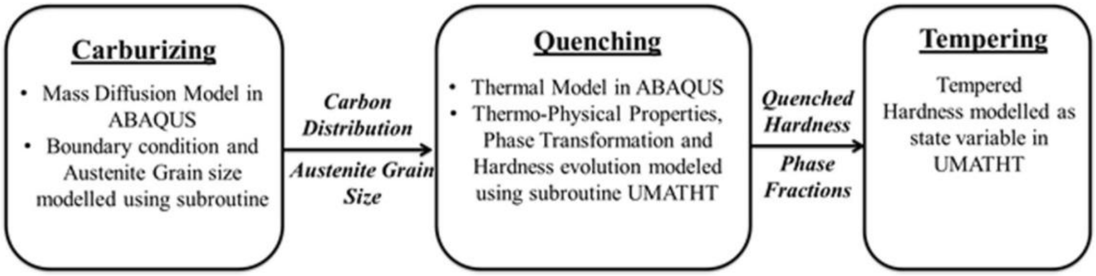

Figure 2. 14: Flow of information between the carburizing, quenching and tempering simulations in the simulation tool created in [33]. [33]

It is possible to see that the carburizing simulation is performed first. The simulation is done considering traditional carburizing and is performed by applying Fick's law of diffusion to study the diffusion of carbon atoms within the component. This method will be discussed in greater detail in the methodology chapter, where the simulation of traditional carburizing is also covered. In order to simulate the flux of carbon atoms from the gas carrying atmosphere to the component surface, a subroutine called DFLUX is used. This subroutine is used in ABAQUS, when performing a mass diffusion analysis, in order to implement a user-defined flux to a surface. In this case, a carbon atoms flux is simulated. Documentation for the DFLUX subroutine is found in [34]. The carburizing study, performed in ABAQUS using also the DFLUX subroutine, provides as output the carbon distribution within the component and the austenite grain size, that is evaluated with an experimental equation.

This information, as shown in Figure 2. 14, is then used as input, along with other process parameters that are describing the operation of the quenching heat treatment, to perform the quenching simulation. This simulation, instead of using a set of subroutines as seen with the previous papers, is performed using only one user subroutine: UMATHT. This subroutine evaluates phase transformation kinetics and the hardness profile, and assigns the thermo-physical properties of the material based on the temperature and amount of different steel phases present. In this study, however, the quenching is considered only as a thermal analysis problem. In this type of study, the strains and stresses are not considered. Information on the deformations is therefore absent.

The steel phase transformations, as mentioned above, cannot be correctly identified by using a method that evaluates the phase transformations staring from the TTT diagram of the material, when the alloying composition is not uniform. For this reason in this study, where the carburizing procedure is considered unlike in those previously discussed: [3], [30] and [35], the diffusive transformations are evaluated using a set of differential semi-empirical equations developed by Li et al. [36]. These equations relate the rate of formation of the steel to the previous austenite grain size, to the amount of steel phases already formed, to the alloying composition, and to the temperature field. With these equations, the varying carbon content is taken into consideration when evaluating the phase transformations. On the other hand, for the non-diffusive transformation that determines the formation of martensite, the Koistinen-Marburger equation, that was used also in the studies analyzed before and that does not depend on the TTT diagrams but only on the undercooling below the starting temperature of formation of martensite, can be applied.

Finally, the tempering simulation is performed using as input the information on the hardness of as-quenched martensite and the amount of the different steel phases present. This information is provided from the results of the quenching simulation. In this study, tempering is not simulated as a physical process by increasing the temperature of the component in the simulation, but rather it is simulated by considering the effects that tempering has on the hardness profile of the component. This is done by considering the Jaffe-Holloman relation and considering previous experimental data on martensite hardness after one-hour tempering for various low alloy steels. This method will also be illustrated in greater detail in the methodology chapter.

This entire procedure is also summarized in the Figure 2. 15, also taken from [33].

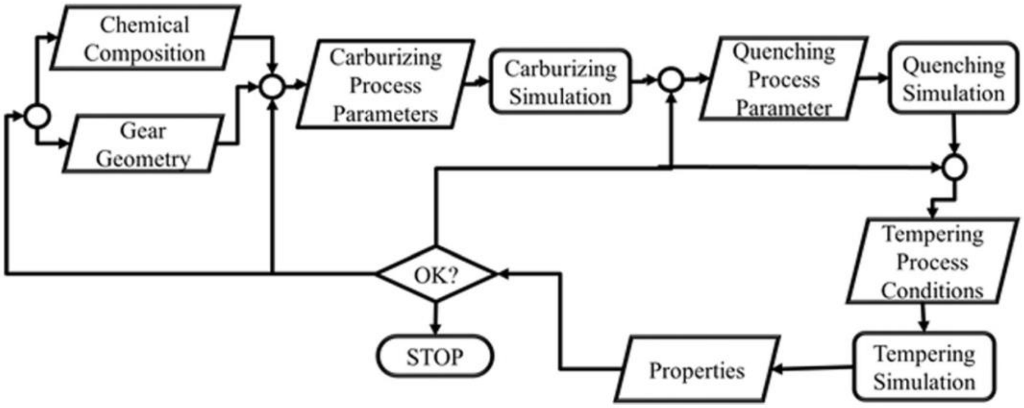

Figure 2. 15: Scheme of simulation tool created in [33]

As mentioned previously, there are many studies that simulated the heat treatments singularly or combinations between two heat treatments as carburizing-quenching or quenching-tempering. Examples of these are [37], [38], [39], [40], [41], [42] and [43]. Many more may be found in literature. The studies explained above ([2], [3], [30] and [33]), were reported and explained as considered particularly relevant for the choice of the methodology used in this study, that will be explained in greater detail in the following chapter.

CHAPTER 3:
METHODOLOGY

The methodology chapter will firstly cover the overview of the simulation tool, showing the overall scheme that the simulation tool follows. Once the general working process of the simulation tool is explained, the detailed methodology with which each effect/phenomenon is simulated for the three heat treatments will be described. Finally, the components that were used in the simulation tool, and of which the simulation outputs are compared to experimental results in the "Results" chapter, are described.

3.1 Simulation Tool Overview

Based on the above-mentioned studies and on the software selection research that was explained in the literature review chapter, the following methodology was selected.

As introduced in the previous chapter, the combination of ABAQUS with some user subroutines is used. The working principle of the simulation tool can be summarized as shown in Figure 3. 1.

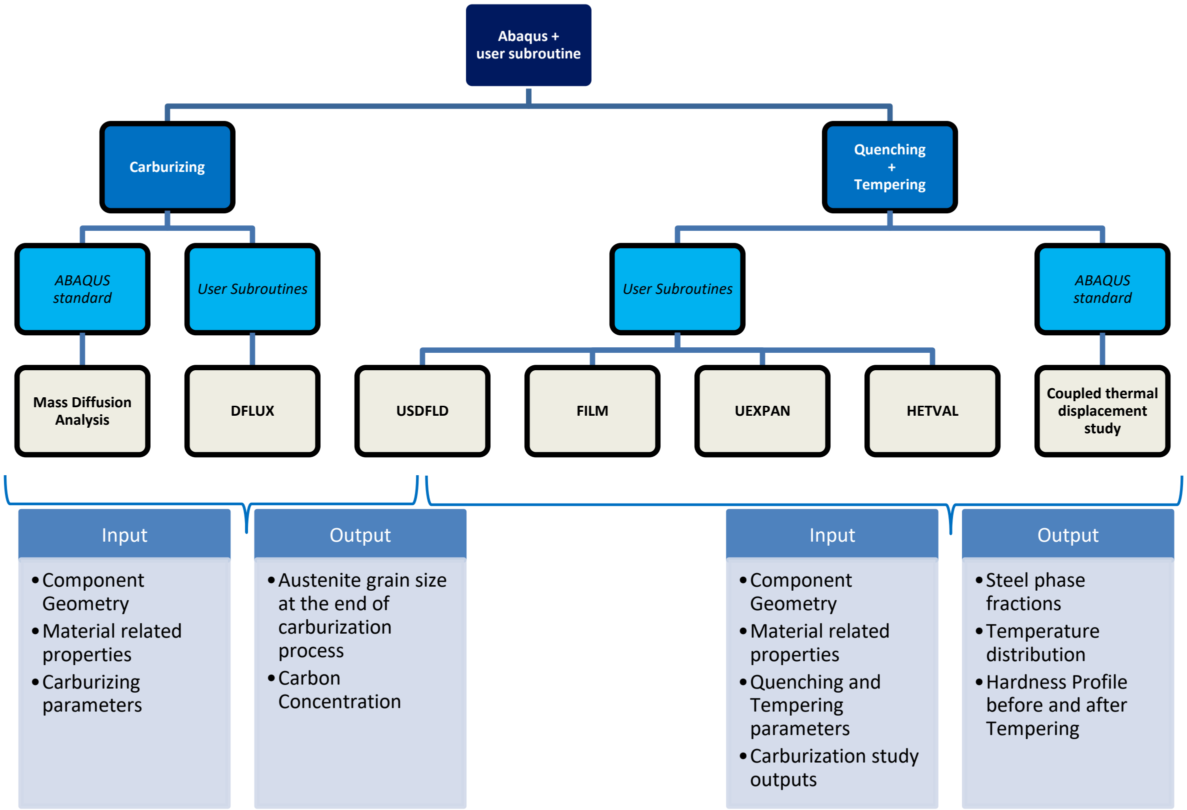

Figure 3. 1: Scheme of simulation tool created in this thesis research.

As it can be seen in Figure 3. 1, the simulation tool has two main modules, a “Carburizing” module and a “Quenching + Tempering” module. The first module deals, as the name suggests, with the simulation of the carburizing procedure. The second module, on the other hand, deals with the simulation of the quenching and tempering processes.

The “Carburizing module” is composed of a “Mass diffusion analysis” study in ABAQUS that is used in combination with the user subroutine DFLUX. The user subroutine DFLUX, as seen with [33], is used to simulate the flux of carbon atoms from the atmosphere to the component. The Carburizing module, as it is possible to see from the scheme above, provides as output the carbon concentration profile and the austenite grain size at the end of the carburizing procedure. The austenite grain size is actually evaluated using an experimental formulation in the subroutine USDFLD, as it will be explained in greater detail in the following paragraphs.

This information is then provided to the "Quenching + Tempering" module that, along with other input information such as the component geometry, the material related properties, and the quenching and tempering time and temperatures, provides as output the amount of the different steel phases present, the temperature distribution, and the hardness profile. The Quenching and tempering simulation is performed in ABAQUS considering a coupled thermal-displacement study. This type of study is used when there is a relation between the temperature field and the stress field. This is the case with quenching, where the strong temperature change determines strains in the component and so influences the stress field. A set of different subroutines is used in this module to implement in ABAQUS different functionalities not already present in the general purpose, as seen for the studies discussed in the literature review chapter. These subroutines are: USDFLD, HETVAL, UEXPAN and FILM. The function of the first three subroutines listed above is the same as that already described when looking at the work of [3] and [30] in the literature review section, and so will not be repeated. The last subroutine listed, FILM, is used in this study to simulate as accurately as possible the interaction between the quenchant fluid and the component during quenching. The exact functionalities of each of these subroutines will be discussed in detail in the following paragraphs.

Tempering in this study, as done also in the paper [33], is simulated not as a physical phenomenon but rather by considering the effects it has on the as-quenched properties.

After this brief introduction explaining the structure of the simulation tool, now the detailed methodology with which each effect/phenomenon is simulated for the three heat treatments will be described.

3.2 Carburizing Simulation

The simulation of the carburizing heat treatment must take into consideration two main effects: the diffusion of carbon atoms withing the component and the increase in grain size due to the high temperature during carburization. These two effects are considered in the simulation software in two different ways.

3.2.1 Carbon Gradient Within Component

During carburizing, as explained earlier, the carbon content within the component is increased. Different types of carburizing are present, and they must be implemented differently in the simulation in order to account for the differences between them. In the following paragraphs, the methodology for simulating traditional and vacuum carburizing will be shown. The main output of this part of the carburizing simulation is the carbon profile that is found inside the component at the end of the carburizing process.

3.2.1.1 Traditional Carburizing

In the gas carburizing process, a carbon carrying gas is inserted in a chamber where the gas reacts with the component releasing carbon atoms at the component's surface. As mentioned earlier, it is possible to distinguish different phases in the process. At first, the carbon is transported from the carbon rich atmosphere to the component surface, where the reactions that allow the carbon to be released at the surface happen. Once this happens, the carbon diffusion from the surface and towards the interior of the component, due to carbon percentage gradient, can occur [44]. The transfer of carbon atoms from the atmosphere to the steel surface is the limiting process, and so the rate-controlling stage of carburizing [44]. The prediction of the carbon profile within the component after traditional carburizing has already been vastly studied in literature, and the simulation method most commonly used is that illustrated in [33], [44], and [45].

In this method, the flux of the carbon directed to the component surface is evaluated by considering the equation 2,

$$J = \beta \cdot \left(C_p - C_s\right) \tag{2}$$

where:

- J is the flux of carbon atoms from the carbon rich atmosphere to the component surface.
- β is the mass transfer coefficient. It defines the carbon content transported to a unit surface per unit time because of the carbon concentration difference.
- C_p is the carbon potential of the carbon rich atmosphere.
- C_s Is the carbon percentage at the surface of the component.

In this equation, the value of the carbon potential of the carbon rich atmosphere is a value that is usually found out by the performing some trial-and-error test, in order to evaluate the best value that gives as output the wanted carbon profile. This value represents the carbon content present in the carbon-rich gas atmosphere found within the carburization chamber. The carbon potential of the atmosphere has a fixed valued that is assumed not to change during the carburization process. On the other hand, the value of C_s is time dependent and varies continuously. In fact, at the start of the carburization process, the amount of carbon at the surface is the same as that found also in the internal part of the component and has as value the amount of the carbon present in the starting steel. The value of C_s than increases as the carburizing gas releases the carbon atoms at the component surface. This increase is proportional to the flux J. As it is possible to see from equation 2, being C_p fixed in value, the flux of carbon atoms toward the component's surface will be maximum at the very start, when the differential between the value of the carbon in the atmosphere and the carbon at the surface is maximum. The flux will than decreases as the amount of carbon at the surface increases, and will eventually become null when the carbon concentration at the surface will equal the value of the carbon potential of the atmosphere. [33] [44] [45]

The value of the mass transfer coefficient β has been studied by different researchers, in particular, in [33] and [44] it was expressed that the value of β ranged from $2 \cdot 10^{-5}$ to $2 \cdot 10^{-4}\ cm/s$ at 800-1000°C, as originally evaluated in [46].

Equation 2 studies the movement of carbon atoms from the carbon rich atmosphere to the surface of the component. On the other hand, the carbon diffusion within the component is evaluated with the use of Fick's law of diffusion that is reported in equation 3. [33] [44] [45]

$$J = -D \cdot \frac{\partial C}{\partial x} \tag{3}$$

This equation however refers to a case where the diffusion occurs only in one direction, the x direction in this case. In order to account for all directions, equation 4 is used instead.

$$J = -D \cdot \nabla C \tag{4}$$

In this equation:

- J is, again, the flux of carbon atoms.
- D is the diffusivity of the steel.
- C is the carbon concentration at any point inside the steel.

The value of the flux J is the same as that calculated in equation 2. The value of the diffusivity has been the focus of different studies. An empirical equation to evaluate the diffusivity, developed by Tibbets [47] and dependent on temperature and carbon percentage, was used in [33].

In this thesis research, however, another diffusivity formulation is utilized for the diffusivity prediction: that developed by Lee et al. in [6]. This formulation was selected as, in the study [9], where many different formulations for the evaluation of the diffusivity form many different authors are shown, the equation developed by Lee et al. in [6] was reported to have shown better prediction for the carbon diffusivities of different alloyed steels with respect to the other formulations.

This experimental formulation, developed by Lee et al. in [6], is reported in equation 5.

$$\begin{aligned} D &= (0.146 - 0.036C \cdot (1 - 1.075Cr) - 0.0315Mn + 0.0509Si - 0.0085Ni \\ &\quad + 0.3031Mo - 0.052Al) \\ &\quad \cdot e^{-\frac{144300-15000C+370C^2-4366.3Mn+4050.7Si-1240.7Ni+7726Cr+12126.6Mo-6788.6Al}{R \cdot T}} \end{aligned} \tag{5}$$

In this equation:

- D is the diffusivity of carbon expressed in cm^2/s.
- C is the carbon content expressed in mass percent.
- The alloying elements symbols represent the mass percent of the alloying materials present.
- R is the gas constant expressed in $J/mol/K$

- T is the temperature expressed in K.

This equation is dependent both on the temperature and on the carbon concentration.

By combining equations 2 and 5, therefore creating equation 6, the carbon concentration withing the component can be found. This is, as mentioned before, one of the two outputs provided by the carburization module. [33] [44] [45]

$$-D \cdot \nabla \mathrm{C} = \beta \cdot \left(C_p - C_s\right) \tag{6}$$

Figure 3. 2, taken from [48], shows graphically the carbon diffusion process and the connection between equations (2) and equation (5).

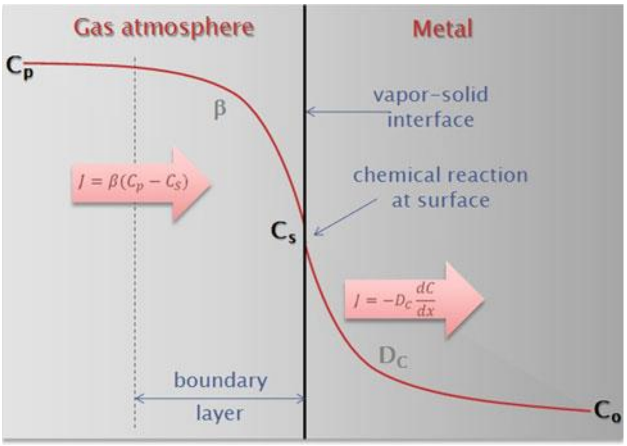

Figure 3. 2: Carbon flux equations in carbon rich atmosphere and within component. [48]

In this figure it is possible to see that equation 2 describes the flux from the atmosphere to the surface, whilst equation 5 describes the flux within the component. In Figure 3. 2 it is also possible to see that the carbon content within the component is greater at the component surface and then decreases when going deeper within the component.

3.2.1.2 Traditional Carburizing FEA implementation

In order to simulate, predict, and display to the user the carbon content within the component during carburizing, the equations just described must be implemented in ABAQUS.

The Fick's equation, for the carbon diffusion within the component, is already present in ABAQUS when a mass diffusion analysis is conducted. In fact, when defining in ABAQUS the material properties, the diffusivity must also be defined. In the diffusivity definition properties, as shown in Figure 3. 3, it is possible to select to utilize Fick’s law of diffusion, and it is also possible to define the value of the Diffusivity in function of Temperature and concentration. In this thesis research, since the Fick’s law of diffusion is utilized, the Fick method is selected, as shown in Figure 3. 3.

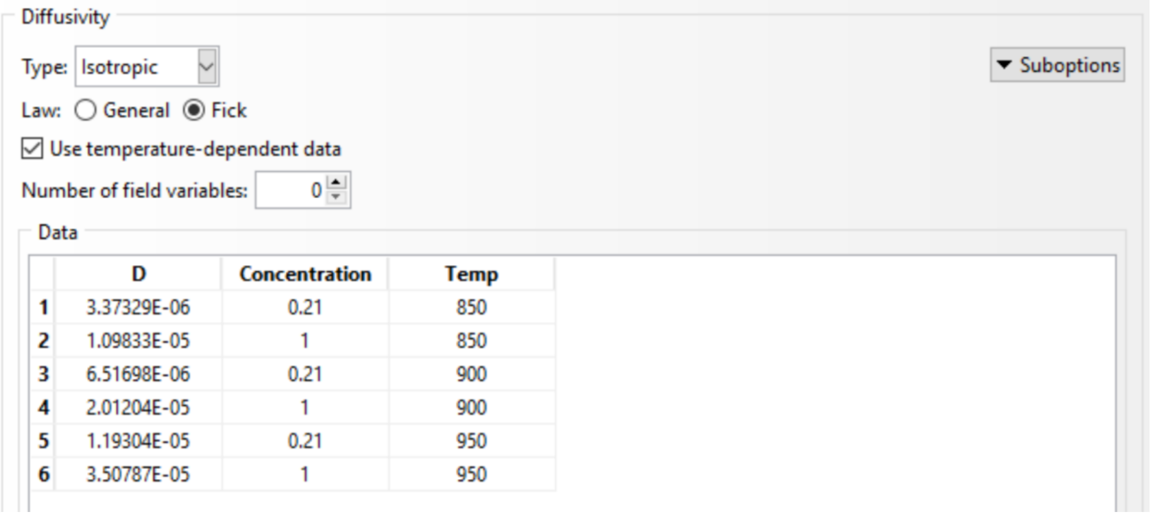

Diffusivity

Type: Isotropic

Law: ○ General ● Fick

☑ Use temperature-dependent data

Number of field variables: 0

Data

	D	Concentration	Temp
1	3.37329E-06	0.21	850
2	1.09833E-05	1	850
3	6.51698E-06	0.21	900
4	2.01204E-05	1	900
5	1.19304E-05	0.21	950
6	3.50787E-05	1	950

Figure 3. 3: Diffusivity material property definition in ABAQUS.

In the example shown in Figure 3. 3, the diffusivity is defined as a function of carbon concentration from 0.2 to 1%, and for different temperatures. Interpolation is used in ABAQUS to obtain diffusivity values referring to values of concentration or temperature that are in-between those reported in the diffusivity property definition table displayed in Figure 3. 3. In order to evaluate the diffusivity at the different temperatures and concentrations, before inserting the diffusivity values in ABAQUS, equation 5 is implemented in MATLAB and graphs showing the values of the diffusivity at different carbon contents and at different temperatures are plotted. These graphs are then used to obtain the diffusivity values to provide as input to ABAQUS, in order to perform the simulations. For the example shown in Figure 3. 3, the MATLAB graphs showing the trend in diffusivity at 850°C, 900°C, and 950°C and for a value of carbon concentration ranging from 0.2 to 1%, from which the values included in the table in Figure 3. 3 are taken, are shown in Figure 3. 4 a, b and c.

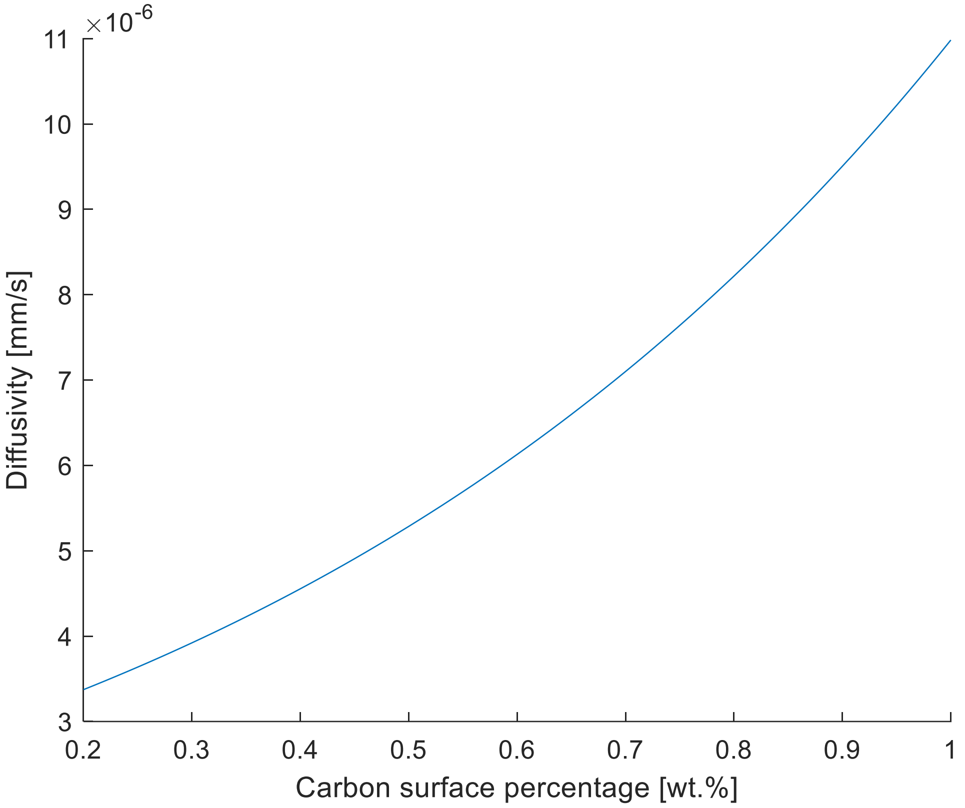

Figure 3. 4-a: Diffusivity for 8260 steel at 850°C for varying carbon content.

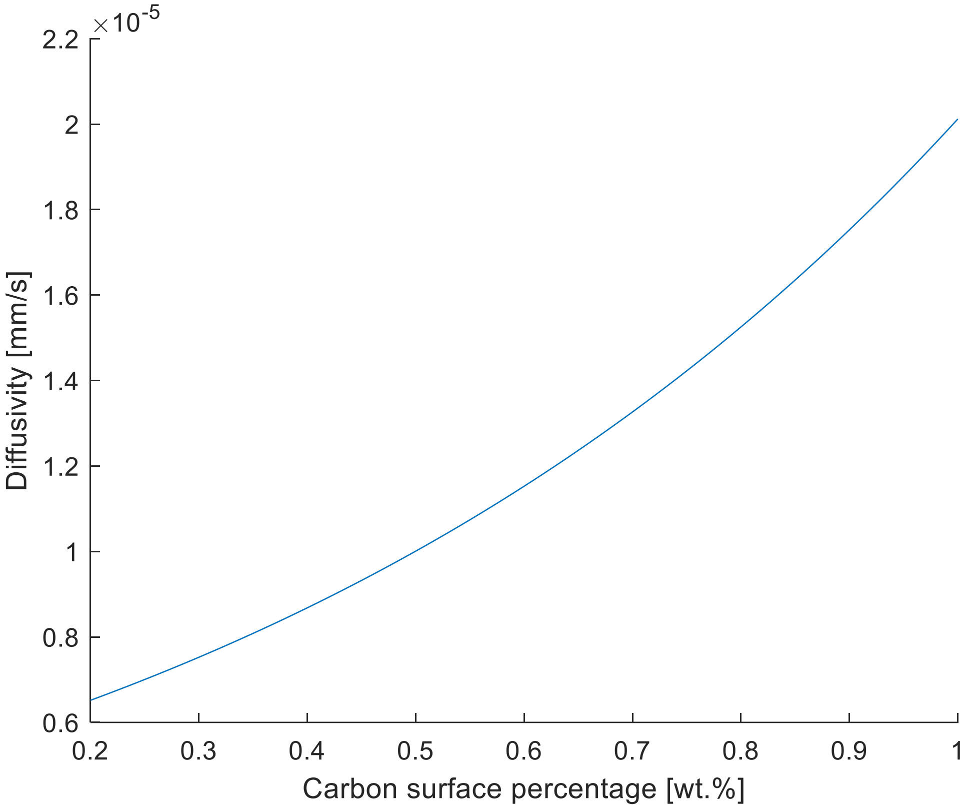

Figure 3. 4-b: Diffusivity for 8260 steel at 900°C for varying carbon content.

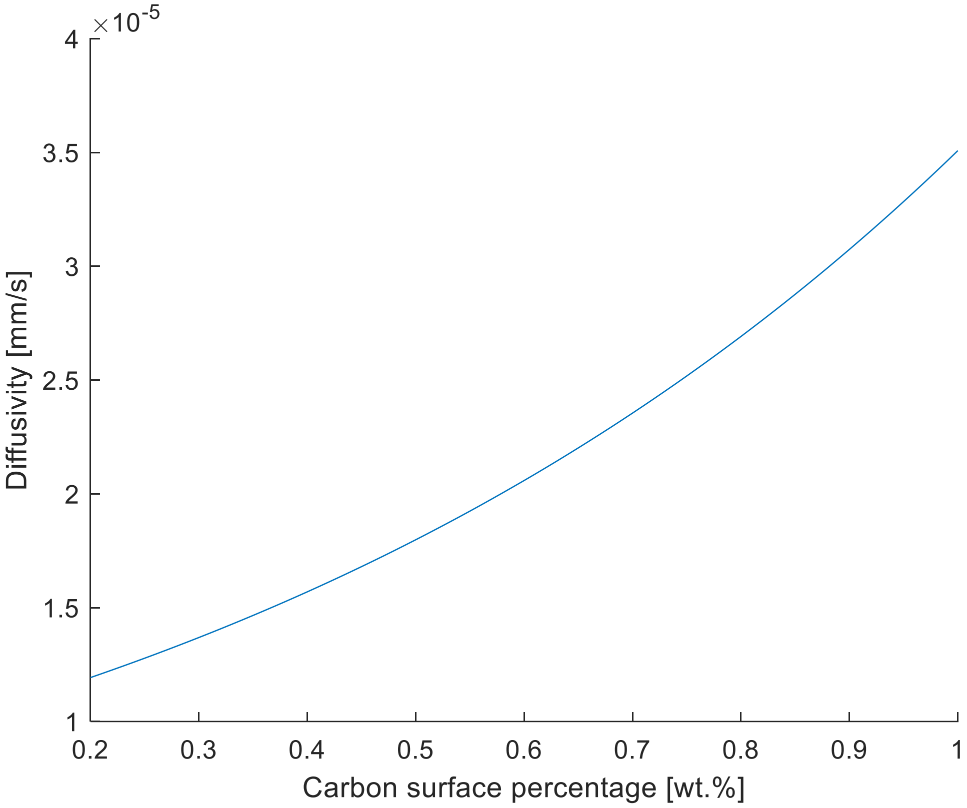

Figure 3. 4-c: Diffusivity for 8260 steel at 950°C for varying carbon content.

Care must be taken when looking at the figures above, as the y-axis scale is changed in magnitude between Figure 3.4 a and Figures 3.4 b and c. It is to be noted that the values of diffusivity, as expressed in equation 5, are dependent also on the alloying composition. In the example shown in Figure 3. 3, an 8260 steel is used, of which the alloying composition is shown in Table 3.1.

Table 3.1: Alloying composition of 8260 steel.

C	Mn	Cr	Si	Ni	Mo	Al
Varying	0.83	0.57	0.25	0.65	0.16	0

On the other hand, the expression in equation 2 is not already present in ABAQUS and so must be implemented separately with external user coding. This is done by adding in ABAQUS a load "Surface concentration flux" on all regions of the component that are exposed to the carburizing gas, and by setting the value of the flux as user-defined. This surface concentration flux, as the name suggests, simulates the surface flux from the carbon rich atmosphere to the component surface.

The external subroutine DFLUX must then be included, in order to assign a magnitude to the flux that has been defined in ABAQUS. In this external subroutine, the value of the mass transfer coefficient and of the carbon potential of the atmosphere, that must be provided as input to the simulation, are defined. Using these values, equation 2 is solved in the DFLUX subroutine. The solution of equation 2 provides the magnitude of the flux J, that is the flux that was defined in ABAQUS as “surface concentration flux”.

Once the two equations mentioned above are set, then, after selecting in ABAQUS the correct temperature and duration of the gas carburizing procedure that is to be simulated, the simulation can be started. The output of the study will be the carbon distribution within the component at each location and instant during the carburization procedure.

An example of the carbon distribution map obtained with such a study is shown in Figure 3. 5.

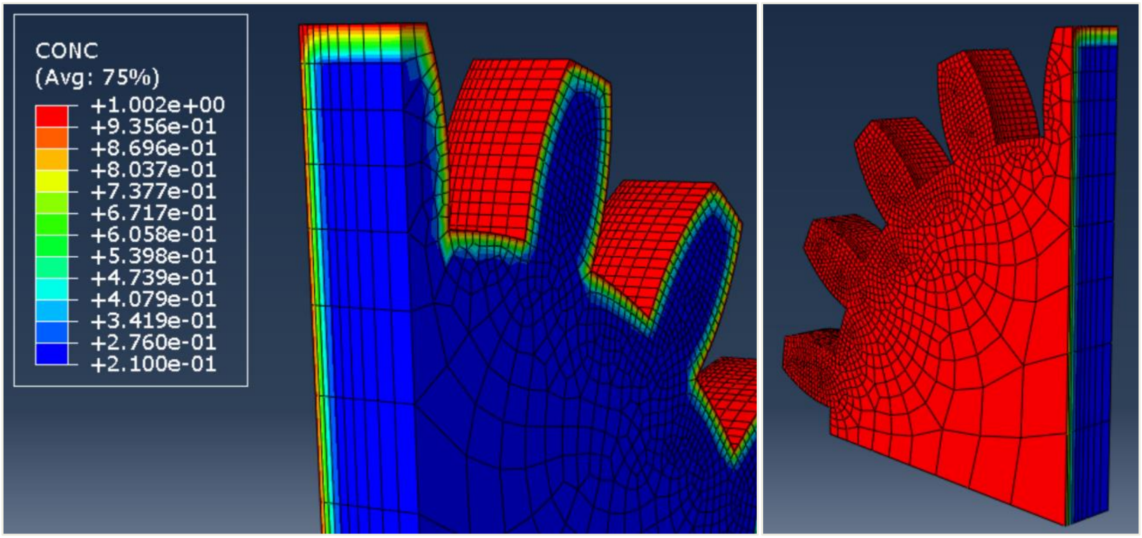

Figure 3. 5: Carbon distribution at the end of traditional carburizing in a quarter-gear model.

It is possible to see that the amount of carbon is shown visually on the component. In this example a quarter gear model is used. For sake of explanation, the areas in red in the component are those exposed to the carburizing gas. On the other hand, the areas where color gradients and blue are found are those where the component was “Cut”, in order to show the situation in the component interior. It is possible to see that the exterior of the component, that is exposed to the carburizing gas, has a higher value of carbon concentration. This is expected, considering what is shown in Figure 3. 2. This higher concentration takes a value very close to the carbon potential of the atmosphere, that for this example was set to 1%. On the other hand, going deeper within the component, the carbon concentration quickly decreases and becomes very close to the starting amount of carbon found in the material, that in this example was 0.2%.

This brief example was included in order to show an example of the output of the carburization study.

To summarize, the carbon profile obtained with traditional carburizing can be simulated by using a mass diffusion analysis in ABAQUS and using a user subroutine DFLUX. The inputs to the simulation are:

- The duration and temperature of the traditional carburizing process, that are used to define the mass diffusion analysis in ABAQUS.
- The value of diffusivity, that is evaluated with equation 5, and of which the values are reported in ABAQUS when defining the material properties, as shown in Figure 3. 3.
- The value of the mass transfer coefficient, that is defined in the subroutine DFLUX, where it is used to solve equation 2.
- The value of the carbon potential, that is defined in the subroutine DFLUX, that is also used to solve equation 2.

3.2.1.3 Vacuum Carburizing (Low pressure carburizing)

Vacuum carburizing has been studied intensively in the past years as, as mentioned earlier, the process is becoming more widespread due to its power reduction and eco-friendliness.

For vacuum carburizing, again, the carbon profile within the component can be predicted by combining the effect of two fluxes, one from the atmosphere towards the component's surface, and the other one from the surface towards the internal part of the component. The evaluation of the carbon profile can again be performed using the Fick's law of diffusion. This is possible because the Fick's law studies the movement of carbon atoms within the component. This movement happens in the same way in traditional and vacuum carburizing. [5] [13] [44] [49]

On the other hand, what is very different for the two carburizing methods, is the evaluation of the flux from the carbon atmosphere towards the component surface. The main issue with vacuum carburizing, that seems to block the possibility to use a formulation such as that used in traditional carburizing and shown in equation 2 for the evaluation of the flux of carbon atoms from the atmosphere towards the surface, is that, as stated in [44], the vacuum carburizing cannot be simulated using a mass balance boundary condition as it was done for the traditional carburizing. This, because the hydrocarbon gas that is introduced in the chamber to react with the component and increase the carbon concentration, may never reach equilibrium and, on some occasions, soot may form at the component's surface. Furthermore, as mentioned in [49], the carbon potential, as seen in the traditional carburizing, cannot be evaluated in vacuum carburizing. This is due to the fact that, due to the vacuum environment of low-pressure carburizing, the carburizing gas concentration is low, and so the carbon concentration in the atmosphere cannot be measured using an oxygen probe as it was done for traditional carburizing. Considering this issue, different solutions were developed for evaluating the magnitude of the flux from the atmosphere to the surface that, used in combination with the Fick's law of diffusion, can lead to the evaluation of the carbon profile within a component.

In the study presented in [44], a constant surface flux is used to simulate the flux of carbon atoms from the environment towards the surface. The value of the latter is evaluated in [44] by applying the formulation shown in equation 7.

$$J_v = \frac{\int_0^{C_0} f(x)}{S \cdot t_b} \tag{7}$$

In this equation:

- J_v is the carbon flux during vacuum carburizing.
- x is the depth.
- $f(x)$ is the carbon concentration as a function of the depth.
- S is the surface area exposed to the carburizing gas.
- t_b is the total boost time.

In this equation, the flux is evaluated by direct integration of carbon profiles from industrial experience data. As mentioned above, the value of the flux evaluated with equation 7 can then be used as input in the Fick's equation to evaluate the carbon profile.

However, to evaluate the flux with equation (7) as shown in [44], data on the carbon concentration as a function of depth is used as input, and so must be already known. This means that this method, although very interesting, cannot be used in the simulation tool created for this thesis research. In fact, in the simulation tool, the carbon profile is provided as an output and not used as an input.

A similar approach is followed also in the study [49]. Also in this study, in fact, it is stated that, due to the very quick release of carbon atoms at the component surface, the atmosphere-to-surface carbon flux cannot be evaluated for vacuum carburizing in the same way as it was done for traditional carburizing. In fact, also in [49], as it was seen for [44], a constant value of atmosphere to surface flux is used. This flux, in [49], is related to the carburizing gas type, pressure, temperature, alloy type, and surface state, and is evaluated experimentally with equation 8, by having previous knowledge on the amount of mass increment occurring during a certain period of carburization.

$$J_v = \frac{\Delta m}{S \cdot t_c} \tag{8}$$

In this equation:

- Δm is the mass increment during a certain period of carburization.

- S is the surface of the component exposed to the carburizing gas.
- t_c is the time duration of the carburizing operation.
- J_v is the surface carbon flux during vacuum carburizing.

However, as seen for [44], here, once again, previous experimental knowledge, this time in terms of incremental mass, must be known in order to apply equation 8. This, however, means that the simulation cannot be applied to study a carburization process that has not yet been experimentally tested and of which data has not been experimentally evaluated. Since the simulation tool created in this thesis research has the objective to be used also to predict the outcomes of carburization processes that have not been experimentally tested, this method, although very interesting, cannot be utilized in the simulation tool.

In the study presented by Smirnov et al. in [13], three different boundary conditions for solving the mass transfer analysis during vacuum carburization are compared. In this study it is specified that the control factor in the vacuum carburizing is the boost time and diffusion time and their alternating cycles.

The first boundary condition analyzed in [13] is the time dependance of the concentration of carbon on the surface of the metal, as expressed in equation 9.

$$C_s = \varphi \tag{9}$$

In this equation:

- C_s is the carbon concentration on the surface.
- φ is the carburizing capacity of the atmosphere that varies as a function of the time of the process.

However, as mentioned in the paper [13], it is virtually impossible to measure the value of $\varphi(\tau)$ at each moment in the process, so this first kind of boundary condition becomes non applicable.

The second kind of boundary condition expressed in [13], takes the form expressed in equation 10.

$$J_v = -D \cdot \frac{\partial C}{\partial x} \tag{10}$$

In this second kind of boundary condition, the Fick's law of diffusion is utilized, where J_v is the flux of carbon atoms from the environment towards the surface during vacuum carburizing. This boundary condition has the same form as the methods described above by [44] and [49], where the flux J_v has a constant value that must be known in order to apply the equation. However, this second boundary condition has the same issues reported above when considering the studies of [44] and [49]. In fact, the flux must be evaluated by having previous knowledge/experimental data on the carburizing simulation, perhaps utilizing equations such as equations 7 or 8, and these experimental results require the process to already have been completed and studied, and require data that is not easy to measure.

Finally, the third type of boundary condition expressed in [13] takes the form shown in equation 11.

$$-D \cdot \frac{\partial C}{\partial x} = J_v = \beta \cdot \left(C_p - C_s\right) \tag{11}$$

It is possible to see that such a formulation is very close to that shown in equation 6 and used for traditional carburizing. However, as mentioned in [13], the values of the carbon potential C_p and of the mass transfer coefficient β must be modified to adapt the formulation to vacuum carburizing.

For what regards the carbon potential value C_p, what is explained in [13] is that, whilst for gas carburizing the value of the carbon potential of the atmosphere is easily measurable and depends on many factors such as flow rate and pressure of the carburizing gas, for vacuum carburizing the value of the carbon potential is basically dependent only on the composition of the saturated steel. This because the acetylene gas, when it enters the chamber and it is placed in contact with the component, it quickly dissociates saturating the surface of the component. This determines the formation of high-carbon phases in the form of a continuous carbon-containing layer on the surface of the component. However, the phases that form on the surface depend on the alloying composition of the steel that is being carburized. For that reason, in [13] a distinction is made between low alloyed steels and complexly alloyed heat resistant steels. For the former, the carbon containing layer consists mainly of soot. For the latter, on the other hand, the carbon containing layer is mainly constituted by carbide phases. This carbon containing layer, being it soot or carbide phase, interacts with both the surface of the component and with the vacuum carburizing atmosphere. For this reason, in [13] it is explained that the value of C_p must have different values depending on the alloying composition of the steel being carburized. In both cases, a high constant value for C_p is considered. For low alloying steels, where the carbon containing layer is mainly amorphous carbon (soot), the value of C_p can be considered to be 100%. On the other hand, for complexly alloyed heat resistant steels, where the carbon containing layer is composed mainly of carbide phases, the value of C_p can be considered to be 6.7%, that is the concentration of carbon in cementite crystals. In this method, the value of the carbon potential is set to the values mentioned above during the pulse phases, when the carburizing gas is in contact with the component. During the diffusion phases, on the other hand, the value of the carbon potential is set to zero. This is done to account for the fact that, since the carburizing gas is not present during diffusion phases, the flux of carbon atoms from the gas towards the component surface will be null, and so the only phenomena that will occur will be the diffusion of carbon from the surface, that has increased in carbon content during the pulse phase, towards the interior of the component.

For what regards the mass transfer coefficient β, the situation is more complicated. In the study [13], due to the complexity of the phenomenon, a parametric formulation for the evaluation of β, dependent on both time and temperature, was developed based on many experimental tests. The value of the parameters in such a paper, however, are not provided.

A similar method to that explained in the third boundary condition in [13] was also used in [50], however introducing some modifications.

In [50], the vacuum carburizing heat treatment of an annulus gear ring is simulated, and an equation as that shown in equation 11 is used. So, again, a very similar approach as that used for traditional carburizing is employed. In this case however, the value of the carbon potential of the atmosphere is not fixed to a very high value during the pulse phase and set to zero during the diffusion phase as it was explained in [13], but rather the carbon potential is set to 1 during the pulse phase and then decreased to 0.8 during the diffusion phase.

Yet another different approach to the value of the carbon potential to be used is described in [5]. In fact, also in this study a formulation as that shown in equation 11, so very similar to equation 6 used for traditional carburizing, is used. Again, as seen for studies [50] and [13], since the carbon potential for vacuum carburizing is impossible to evaluate, the carbon potential is not an input to the study as for traditional carburizing, but it must be determined in some alternative way. In this study, a value of carbon potential of 1.39 at 950°C is used. This particular value was selected based on the fact that, in [35], an Armco foil was tested with glow discharge optical emission spectrometry, and it was found out that the carbon content will reach a maximum value at the surface of the component after about 20 minutes of carburization and, after that, it will keep a nearly constant value. This can be seen in Figure 3. 6, that is taken from [5].

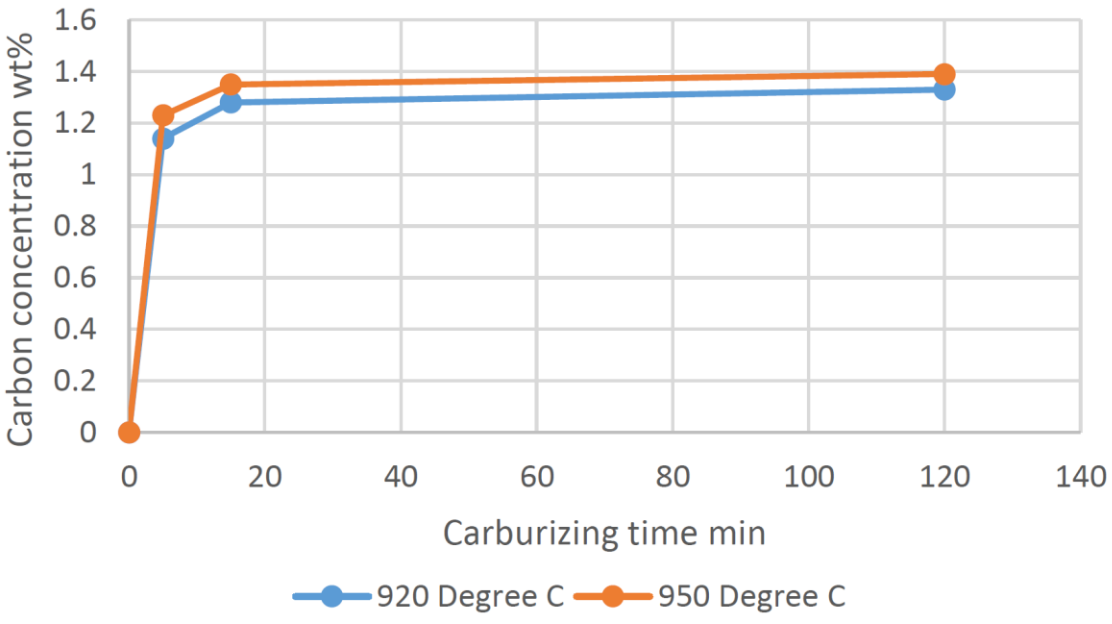

Figure 3. 6: Graph showing the carbon concentration as a function of time during vacuum carburization. [5]

In the study [5], it was proposed to use the value of the carbon content after 20 minutes, when it becomes close to constant, as the value of the carbon potential. So, the value of the carbon potential is selected to be 1.39 for vacuum carburization at 950°C, and around 1.37 for vacuum carburization at 920°C. In the model presented in [5], several new assumptions are also considered. In particular, it is considered that the dissolution of carbides does not influence the carbon diffusivity coefficient. Another important assumption that is done in this method, is that the pulse time is extended of about 50%, to account for the existence of carbon deposits. The study presented in [5] was considering a 9130-alloy steel. However, in [5] it is also mentioned that the model was tested on more alloys treated with low pressure carburizing and showed good results.

In the study presented in [51], a similar approach to that used in [50], [5], and in the third boundary condition defined in [13], is utilized. In this paper, however, a formulation to evaluate β is shown. In this paper, the mass transfer coefficient β is evaluated with a formulation as that shown in equation 12.

$$\beta = S_{re} \cdot m_c \cdot I_z \cdot \rho_m \tag{12}$$

In this equation:

- β is the mass transfer coefficient.
- S_{re} is a dimensionless reaction efficiency that is defined as the ratio between the number of particles of the carburizing gas that are reacting at the surface to the total number of molecules that are reaching the surface. This value, as mentioned in the same paper [51], is of about 70-80% for acetylene.
- ρ_m is the density of the steel.
- I_z represents the number of molecules of vacuum carburizing gas reaching the steel surface.
- m_c represents the mass of carbon per one mole of vacuum carburizing gas.

I_z can be evaluated as shown in equation 13.

$$I_z = \frac{p}{\sqrt{6 \cdot R \cdot T_c \cdot M_g}} \tag{13}$$

In this equation:

- p is the pressure of the carburizing gas.
- R is the gas constant.
- T_c is the carburizing temperature.
- M_g is the molar mass of the carburizing gas, that, in the case of acetylene, is $26.0373 \frac{\mathrm{g}}{\mathrm{mol}}$.

To conclude, by considering all of these different models with which to simulate the vacuum carburizing procedure, in the simulation tool developed for the thesis research, a similar approach to that used in [5], [13], [50], and [51], is used. In fact, an equation as that expressed in equation 11 is employed. This approach was chosen as it does not require experimental data as input for conducting the study and because it has a formulation very similar to that presented in equation 6 for traditional carburizing. In fact, the only differences between the two applications are the values assigned to β and C_p in the equation. Whilst the value of C_p and β, as mentioned in the paragraph referring to traditional carburizing, are usually readily available when considering traditional carburizing, this is not the case with vacuum carburizing. In the simulation tool, the value of β is evaluated with equation 12 as shown in [51], whilst the value of C_p is selected as shown in the model described in [5]. In order to comply with the assumptions of the model as presented in [5], the boost time considered during the simulation is also extended of about 50%.

3.2.1.4 Vacuum Carburizing (Low pressure carburizing) FEA Implementation

The implementation of vacuum carburizing, as mentioned in the previous paragraph, is very similar to that used for traditional carburizing. The only difference between the two being the values of C_p and β used in the equation 11 that is implemented in the DFLUX subroutine.

The value of β is evaluated by using the equations 12 and 13, and is then reported in the user subroutine DFLUX. The latter is again used to simulate the carbon flux towards the component's surface. So overall, a very similar subroutine and so methodology to that seen for traditional carburizing is used also for vacuum carburizing, with the only difference that a different value is assigned to C_p, and equations 12 and 13 are used to evaluate β that is then defined in DFLUX.

To summarize, the carbon profile obtained with vacuum carburizing, using acetylene gas, can be simulated by using a mass diffusion analysis in ABAQUS and using a user subroutine DFLUX, where the inputs to the simulation are:

- The duration and temperature of the vacuum carburizing process. In particular, the duration of each pulse and diffusion phase must be defined. The pulse phases, since the method described in [5] is used for the definition of the carbon potential of the atmosphere, are extended of about 50% with respect to those defining the real carburizing process that is being simulated. The definition of the time and temperature for each of the pulse and diffusion phases is done when defining the mass diffusion analysis steps in ABAQUS. The surface concentration flux is created in ABAQUS as seen for traditional carburizing. This flux, however, is applied to the surfaces only during pulse phases, when the carburizing gas is in contact with the component.

- The value of the carbon diffusivity that is evaluated with equation 5, and of which the values are reported in ABAQUS when defining the material properties as shown in Figure 3. 3.

- The value of the carbon potential, that is reported in the subroutine DFLUX. The value of the carbon potential is selected depending on the carburization temperature using the method described in [5]. The value of the carbon potential selected is then reported in the DFLUX subroutine where it can be used to evaluate the carbon flux from the atmosphere towards the surface.

- The value of the mass transfer coefficient, that is defined in the subroutine DFLUX. The value of this parameter that is reported in the subroutine DFLUX, has been previously evaluated using equations 12 and 13, and considering acetylene as the carburizing gas.

3.2.2 Austenite Grain Size Increase

Carburizing is usually performed at high temperatures in order to facilitate carbon diffusion. The high temperature environment however also determines an austenite grain enlargement [33]. This effect must be simulated as this value is of great importance for different material properties since it affects the phase transformations. Grain growth, as explained in [52], occurs in order to reduce the grain boundary free energy. The grain growth is generally hindered by the increasing amount of alloying materials. Alloying materials in fact, as explained in greater detail in [52], have important effects on the grain size. In [52], an empirical equation is proposed for the evaluation of the austenite grain size of low alloy steels. The results presented in that study are based on experiments performed on 16 different low alloy steels.

In that study, the grain diameter is expressed with equation 14.

$$d = 766671 \cdot e^{\left(-\frac{89098+3581C+1211Ni+1443Cr+4031Mo}{RT_c}\right)} \cdot {t_C}^{0.211} \tag{14}$$

In this equation:

- d represents the austenite grain size in micrometer.
- R represents the gas constant expressed in $\frac{\frac{J}{mol}}{K}$.
- T_c is the carburizing temperature in Kelvin.
- t_C is the carburizing time in seconds.
- The chemical elements symbols represent the weight percent of the alloying elements in the steel.

This equation is experimentally derived in [52] starting from the Arrhenius type equation, that has a form such as that expressed in equation 15.

$$d = A_a \cdot e^{\left(-\frac{Q}{RT_C}\right)} \cdot {t_C}^{n} \tag{15}$$

In this equation:

- d represents the austenite grain size in micrometer.
- A_a is a constant.
- Q is the activation energy expressed in $\frac{J}{mol}$.
- R represents the gas constant expressed in $\frac{\frac{J}{mol}}{K}$.
- T_c is the carburizing temperature in Kelvin.
- t_C is the carburizing time in seconds.
- n is a time exponent.

Equation 14 is obtained starting from equation 15 by evaluating the different constants and activation energy by using experimental results. The validity of such a formulation is then also confirmed in the study [52], where its results are compared and are seen to be in accordance with experimental results.

In the simulation tool, the austenite grain size increase during carburization is studied by implementing the equation 15 in the user subroutine USDFLD. This subroutine will be described in greater detail in the following paragraph.

3.3 Quenching Simulation

When simulating quenching, the phase transformations, the heat released during phase transformations, and the strains determined by quenching, must be considered. All of these phenomena and the way in which they are simulated are explained in greater detail in the next paragraphs.

However, before going in detail with these explanations, a brief description on how the carbon values are imported for the carburizing simulation to the quenching simulation is included.

3.3.1 *Updating Carbon Values*

Before starting the simulation of the quenching process, the information regarding the carbon distribution after carburizing must be imported from the carburization simulation. This, in order to make it available as input for the subsequent quenching simulation.

In order to do so, the following procedure is performed. At the end of the carburizing simulation, the carbon value at each node of the component's mesh is probed so that its value is revealed. This information is then reported in a ".dat" file that is saved in the computer used to perform the simulations. In this ".dat" file, the data for each node is reported as shown in Figure 3. 7.

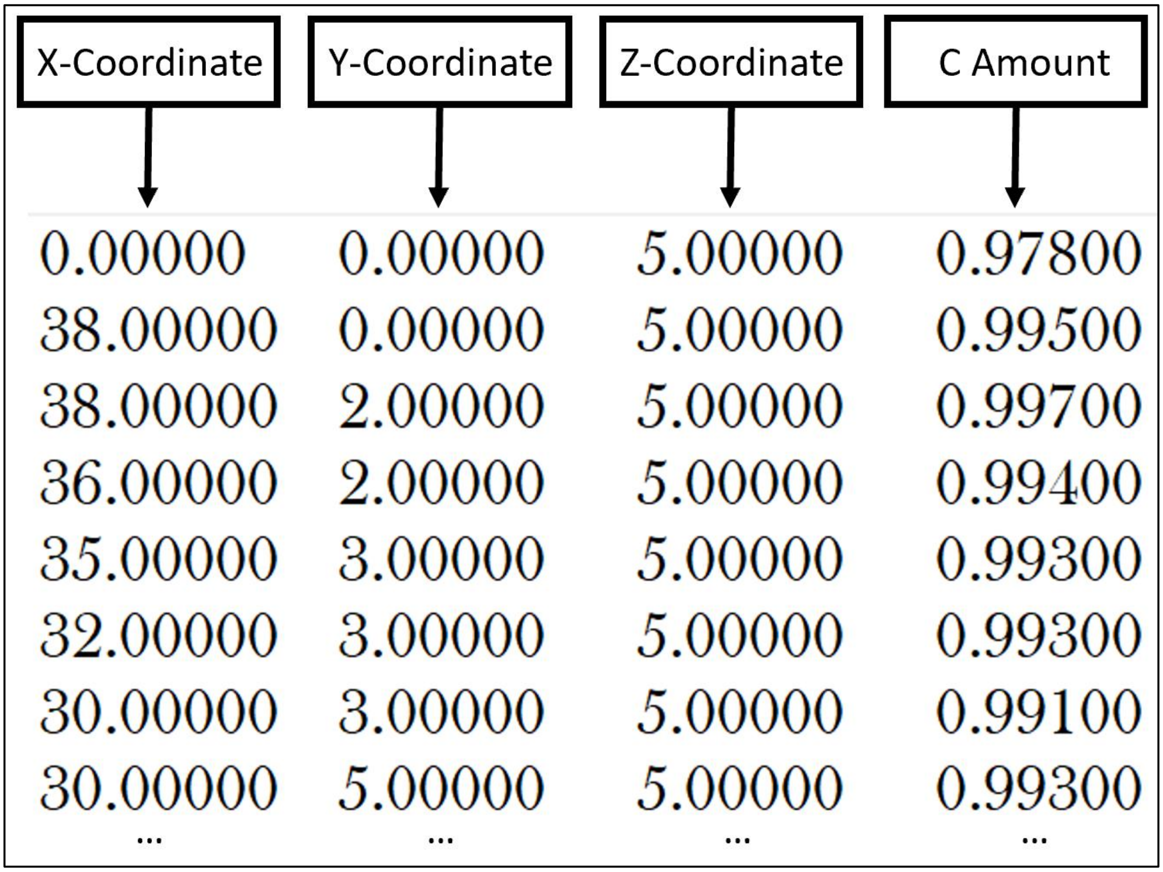

X-Coordinate	Y-Coordinate	Z-Coordinate	C Amount
0.00000	0.00000	5.00000	0.97800
38.00000	0.00000	5.00000	0.99500
38.00000	2.00000	5.00000	0.99700
36.00000	2.00000	5.00000	0.99400
35.00000	3.00000	5.00000	0.99300
32.00000	3.00000	5.00000	0.99300
30.00000	3.00000	5.00000	0.99100
30.00000	5.00000	5.00000	0.99300
...	...	...	...

Figure 3. 7: Example of format with which data obtained from carburizing simulation is saved in ".dat" file.

The data, as shown in Figure 3. 7, is organized in such a way to define in each line the location of a specific point inside the component and the concentration of carbon found at that point. In fact, the first column in each line is defining the x coordinate, the second column the y coordinate, and the third column the z coordinate. The amount of carbon for the specific point of which the coordinates have been defined in the first three columns, is then expressed in the fourth column.

This “.dat” file is then opened during the quenching simulation from the subroutine USDFLD. This is done by including inside this subroutine some coding especially dedicated to this purpose.

The USDFLD user subroutine runs at each node within the component, at each time step. This being the case, during the start of the quenching simulation, at each node composing the component’s mesh, the subroutine will compare the current values of the coordinates of the node which is being analyzed in that moment, to all of the coordinates found in the first three columns in the “.dat” file. If the coordinates of the analyzed node match perfectly to a set of x, y and z coordinates reported in the “.dat” file, then, the value of carbon correspondent to that particular set of coordinates is selected for that node.

If none of the coordinates in the “.dat” file show a perfect match, perhaps because the mesh used for the carburizing simulation is different from that used for the quenching simulation, the value of carbon correspondent to the closest point to that that is being investigated, is selected. This is done by evaluating the norm, as shown in equation 16, between the node that is currently being analyzed, and each point defined in the “.dat” file as a set of x, y and z coordinates, and then assigning to the node being analyzed the value of carbon correspondent to the set of x, y and z coordinates that determine the lowest norm.

$$norm = \sqrt{(x_{actual} - x_{\text{".dat" file}})^2 + (y_{actual} - y_{\text{".dat" file}})^2 + (z_{actual} - z_{\text{".dat" file}})^2} \quad (16)$$

In this equation:

- The $actual$ subscript indicates that the coordinate is that of the node that is currently being analyzed in the quenching simulation.
- The ".dat" file subscript indicates that the coordinate is that found in the “.dat” file.

With this procedure, the value of carbon at each location is updated stating from the results of the carburizing simulation. This technique, however, is very computationally expensive and, for this reason, it is performed only once, right before the start of the quenching simulation. An ABAQUS step, previous to that in which the temperature of the component is dropped due to quenching, is in fact included in order to perform this carbon value update before proceeding with the actual quenching simulation.

In alternative to the solution described above, the value of the carbon concentration at each location can be imported from the carburizing simulation directly into ABAQUS, by creating a "field variable". The field variable, created in ABAQUS directly, is then set to obtain the carbon concentration values from the results file (.odb), created by ABAQUS at the end of the carburizing simulation. This solution is easier to implement and less computational expensive with respect to that explained above. However, this solution requires the presence of the ABAQUS simulation files from the carburization study on the device where the quenching simulation is performed.

In the following paragraph, the way in which the quenching simulation is set up in ABAQUS in the simulation tool will be shown and explained.

3.3.2 Setting Up Quenching Simulation

The quenching simulation is performed in ABAQUS by creating a step, subsequent to that where the carbon amount is updated if the first method explained above for carbon content update is used, where the interaction between the quenching fluid and the component is simulated. The quenching fluid considered in this simulation tool is an inert gas.

The quenching process is simulated in ABAQUS with a coupled temperature-displacement study. This step, as mentioned in the ABAQUS documentation [53], is needed when the stress analysis is dependent on the temperature distribution, and the temperature distribution is affected by the stress solution. This is done in order to have the possibility to study in the same simulation the temperature related effects and the stresses and strains.

Within the coupled temp-displacement study, the interaction between the quenching agas and the component is simulated in ABAQUS by setting a "Surface Film interaction". The latter, is used in ABAQUS in order to study the heat exchange by convection between a component and a fluid. This heat exchange, in the case of quenching, determines the drop in temperature in the component. This interaction can be set-up in ABAQUS by plugging-in all of the relevant properties of the quenching fluid such as its heat transfer coefficient and its temperature, and by pointing out all of the surfaces of the component that are coming in contact with it.

The value of the heat transfer coefficient, that is necessary to simulate the quenching gas, is dependent on some very important factors such as the flow rate of the gas in the quenching chamber, the pressure of the gas, and the temperature [16]. The study presented in [16] has proven very useful in understanding the relations between the heat transfer coefficients and the factors mentioned above. In that study, in fact, the variation of the heat transfer coefficients is plotted against the temperature for different values of mass flow rate and pressure of the quenching gas. Important outcomes of this study are that the values of the heat transfer coefficients rise greatly with an increase in mass flow rate and pressure of the quenching gas, and that the coefficients remain quite constant over a very wide temperature range. These last concepts can be easily seen when looking at Figure 3. 8, that was taken from [16].

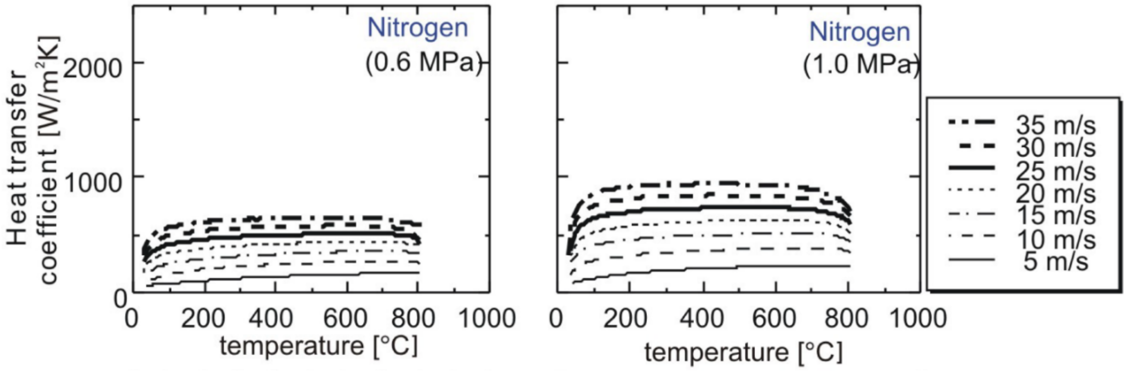

Figure 3. 8: Heat transfer coefficient of nitrogen as a function of temperature and mass flow rate, for two different values of pressure. [16]

In this image, the trend of the heat transfer coefficient for nitrogen gas is shown for different quenching gas mass flow rates (35 m/s, 30m/s, 25m/s 20 m/s, …) and pressures (6 bar, 10 bar), and over a broad temperature range (10°C to 800°C). It is possible to see that the graph on the right, referring to the case where the nitrogen is at 10 bar of pressure, shows greater values with respect to the graph on the left where the pressure of the quenchant is of only 6 bar. Furthermore, in both graphs it is possible to see that the higher the mass flow rate of the quenchant gas, the higher is the value of the heat transfer coefficient. Lastly, it is evident that the graphs for both pressure values are quite flat, demonstrating the very little dependency of the heat transfer coefficient on temperature. In Figure 3. 8, that was inserted just for ease of explanation, only two pressure values are shown, however in the original paper [16], many more are displayed. Furthermore, in the study [16], also different inert gases and mixture between different inert gases are studied.

The negligible temperature dependance is particularly important as it allows to make a very reasonable approximation, and set the value of the heat transfer coefficient as independent on temperature. On the other hand, however, usually in inert gas quenching chambers, the pressure at which the gas operates inside the chamber varies with time and, for this reason, so does the value of the heat transfer coefficient. In fact, when the gas in injected inside the chamber, in order to fill the chamber as quickly as possible, the pressure of the gas at the start of the process could obtain a value higher with respect to that found in the rest of process. The pressure then usually settles down after the initial spike. Furthermore, in the quenching process, also the temperature of the inert gas changes with time. In fact, it increases at the start of the quenching procedure, and then goes back to it's starting injection temperature value after the initial spike. To account for these variations, in the simulation tool, the subroutine FILM is used. This subroutine can change the values of the heat transfer coefficient and of the sink temperature, that is the temperature of the inert gas. This is done in order to correctly simulate the inert gas pressure and temperature variations that occur in the real quenching chamber. Following this logic, the correct values of the heat transfer coefficients are chosen for the different pressure and flow rate values by consulting the graphs in [16], and then they are reported in the subroutine FILM as a function of time. Following the same reasoning, also the sink temperatures are defined as a function of time in the FILM subroutine. In this way, the interaction between component and fluid can be completely simulated. If the real quenching gas pressures and temperatures are not known, perhaps because the process that is being simulated is not existing and so no previous information of the pressure and temperature of the quenchant is available, then the expected values, perhaps based on previous experience, can be used instead.

Having set the surface film interaction in ABAQUS and using the FILM subroutine, the temperature drop in the component is simulated. However, all of the metallurgy-related-effects that happen during quenching due to this quick decrease in temperature, are not simulated by ABAQUS alone, and, for this reason, must be implemented separately with the use of subroutines. These phenomena, along with the formulations with which they are simulated, will be described in greater detail in the next paragraphs.

3.3.3 Material Modelling

Before performing the quenching simulation, different material properties must be defined in ABAQUS. The material properties required to perform the simulation are: Young's modulus, Poisson's ratio, thermal conductivity, specific heat, and density. These properties are all included in ABAQUS when creating and defining the properties of a new material. In order to ensure the versatility of the simulation tool and allow the possibility for the tool to be used in different scenarios involving also different steels, it was decided to use phase dependent properties. In this way, the properties of the steel at each location are evaluated solely based on the particular microstructure and temperature found at that particular location. In this way, the same ABAQUS material property definition can be used for different steels, as the properties will be evaluated during the simulation depending on the microstructure and temperature information. If instead of this method, the trend of a material property for a very specific steel alloy would be implemented in ABAQUS, that material property would work well only with simulations concerning that particular alloy.

The information regarding the different phase transformations, and so amount of different steel phases present, is evaluated with the subroutine USDFLD, as it will be described in greater detail in the following paragraph. This information is than passed from the subroutine USDFLD into ABAQUS by means of field variables. These variables can be used in the material property definition to relate the value of a material property to the amount of different steel phases present. The value of the material property is then evaluated in ABAQUS using a linear mixture rule between the value of a property at a certain temperature for a certain steel phase, and the amount in which that steel phase is present. This procedure is done for most of the properties mentioned above.

Greater information on the simulation of these material properties is given in the following paragraphs.

3.3.3.1 Young's Modulus

The young's modulus of a steel, or elastic constant, indicates the ability of the steel to undergo stresses without incurring into permanent deformations [7]. The young's modulus is generally an experimentally derived parameter. It is defined with Hook's law, shown in equation 17, as: [7]

$$E = \frac{\sigma}{\varepsilon} \tag{17}$$

In this equation:

- E is the young's modulus.
- σ is the stress evaluated in the experimental test.
- ε is the strain evaluated in the experimental test.

Equation 17 portrays a linear relation between the stress and strain with the elastic modulus as slope. This relation is true for the elastic field of the steel and describes its elastic behavior. [7]

In this simulation tool, the elastic modulus will be evaluated with the equations described in [2] for the elastic modulus. In that study, different equations are provided for evaluating the elastic modulus for austenite and for the ferritic phases (ferrite, perlite, bainite and martensite) as a function of temperature. These equations are reported below.

For austenite:

$$E = 1.985 \cdot 10^{11} - 4.462 \cdot 10^{7} \cdot T - 9.09 \cdot 10^{4} \cdot T^{2} - 2.059 \cdot T^{3} \tag{18}$$

For ferrite, perlite, bainite and martensite:

$$E = 2.145 \cdot 10^{11} - 3.097 \cdot 10^{7} \cdot T - 9.208 \cdot 10^{-4} \cdot T^{2} - 2.797 \cdot T^{3} \tag{19}$$

Expression 28 and 19 are reported in Pascal units.

These equations, to better understand their trends, were plotted on MATLAB and are reported in Figure 3. 9.

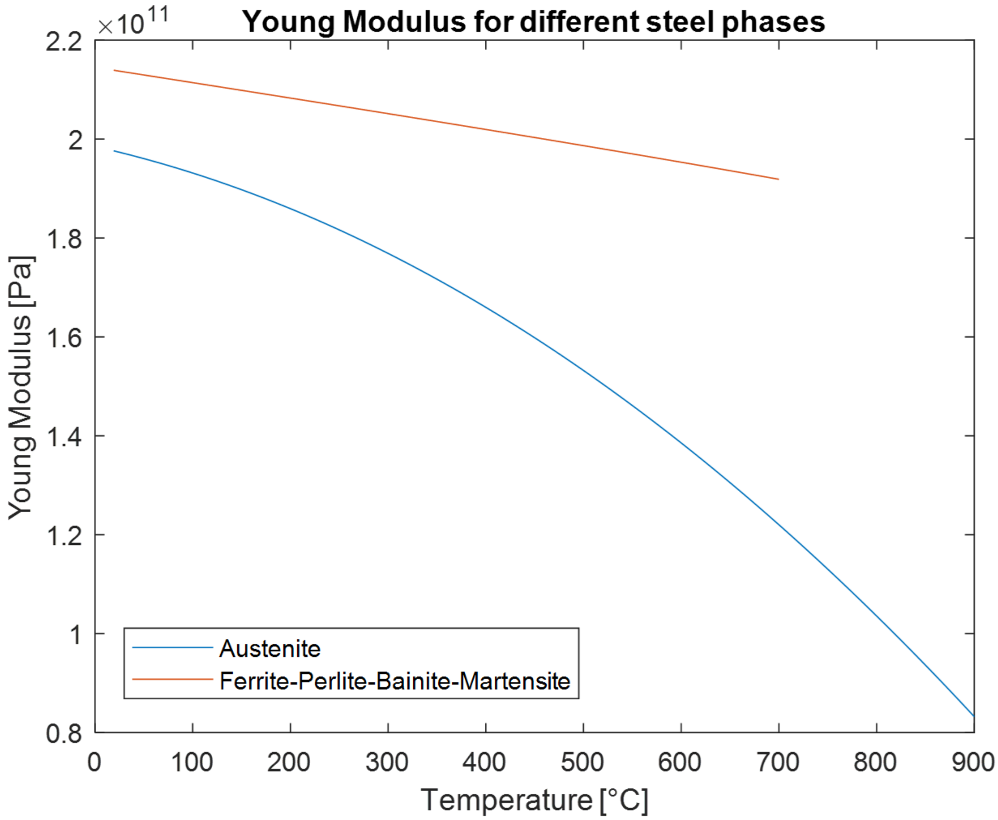

Figure 3. 9: Young’s modulus as a function of temperature for different steel phases. Plot obtained in MATLAB starting from equations reported in [2].

It is clear to see from Figure 3. 9 that the elastic modulus has a very high temperature dependance and tends to decrease quite dramatically at high temperatures.

It is also to be noted that the elastic modulus changes very little between the different steel phases. In fact, the value of the elastic modulus is considered to be the same for all of the ferritic phases such as ferrite, perlite, bainite and martensite.

3.3.3.2 Poisson’s Ratio

The poisons ratio is theoretically defined as the ratio between the lateral strain and the axial strain. This value is important as it described the way in which the stress in one direction affects the stress in the opposite direction. The value of this parameter is usually assumed to have a constant value and independent on temperature. This assumption is also adopted for the simulation tool. The value of this parameter is specific of the steel used in the simulation tool. [7]

3.3.3.3 Density

The density of a steel is a parameter that defines the amount of mass that is contained in a unit volume of material. The value of the density for steels can often assumed to be temperature independent [7]. For this reason, in the simulation tool, the assumption is made that the density is a constant. The value of the density of the steel changes dependent on its alloying composition, for this reason, as for the Poisson's ratio, different values must be provided as inputs in ABAQUS when different steels are simulated.

3.3.3.4 Thermal Conductivity

The thermal conductivity describes the heat transfer inside a material without material flow. In practice, it is used to model the way in which the heat is conducted within the steel component from regions with higher temperature to cooler regions. [7]

As for the Young's modulus, also the values of the thermal conductivity for the different steel phases are reported as function of temperature in a set of equations that are taken from [2] and are reported below.

Phase:	**Temperature Range**	**Thermal conductivity λ: $\left(W/_{m\,°C}\right)$**	
Austenite	$T < 200\,°C$	$\lambda = 18$	(20)
	$200\,°C \le T \le 900\,°C$	$\lambda = 10.41 + 2.51 \cdot 10^{-8} \cdot T^{2.5} + 4.653 \cdot 10^{-1} \cdot T^{0.5}$	(21)
Ferrite, pearlite	$19\,°C \le T \le 900\,°C$	$\lambda = 44.01 - 3.863 \cdot 10^{-5} \cdot T^{2} - 3.001 \cdot 10^{-7} \cdot T^{2.5}$	(22)
Bainite	$19\,°C \le T \le 600\,°C$	$\lambda = 44.04 - 4.871 \cdot 10^{-4} \cdot T^{1.5} - 1.794 \cdot 10^{-8} \cdot T^{3}$	(23)
Martensite	$19\,°C \le T \le 400\,°C$	$\lambda = 44.05 - 5.019 \cdot 10^{-4} \cdot T^{1.5} - 1.611 \cdot 10^{-8} \cdot T^{3}$	(24)

These equations have been plotted in MATLAB and are shown graphically in Figure 3. 10.

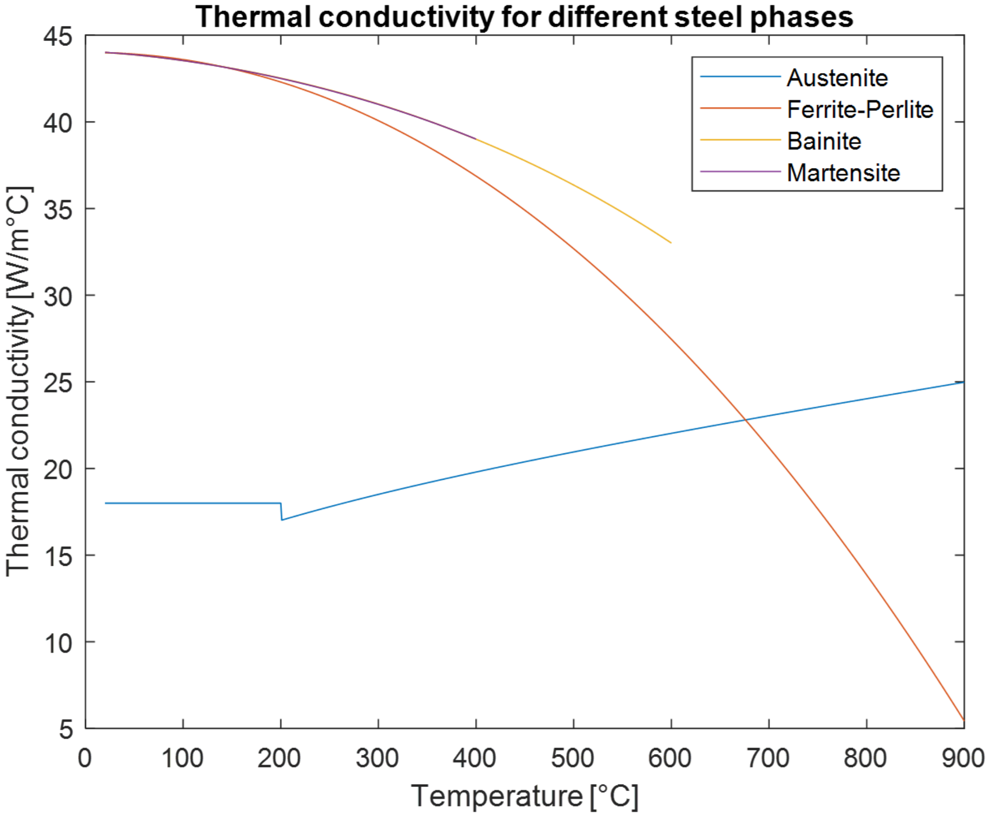

Figure 3. 10: Thermal conductivity as a function of temperature for different steel phases. Plot obtained in MATLAB starting from equations reported in [2].

What can be seen is that the values of the thermal conductivity for austenite tend to decrease with decreasing temperatures. On the other hand, the ferritic phases show an opposing trend with the values of the thermal conductivities increasing with a decrease in temperature.

3.3.3.5 Specific Heat

The specific heat of the steel represents the amount of heat that must be supplied to one unit mass of that substance in order to cause it to increase of one unit of temperature and is defined with the unit $J/kg \cdot {}^{\circ}C$. As for the Young's modulus and the thermal conductivity, also in this case, some formulations evaluating the value of the volumetric heat capacity for each steel phase as a function of temperature were found in [2]. The volumetric heat capacity is defined with the unit $J/m^3 \cdot {}^{\circ}C$. Starting from the volumetric heat capacity, the specific heat can be easily obtained by dividing the volumetric heat capacity by the density of the steel.

The equations found in [2] are reported below for the different steel phases.

Phase:	**Temperature Range**	**Volumetric heat capacity ρc: $\left(J/_{m^3\,°C}\right)$**	
Austenite	$T < 200\ °C$	$\rho c = 4.29 \cdot 10^6$	(25)
	$200\ °C \le T \le 900\ °C$	$\rho c = 4.019 \cdot 10^6 + 4.034 \cdot 10^{-1} \cdot T^2 + 2.015 \cdot 10^4 \cdot T^{0.5}$	(26)
Ferrite, pearlite	$19\ °C \le T \le 900\ °C$	$\rho c = 3.42 \cdot 10^6 + 1.347 \cdot 10^{-1} \cdot T^{2.5} - 3.745 \cdot 10^{-3} \cdot T^3 + 2.698 \cdot 10^{-2} \cdot T^{0.5}$	(27)
Bainite	$19\ °C \le T \le 600\ °C$	$\rho c = 3.487 \cdot 10^6 + 1.404 \cdot 10^3 \cdot T + 5.715 \cdot 10^3 \cdot T^{0.5}$	(28)
Martensite	$19\ °C \le T \le 400\ °C$	$\rho c = 3.41 \cdot 10^6 + 3.215 \cdot 10^{-3} \cdot T^3 + 2.919 \cdot 10^4 \cdot T^{0.5}$	(29)

However, in ABAQUS, the value to be inserted is the specific heat. For this reason, for this simulation tool, the values obtained with the equations provided in [2] and shown in equations 25 to 29, are divided by the density of the particular steel used, as defined in paragraph 6.3.3, in order to obtain the value of the specific heat.

To better understand the trend of the specific heat for the different steel phases as a function of temperature, the values of the specific heat for a AISI 4140 steel, whose density is of 7850 kg/m^3 [54], were plotted on MATLAB and are displayed in Figure 3. 11.

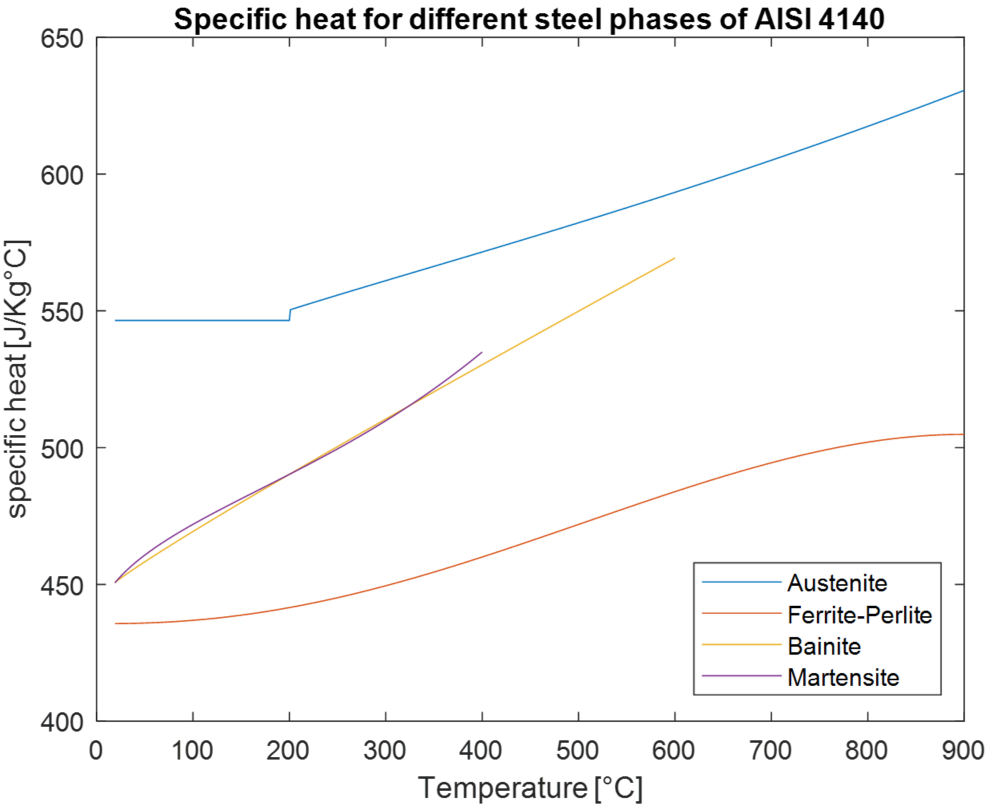

Figure 3. 11: Specific heat as a function of temperature for different steel phases in AISI 4140 steel. Plot obtained in MATLAB starting from the equations reported in [2].

What can be seen, is that the trend of the specific heat is to decrease with decreasing temperature for all of the steel phases. Although Figure 3. 11 refers to values of the specific heat of AISI 4140 steel, since the graphs are obtained by plotting equations 25 to 29, and dividing the results of such equations by the density of the AISI 4140 steel, that is a constant, similar trends should be found for every steel, with the results varying only because of the different densities of the different steels.

3.3.3.6 Material Modelling Final Remarks

In conclusion, the simulation tool, to perform the quenching simulation, requires some material properties. Of these properties, the Young's modulus, the thermal conductivity and the specific heat, are evaluated directly during the simulation, as function of the temperature and of the amount of the different steel phases present. In order to do so, the values of these three material properties for the different steel phases and as a function of temperature, are evaluated by using the equations reported above. These values, for each material property, are then reported in ABAQUS in the material definition section. Starting from this input data, during the simulation, at each iteration, the field variables carrying information on the different steel phases present, and the information on the temperature found during the current iteration, are used by ABAQUS to determine the most correct values for the material properties to be used in that iteration.

For both of the other two material properties that are required: the density and the Poisson's ratio, on the other hand, a fixed value dependent on the alloying composition of the considered steel is utilized. Also these values must be defined in ABAQUS before starting the simulation.

3.3.4 Phase Transformations

A very important consequence of the quenching process, as reported also in the literature review chapter, is the onset of the phase transformations. As seen in the literature review chapter when introducing the most relevant steel phases, different steel phase transformations occur according to different physical phenomena. Nevertheless, a classification can be done according to which the steel phase transformations are grouped in two categories: diffusion and non-diffusion transformations. In particular, diffusion transformations upon cooling are those in which the carbon atoms are allowed to diffuse within the component during cooling, and include the transformation of austenite into ferrite, perlite and bainite. On the other hand, non-diffusion transformations are those in which the carbon atoms diffusion during cooling is not possible. This is usually the case, when the cooling is very rapid and so the diffusion is not possible due to the very little available time for it to occur. An example of a diffusionless transformation is the transformation from austenite into martensite. Different formulations and methods are generally present for the prediction of diffusion and diffusionless transformations. These are shown and explained in the following paragraphs.

3.3.4.1 Diffusion Transformations

Regarding diffusion transformations, different FEA methodologies have been used over the years to predict phase transformations. In particular, one first approach used in a very large number of studies dealing with the phase transformations and simulating the phase changes, is based on the TTT experimental diagrams. The concept of TTT diagram was already introduced in the literature review chapter. These diagrams are used to illustrate the temperatures and times for the transformation of the austenite into the different steel phases during cooling. An example of the TTT diagram, showing also some reference temperature values, is shown in Figure 3. 12 [55]. As explained in the literature review chapter, since the transformation temperatures are dependent on the alloying composition, there does not exist a single TTT diagram that can be used for all steels, but rather many different TTT diagrams can be found when looking at steels with differing alloying composition.

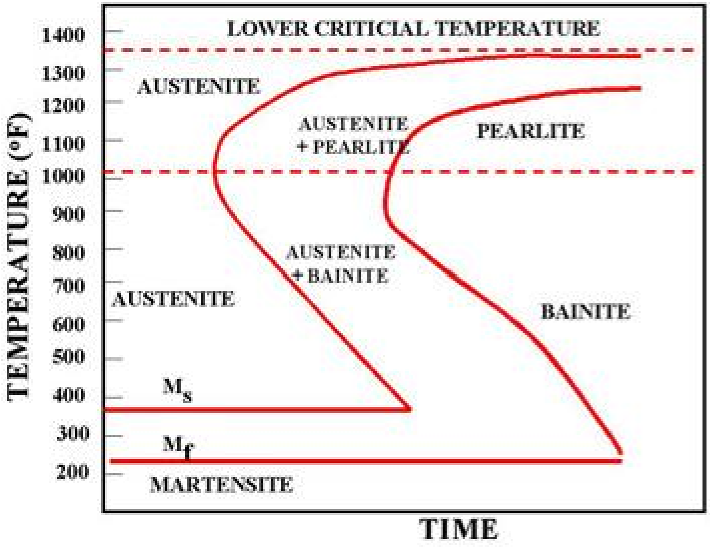

Figure 3. 12: TTT diagram example. Image taken from [55]

The method that uses the TTT diagram to evaluate the phase transformations is based on the application of the Johnson–Mehl–Avrami equation and works as follows.

As explained in [56], the diffusion transformation can be expressed by using the Johnson–Mehl–Avrami–Kolmogorov (JMAK) equation [57][58][59]. This formulation, as expressed in [56], is reported in equation 30. It is an exponential equation that relates the volume fraction of the diffusion phase that is generated, to the time. This is done by using two material related parameters: A and B.

$$\xi_i = 1 - e^{-A \cdot t^B} \tag{30}$$

In this equation:

- ξ_i represents the phase fractions of the different diffusion transformation phases. In this case, “i” can take the values of “p” to represent perlite, “b” to represent bainite and “f” to represent ferrite.
- t represents the time.
- A and B are material related parameters.

A and B can be obtained from the TTT diagram mentioned above. This can be done by considering some particular points in the TTT diagram. In particular, as explained in [56], at a fixed temperature, the transformation times that determines the generation of a 1% (0.01) and 99% (0.99) amount of a diffusion phase are recorded. In this way the following information can be obtained:

- F_θ, that is equal to 0.01, is the starting phase fraction of the diffusion phase.
- $F_\emptyset$, that is equal to 0.99, is the ending phase fraction of the diffusion phase.
- θ is the time required to have a F_θ phase fraction.
- $\emptyset$ is the time required to have a $F_\emptyset$ phase fraction.

$\emptyset$, θ , $F_\emptyset$ and F_θ define the location of two points in the TTT diagram. These points can be located in the TTT diagram for each diffusional phase, as shown in Figure 3. 13, that was taken from the study [56].

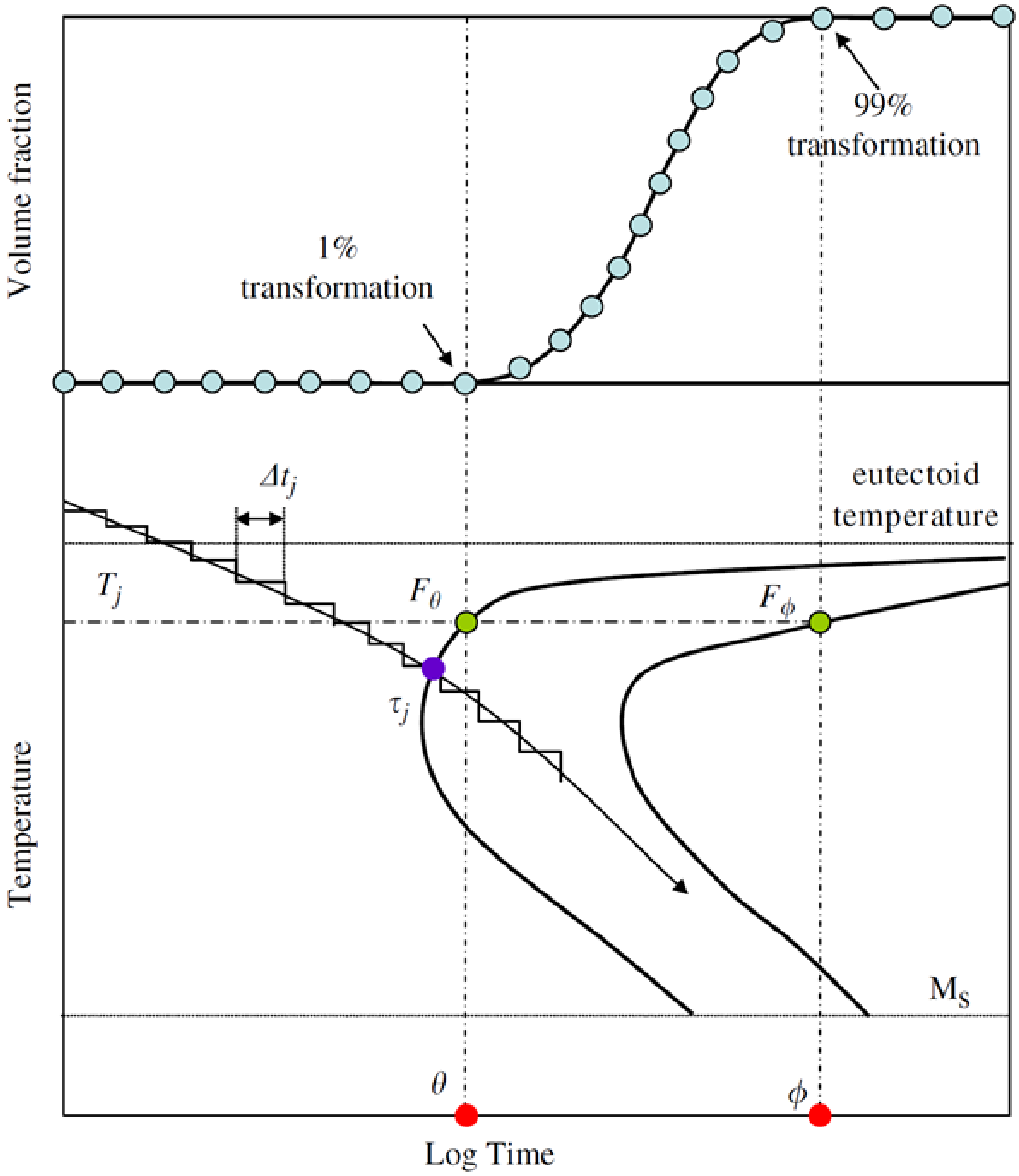

Figure 3. 13: Explanatory diagram for phase fraction evaluation from TTT diagrams. [56]

Knowing the values of F_θ, $F_\emptyset$, θ and $\emptyset$, the parameter A can be obtained with equations 31 or 32 that are obtained by rearranging equation 30, and inserting the values of F_θ or $F_\emptyset$ instead of F_i, and the values of θ or $\emptyset$ instead of t.

$$A = -\frac{\ln(1 - F_\theta)}{\theta^B} \tag{31}$$

$$A = -\frac{\ln(1 - F_{\emptyset})}{\emptyset^{B}} \tag{32}$$

In order to evaluate the parameter A, however, parameter B must be known. The latter can be evaluated with the formulation expressed in equation 33.

$$B = \frac{ln\left(\frac{\ln(1 - F_{\theta})}{\ln(1 - F_{\emptyset})}\right)}{ln\left(\frac{\theta}{\emptyset}\right)} \tag{33}$$

Equation 33 is just obtained by combining the equation 31 and 32.

Once the parameters A and B are evaluated, the equation 30 can be used to evaluate the phase fraction of the diffusive phase. It must be noted that, as explained in [56], when using equation 30, the value of the transformation time t to be used, is evaluated as shown in equation 34, by adding the value of time increment used in the simulation to the time obtained based on the value of the phase fraction at the precious step.

$$t_j = \Delta t_j + \left[-\frac{\ln(1 - F_{j-1})}{A}\right]^{1/B} \tag{34}$$

Where:

- t_j is the value of t to be used in equation 30, for the j^{th} iteration.
- Δt_j is the time increment in the j^{th} iteration in the simulation.
- $\left[-\frac{\ln(1 - F_{j-1})}{A}\right]^{1/B}$ is the time corresponding to the phase fraction in the previous simulation iteration (j-1).

However, as expressed in [56], the JMAK equation can be used only for isothermal transformation processes. This is not the case when considering the quenching process, where the temperature decreases very quickly and does not remain constant. In order to use this equation even though the quenching procedure is not isothermal, the Scheil's additivity rule is utilized [56]. In this way, the cooling curve that the component experiences is divided in many different isothermal segments as shown in Figure 3. 13. At this point, the equation 30 can be used without any issues for each isothermal segment. Due to nucleation of the different diffusive steel phases, the transformation is supposed to start when the condition expressed in equation 35 is satisfied [56].

$$\sum_j \frac{\Delta t_j}{\tau_j} = 1 \tag{35}$$

This last expression states that the transformation starts only when the sum of the time of the isothermal segments becomes greater than a value τ_j ,that is the transformation beginning time at the j^{th} iteration of the simulation. The meaning of τ_j and of the equation 35 can be easily understood when looking at Figure 3. 13.

This method has been used in a very large number of studies dealing with heat treatments and phase transformations such as [2], [3], [30], [38], [39], [40], [42], [56], and [60].

However, this method has a great drawback that impairs the possibility to use it in the simulation tool developed in this thesis research. In fact, this method requires a TTT diagram in order to evaluate the material parameters A and B that are used in the simulation. The TTT diagram however, as mentioned in the literature review chapter, is greatly dependent on the alloying composition of the steel. The simulation tool that is being developed in this research, is used to simulate a sequence of carburizing quenching and tempering. In this scenario, the component that is quenched, has previously been carburized and so displays a varying carbon concentration. For this reason, using a single TTT diagram to simulate the phase transformations would lead to incorrect results as different TTT diagrams for each alloying compositions should be used instead. This issue was already introduced in the literature review chapter.

For this reason, a different type of solution that takes into consideration also the carbon percentage at each location must be used when also carburizing is considered. This is the case with the phase transformation model developed by Kirkaldy et al. in [61].

The model consists of a set of three differential semiempirical equations that simulate the transformations from austenite into ferrite, perlite and bainite. The three equations relate the rate of formation of the steel phase to the alloying composition of the steel, to the grain size of the austenite from which the steel phases are generated, to the undercooling below the phase transformation start temperature, and to the amount of each phase transformed.

The equation proposed by Kirkaldy for ferrite is:

$$\tau_F = \frac{59.6 \cdot Mn + 1.45 \cdot Ni + 67.7 \cdot Cr + 244 \cdot Mo}{0.3 \cdot 2^{\frac{G-1}{2}} \cdot (Ae_3 - T)^3 \cdot e^{-\frac{23500}{R \cdot T}}} \cdot I(X) \tag{36}$$

The equation proposed by Kirkaldy for perlite is:

$$\tau_P = \frac{1.79 + 5.42 \cdot (Cr + Mo + 4 \cdot Mo \cdot Ni)}{2^{\frac{G-1}{2}} \cdot (Ae_1 - T)^3 \cdot D'} \cdot I(X) \tag{37}$$

The equation proposed by Kirkaldy for bainite is:

$$\tau_B = \frac{(2.34 + 10.1 \cdot C + 3.8 \cdot Cr + 19 \cdot Mo) \cdot 10^{-4}}{2^{\frac{G-1}{2}} \cdot (B_s - T)^3 \cdot e^{-\frac{27500}{R \cdot T}}} \cdot I'(X) \tag{38}$$

Where:

$$\frac{1}{D'} = \frac{1}{e^{-\frac{27500}{R \cdot T}}} + \frac{0.01 \cdot Cr + 0.52 \cdot Mo}{e^{-\frac{37000}{R \cdot T}}} \tag{39}$$

$$I(X) = \int_0^x \frac{1}{X^{0.66 \cdot (1-X)} \cdot (1 - X)^{0.66 \cdot X}} dX \tag{40}$$

$$I'(X) = \int_0^x \frac{e^{X^2 \cdot (1.9 \cdot C + 2.5 \cdot Mn + 0.9 \cdot Ni + 1.7 \cdot Cr + 4 \cdot Mo - 2.6)}}{X^{0.66 \cdot (1-X)} \cdot (1 - X)^{0.66 \cdot X}} dX \tag{41}$$

In the above equations: D' is the effective diffusion coefficient and is defined as expressed in equation 54, the symbols of the different chemical elements represent the percentage of the different alloying elements in the steel, T represents the temperature at which the phase fraction is being evaluated in Kelvin units, and R represents the gas constant expressed in $^{cal}/_{mol \cdot K}$.

The $I(X)$ and $I'(X)$ integration terms for ferrite and perlite, and for bainite respectively, are a function of the normalized phase fraction X. The functions $I(X)$ and $I'(X)$, represent the sigmoidal behavior of the phase transformation. The trend of $I(X)$, just for sake of understanding, is shown below in Figure 3. 14.

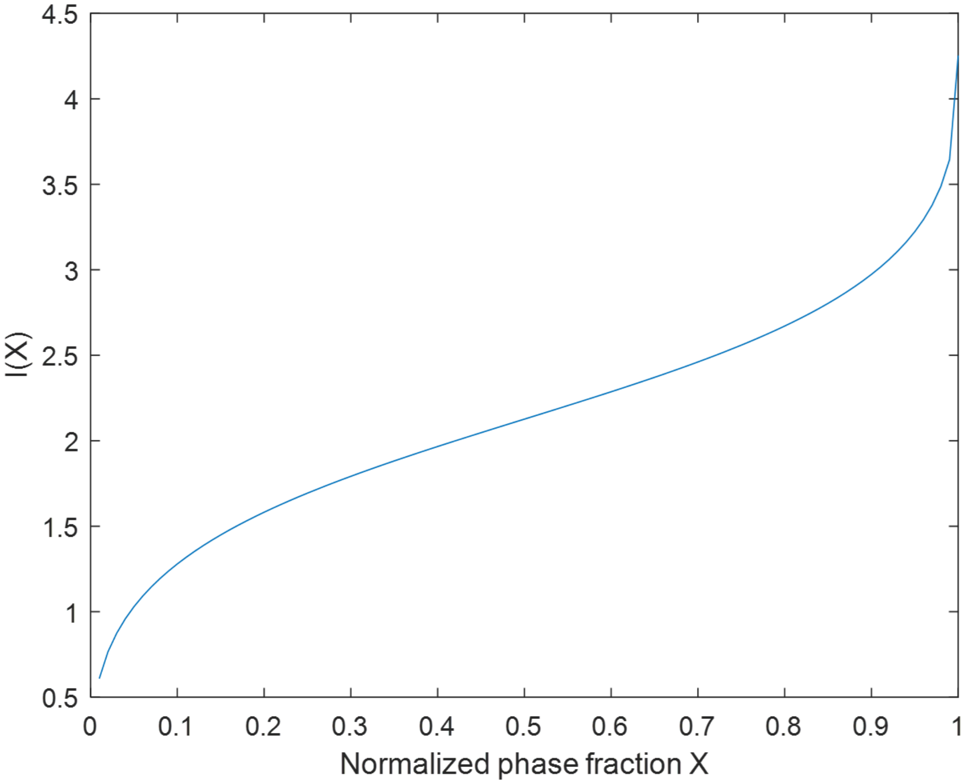

Figure 3. 14: Plot of sigmoidal term $I(X)$ found in Kirkaldy's experimental equations.

The trend of $I'(X)$ is very similar to that of $I(X)$, however, it depends also on the alloying composition.

In equations 36 to 38, G is the austenite grain size diameter expressed in ASTM. In this standard, the ASTM grain size number G is related to the number of austenite grains per square inch that can be counted in a 100X magnification image, that is expressed as N, as shown in equation 42 [62].

$$N = 2^{G-1} \tag{42}$$

In this simulation tool, the value of G is evaluated starting from the austenite grain size at the end of the carburizing procedure. The latter is evaluated as discussed previously in the carburizing simulation chapter.

The factors Ae_3, Ae_1 and B_s represent phase transformation starting temperatures. In particular, the temperature Ae_3 is the austenite-ferrite transformation temperature, Ae_1 is the temperature below which ferrite starts to form and B_s is the temperature below which bainite starts to form. These temperatures vary with the alloying composition. Different formulations have been proposed throughout the years to evaluate these temperatures when knowing the alloying composition. In this study, the following formulation are used.

$$Ae_3 = 910 - 203 \cdot \sqrt{C} - 15.2 \cdot Ni + 44.7 \cdot Si + 104 \cdot V + 31.5 \cdot Mo + 13.1 \cdot W - 30 \cdot Mn - 11 \cdot Cr - 20 \cdot Cu + 700 \cdot P + 400 \cdot Al + 120 \cdot As + 400 \cdot Ti \tag{43}$$

$$Ae_1 = 723 - 10.7 \cdot Mn - 16.9 \cdot Ni + 29 \cdot Si + 16.9 \cdot Cr + 290 \cdot As + 6.4 \cdot W \tag{44}$$

$$B_s = 656 - 58 \cdot C - 35 \cdot Mn - 75 \cdot Si - 15 \cdot Ni - 34 \cdot Cr - 41 \cdot Mo \tag{45}$$

These equations were taken from [63], however, the original studies where the formulations were developed are: [24] for Ae_1 and Ae_3 and [64] for B_s.

Finally, the values of τ_F, τ_P and τ_B in equation 36 to 38 are representing the amount of time that is necessary for the diffuse phase to achieve a value X of normalized phase fraction.

For each diffusive transformation phase, the values of time necessary to achieve a 1% of transformation and a 99% of transformation from austenite to ferrite, perlite, and bainite, respectively, are evaluated and are called $\tau_{F,1\%}$, $\tau_{P,1\%}$, $\tau_{B,1\%}$ and $\tau_{F,99\%}$, $\tau_{P,99\%}$, $\tau_{B,99\%}$. These can be obtained by applying equations 36 to 38 and placing the value of X equal to 1% and 99%.

By knowing these values, then the amount of phase fraction of the diffuse transformation phases can be determined with the procedure shown below [65].

As a first step, the nucleation time is taken into consideration. For this reason, the transformation is considered to start once the phase fraction reaches a value of 1%. In the simulation tool, this is done by evaluating the steel phase fractions only once the relations shown in equations 46, 47 and 48, for ferrite, perlite and bainite respectively, are fulfilled.

$$\sum_j \frac{\Delta t_j}{\tau_{F,1\%}} = 1 \tag{46}$$

$$\sum_j \frac{\Delta t_j}{\tau_{P,1\%}} = 1 \tag{47}$$

$$\sum_j \frac{\Delta t_j}{\tau_{B,1\%}} = 1 \tag{48}$$

Where, in equations 46 to 48, the Δt_j is the time increment of the j^{th} iteration. These equations are fulfilled when the sum of the different time increments in the subsequent iterations becomes greater than the amount of time needed for the different diffusive transformation phases to nucleate. Once the above equations are fulfilled, then the normalized phase fraction of the diffusive transformation phases can be evaluated with equations 49 to 51.

$$X_F = \sum_j \frac{\Delta t_j}{\tau_{F,99\%} - \tau_{F,1\%}} \tag{49}$$

$$X_P = \sum_j \frac{\Delta t_j}{\tau_{P,99\%} - \tau_{P,1\%}} \tag{50}$$

$$X_B = \sum_j \frac{\Delta t_j}{\tau_{B,99\%} - \tau_{B,1\%}} \tag{51}$$

With equations 49 to 51, the normalized volume fractions of ferrite, perlite and bainite respectively are calculated. The normalized fraction is defined as the ratio between the real amount of phase fraction present, and the maximum amount that could be present in the particular condition that is analyzed. The actual phase fraction can then be discovered starting from the normalized phase fraction amount.

This method, described in [65], is based on the equations 36 to 41 that were developed by Kirkaldy in [61]. These equations were used in different studies, as for example [66] and [65], where they were used to study the transformation of austenite into ferrite, perlite and bainite during the cooling occurring after welding, and obtained good approximation results. However, the studies performed by Li et al. [36], and by other researchers previous to that, stated that these set of equations developed by Kirkaldy (equations 51 to 56), worked well with steels with low amounts of alloying materials, however, they worked less well when considering steels with a higher alloy concentration. To tackle this issue, Li et al. created a new set of empirical equations based on phase transformation theories and empiricism.

These equations are based on those created by Kirkaldy. The greatest differences between the two set of equations are found in the value of the sigmoidal term, and on the expressions, function of the alloying composition, that are found at the nominators of the set of equations. Li et al.'s equations are reported below:

The equation proposed by Li et al. for ferrite is:

$$\tau_F = \frac{e^{1+6.31C+1.78Mn+0.31Si+1.12Ni+2.70Cr+4.06Mo}}{2^{0.41G} \cdot (Ae_3 - T)^3 \cdot e^{-\frac{27500}{R \cdot T}}} \cdot S(X) \tag{52}$$

The equation proposed by Li et al. for perlite is:

$$\tau_P = \frac{e^{-4.25+4.12C+4.36Mn+0.44Si+1.71Ni+3.33Cr+5.19Mo^{0.5}}}{2^{0.32G} \cdot (Ae_1 - T)^3 \cdot e^{-\frac{27500}{R \cdot T}}} \cdot S(X) \tag{53}$$

The equation proposed by Li et al. for bainite is:

$$\tau_B = \frac{e^{-10.23+10.18C+0.85Mn+0.55Ni+0.90Cr+0.36Mo}}{2^{0.29G} \cdot (B_s - T)^2 \cdot e^{-\frac{27500}{R \cdot T}}} \cdot S(X) \tag{54}$$

Where:

$$S(X) = \int_0^x \frac{1}{X^{0.4 \cdot (1-X)} \cdot (1-X)^{0.4 \cdot X}} dX \tag{55}$$

In these equations, the terms have the same meaning as that described above for the Kirkaldy equations.

$S(X)$ is the sigmoidal term, that is one of the points of divergence between Kirkaldy's and Li et al.'s equations. This sigmoidal curve is shown below, in Figure 3. 15.

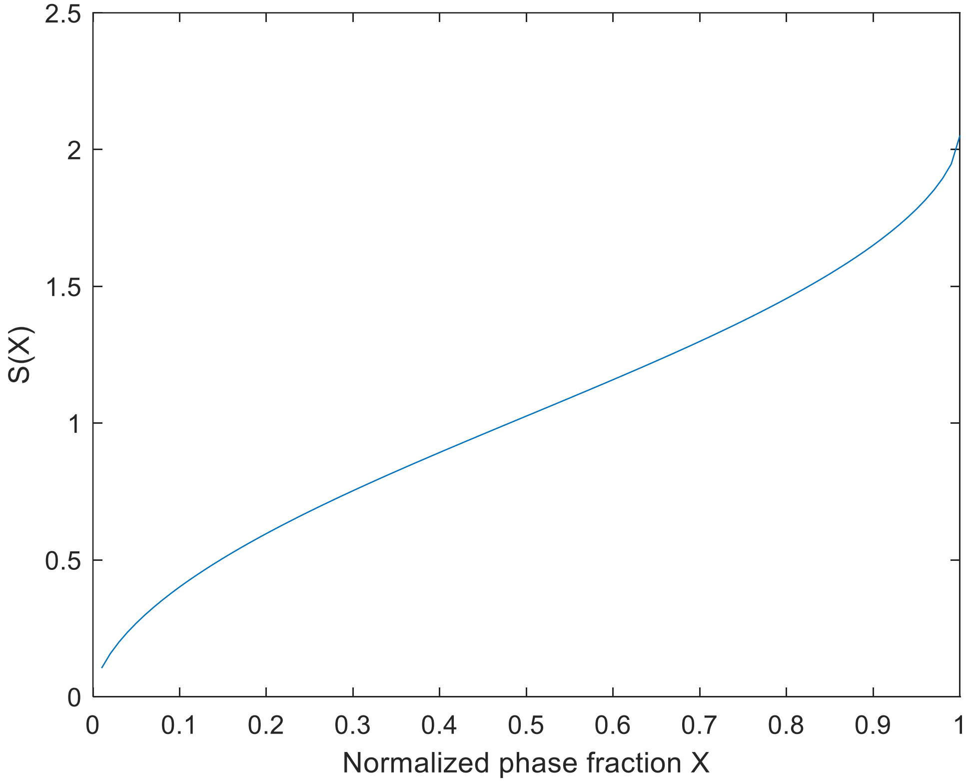

Figure 3. 15: Plot of sigmoidal term $S(X)$ found in Li et al.'s experimental equations.

When comparing Figure 3. 15 to Figure 3. 14, it is possible to see that the sigmoidal curve is greater for the Kirkaldy equations with respect to what is found with the Li et al. equations. This, as expressed in [36], means that the reaction rate is three times faster in the Kirkaldy model that it is in the Li et al. model.

This method, that was used by different studies such as [9] and [33], is reported in [36] to be in good agreement with experimental results.

Starting from Li et al.'s semiempirical equations, the different phase fractions can be evaluated by using equations 46 to 51, as seen previously for the Kirkaldy equations.

A very comprehensive comparison between the Kirkaldy and Li et al. models was done in the work of Chipalkatti J. [67]. In [67], comparisons are made between TTT diagrams evaluated by using the two models, and experimental TTT diagrams for AISI 4140 steel. What resulted from [67], is that the two models can be used to represent the overall shape of the TTT diagrams for that steel.

In the simulation tool prepared for this thesis research, based on the above information, it was decided to use the Li et al. method to evaluate the steel phases. This, because this method permits to have a good approximation of the phase transformation behavior of the steel, considering also the varying alloying composition within the component. The Li et al. model was selected over the Kirkaldy method as it is an improvement of the latter, that had issues with steels having high alloying composition.

3.3.4.2 Diffusionless transformations

The prediction of the non-diffusion transformation phase fraction is implemented in the simulation tool by using a different methodology to that used for diffusive transformations. Unlike what seen for the diffusion transformation phases, where different methodologies to evaluate the phase fractions were used in different studies, for the non-diffusion transformations a single method was used in basically all studies encountered in the literature review. This method consists in applying the Koistinen-Marburger equation [24]. This equation, reported in equation 56, relates the value of the phase fraction of martensite formed during cooling, to the undercooling below the martensite start-of-formation temperature.

$$\xi_m = 1 - e^{-0.011 \cdot (M_s - T)} \tag{56}$$

In equation 56, the phase fraction of martensite ξ_m is evaluated by having information on the current temperature T and on the martensite transformation starting temperature M_s.

The formulation to evaluate the martensite transformation starting temperature M_s, just as seen in the previous paragraph for Ae_3, Ae_1 and B_s, was taken from the study [63] and was originally developed by [64]. This formulation is reported in equation 57.

$$M_s = 550 - 360 \cdot C - 40 \cdot Mn - 20 \cdot Ni - 40 \cdot Cr - 30 \cdot Mo \tag{57}$$

In equation 57, as seen also with previous equations, the chemical elements symbols represent the percentage of the different alloying elements.

As reported in [8], the Koistinen and Marburger equation is based on the most accurate technique for determining small amounts of retained austenite, X-ray analysis. For this reason, as reported in [8], "this equation is considered to give the best representation of martensite transformation over the entire range of undercooling".

3.3.4.3 Phase Transformations Final Remarks

In the simulation tool, the phase transformations are implemented utilizing the equations shown above for diffusive and non-diffusive transformations. As expressed in [40], for both diffusive and non-diffusive transformations, the effect of the latent heat of transformation, that is a certain amount of heat that is released when phase transformation occurs and that will be discussed in more detail in the following section, may generate errors when calculating the phase fractions. In fact, the heat released during phase transformations, may cause a slight temperature increase, that may cause the simulation tool to believe that there is a decrease in a phase fraction that was already generated from austenite. To avoid this, the equation reported below is also implemented for each steel phase.

$$\xi(j) = \begin{cases} \xi(j), & \xi(j) \geq \xi(j-1) \\ \xi(j-1), & \xi(j) < \xi(j-1) \end{cases} \tag{58}$$

In this equation:

- ξ is the phase fraction of either ferrite, bainite, perlite, or martensite.
- j is the current iteration in the simulation.
- $(j-1)$ is the previous iteration in the simulation.

In this way, the phase fraction that is created from austenite upon cooling, cannot transform back to austenite due to the effect of the latent heat of transformation.

The phase fraction calculations are not done directly in ABAQUS and so must be implemented separately with the use of a subroutine. The subroutine used is USDFLD. As already explained in the literature review chapter, this subroutine has a very important function as it allows the user to create some user-defined variables. These variables have a meaning that is defined by the creator of the subroutine and can be visualized in the

ABAQUS post processing. In particular, for the phase transformation simulation, the phase fractions evaluated with the methodology described above are saved in these user-defined variables so that they can be visualized in the post processing. Furthermore, these variables are provided also to other user-defined codes used in the simulation tool, where they are used for the evaluations of the latent heat of transformations, strains, and hardness profile. This last concept will be described in greater detail in the following paragraphs.

Additionally, the results of these phase transformation simulations, are also used in the main ABAQUS program in order to select the values of the young’s modulus, thermal conductivity and specific heat, that, as discussed in the material modelling paragraph, are evaluated with a linear mixture rule by knowing the amount of the different steel phases present, and the value of the property of the particular steel phase as a function of temperature.

Once the phase transformations have been evaluated and the percentage of the different phases at each instant is known, the effects determined by the phase transformations must be simulated. This will be discussed in the following sections where the effects of the transformations on the strains and on the heat rates are discussed.

3.3.5 Latent Heat of Transformation

A very important consequence of the phase transformations is the latent heat of transformation. In fact, each phase transformation from the parent austenite is accompanied with a heat release, where the amount of heat in question depends on the phase that is formed from the parent austenite. This heat release has a very important effect on the temperature distribution during the quenching simulation. [2] [30]

Different formulations are present to evaluate the latent heat for the transformation from austenite to the different steel phases.

In [2], the latent heat of transformation from austenite to the different phases is evaluated with the formulations shown below.

For the austenite to ferrite transformation:

$$\Delta H = 1.082 \cdot 10^{2} - 0.162 \cdot T + 1.118 \cdot 10^{-4} \cdot T^{2} - 3 \cdot 10^{-8} \cdot T^{3} - 3.501 \cdot 10^{4} \cdot T^{-1} \tag{59}$$

where T is the temperature expressed in kelvin scale.

For the austenite to perlite or bainite transformation:

$$\Delta H = 1.56 \cdot 10^{9} - 1.50 \cdot 10^{6} \cdot T \tag{60}$$

where T is the temperature expressed in Celsius scale.

For the austenite to martensite transformation:

$$\Delta H = 6.40 \cdot 10^{8} \tag{61}$$

In these equations, taken from the study of [2], the latent heat for the transformation of austenite to ferrite, bainite, perlite, and martensite are expressed in $\left({}^{J}/_{m^3} \right)$ as a function of temperature.

The equation 60 for the austenite to perlite transformation is utilized also in the study [39].

In the simulation tool proposed in this thesis research, however, another set of values is used to describe the latent heat of transformation. In particular, the values for the latent heat of transformation that are used, are reported in the Table 3. 2.

Table 3. 2: Latent heat of transformation for austenite transformation into bainite, ferrite, martensite and perlite.

Latent heat of transformation		**Units**
Austenite to Bainite	$6.2 \cdot 10^{8}$	${}^{J}/_{m^3}$
Austenite to Ferrite	$5.9 \cdot 10^{8}$	${}^{J}/_{m^3}$
Austenite to Martensite	$6.5 \cdot 10^{8}$	${}^{J}/_{m^3}$
Austenite to Perlite	$6.0 \cdot 10^{8}$	${}^{J}/_{m^3}$

These values were taken from the studies [40] and [41], where they were implemented to simulate the latent heat due to phase transformation during a quenching simulation. The studies mentioned above reported results that were validated successfully, therefore giving a confirmation of the validity of the latent heat of transformation expressions reported above in Table 3. 2.

The effect of the latent heat of transformation is implemented in the simulation tool with the use of the following equation:

$$\dot{Q} = \frac{\Delta H_i \cdot \Delta \xi_i}{\Delta t} \tag{62}$$

In this equation:

- $\dot{Q}$ is the heat generation rate due to the phase transformation.
- ΔH_i is the latent heat of transformation from austenite to the phase i.
- $\Delta \xi_i$ is the increase in phase percentage of phase i.
- Δt is the time increment in the simulation.

This equation describes the way in which the heat is released during phase transformations and was utilized in many different studies such as [2], [30], [37], [38], [39], [40], [41], [68], and probably many more.

The latent heat of transformation is then simulated in the simulation tool by implementing equation 62 in a user subroutine called HETVAL. This subroutine serves only this function in the simulation tool and is completely described in [28]. HETVAL works by recovering the phase transformation information in the form of the user-defined variables created in USDFLD, and then solving equation 62 using the phase transformation information recovered, the latent heat of transformation defined in Table 3. 2 and the information on the time increment that is provided by ABAQUS. The result of equation 62, as calculated in HETVAL, is then provided back to ABAQUS for it to be used in the ABAQUS calculations.

3.3.6 Quenching Strains

During the quenching process, due to the very high temperature gradient experienced by the component and to the phase transformations it determines, the component being quenched is subjected to different strains having different magnitudes. In particular, five different strains can be distinguished during the quenching procedure. The sum of these different strain contributions, as shown in equation 63, determines the overall strain. [2] [30] [56]

$$\varepsilon_{tot} = \varepsilon_e + \varepsilon_p + \varepsilon_{th} + \varepsilon_{tr} + \varepsilon_{tp} \tag{63}$$

In this equation:

- ε_{tot} is the total strain.
- ε_e is the elastic strain.
- ε_p is the plastic strain.
- ε_{th} is the thermal strain.
- ε_{tr} is the transformation strain.
- ε_{tp} is the transformation induced plasticity strain.

Each of these strain factors will be discussed in greater detail in the next paragraphs.

3.3.6.1 Elastic Strain

The elastic strain is the strain that is experienced by the component in the elastic field. The deformations experienced by the component in the elastic phase are generally reversible and disappear once the load that is causing the deformation is reduced. This strain is related to the stress in the elastic field by the young modulus, as explained in the material modeling paragraph and reported in equation 17. This strain component is already calculated in ABAQUS and requires no additional user coding to be implemented [30].

3.3.6.2 Plastic Strain

Plastic strain is the strain experienced by the component in the plastic region. In the plastic regions, the deformations that the component experiences are irreversible and are not completely recovered once the load that caused them is removed. As with the elastic strain, in the simulation tool created for the thesis research this strain component has no additional user coding implementing it in the simulation.

3.3.6.3 Thermal Strain

The thermal strain is determined by the fact that a temperature differential always determines the component to expand if the component is heated, or shrink if the component is cooled. The expansion or shrinking determines some strains that, in the case of quenching, are quite substantial due to the very high temperature differential involved in the process. The thermal strain is implemented with a formulation as that shown in equation 64.

$$\varepsilon_{th} = \alpha \cdot \Delta T \tag{64}$$

In this equation:

- ΔT is the temperature differential.
- α is the thermal expansion coefficient.

The latter is a parameter that is expressed in the units of $°C^{-1}$ and relates the strain experienced by the component to the temperature change that has caused such strain.

Equation 64 evaluates the value of the thermal strain as wanted, however, different phases are present during the quenching operation at different time instants and at different locations, and the different steel phases have different thermal expansion coefficients α. To account for this difference in α between the different phases, equation 65 is used.

$$\varepsilon_{th} = \Delta T \cdot \sigma_k \cdot \sum_i \alpha_i \cdot \xi_i \tag{65}$$

In this equation, the “i” subscript is used to represent the different phases. So, basically, equation 65 is performed for each steel phase and it is dependent on the amount of the different steel phases present. Furthermore, in equation 65, the σ_k is used to define the Kronecker delta. This is a tensor that is null in all values not on the tensor diagonal. This factor is included into the equation to account for the fact that the thermal strain is considered to be isotropic. The values of the thermal expansion coefficients for the different phases were taken from the study [2] and are displayed in the table 3. 3.

Table 3. 3: Coefficient of thermal expansion of austenite, ferrite, perlite, bainite, and martensite.

Phase	**Coefficient of thermal expansion α**	**Units:**
Austenite	$2.20 \cdot 10^{-5}$	$°C^{-1}$
Ferrite	$1.61 \cdot 10^{-5}$	$°C^{-1}$
Perlite	$1.53 \cdot 10^{-5}$	$°C^{-1}$
Bainite	$1.34 \cdot 10^{-5}$	$°C^{-1}$
Martensite	$1.15 \cdot 10^{-5}$	$°C^{-1}$

It must be noted that in the study [2], the coefficient of thermal expansion of bainite is actually not reported. The value present in Table 3. 3 was in fact evaluated separately as an average between the value reported in [2] for perlite and for martensite. This because the structure of bainite is similar to that of perlite when considering upper bainite and similar to that of martensite when considering lower bainite. For this reason, a value of thermal expansion coefficient in the middle between that of perlite and martensite seems to be an appropriate approximation.

The formulation shown in equation 65 has been utilized in different studies, such as [2], [30], and [56], in order to evaluate the thermal expansion strain during quenching.

The thermal strain is not evaluated in ABAQUS and so must be implemented separately with some user coding. This is done by implementing equation 65 and utilizing the values of α defined in table 3. 3, and the temperature information coming directly from the ABAQUS simulation. The user code where equation 65 is implemented is called UEXPAN and has the sole function of implementing the thermal, transformation and transformation induced plasticity strains, that are not already calculated in ABAQUS. A better explanation on the use of this subroutine is presented in the online guide at [32]. In the following paragraphs, the formulations with which the transformation and transformation-induced-plasticity strains are evaluated, are presented and explained.

3.3.6.4 Transformation Strain

As mentioned in [56], phase transformations during quenching lead not only to different values for the thermal expansion coefficient for the thermal strain, but also to another type of strain that is related to the fact that the different steel phases have different structures. In fact, as mentioned in the literature review chapter, the different steel phases have different structures, (FCC for austenite, BCC for ferrite and tetragonal for martensite), and so occupy different volume quantities. This strain due to the different volume occupation of the different steel phases is called transformation strain.

This strain is proportional to the volume fractions of the different steel phases, and to a factor that is representing the volume differences between them, as shown in equation 66.

$$\varepsilon_{tr} = \sigma_k \cdot \sum_i \left(\frac{\Delta V}{3V}\right)_i \cdot \Delta\xi_i \tag{66}$$

It is possible to see that in this equation, as for the thermal expansion strain, the strain is considered as isotropic, reason for which the Kronecker delta is included in the equation.

In this equation, the factor that is representing the volume differences between the different phases is $\frac{\Delta V}{3V}$.

This factor has a different value for each transformation from austenite to the different phases. The values for such a factor were obtained from the study [2] and are reported in the table 3. 4. In the study [2], the values are said to be obtained from experimental data.

Table 3. 4: Factor representing the volume differences between the different phases during transformation of austenite into ferrite, perlite and bainite. [2]

Phase obtained from transformation from Austenite	$\frac{\Delta V}{3V}$
Ferrite	0.126
Perlite	0.110
Martensite	0.342

It is possible to see that the value of this factor regarding the transformation from austenite to bainite is missing. For this reason, a similar reasoning to that explained previously for the thermal expansion coefficient is considered, and an average value between that found for the transformation to perlite and the transformation to martensite is used. With this reasoning, the value of this factor for the transformation from austenite to bainite is considered to be of 0.226.

In equation 66, the amount of strain is evaluated by summing up the effect due to the different phase transformations and the different volume changes they determine. In fact, a multiplication between the amount of phase that has transformed from the parent austenite, and the factor mentioned above for the transformation to that particular phase, is performed for each phase transformation that occurs.

Equation 66 was taken from different studies such as those presented in [2], [30], and [56], where it was used to evaluate this type of strain during heat treatments.

As mentioned above, as for the thermal expansion strain, the transformation strain is not evaluated in ABAQUS directly and so must be implemented separately in the subroutine UEXPAN. This is done by implementing in UEXPAN the equation 66, where the phase transformations information is taken directly from the results of the phase transformation calculations performed in the subroutine USDFLD, and the values of the $\frac{\Delta V}{3V}$ factor are defined directly in the UEXPAN subroutine and are the same as those shown in Table 3. 4.

3.3.6.5 Transformation Induced Plasticity Strain

The last important factor that causes strain during quenching is that related to the effect of transformation induced plasticity. Transformation induced plasticity causes local plastic deformations in the component also in locations where the stress is lower with respect to the yield strength of the component. As reported in [56], it has been determined theoretically and experimentally that this particular strain is proportional to the transformation rate of each phase that is being generated from austenite and to the deviatoric stress. This proportionality is expressed in equation 67, taken from [56].

$$\varepsilon_{tp} = \sum_{i} -\eta_i \cdot \Delta\xi_i \cdot (1 - \xi_i) \cdot s \tag{67}$$

In this equation:

- ξ_i represents the phase fraction of the steel phase i.
- $\Delta\xi_i$ represents the phase growth of the steel phase i from austenite.
- s represents the deviatoric stress.
- η_i represents a material parameter that is different for the transformation from austenite into the different steel phases.

As reported in [56], η_i assumes a value of $4.18 \cdot 10^{-5}\ MPa^{-1}$ for the transformation from austenite to ferrite, perlite and bainite. On the other hand, it assumes a value of $5.08 \cdot 10^{-5}\ MPa^{-1}$ for the transformation from austenite to martensite.

It is possible to see that in this case, unlike what seen for the thermal and transformation strain, the strain is anisotropic. For this reason, the Kronecker delta found in the expressions for the previously discussed strains, is here replaced by the directional deviatoric stress.

This strain, as for the thermal and transformation strain, is not present directly in ABAQUS and so must be implemented separately in the user subroutine UEXPAN. This is done by implementing the equation 67 in the user subroutine by: plugging in the η values as described above, using the stress information coming directly from ABAQUS, and using the information regarding the phase fractions and phase transformations coming from the phase transformation calculations performed in the subroutine USDFLD.

The method just described for evaluating the transformation induced plasticity strain was presented in [56], however other equally valid methods to evaluate such a strain were also presented in [2] and [30].

3.3.6.6 Quenching Strains Final Remarks

To sum up, five different types of strains are distinguished during the quenching process: the elastic, plastic, thermal, transformation and transformation induced plasticity strains.

Of these, the first two do not have additional coding in the simulation tool. Regarding the last three, on the other hand, their effects are not evaluated in ABAQUS directly and so must be evaluated separately with some user coding. This is done by implementing the relevant equations described above, equations 65 to 67, in a user subroutine called UEXPAN, that obtains the required input information from the phase transformation study performed in USDFLD and from ABAQUS directly, and provides as output the strain contributions related to the thermal, transformations and transformation-induced-plasticity effects.

In the next paragraph the hardness evaluation methodology at each instant and location is shown and explained.

3.3.7 Hardness Prediction

A very important information that must be provided as output from the simulation tool is the hardness of the steel in each location. The hardness is dependent on the type of steel and alloying composition, on the cooling rate, and also on the microstructure at the location where the hardness is analyzed [69]. All these factors have a different effect on the hardness. Different relations were proposed in different studies to relate the factors mentioned above and evaluate the hardness. Of particular interest is the set of equations developed by Mayner et al [69]. In these equations, the hardness is evaluated for each steel phase as function of the alloying composition and cooling rate. These equations, for the different steel phases are shown below.

The hardness of martensite is evaluated as:

$$HV_M = 127 + 949C + 27Si + 11Mn + 8Ni + 16Cr + 21 \log V_r \tag{68}$$

The hardness of bainite is evaluated as:

$$\begin{aligned} HV_B = {} & 323 + 185C + 330Si + 153Mn + 65Ni + 144Cr + 191Mo \\ & + (89 + 53C - 55Si - 22Mn - 10Ni - 20Cr - 33Mo) \log V_r \end{aligned} \tag{69}$$

The hardness of ferrite and perlite is evaluated as:

$$\begin{aligned} HV_{A-F-P} = {} & 42 + 223C + 53Si + 30Mn + 12.6Ni + 7Cr + 19Mo \\ & + (10 - 19Si + 4Ni + 8Cr + 130V) \log V_r \end{aligned} \tag{70}$$

In the above equations:

- HV_M is the martensite hardness expressed in Vickers scale.
- HV_B is the bainite hardness expressed in Vickers scale.
- HV_{A-F-P} is the ferrite, perlite and austenite hardness in Vickers scale.
- V_r represents the cooling rate at 700°C.
- The chemical elements symbol represents the percentage of the different alloying elements present in the steel.

The cooling rate at 700°C is considered, as it is believed that the cooling rate found at that particular temperature represents closely the average cooling rate found in the entire quenching process.

What can be clearly seen from equations 68 to 70 is that the carbon content has a very strong effect on the hardness, especially on that of martensite. This can be seen when looking at the very high coefficients that multiply the carbon amount in the equations. This also confirms the importance of the carburizing process that determines the carbon profile.

With equations 68 to 70, the hardness of the different phases as function of the alloying composition and cooling rate is evaluated. With this information, and knowledge on the amount of the different steel phases present, the hardness at a certain location can be evaluated. This is done by using a linear mixture between the hardness of the different steel phases, and the amount at which they are present at the particular location. This relation is shown in equation 71.

$$HV = \xi_m \cdot HV_M + \xi_b \cdot HV_B + \xi_f \cdot HV_{A-F-P} + \xi_p \cdot HV_{A-F-P} + \xi_a \cdot HV_{A-F-P} \tag{71}$$

In this equation, HV is the overall hardness expressed in Vickers scale, and ξ_m, ξ_b, ξ_f , ξ_a, and ξ_p are the phase fractions of martensite, bainite, ferrite and perlite respectively, that are evaluated in the USDFLD subroutine as explained in the phase transformations paragraph.

The hardness profile is then calculated in the simulation tool prepared for this thesis research, by using equations 68 to 70, and then applying equation 71. These equations are implemented in the subroutine USDFLD. The hardness provided by equation 71 is then saved as a user-defined variable so that it can be displayed in the ABAQUS postprocessing.

Equations 68 to 71 provide hardness values in Vickers scale, however, these can easily be reported in a different scale by performing a conversion between the different scales. In the study [33], the following equation is used to convert from Vickers scale to Rockwell scale, where HR_c is the hardness in Rockwell scale.

$$HR_c = 193 \cdot \log HV - 21.41(\log HV)^2 - 316 \tag{72}$$

Also the hardness in Rockwell scale, evaluated with equation 72, is saved as a user-defined variable in order to be able to display it in the ABAQUS postprocessing.

These equations developed by Mayner et al. for the hardness prediction have been utilised in many different studies such as those presented in [33], [36], and [40], where validations of the results proved that the equations were able to correctly predict the hardness values.

Having described in the above paragraphs the main factors that are considered when simulating the quenching process, in the next chapter, the simulation of the tempering process will be investigated.

3.4 Tempering Simulation

Tempering in this thesis research, as mentioned in the simulation tool overview section, will be modelled not as a physical phenomenon, but rather by simulating the effects that tempering has on the component hardness properties. The procedure used is the same as that used in [33]. In fact, the tempering is not implemented in the simulation tool by increasing the temperature of the component, but by adding some coding that permits to understand how tempering affects the hardness profile.

This can be done because this tool, as previously stated, is designed to be used for automotive powertrain components. These components, as mentioned in [70] and [71], are usually tempered at a temperature range between 150°C and 200°C. This temperature is quite low considering that the tempering can be conducted anywhere below the austenitizing temperature, that is usually above 700°C. Temperature has a big impact on the diffusion time of carbon atoms within the component. In fact, a too high tempering temperature causes the carbon atoms to diffuse quicker, consequently quickly reducing the high hardness and strength of martensite. Generally, the tempering time for these components is also quite low, around one to two hours, as mentioned in [33].

In these conditions, the tempering will affect mostly martensite and very little the other phases. In fact, as reported in [33], where the original source was reported to be [72], at those "low" tempering temperatures and time, the only effect that is found in the component is the diffusion of carbon atoms away from the martensite, determining a lower hardness martensite and the formation of carbide precipitations. Being this the case, the tempering is simulated only by simulating the martensite hardness change that occurs during tempering, and the assumption will be made the other steel phases present are not affected by tempering.

The procedure to discover the martensite hardness after tempering is based on the theory developed by Jaffe Holloman in [73], and on experimental tempered martensite hardness evaluations, as described in [33]. The Jaffe-Holloman theory, as expressed in [74], states that any two tempering treatments having the same tempering parameters are considered to be equivalent. This means that a tempering process with its particular tempering temperature and time, produces the same effects as any another tempering process, having different tempering time and temperature, that however exhibits the same tempering parameter. The tempering parameter, as determined by Jaffe-Holloman in [73], is shown in equation 73.

$$TP = T_t \cdot (\log(t_t) + c_t) \tag{73}$$

In equation 73:

- T_t is the tempering temperature expressed in Kelvin units.
- t_t is the tempering time expressed in hours.
- c_t is a constant used in the Jaffe Holloman equation that varies for different alloying compositions.

As reported in [74]: "The tempering parameter has become ubiquitous in the field of steel metallurgy, and it is now widely accepted that equivalent tempered hardness values for a given steel imply an equivalent degree of tempering and similar mechanical behavior".

In the work of [5], the values of the constant c_t from the original work of Jaffe-Holloman [73], are reported as a function of different classes of steels, where the different steel classes are selected depending on their alloying content. These values taken from [5] are reported in Table 3. 5.

Table 3. 5: Values of the Jaffe-Holloman parameter. [5]

Value of the c_t constant	15	19.5	20	30
Carbon content in steels (wt.%)	0.90-1.20	0.15-0.45	C-Mn and low-alloy steels	High alloy steels

Utilizing the concept that two tempering treatments can be considered as equivalent if the same tempering parameter TP is found, starting from whatever tempering temperature and time are used in the process that is to be simulated in the simulation tool developed for the thesis research, an equivalent tempering process that determines the same final properties using however a tempering time of one hour, can be found.

This can be done by following the following sequence of steps. Firstly, the TP for the tempering process that is to be studied is evaluated with equation 73. Secondly, the TP parameter just calculated is used as input in equation 74, where the value of t_t is set to one hour.

$$T_t = \frac{TP}{(\log(t_t) + c_t)} \tag{74}$$

In this way, the tempering temperature that, if maintained for one hour, leads to the same mechanical results as the original tempering process, is evaluated.

Once this temperature has been found, it can be used for determining the value of tempered martensite hardness. This can be done because, as reported in [33], in the works of Grange et al. [75], the hardness values of martensite that has been tempered at different temperatures for one hour, are reported for different alloying compositions, along with the values of the as-quenched martensite hardness. This data was then used in [33] to create a factor f that related the value of the tempered martensite found after a one-hour tempering, to the value of the as-quenched martensite and to the tempering temperature. This factor f represents the ratio between the value of the hardness of the tempered martensite to the hardness of the as-quenched martensite, as shown in equation 75.

$$f = \frac{{HV_M}^T}{HV_M} \tag{75}$$

In equation 75, ${HV_M}^T$ is the hardness of the tempered martensite and HV_M is the value of the as-quenched martensite. The equation to evaluate the factor f, developed in [33], is reported below in equation 76.

$$f = \begin{cases} 1.304 \cdot (1 - 0.0013323 \cdot T_t) \cdot (1 - 0.3619482 \cdot C), & C < 0.45 \\ 1.102574 \cdot (1 - 0.0016554 \cdot T_t) \cdot (1 + 0.19088063 \cdot C), & C \geq 0.45 \end{cases} \tag{76}$$

In equation 76, the symbol C represents the carbon content in weight percent. Considering the above explanations, the value of f is evaluated using as T_t the tempering temperature that, kept for one hour, leads to the same results as the original tempering process.

Finally, considering the Jaffe-Hollomon equivalence, by using the value of f just calculated, and the value of the as-quenched martensite hardness calculated in USDFLD as shown in the hardness prediction paragraph, the value of the hardness for tempered martensite can be evaluated with equation 75.

Once the value of the hardness for tempered martensite is evaluated, since, as mentioned earlier, it is assumed that only martensite is affected by the tempering operation, the overall hardness after tempering can be evaluated with equation 77.

$$HV^T = \xi_m \cdot {HV_M}^T + \xi_b \cdot HV_B + \xi_f \cdot HV_{A-F-P} + \xi_p \cdot HV_{A-F-P} + \xi_a \cdot HV_{A-F-P} \tag{77}$$

In equation 77, HV^T is the overall hardness after tempering. This equation is very similar to that seen in equation 71, with the only difference that, in this case, the hardness used for martensite is the hardness of tempered martensite. The values of the hardness for the other phases are the same as those found after quenching and calculated as shown in the hardness prediction paragraph. This hardness is expressed in Vickers scale, however, as also seen before, it can be converted into Rockwell scale by using equation 72.

The above equations, that are used to calculate the value of the hardness after tempering, are also implemented in the USDFLD subroutine. The inputs to these equations would be the original tempering temperature and time, and the as-quenched hardness for the different phases as calculated in the hardness prediction paragraph.

Now that the methodology for the three different heat treatments has been covered, the simulation results for two automotive components will be presented and discussed. Before going in detail with what was found from the simulations, the component geometries on which the simulations and experimental tests were performed are shown and discussed.

3.5 Components Geometries

The simulation tool is tested on two automotive geartrain components: a shaft and a gear. The exact geometry of these components will not be declared as it is proprietary information of the well-known OEM that is the owner of these components. Experimental tests were carried out on these two components by operators of the OEM. The experimental results were then compared to the simulation results in terms of microhardness and microstructure. Whilst the results comparison and discussion will be carried out in the next chapter, in this paragraph the two geometries will be introduced.

3.5.1 Gear Geometry

The first component for which the simulation outputs will be compared to experimental results is a gear. This component is part of a geartrain assembly. The exact geometry of the gear utilized, as mentioned earlier, will not be disclosed because considered as proprietary information of the OEM that performed the experimental simulations. However, a similar component in dimensions and features is shown in Figure 3. 16. The component shown in Figure 3. 16 is also that that was implemented in ABAQUS for the simulations.

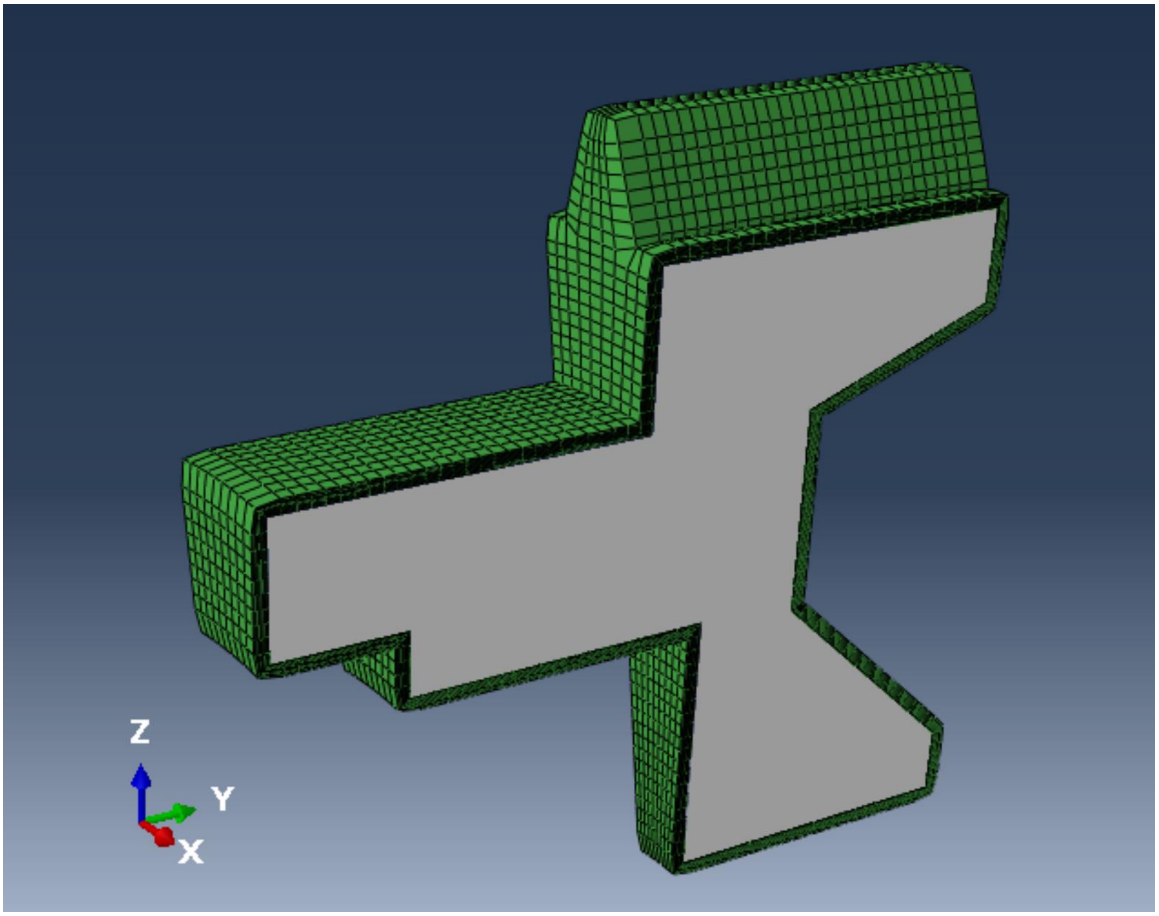

Figure 3. 16: Gear component part implemented in ABAQUS.

Actually, what is shown in Figure 3. 16, is only a part of the real object. In fact, the gear component is axisymmetric, where the axis of symmetry is the y-axis. Therefore, what is shown in Figure 3. 16 is only a part of the component, that, if repeated multiple times around the y-axis, determines the final component's geometry. This small part of the component is sufficient to perform the simulations, due to symmetry. In fact, symmetry boundary conditions can be inserted on all of the surfaces of the component where the real component would continue. These boundary conditions simulate the presence of the rest of the component that is not actually present when considering only the small part shown in Figure 3. 16. These surfaces are highlighted in red in Figure 3. 17.

The choice of using only a small part instead of using the entire component, is taken because, with symmetry, the same results as if the entire component was simulated can be obtained using however a smaller part of the component and so a smaller number of mesh elements. A smaller amount of mesh elements, in turn, reduces the computational power and time required for the simulation.

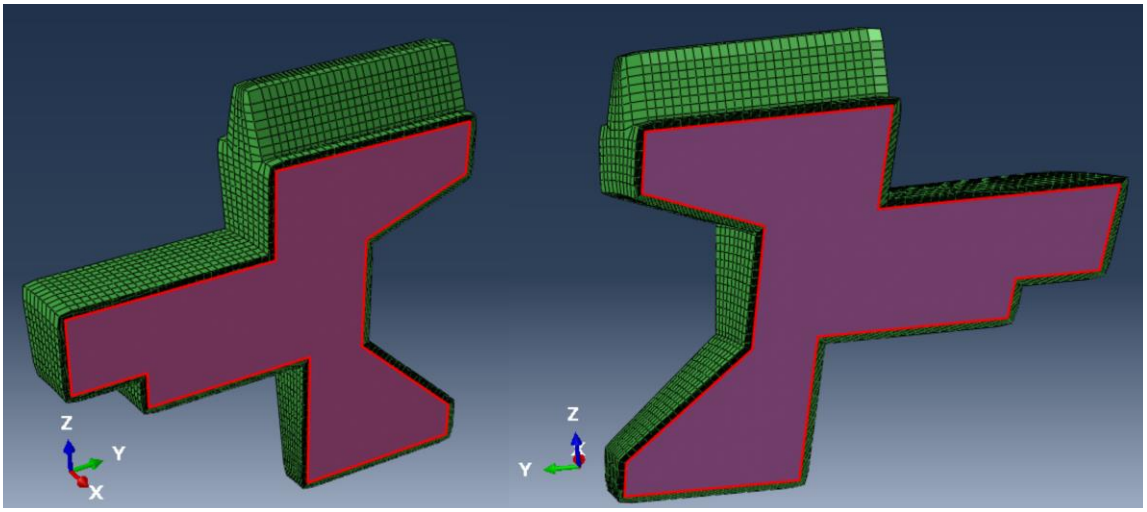

Figure 3. 17: Regions of the gear component implemented in ABAQUS where the real component would continue, and where the symmetry boundary conditions are applied.

The same regions highlighted in red in Figure 3. 17 are also those that are not exposed to the carburizing gas and quenching medium in the simulations. This can be clearly understood considering that these areas would not be visible in the entire component, since the rest of the object would be there. The regions exposed to the carburizing gas or quenching fluid are therefore those not highlighted in red in Figure 3. 17.

For frame of reference, although the correct dimensions cannot be given because considered confidential information of the OEM, the pitch diameter of the gear, of which one tooth is seen right at the top of the component in Figure 3. 16, is of about 150 mm.

The gear is made of a steel grade that is an internal standard of the OEM that owns the component. However, the commercial steel grade that is the closest to that composing the component, is 20MnCr5 steel. The 20MnCr5 steel was simulated in the simulation tool by using the alloying composition that is shown in the Table 3. 6.

Table 3. 6: Alloying composition of 20MnCr5 steel.

Element	C (wt%)	Mn (wt%)	Si (wt%)	Cr (wt%)	B (wt%)	Ti (wt%)	Cu (wt%)	S (wt%)	Al (wt%)
	0.165	1.35	0.15	1.25	0.002	0.0025	0.15	0.020	0.035

In Table 3. 6, the amount of the different alloying elements is reported in weight percent.

As mentioned earlier, on this component, a set of microhardness measurements and microstructure images were taken by some technicians at the OEM. These were taken at the surface and at different locations within the case depth. This information was then used to make a comparison with the results obtained in the simulation. In the following "Results and Discussion" chapter, the simulation results from the carburization and quenching-tempering studies on this component will be shown and compared to the experimental measurements. On the other hand, in the continuation of this chapter, the second component that is studied will be introduced.

3.5.2 Transmission Shaft Geometry

The second component for which the simulation outputs will be compared to experimental results is a transmission shaft. This component has the structure of a hollow shaft on top of which different features are present. A picture of a transmission shaft taken from the internet [76] is displayed in Figure 3. 18. It must be noted that the shaft shown in Figure 3. 18 is inserted just as reference and is not the transmission shaft that is being studied. This because that component, as previously mentioned, cannot be displayed because considered proprietary information of the OEM.

Figure 3. 18: Transmission shaft image taken for reference from the internet. [76]

On this component, as for the gear, different experimental microhardness tests were conducted, and several microstructure images were taken. In particular, the zone in which such experimental tests were conducted was one where the component had no toothed regions, and so the sample basically consisted of a hollow cylinder.

For this reason, in the simulation tool, the part that is implemented in ABAQUS is not the entire shaft component but rather only a small part of it, a hollow cylinder. This is done in order to correctly simulate the part of component where the experimental measurements are taken from, without increasing the complexity and computational requirement of the simulation by considering the entire component.

Furthermore, of the hollow cylinder, only a quarter of the part is simulated on. This can be done because of the symmetry of the hollow cylinder, that can be exploited as previously seen for the gear component. The geometry implemented in ABAQUS is that shown in Figure 3. 19. Although the exact dimension of the shaft cannot be disclosed, for reference, the external diameter of the transmission shaft component is of around 45mm.

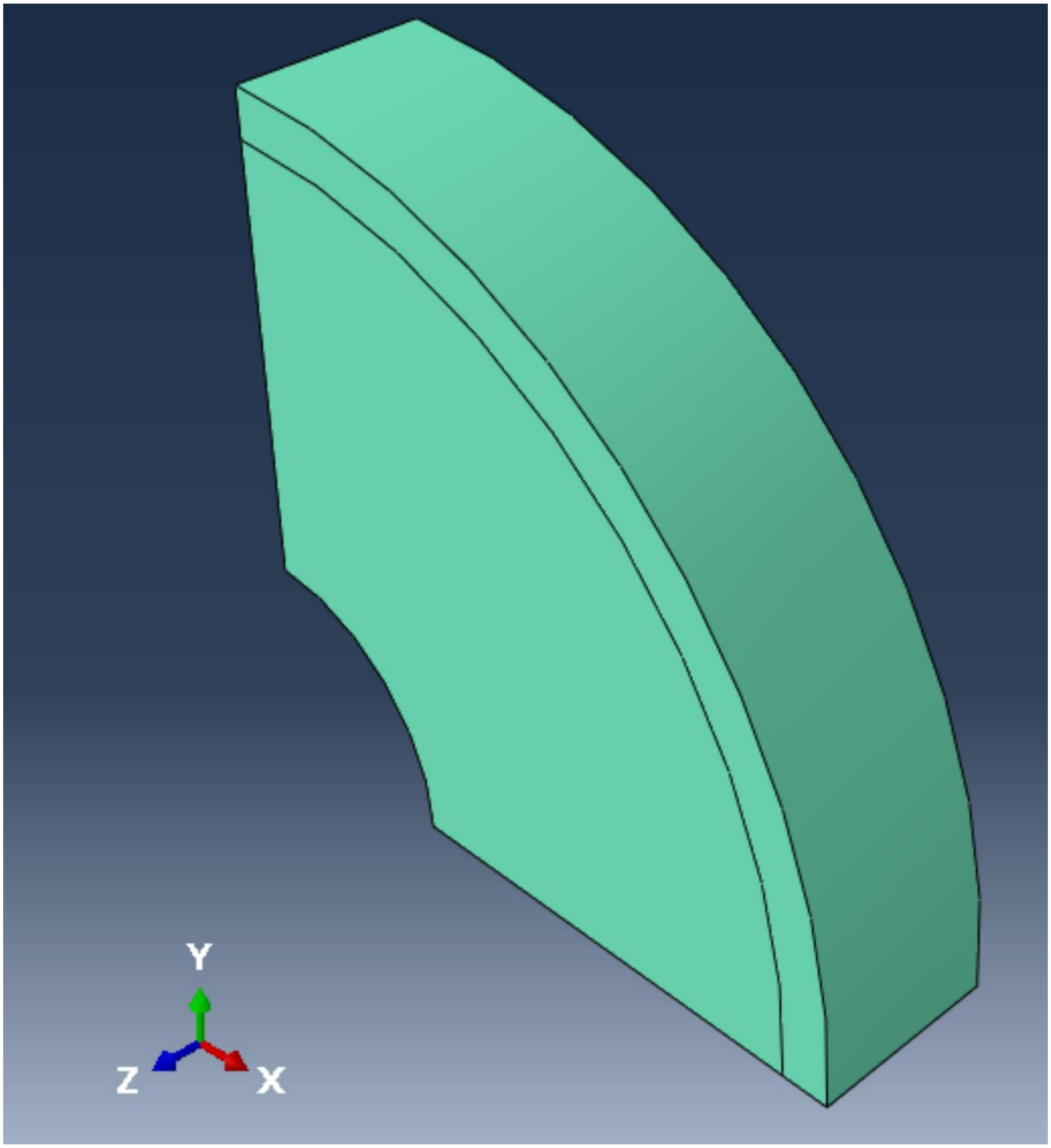

Figure 3. 19: Geometry implemented in ABAQUS for the transmission shaft simulation.

The symmetry can be exploited by inserting symmetry boundary conditions at the surfaces where the real component would continue, as seen previously for the gear component. These surfaces are shown in Figure 3. 20.

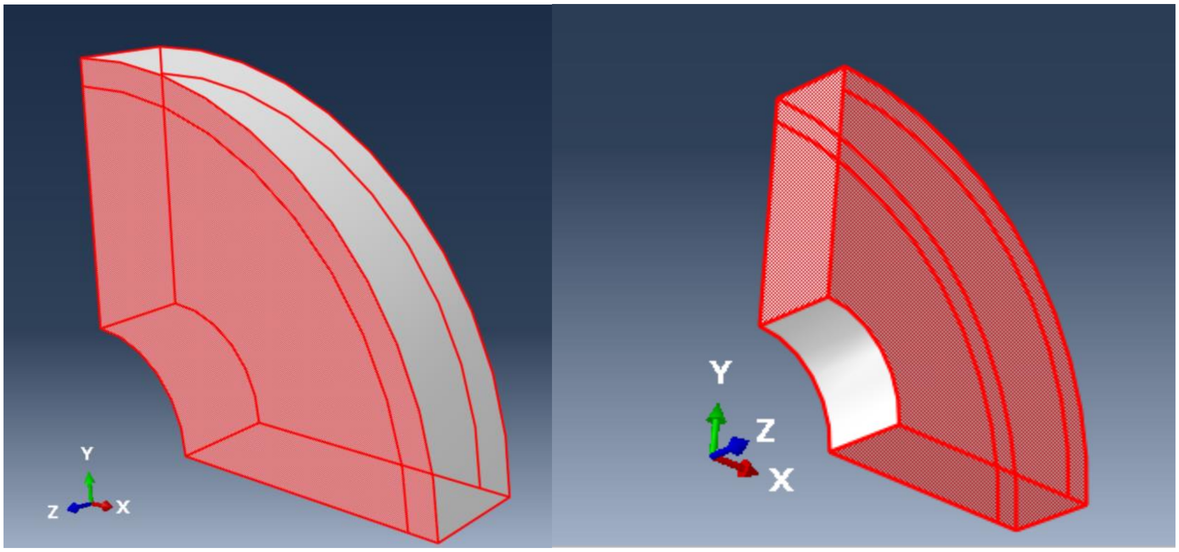

Figure 3. 20: Regions of the transmission shaft component implemented in ABAQUS (in red) where the real component would continue, and where the symmetry boundary conditions are applied.

In Figure 3. 20, the surfaces highlighted in red are surfaces where the real component would continue with respect to the simulated one. Basically, the only regions that are not red are the internal and external surfaces of the hollow cylinder. In the simulation, the region of the component that is exposed to the carburizing environment and to the quenching fluid is the external surface of the hollow cylinder.

The steel used in the simulation is 27MnCr5. This material was simulated using the alloying composition that is shown in the Table 3. 7 reported below.

Table 3. 7: Alloying composition of 27MnCr5 steel.

Element	C (wt%)	Mn (wt%)	Si (wt%)	Cr (wt%)	B (wt%)	Ti (wt%)	Cu (wt%)	S (wt%)	Al (wt%)
	0.25	1.25	0.25	1.15	0.0005	0.005	0.15	0.020	0.0275

In Table 3. 7, the amount of the different alloying elements is reported in weight percent.

In the following chapter, the carburizing and quenching-tempering simulation results will be presented and discussed for both the gear and the transmission shaft component. These will then be compared to some experimental measurements taken on the real components by the OEM.

CHAPTER 4:
RESULTS AND DISCUSSION

In this chapter, the main results obtained using the simulation tool will be displayed for both components. These results, in terms of the microstructure information and the microhardness values, are then compared to information obtained from experimental tests performed on the real components. In this chapter, two separate sub-chapters are present: one dealing with the gear component, and one dealing with the transmission shaft component. This division is done as, since these two components present different geometries and follow different heat treatment recipes, they also present different microstructures and microhardness values.

4.1 Gear Geometry

In order to present the simulation results obtained when considering the gear component, in this sub-chapter, two paragraphs are present: one dealing with the carburizing study results, and the other one dealing with the quenching-tempering results and comparison with experimental measurements.

4.1.1 Gear Carburizing Simulation

The gear component is carburized by vacuum carburizing, using Acetylene as carbon carrier. Therefore, the methodology described in the vacuum carburizing section of the methodology chapter is used to evaluate the carbon diffusivity, mass transfer coefficient and carbon potential. In fact, equation 5 is applied, using the alloying composition reported in Table 3. 6 for 20MnCr5, to evaluate the carbon diffusivity values to be inserted in ABAQUS as input. With what regards the mass transfer coefficient, the equations 12 and 13 are used, where Acetylene is considered as carburizing gas, and the values of the carburizing temperature and pressure are taken to be the same as those used on the component on which the experimental tests were performed. The values of the carburizing temperature and pressure, however, cannot be reported as considered confidential information of the OEM performing the carburizing procedure.

Finally, the value of the carbon potential, as described in the methodology chapter, is taken from the study [5]. However, the temperature of the carburizing process that is used for the carburizing of the transmission shaft component, is not the same as the 950°C for which a value of 1.39 of carbon potential was evaluated in [5]. However, it is very close in value, and for this reason, since in [5] two values of carbon potential are found at two different temperatures, at 920°C and 950°C, the value used in the simulation is adjusted to reflect the actual carburizing temperature of the transmission shaft component, by considering the values of the carbon potential at 920°C and 950°C.

The surfaces exposed to acetylene, as mentioned earlier, are those not highlighted in red in Figure 3. 17.

In the following paragraph, the mesh utilized for the carburizing study will be discussed.

4.1.1.1 Description of Mesh used in gear geometry

In the carburizing simulation, the following mesh shown in Figure 4. 1 was utilized.

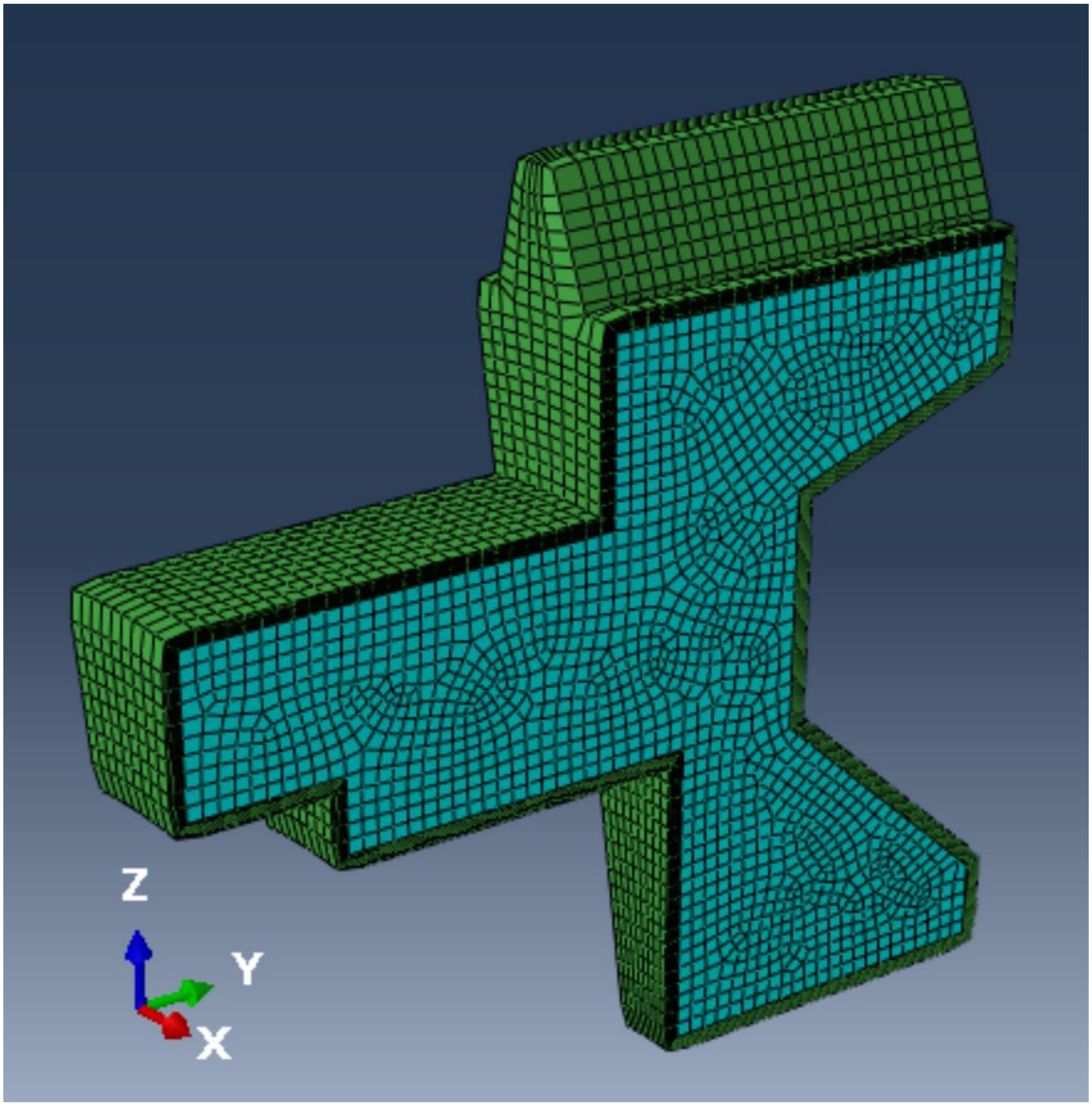

Figure 4. 1: Mesh used in gear component.

What can be seen from the Figure 4. 1 is that a quite fine mesh is used in the core of the component, and then, in order to have more accurate results, a mesh refinement is also applied at the surface to have smaller elements and so greater accuracy. In fact, as it is well known, the FEA simulation has an intrinsic tradeoff, that between the mesh containing many elements, that generally leads to more accurate results but longer computational expense and time, and a mesh containing few elements, that determine less accurate results but in shorter amount of time and with less computational power required. This being the case, a finer mesh is used at the surface, where the effect of the carbon content variation during carburization is the greatest, and a coarser mesh is used in the core of the component, where the carbon content is not expected to vary. In this way, the simulation can provide good results without requiring loads of time and computational power. The mesh at the core of the component is composed of 1mm “Hex” elements, whilst the mesh at the surface is still composed of “Hex” elements, but having smaller depth dimension. In particular, ten small layers of 0.1 mm thickness are present at the component’s surface. “Hex” stands for “hexahedral”, and “Hex” elements are three-dimensional features having a hexahedral shape.

A closer view at the mesh refinement at the surface is provided in Figure 4. 2.

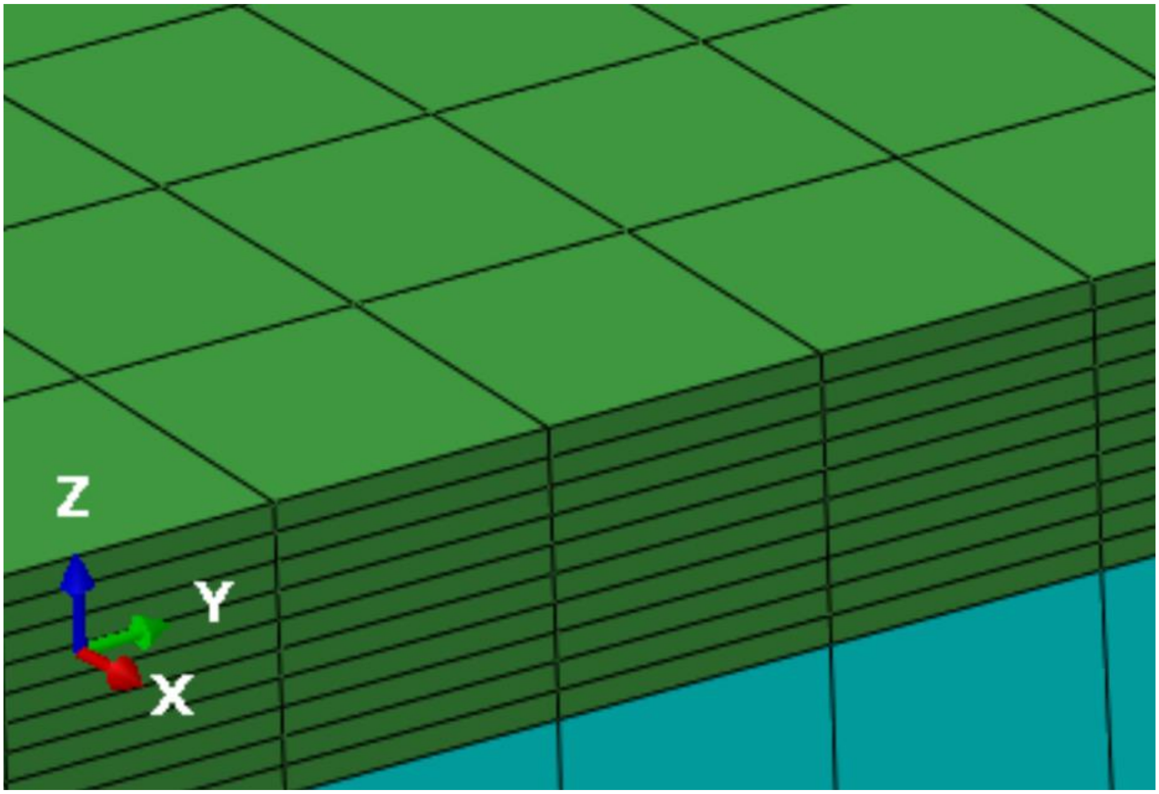

Figure 4. 2: Mesh refinement at the gear’s surface.

Now that the mesh used in the simulation has been discussed, the results in terms of carbon distribution within the component will be presented.

4.1.1.2 Carbon Content Simulated in Gear Geometry

The carbon content distribution within the component can be seen in Figure 4. 3.

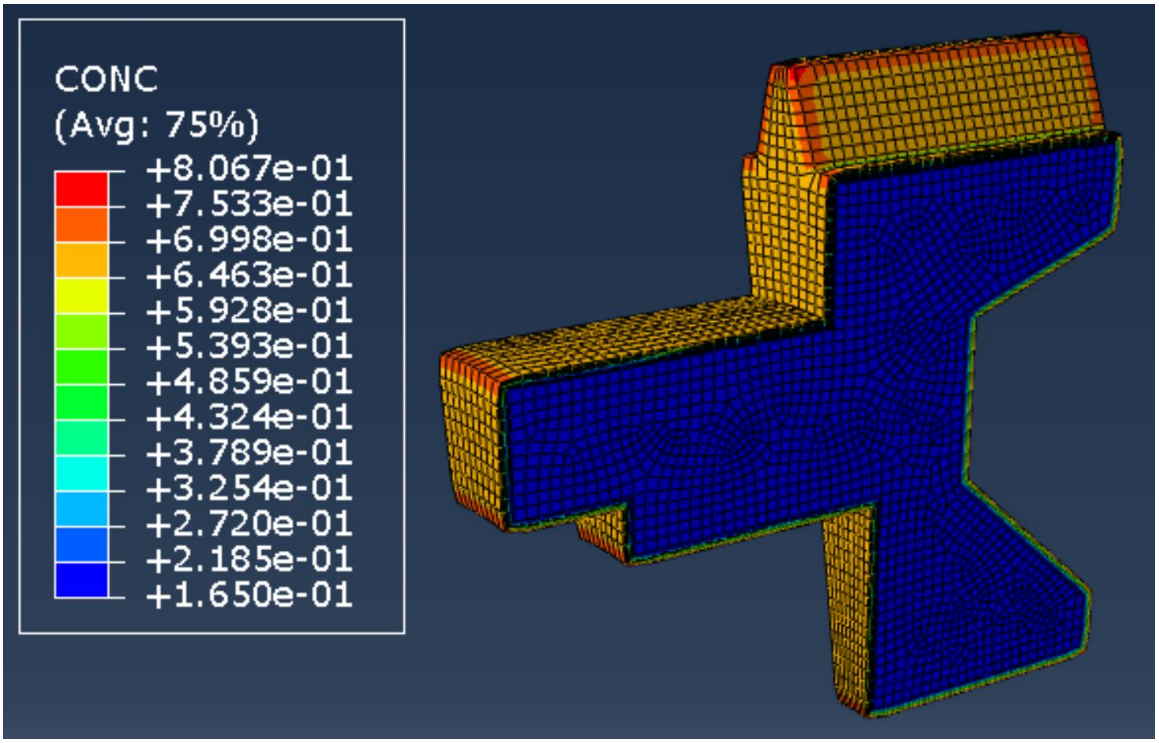

Figure 4. 3: Carbon concentration found at the end of carburization process within gear component.

What can be seen from Figure 4. 3, is that the greatest amount of carbon concentration, as expected, is found at the gear's surface. The carbon concentration then decreases along the component's depth, and eventually reaches the value of the carbon content that was present in the original steel on which carburizing was performed. As mentioned earlier, the starting value of carbon is of 0.165%. In the legend present in Figure 4. 3, the variable "CONC" indicates the concentration of diffusing atoms, and the symbol "e-X" sands for the function "10^{-X}". For example, "1.650e-01" means "$1.650 \cdot 10^{-01}$", and so 0.165. The value found in the legend is the weight percent of the carbon present within the component.

It is possible to see from Figure 4. 3, that the regions of the gear that have a greater amount of surface exposed to the carburizing environment, will display a greater value of carbon concentration. This can be seen basically at all edges where two or more surfaces are meeting. This, because the dissociation of acetylene, that is responsible for the carbon diffusion to the surface, occurs at all surfaces. At the edges, that are the meeting point for different surfaces, the carbon content will be higher because it will "feel" the effect of the carbon increase due to the acetylene dissociation, from both of the meeting surfaces. Exception made of the edge regions, the rest of the gear seems to have a uniform carbon content at the surface, as expected.

A closer look at the carbon content variation at the surface, in a non-edge location, is shown in Figure 4. 4.

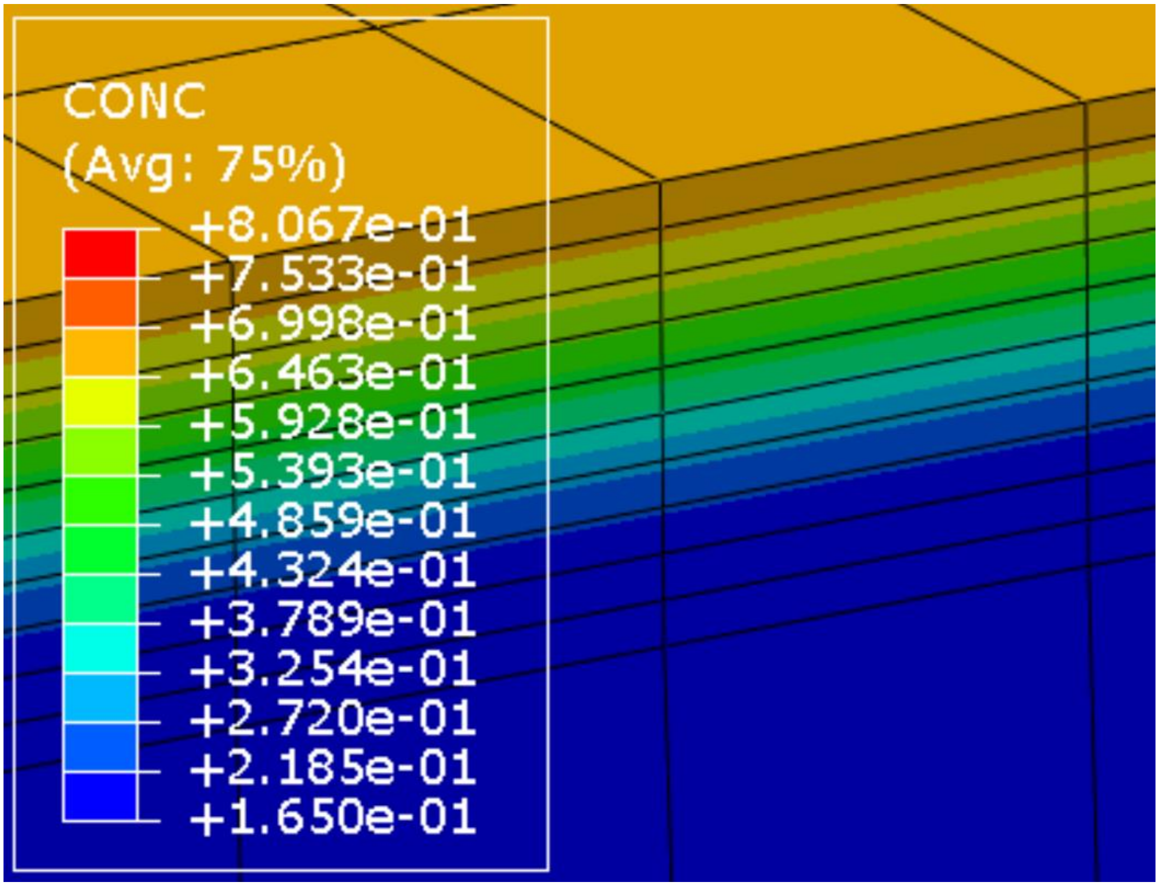

Figure 4. 4: Carbon content at the surface in a non-edge location.

What can be seen from Figure 4. 4, is that the carbon content variation determined by the carburization process affects only a very limited depth. It is also possible to see that the mesh refinement at the surface is effective in comprising all of the depth affected by the carburization process.

In Figure 4. 5, a “cut-view” of the component, showing the situation inside the tooth region, is shown.

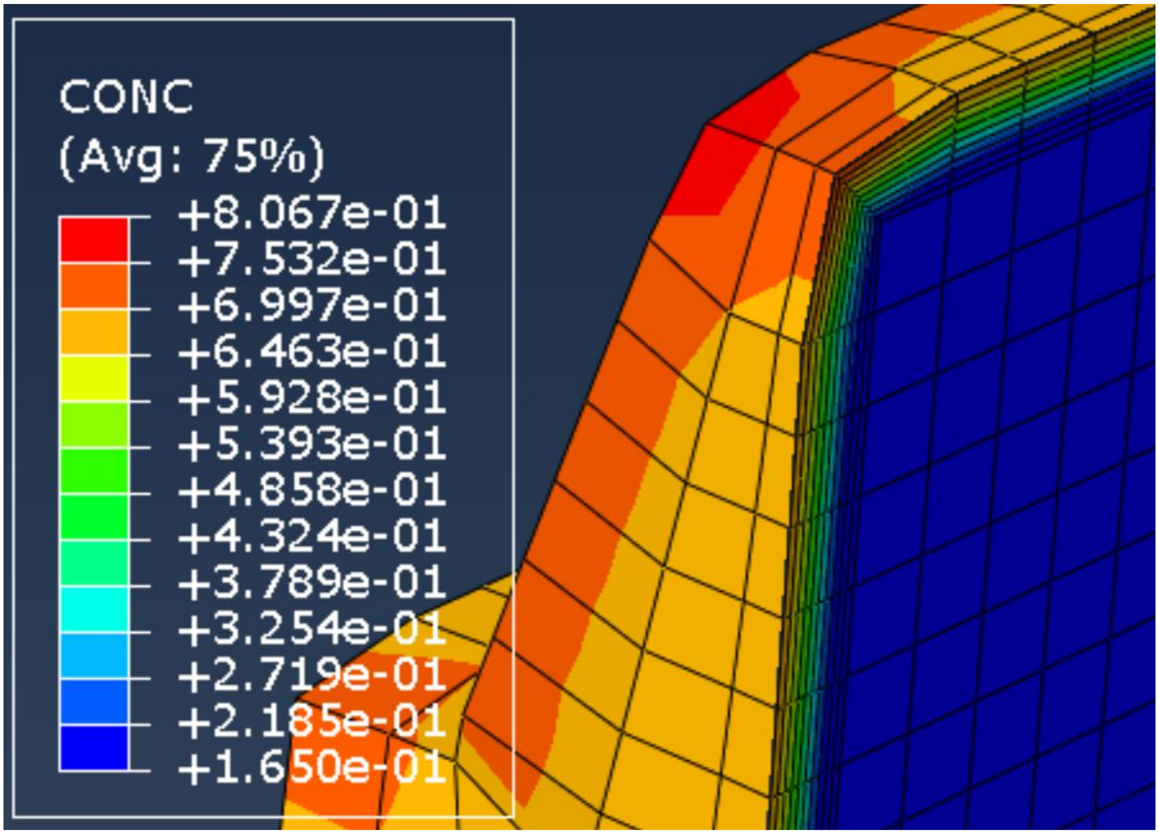

Figure 4. 5: Carbon content in a cut-view of the tooth region of the gear component.

What can be seen in Figure 4. 5, is that, also in the tooth region, the carbon content decreases very rapidly, in less than 1 mm, from the high value found at the surface to the carbon content value found starting steel. From Figure 4. 5, it is also possible to see that the carbon content has a bright red color in the edge at the tip of the tooth where three surfaces are meeting, and a dark orange color where two surfaces are meeting. In the rest of the component, where there are no edges, the carbon content is shown by the light orange color. The bright red color, as seen in the color scale shown in the Figure 4. 5, represents a carbon content of about 0.8 %. The dark orange and bright orange colors, on the other hand, represent carbon contents of about 0.72 % and 0.68 % respectively. This confirms what explained previously, that the locations in the component that are more exposed to the carburizing gas display a greater carbon content.

The graph shown in Figure 4. 6, shows the carbon content as a function of depth for a non-edge location (bright orange region).

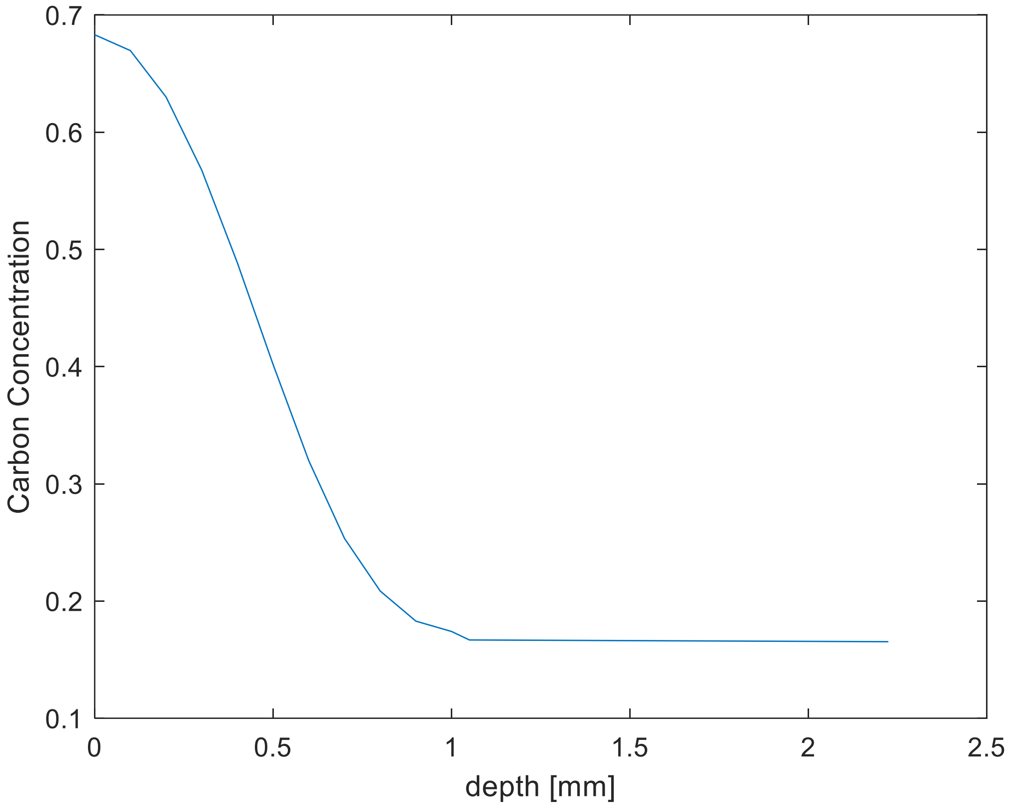

Figure 4. 6: Carbon content as a function of depth for non-edge region in gear component.

From Figure 4. 6, it can be seen that the carbon content varies from the high value at the surface, that in this case is found to be of 0.6734 %, to the value found in the starting steel, that in this case is 0.165 %, in just below 1 mm.

Whilst Figure 4. 6 shows the carbon variation as a function of depth at the end of the carburizing process, it gives no information on the history of the carbon content, that lead to such a result. In order to better comprehend the carbon variation during the entire carburizing process, Figure 4. 7 is introduced. In Figure 4. 7, the carbon content variation during the entire carburizing operation in a non-edge location, is shown for three points: A, B, and C. Point A is located right at the surface of the component, and so it is the most affected by the carburizing operation. Point B, instead, is located at a depth of 0.5mm from the surface. At this location, as it is possible to see from Figure 4. 6, the carbon content is still greater than the starting one, but it is lower with respect to that found at the surface. Finally, point C is located at a depth of 1 mm. At this location, as it is possible to see from

Figure 4. 6, the carbon content is not increased during carburization, and so has the same value as that found in the starting steel. The location of the points A, B, and C is shown also in Figure 4. 8.

At point A, that is right at the surface, the carbon content varies the most. In fact, it is possible to see that the carbon concentration trend seen for point A varies greatly and has a saw-shaped behavior. In fact, it is possible to distinguish in the image periods of time in which the carbon content increases greatly, and periods of time where the carbon content decreases. This is due to the alternation between the "pulse" phases and the "diffusion" phases. The time periods in which the carbon content increases rapidly are the pulse phases. In fact, during these phases, as mentioned in the literature review chapter, the acetylene gas is injected in the chamber and rapidly dissociates at the surface, therefore releasing the carbon in the surface. The increase in carbon is quite quick, due to the fast decomposition of acetylene. It can be seen that the carbon content during the pulse phase increases quickly and then reaches a value that it keeps for the rest of the duration of the pulse phase. This value is the amount of the carbon potential that was selected starting from the work of [5]. When the pulse phase ends, and the diffusion phase commences, the acetylene injection is stopped, and so the flux of carbon atoms at the surface is ceased. In this period, however, the high temperature still allows the carbon atoms to diffuse from the high carbon surface towards the interior of the component, therefore reducing the carbon content at the surface. It must be noted that the diffusion of carbon atoms from the surface towards the interior of the component happens also during pulse phases. The pulse and diffusion phases are alternated and produce the sawtooth shape shown in Figure 4. 7 for point A. In the graph, the duration of each pulse and diffusion phase is not reported because proprietary information of the OEM. What can be seen, however, is that the first pulse phase is longer with respect to the subsequent ones. It is also possible to see that the diffusion phases tend to become bigger, one with respect to the previous one, in the alternating sequence. It is finally possible to see that the pulse and diffusion alternating sequence terminates with a long diffusion phase, where the component is kept for a prolonged amount of time at the carburization temperature without introducing acetylene gas.

For what regards point B, that is below the surface, the carbon content increases steadily over the carburization process. In fact, at point B, the carbon increase is due to the diffusion of the carbon atoms from the carbon rich surface towards the interior of the component. It therefore does not feel the rapid grow in carbon due to the acetylene dissociation, followed by a decrease due to diffusion. It is possible to see that the greater increase in carbon for point B is found at the end of the carburization process, where the component is kept at the high carburization temperature for a prolonged period of time, therefore allowing for a lot of diffusion of carbon atoms to occur from the carbon rich surface towards the interior of the component. This phase, in fact, is also the one in wich the surface carbon concentration (point A) decreases the most. However, as mentioned earlier, the carbon diffusion from the surface towards the interior of the compoent happens also during pulse phases. This is also confirmed by the continuous grow in carbon concentration seen in B.

Lastly, at point C, the carbon concentration does not vary. This happens because this depth is not affected by the carburization operation. Therefore, the carbon concentration remains the same over the entire carburization period.

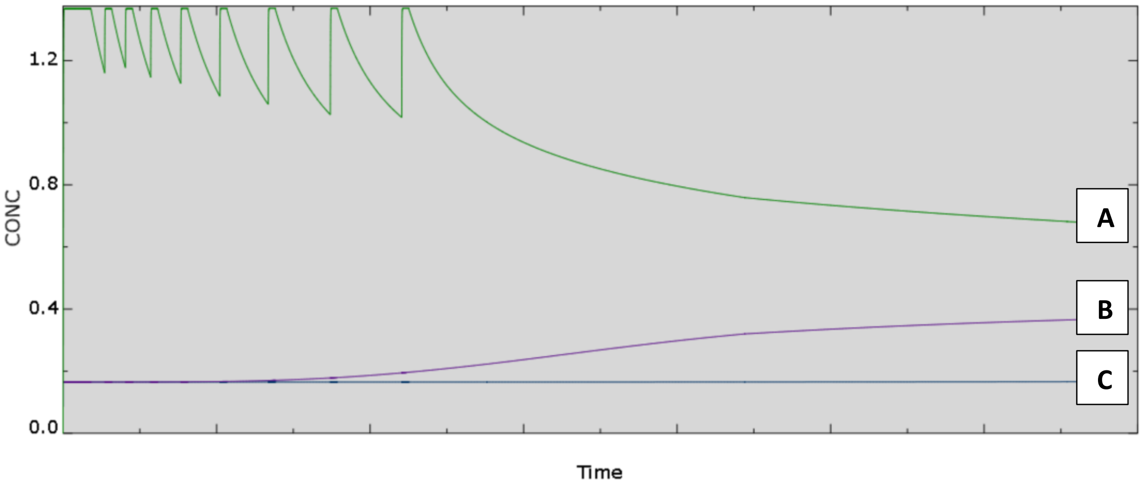

Figure 4. 7: Carbon content variation with respect to carburizing time for three points, A, B, and C, at different depths in gear component.

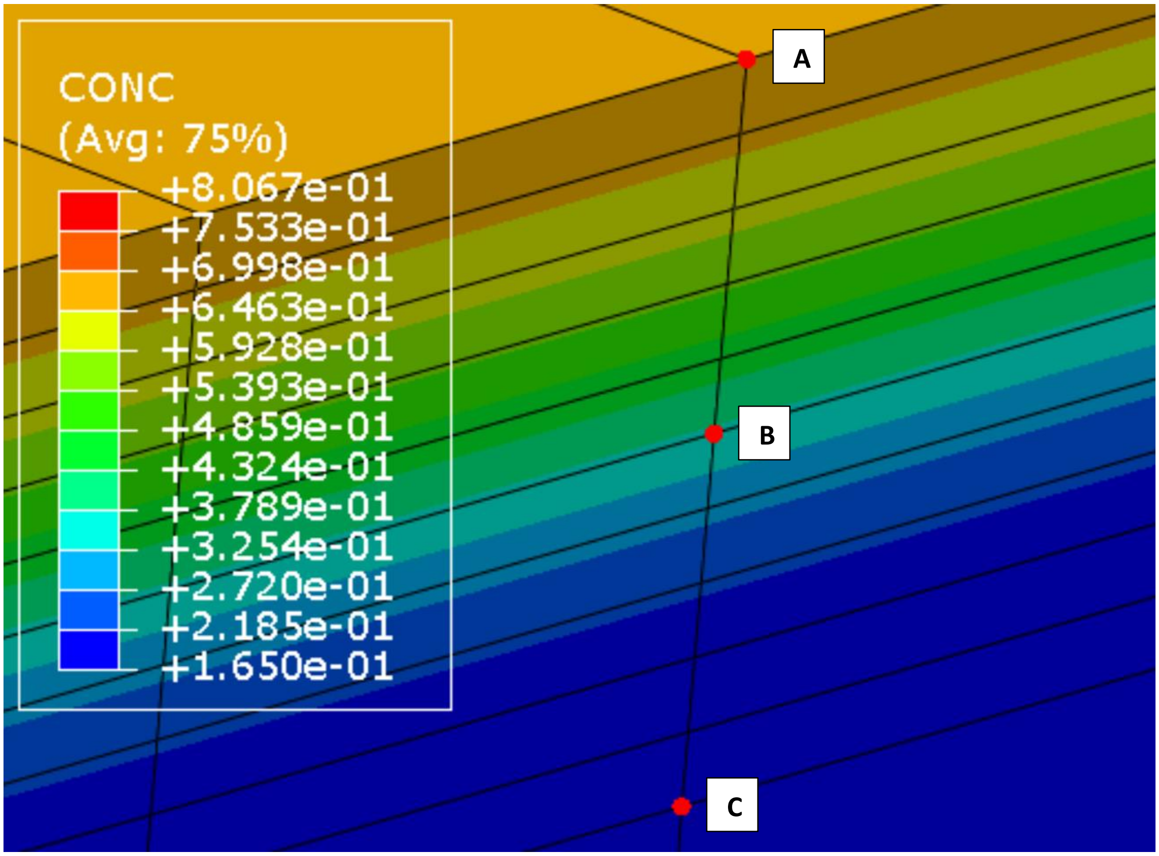

Figure 4. 8: Location of points A, B, and C in gear component.

4.1.1.3 Austenite Grain Size found at the end of Gear Geometry carburization

The austenite grain size at the end of the carburization process is reported in Figure 4. 9.

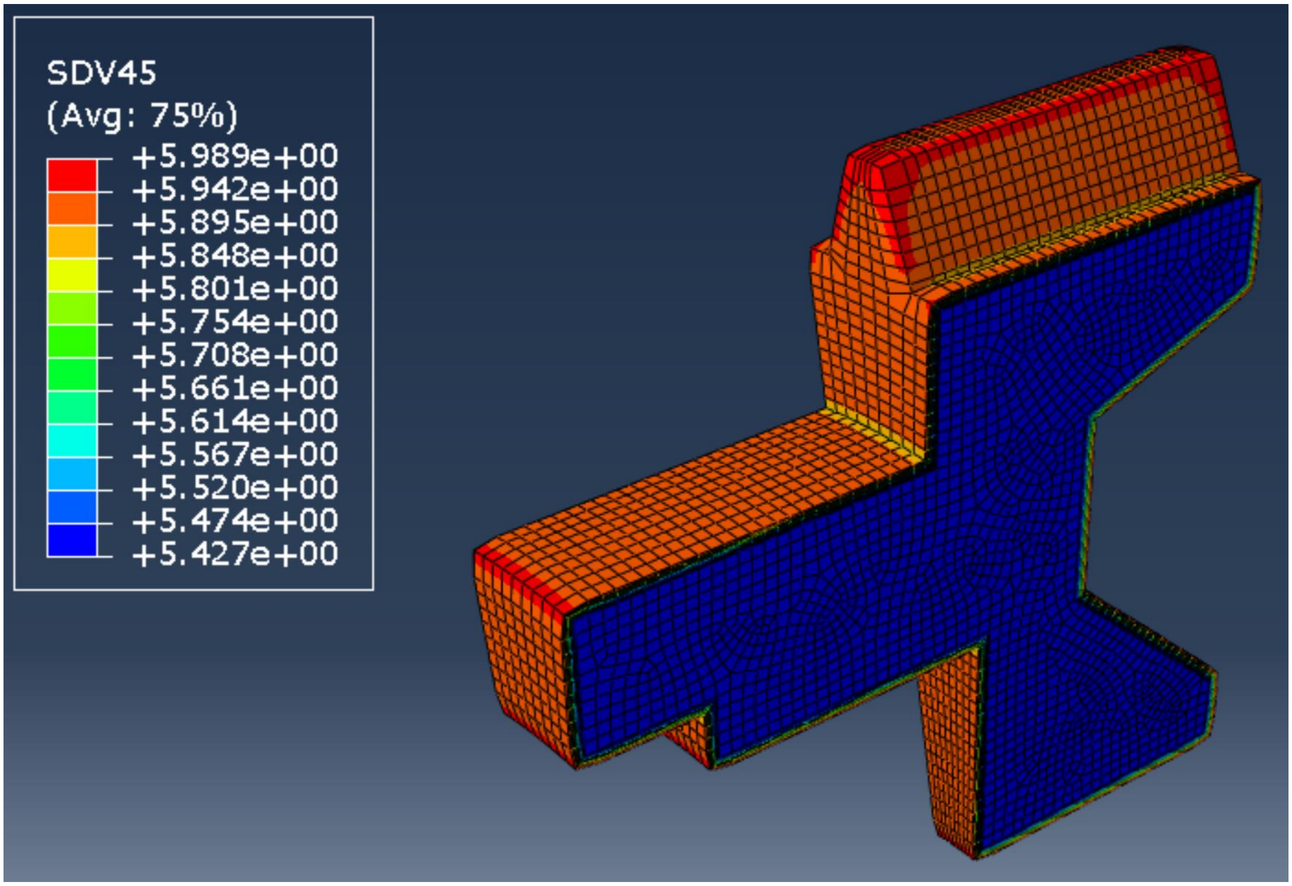

Figure 4. 9: ASTM Austenite grain size at the end of the carburization process in gear component.

In Figure 4. 9, “SDV45” is the user-defined variable that is used to describe the austenite grain size expressed in the ASTM standard. This standard, as explained earlier in the methodology chapter, represents the value of the number of austenite grains per square inch that can be counted in a 100X magnification image. This value is then used in the quenching-tempering simulation, where it is used as one of the inputs to evaluate the diffusive phase transformations with the Li et al formulations, as described in the methodology chapter.

It is possible to see that this value changes with the depth of the component, this variation, at non-edge region of the component, is better shown in Figure 4. 10.

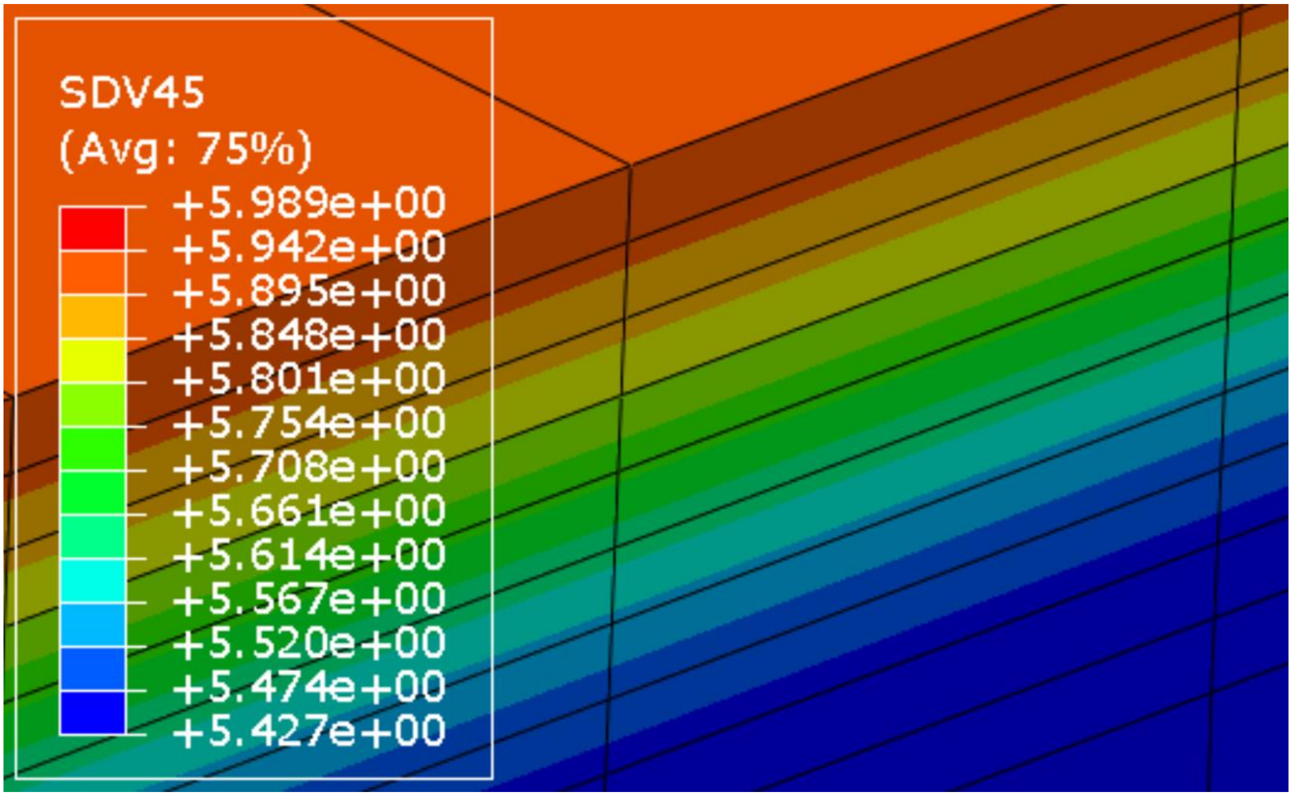

Figure 4. 10: ASTM Austenite grain size at the end of the carburization process, found at the surface of gear component in non-edge regions.

This variation with depth is due to the carbon gradient at the component's surface. In fact, the austenite grain size reported in ASTM standard in Figure 4. 9 and Figure 4. 10, is evaluated starting from the average austenite grain diameter at the end of the carburizing process, that is evaluated using equation 14. It is possible to see, however, that equation 14 is dependent also on the carbon content. In particular, since in equation 14 a minus sign is used at the nominator of the exponential term, where the carbon content is considered, a greater amount of carbon will determine a smaller average austenite grain size in micrometers. A smaller austenite grain size, in turn, determines a greater amount of austenite grains per square inch that can be seen in a 100X image, hence a bigger value of the ASTM number. The opposite situation is experienced when a low carbon content is found. This explains the higher values of ASTM austenite grain size number found at the surface with respect to the internal part of the component. An ASTM grain size number of just below six is found at the surface, in a non-edge region.

In the following section, the results from the quenching and tempering study will be discussed.

4.1.2 Quenching and Tempering simulation and comparison with experimental findings for gear component

As mentioned in the methodology chapter, the outputs of the carburizing study, in terms of carbon concentration within the component and austenite grain size at the end of carburizing, are then used as input in the quenching-tempering simulation. In this paragraph, the simulation outputs in terms of microhardness will be compared to experimental results obtained by microhardness evaluations performed on the real component, and microstructure images taken from the real component will be compared to simulation outputs in terms of steel phase fractions.

In the quenching and tempering simulation, the same mesh as that used for carburizing simulation and shown in Figure 4. 1 and Figure 4. 2, is again applied.

The gear component was quenched using helium as quenching medium. In ABAQUS, as explained in the methodology chapter, the interaction between the component and the quenching fluid is simulated by using a surface film condition at the surface that is coming in contact with the fluid. In defining the surface film condition, the values of the heat transfer coefficient and the temperature of the quenching fluid must be reported. In the simulation, these values are implemented with the use of the subroutine FILM that, as explained in the methodology chapter, permits the user to modify the quenching fluid temperature and heat transfer coefficient, as a function of time. In this simulation, the sink temperature as a function of time was selected in order to match what was observed in the process that the real component underwent. For what regards the heat transfer coefficient, the variation of this coefficient over time, as explained in the methodology chapter, was evaluated by looking at the tables presented in [16], and by knowing the variations over time of the helium speed and pressure, that were observed in the process that the real component underwent. So, the variations of the helium temperature and pressure over time, that were observed for the real component, were implemented in the simulation. This information was provided by the OEM that is the owner of the component and of the heat treatment recipe used to treat it. These values cannot be reported because considered proprietary information of the OEM.

As mentioned in the methodology chapter, since only a small part of the component is simulated, different boundary conditions must be implemented in the component to account for the presence of the rest of the object that is not simulated. These boundary conditions basically impede all displacements and rotations that occur where the rest of the component would be, and so that would not be present if the entire component was simulated.

These boundary conditions are applied to all surfaces displayed in red in Figure 3. 17, that are the surfaces where the real component would continue with respect to the simulated one. These boundary conditions are displayed as the blue and orange arrows in Figure 4. 11.

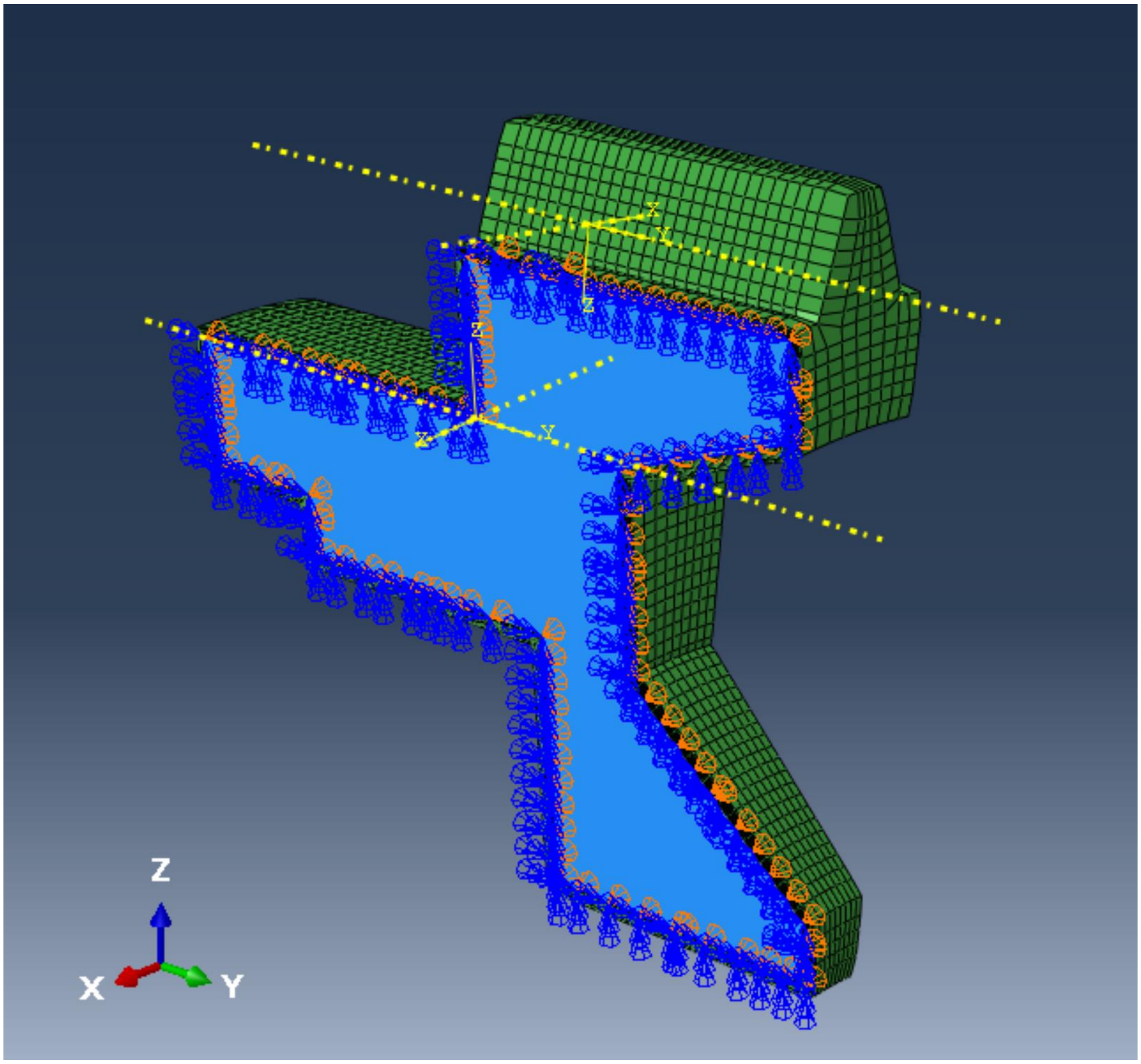

Figure 4. 11: Symmetry boundary conditions applied to the shaft component being simulated.

Now that the mesh and loads used in ABAQUS to simulate the quenching-tempering process have been reported, in the following paragraphs, the simulation results will be displayed.

The microstructure, and so microhardness, varies inside the component due to the different carbon concentrations and cooling rates that are found at different locations. This, because the carbon concentration varies the steel transformation starting temperatures, and the cooling rates affect the time that is available for the different steel transformations to occur. In particular, the regions that have more surfaces exposed to the quenching fluid will have a quicker cooling rate and so will present higher traces of martensitic phase, since less time is available for bainitic transformation. On the other hand, at locations that are less exposed to the quenching fluid, the cooling rates will be lower and so the martensitic concentration will also be lower with respect to the case just described above, leaving more space to bainitic structures.

To give an example, the tooth region of the component, indicated as “Region A” in Figure 4. 12, will present a different, more martensitic structure, with respect to the “Region B”, that is in a bulkier region of the component that also has less regions exposed to the quenching fluid.

These observations can be seen in Figure 4. 13, that shows the simulated percentage of martensite, defined as the user-defined variable “SDV4”, that is present in the component. In the Figure 4. 13, the component is cut in the “y-z plane” in such a way to cut in half the gear tooth, in order to reveal the situation inside the tooth. In Figure 4. 13, what was explained earlier is confirmed. In fact, it is possible to see that in the tooth zone (Region A in Figure 4. 12), the amount of martensite is greater with respect to what is seen in the region that was defined as B in Figure 4. 12.

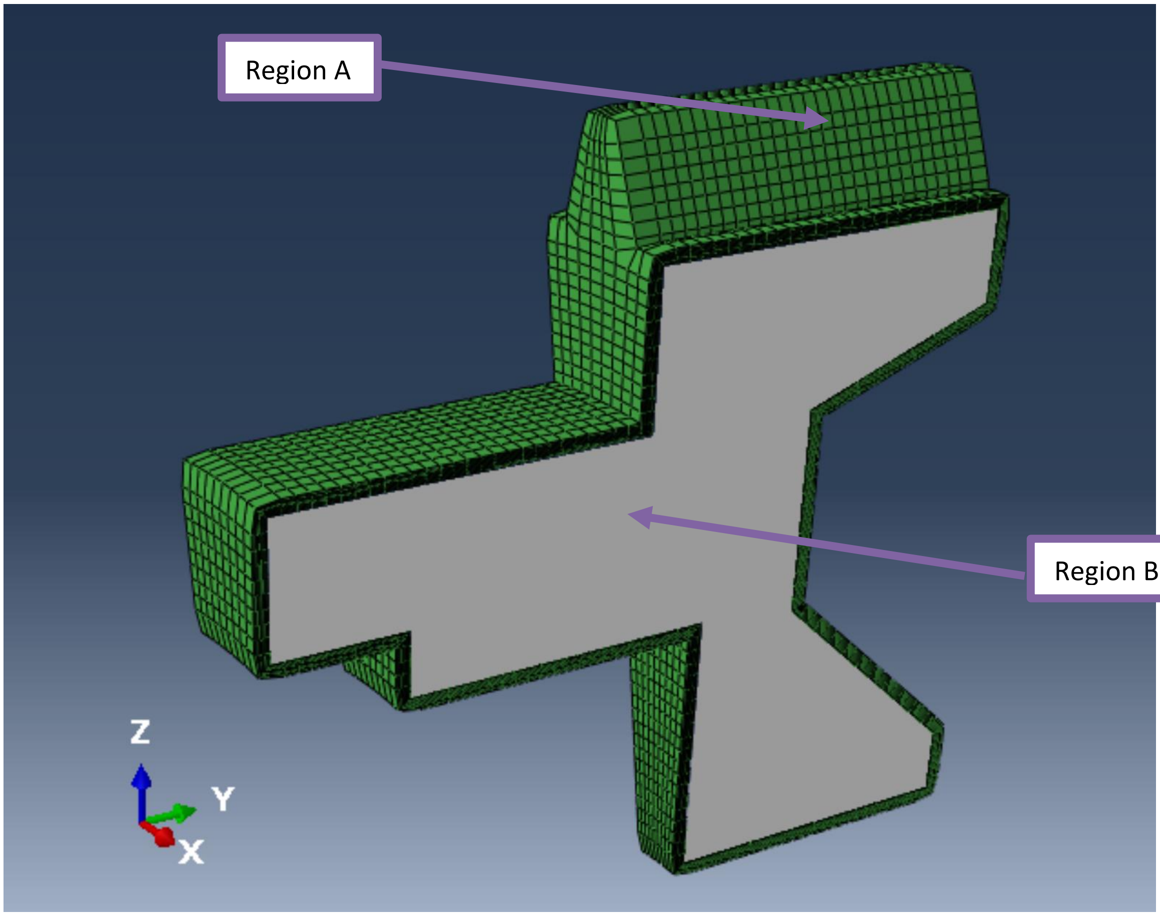

Figure 4. 12: Location of Regions A and B in the gear component.

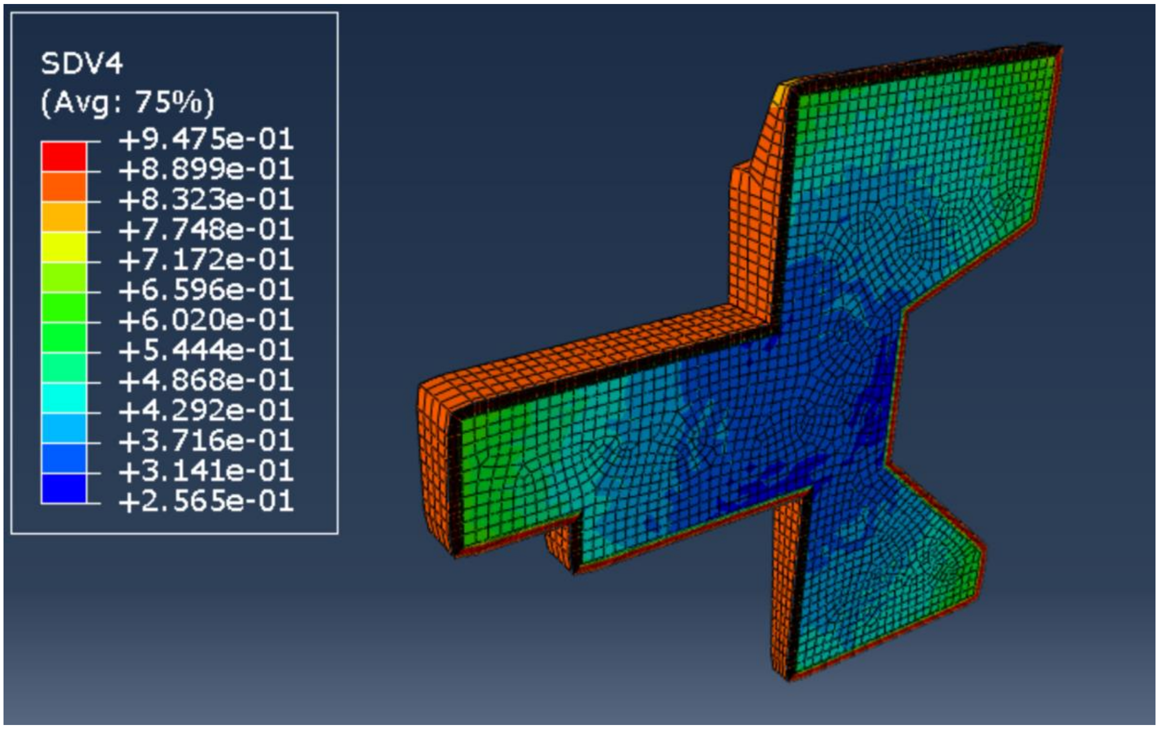

Figure 4. 13: Martensite concentration in gear component.

For this reason, for this gear geometry, the results of the simulation in terms of microhardness and microstructure will be compared to experimental results considering two different locations. The two locations are the gear tooth and the gear hub. These two locations, in fact, should present slightly different results due to the different microstructures found. These experimental measurements were conducted by operators of the well-known OEM owner of the component.

For this reason, in the continuation of this chapter, two separate discussions for what regards the microstructure and microhardness simulation predictions and comparison with experimental measurements will be made for the two different locations.

4.1.2.1 Gear Tooth Location

4.1.2.1.1 Steel Microstructure found at gear tooth and qualitative comparison with microstructure images

In the gear tooth region, as mentioned earlier, there are a lot of surfaces that are exposed to the quenching fluid, and, since the amount of steel is quite small, the cooling rate experienced in this region should be quite higher with respect to that experienced in the rest of the gear, where more steel is present, and less surfaces are exposed to the quenching fluid. Since a higher cooling rate is usually associated with a higher amount of martensitic structure, in this region the martensite content should be quite substantial.

The steel microstructure was simulated in the simulation tool by using the Li et al. equations for the diffusive phase transformation, so the transformation from the parent austenite to ferrite, perlite, or bainite, and with the Koistinen-Marburger equation for the transformation from austenite to martensite. The application of these equations, as explained in the methodology chapter, was implemented in the USDFLD subroutine.

The phase transformation simulations provide different interesting insights on the component. One first outcome of the simulation is the fact that, as expected, no ferrite or perlite are formed during the simulation. In fact, considering the simulation results, the reported percentage of ferrite and perlite at the end of the process is of zero percent. This result is expected as the quenching process is determining a very quick drop in temperature, that is too quick to allow for the phase transformations of austenite into ferrite or perlite to happen. As a consequence, the microstructure found within the component is completely made up of bainite, martensite, and retained austenite.

Considering the outputs of the simulation taken from the lateral surface of the tooth, in a non-edge region, the following results were obtained for these three phases.

In Figure 4. 14, the fraction of martensite in percentage is shown as a function of depth.

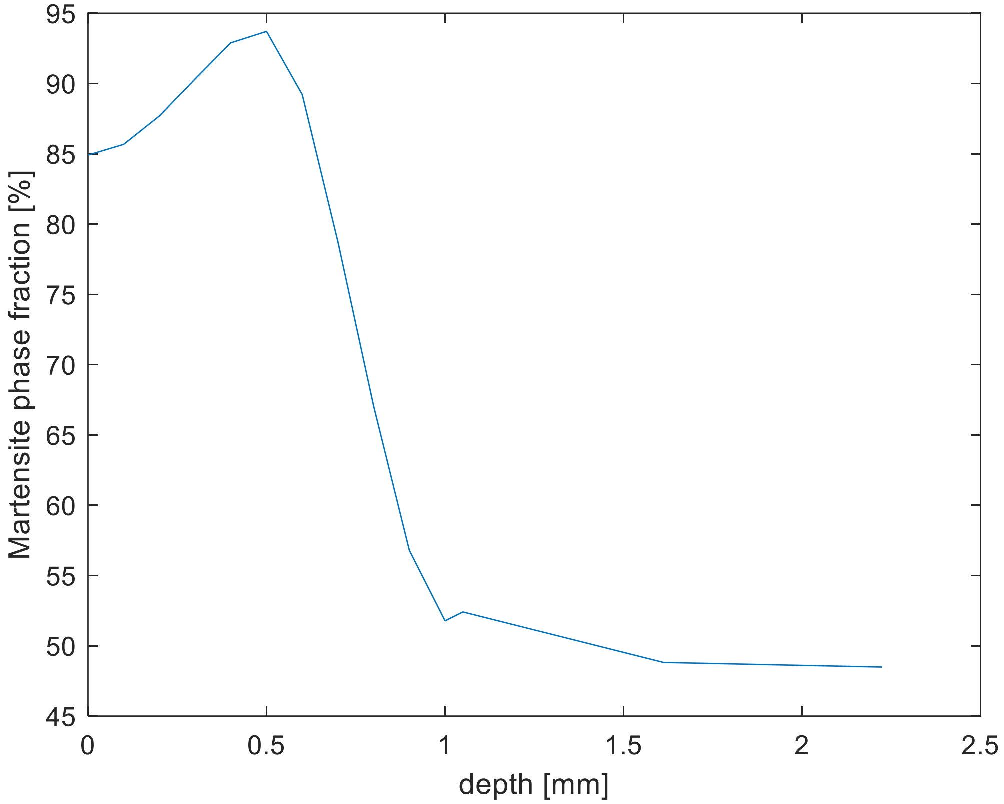

Figure 4. 14: Fraction of martensite as a function of depth from the surface of the gear tooth.

In Figure 4. 14, only the situation close to the surface is shown as this location is where the major changes in steel phase fractions are found.

What can be seen from Figure 4. 14, is that the highest amount of martensite is found very close to the surface. The martensite percentage, then decreases when going deeper within the component. It can also be seen that the maximum amount of martensite is not found at the component's surface, but rather a little below it. In fact, right at the surface, martensite is present, according to the simulation, at about 85%. The remaining 15% circa, is in fact retained austenite, so austenite that did not transform during cooling. The percentage of the retained austenite, that is present at the tooth's surface, is shown in Figure 4. 15.

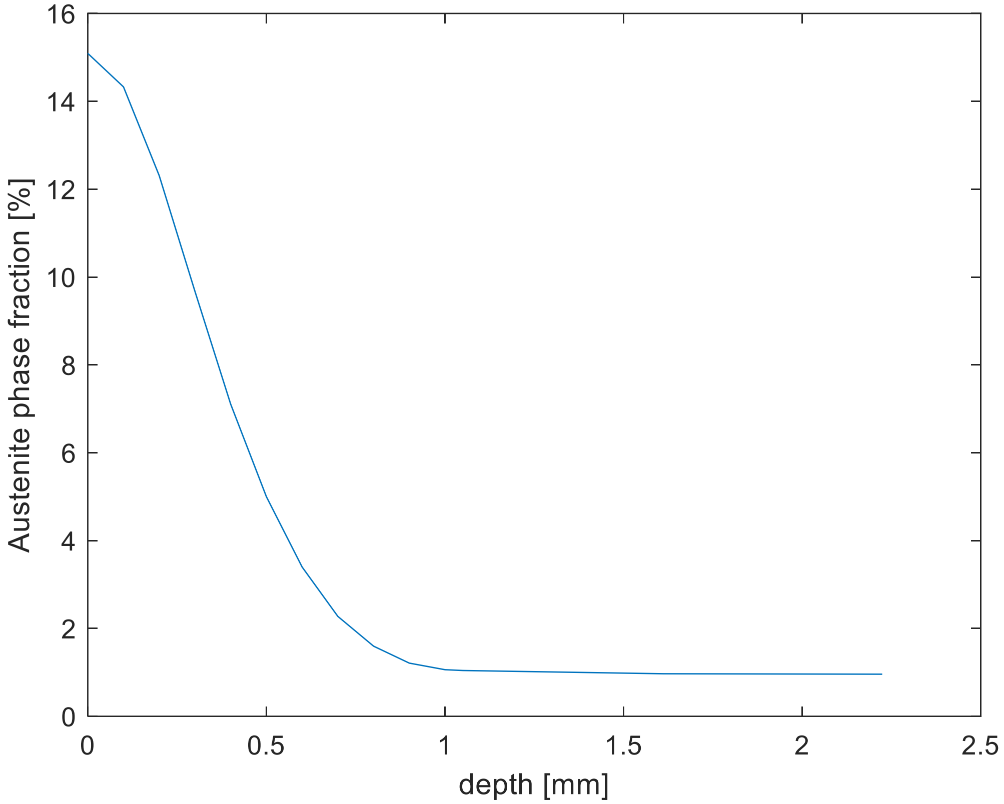

Figure 4. 15: Fraction of retained austenite as a function of depth from the surface of the gear tooth.

What can be seen in Figure 4. 15, in fact, is that the amount of retained austenite at the surface completes the phase composition at the surface of the component. As explained in the literature review chapter, the fact of having traces of retained austenite at the component's surface is quite common in carburized steels. This happens because the transformation of austenite into martensite upon cooling, as seen in the methodology chapter, is highly dependent on the starting transformation temperature for martensite formation M_s. This relation is shown in the Koistinen -Marburger equation (equation 56). In particular, what is expressed in equation 56, is that the transformation of austenite into martensite happens when the temperature is below the M_s temperature. However, the value of M_s, as expressed in equation 57, is greatly dependent on the alloying composition, and, in particular, to the percentage of carbon. Specifically, where the carbon concentration is the highest, the M_s temperature will be the lowest. Therefore, in the regions with low M_s

values, the temperature interval in which the martensite will be able to form will be smaller. The value of the temperature M_s, expressed in °C, is shown in Figure 4. 16 as a function of depth.

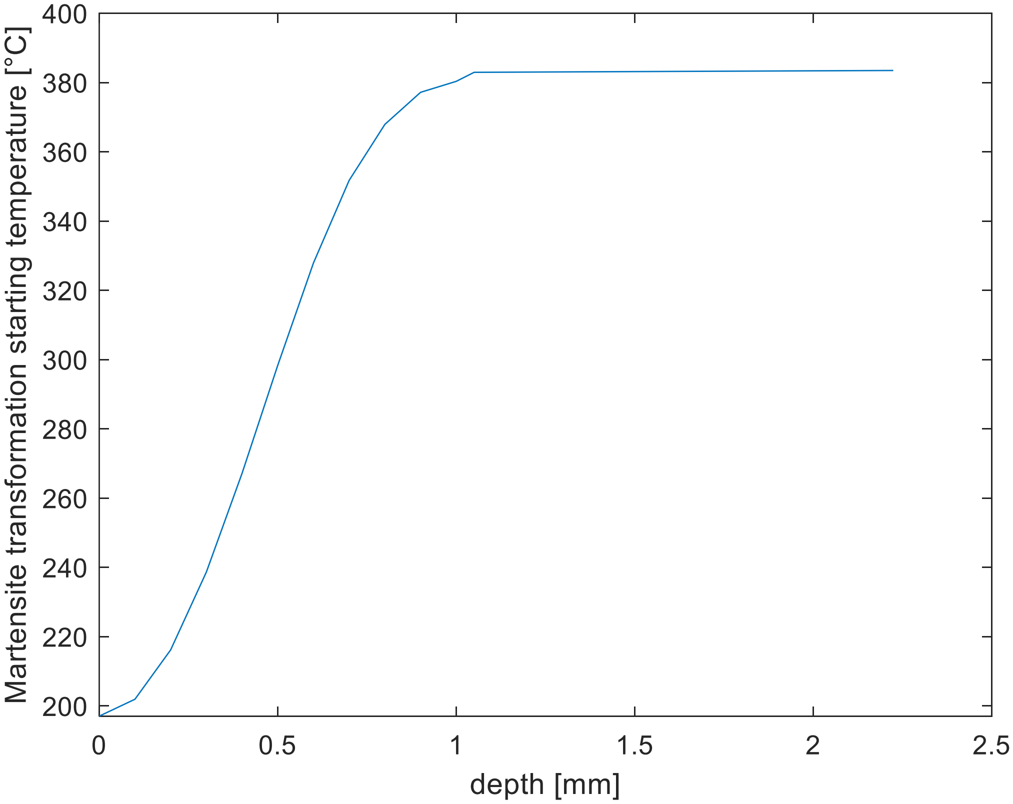

Figure 4. 16: Variation in martensite transformation starting temperature M_s, expressed in °C, at the surface of the gear tooth region.

What can be seen is that the M_s value at the surface is very low, it is in fact below 200°C. Therefore, the martensite at the surface will be able to form only below 200°C, therefore having a smaller temperature interval for formation with respect to the other zones of the component, where the carbon concentration is lower and so the M_s value is higher. This fact, coupled to the cooling rate of the component that, due to the direct contact of the surface with the quenching gas, is greatest at the component's surface and then decreases whilst going deeper in the component, determines the fact that martensite during cooling actually starts forming firstly below the surface where the M_s value is higher and so is firstly reached during cooling, and only after at the component's surface. The presence of retained austenite at the surface, is therefore due to the high amount of carbon at the surface that decreases the transformation starting temperature for martensite M_s. If the carburizing procedure was not performed, the highest amount of martensite would be found at the surface as, since the M_s value would be uniform in all the component due to the absence of carbon variation, the first points to reach the M_s temperature value, below which martensite starts to form, would be those at the surface.

As it is possible to see from Figure 4. 15, the amount of retained austenite than decreases when moving further away from the surface and becomes almost negligible. Far away from the surface, in fact, the lower cooling rates and the higher M_s values determine an almost complete transformation of austenite into either martensite or bainite.

In Figure 4. 16, it is possible to see also that the martensite percentage decreases very much when moving further away from the surface. This is due to the fact that, moving further away from the surface where the cooling gas is applied, the cooling rates experienced will decrease. Lower cooling rates with respect to those experienced in the martensite formation, can determine the formation of bainite. This is exactly what happens, as it is possible to see from Figure 4. 17 that shows the percentage of bainite that is present close to the gear tooth surface. In fact, the amount of bainite increases when increasing the distance from the surface, and so going towards zones where lower cooling rates are experienced.

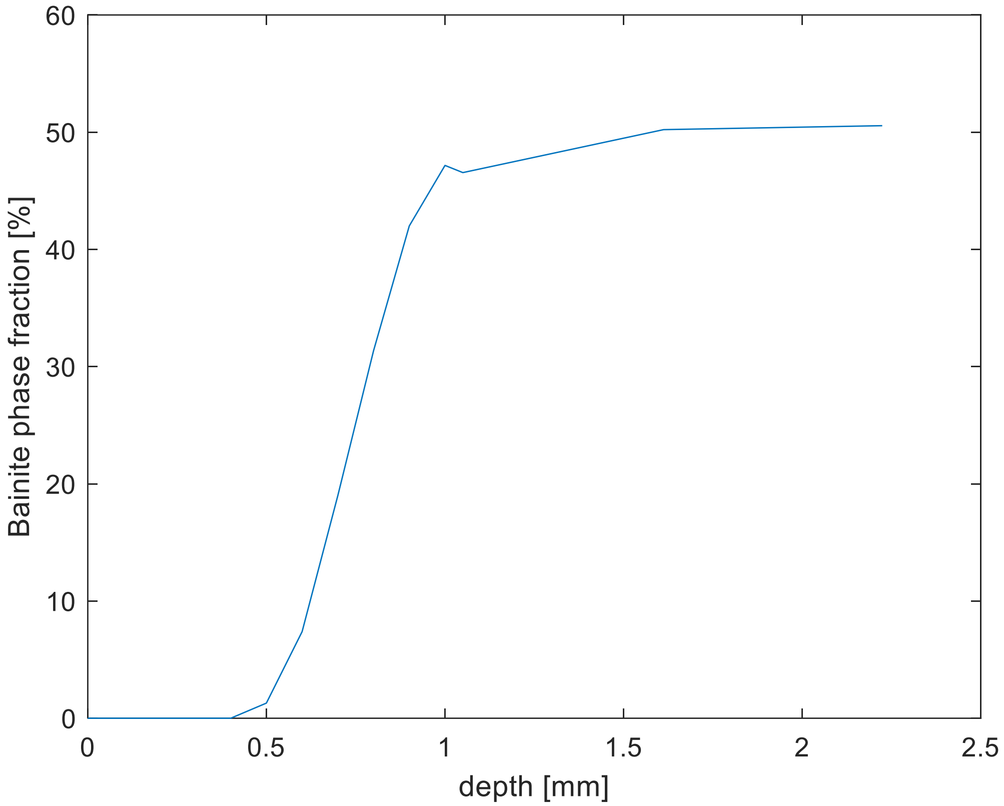

Figure 4. 17: Fraction of bainite as a function of depth from the surface of the gear tooth.

To summarize what has been described so far, the amounts of bainite, martensite, and retained austenite, that are present close to the gear tooth surface, are shown in Figure 4. 18.

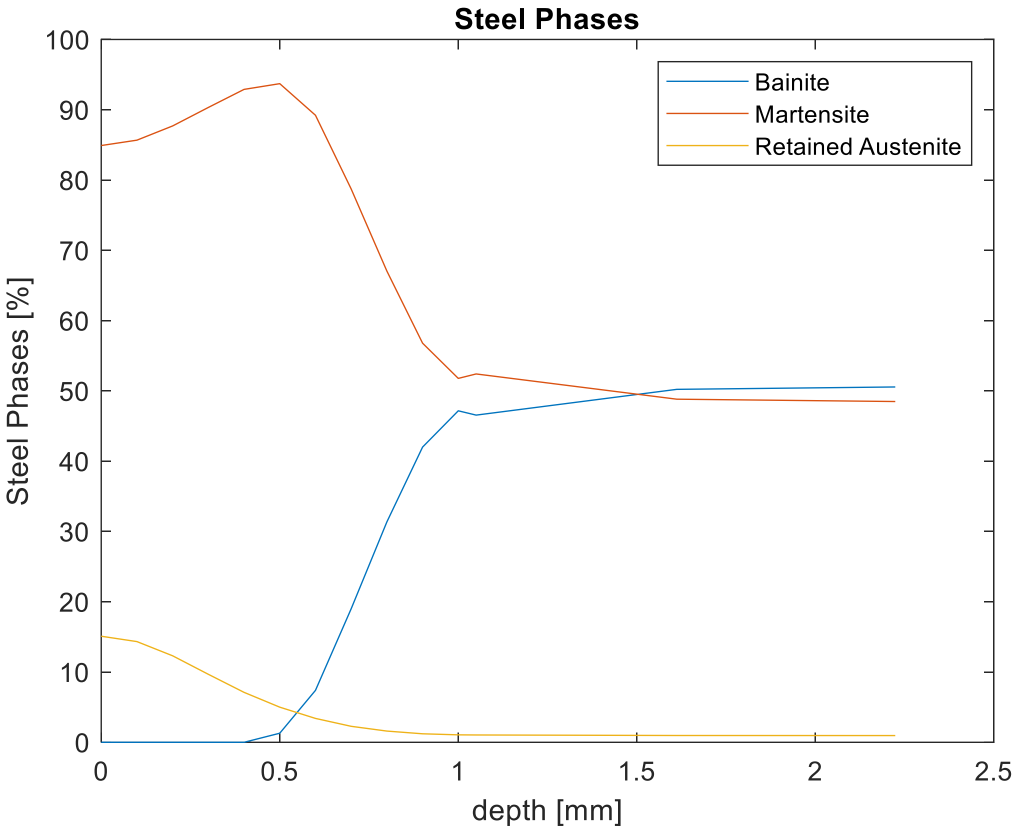

Figure 4. 18: Percentage of different steel phases as a function of depth from the surface of the gear tooth.

From this image it is clearly visible that at the surface the greatest amount of retained austenite is present due to the reasons explained before. The amount of retained austenite than decreases and becomes almost negligible when moving deeper within the component. Close below the surface, the amount of martensite reaches its peak value at about 94%, starting from the already high value of 85% found at the surface. After the peak, the amount of martensite decreases along the depth and reaches a value of about 48.5%. The rest of the structure at this point, is therefore mostly composed of bainite, that accounts for slightly more than 50% of the steel phase composition.

This microstructure shown in Figure 4. 18, would therefore provide a great strength and hardness at the surface due to the great amount of martensite present. The core of the component would instead present a greater amount of bainite that provides a quite good toughness.

In order to test the validity of the results, these steel phase predictions are compared to the microstructural images that were taken, using an optical microscope with a 500X magnification, by the operators at the well-known OEM. In particular, five images, looking at the microstructure at five different depths within the gear tooth, were taken. The gear tooth sample on which the microstructure images were taken, in order to prepare it, was polished and etched with Nital, where the latter is a solution of alcohol and nitric acid.

The first microstructure image was taken at a depth of 0.05 mm from the surface. This image is reported in Figure 4. 19.

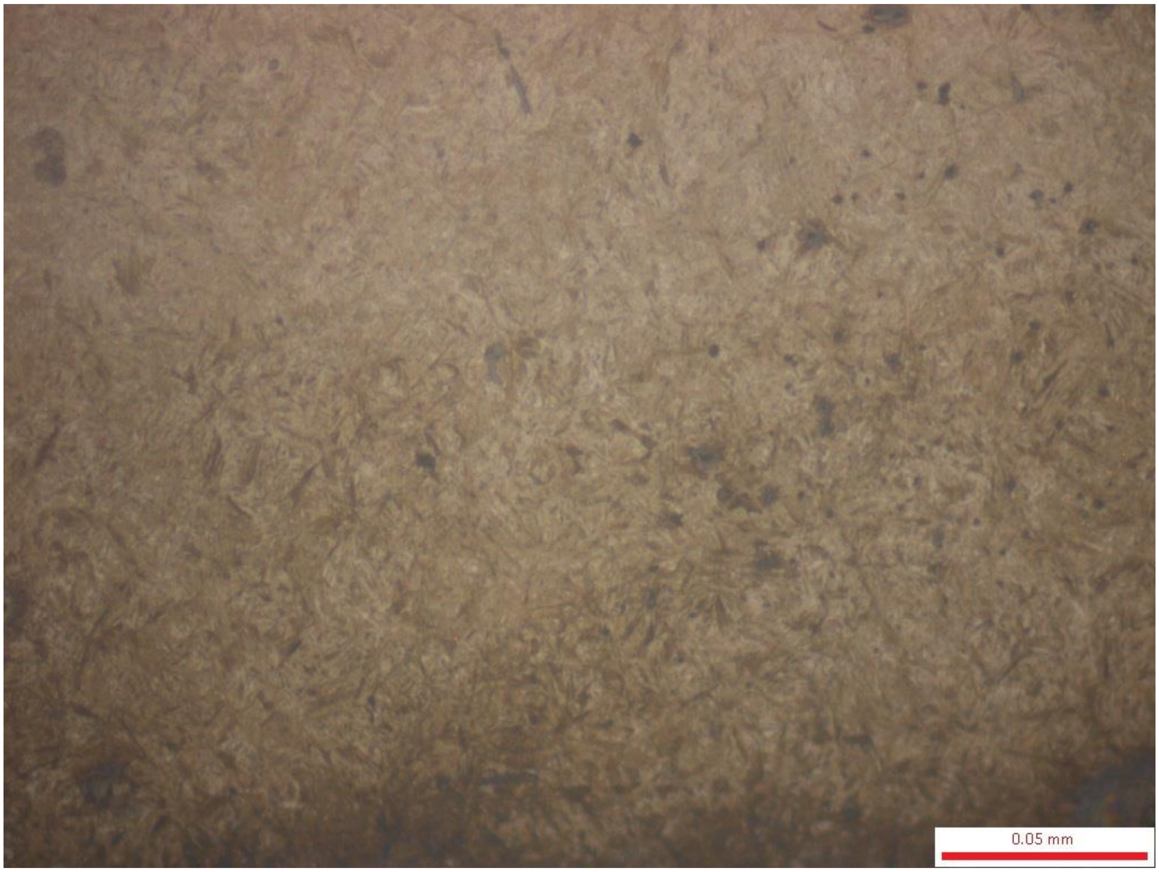

Figure 4. 19: Optical microscopy image at 0.05 mm depth from the surface of the gear tooth.

Since Nital is used as etchant fluid to prepare the sample, the austenite phase should appear as a very bright white region. In Figure 4. 19 it can be seen that there are no bright white regions. This indicates that little amount of retained austenite is found at the gear's tooth surface, and so an almost complete transformation into martensite is achieved. The entirety of the microstructure is therefore composed of martensite. In Figure 4. 19, some black needle-like shapes can be recognized. These structures are typical of martensite. The brownish color region is also martensite. In fact, in this brownish region some very small needle shapes can be found. However, there are also some brownish regions where no discernible needle structure can be found. Also these regions identify as martensite, where however the very fine martensite features do not appear as a magnification of 500X is not enough to correctly visualize and identify them. In this figure, and also in the following ones taken at different depths, some black circular points can be seen. These are remnants of imbedded polishing grit. These are due to the polishing during the sample preparation, and therefore bare no meaning in the steel microstructure.

At the surface of the tooth region in the simulation tool, a composition of 85% martensite and 15 % austenite is found. This means that, at this location, the simulation program is predicting a higher amount of residual austenite with respect to that that has been found experimentally. However, the absence of austenite from the Figure 4. 19 does not mean that no austenite is present. In fact, some residual austenite might have transformed into martensite during the sample preparation due to the effect of transformation induced plasticity. This effect determines the transformation of austenite into martensite due to stresses. If this is the case, in the experimental microstructure images the austenite would not appear because transformed into martensite. It is not possible to know, however, if this transformation actually occurred. Another possible reason for which the retained austenite could not be visible, could be that the magnification with which the images are taken is not high enough to see the retained austenite regions. However, also this cannot be known with certainty. However, perhaps for a future study, an examination of the retained austenite at the surface could be conducted with a higher magnification scale, in order to evaluate if the retained austenite that is not visible in the Figure 4. 38 becomes visible with higher magnifications.

Overall, the simulation tool then predicts that, apart for residual austenite, only martensite is present. This is confirmed from Figure 4. 19 where no traces of bainite are found. In fact, the lower bainitic structure can be recognized by features similar to the needles that are typical of martensite, but thicker and with more rounded edges, having a "feathery" appearance rather than a needle-looking one [23], and none of these features are visible in Figure 4. 19.

The second image, that is shown in Figure 4. 20, was taken at a depth of 0.23 mm from the surface.

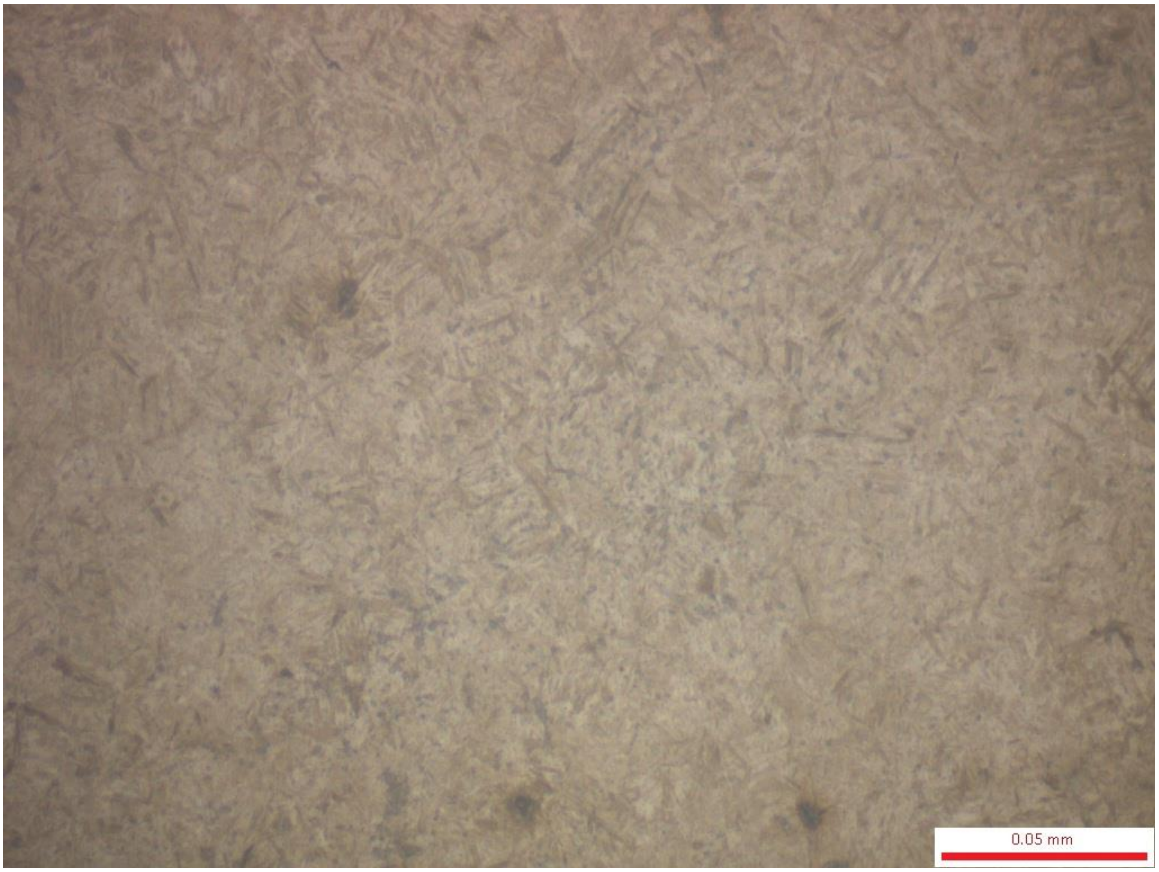

Figure 4. 20: Optical microscopy image at 0.23 mm depth from the surface of the gear tooth.

Very similar observations to those made when considering the surface can also be made when considering a depth of 0.23 mm. In fact, in Figure 4. 20, mostly only martensite is visible, and no retained austenite seems to be present, due to the absence of bright white regions in the image.

The simulation tool predicted at this location the presence of 88% martensite and 12% retained austenite. With respect to what observed at the surface, the amount of retained austenite predicted is lower, however, this predicted value is still higher with respect to the negligible amount of retained austenite found in the experimental microstructural images. This however could be due to the same reasons explained above.

The third image, that is shown in Figure 4. 21, was taken at a depth of 0.4 mm from the surface.

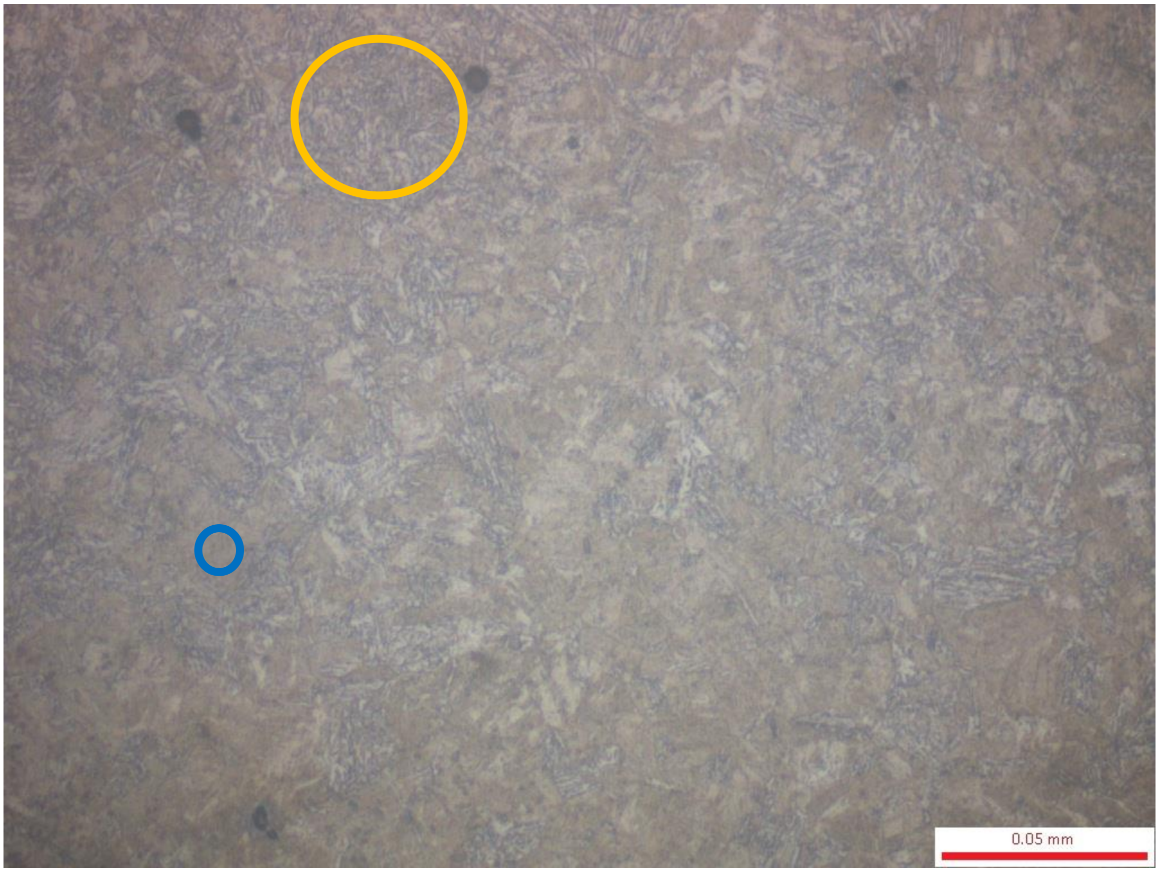

Figure 4. 21: Optical microscopy image at 0.4 mm depth from the surface of the gear tooth.

In Figure 4. 21, that shows the microstructure at the tooth region at 0.4 mm from the surface, the bainitic phase appears. Bainite can be identified as the structure shown within the yellow circle in Figure 4. 21. In fact, in the purple/white region enclosed in the yellow circle, it is possible to distinguish areas showing less of a needle shape and more of a feathery shape, that is typical of bainite. The same structure as that enclosed in the yellow circle can be found also in other parts of Figure 4. 21. In the image, it is also possible to see the same brownish colored areas that were present in the previous figures. An example of these areas is enclosed in the blue circle. These brownish zones, as mentioned before, represent the martensite phase, where however the martensite features are not recognizable due to the magnification of the image, and also, perhaps, due to the polishing during the sample preparation, that might have hidden them.

It is possible to see that the brownish area is more extended with respect to the areas showing a bainitic structure, therefore indicating a greater presence of martensite with respect to bainite. Again, also in Figure 4. 21 no bright white regions are found, indicating the presence of none, or negligible, residual austenite.

At this location, the simulation tool finds that there is no bainite, and so mostly only martensite is present. In fact, it is possible to see from Figure 4. 17 that the fraction of bainite starts showing up and growing only immediately after the 0.4mm depth. This means that the simulation tool at this location is not predicting any bainite when instead it is present, however, the simulation tool starts to predict the presence of bainite immediately after the depth of 0.4mm. The fact that the bainite percentage in the simulation starts showing up immediately after 0.4mm depth, could be due to the mesh refinement at the surface. In fact, at the surface, as shown in Figure 4. 2, ten small elements with a depth of 0.1mm each are found. The depth of 0.4mm is therefore the location of one of the nodes of the elements. Perhaps, if an even finer mesh had to be created at the surface, the Figure 4. 17, that shows the bainite percentage trend as a function of depth, would have a smoother appearance and perhaps the bainite could be found also at the location of 0.4mm instead of starting immediately after.

The fourth image, that is shown in Figure 4. 22, was taken at a depth of 0.58 mm from the surface.

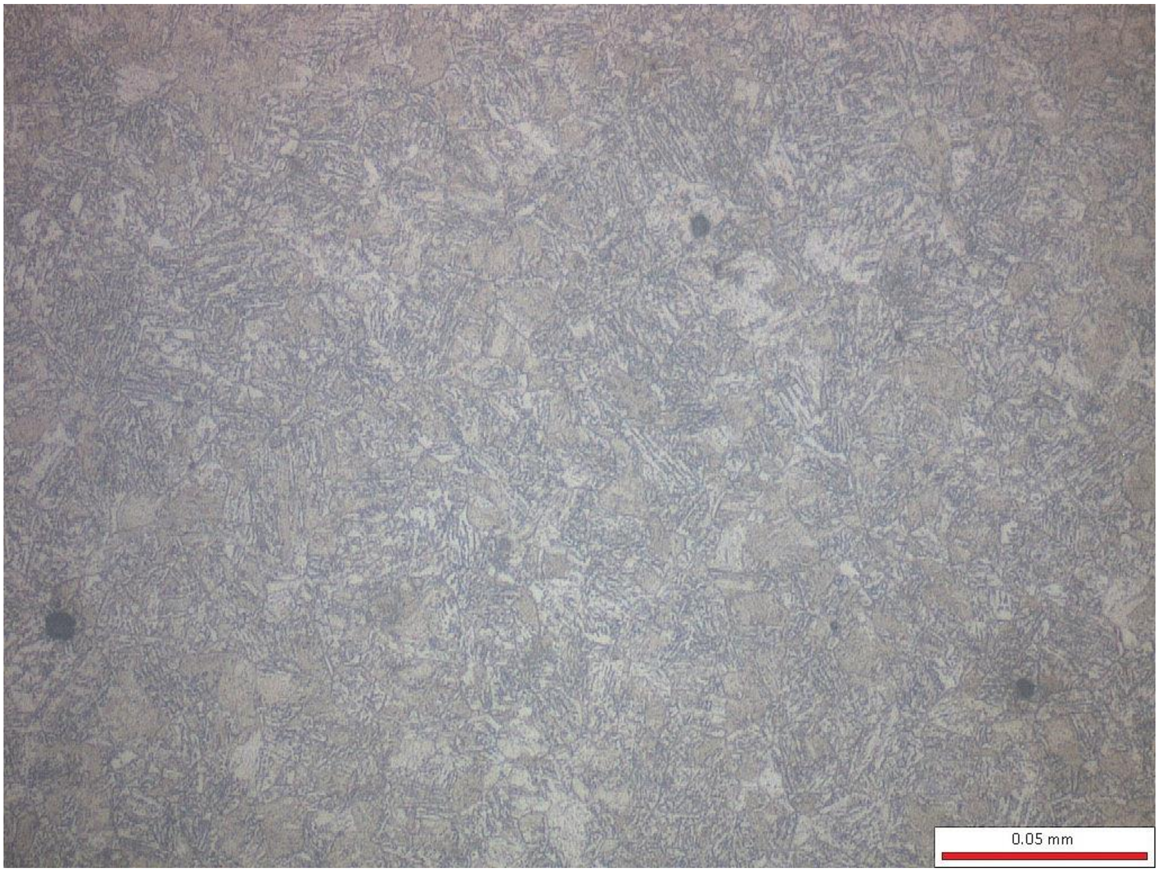

Figure 4. 22: Optical microscopy image at 0.58 mm depth from the surface of the gear tooth.

The situation found in Figure 4. 22 is similar to that described for Figure 4. 21. In this case, however, a greater amount of bainite can be distinguished. At this location, the simulation tool predicts the presence of bainite. So, it is possible to see that at this location the simulation tool has predicted the correct phases present at that particular location: martensite and bainite.

Finally, the fifth image, that is shown in Figure 4. 23, was taken at a depth of 0.75 mm from the surface.

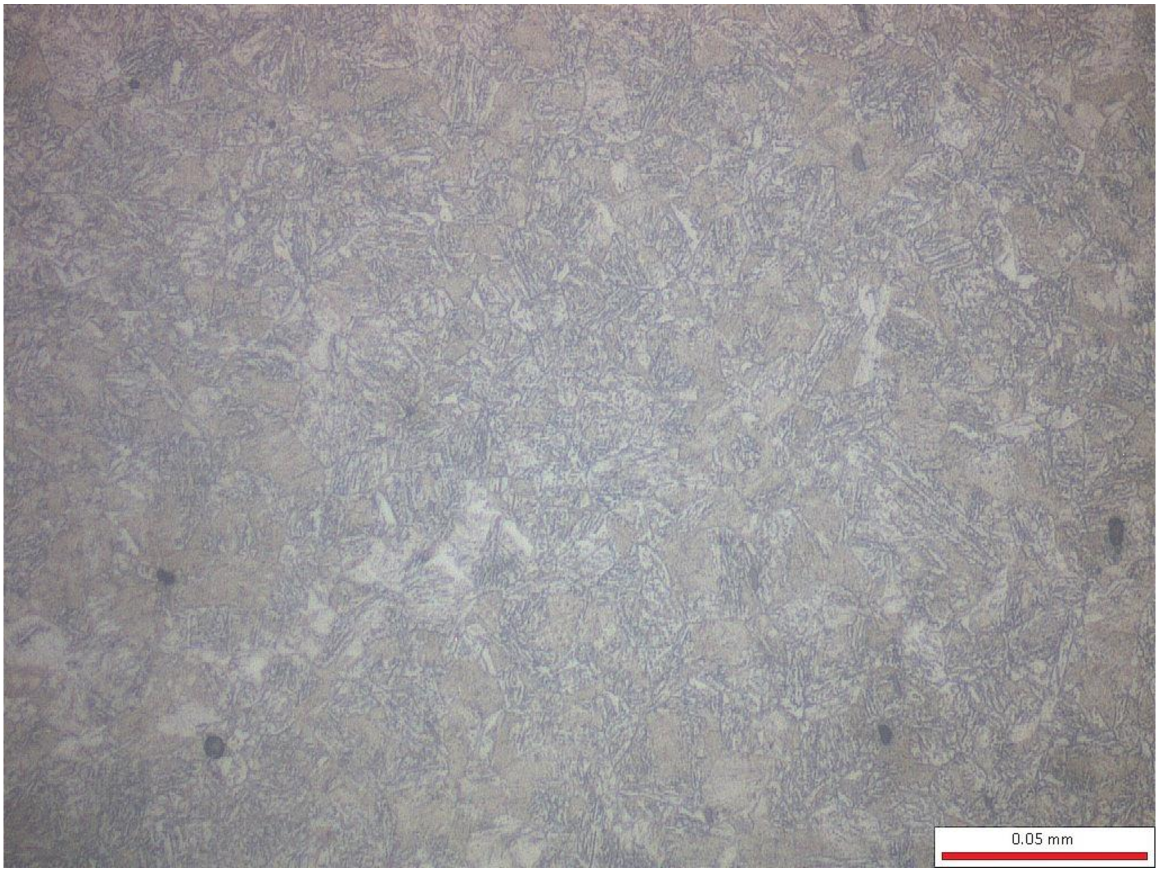

Figure 4. 23: Optical microscopy image at 0.75 mm depth from the surface of the gear tooth.

In this image, similar features to those found in the two previous images can be seen. In fact, the microstructure seen in the image is composed of martensite and bainite.

At this location, again, also the simulation tool predicts that the microstructure is composed mostly of martensite and bainite.

Overall, it can be seen that the simulation tool is predicting results that right close to the surface show a great amount of martensite with a slight presence of retained austenite. These results are partly confirmed by the microscopy images taken on the component, as these show a great amount of martensite, but with negligible presence of retained austenite. This however, as mentioned earlier, could be due to the fact that the retained austenite present on the component after the heat treatment, may have transformed into martensite during the polishing performed when preparing the sample. Furthermore, it could also be due to the magnification of the image, not high enough to correctly identify the austenitic features. These suppositions however are not known with certainty. Moving further away from the surface, the presence of bainite can be spotted in the image taken at 0.4 mm from the surface. At this depth no bainite is predicted by the simulation tool. In fact, the start of the bainite formation is predicted in the simulation tool starting from very slightly after 0.4mm of depth. In the images taken at a depth of 0.58mm and 0.75mm, bainitic and martensitic structures can be seen. This confirms the prediction of the simulation tool, that also predicts a structure composed of mainly bainite and martensite at these locations.

Therefore, the simulation tool seems to give appropriate qualitative results by identifying the correct phases present. It is difficult to perform a quantitative analysis as it is very difficult to correctly and uniquely identify the different steel phases in the images. In fact, it can be very difficult to distinguish between the needle looking features typical of martensite from the very fine feathery looking features of lower bainite.

Now that the microstructure has been described, in the following paragraph the simulated microhardness for the gear tooth will be presented. The simulated microhardness will then be compared to the experimental results.

4.1.2.1.2 Microhardness simulation results and comparison with experimental microhardness measurements at gear tooth

The microstructure shown above clearly influences the hardness of the component. For example, it is known that martensite is the hardest steel phase and that it is slightly harder than bainite and largely harder than residual austenite. The hardness in the simulation was predicted, as shown in the methodology chapter, by applying the set of equations developed by Mayner et al. in the user subroutine USDFLD. These equations, (equations 68 to 70), evaluate the hardness of the different steel phases as a function of the alloying composition. It is possible to see from the Mayner et al. equations that the amount of carbon in the component greatly affect the hardness values. In fact, in all of the equations, one of the terms is represented by the carbon content at that location multiplying a certain coefficient. It is also possible to see that, since the coefficient multiplying the carbon content in the martensite hardness equation is the greatest (949), this indicates that the hardness of martensite is the most dependent on the carbon concentration. In the images, Figure 4. 24, Figure 4. 25, and Figure 4. 26, the hardness values of the different steel phases close to the tooth surface are shown. In these figures, the hardness of bainite is expressed as the user-defined variable “SDV36” and is shown in Figure 4. 24, the hardness of martensite is expressed as the user-defined variable “SDV37” and is shown in Figure 4. 25, and finally the hardness of austenite is expressed as the user-defined variable “SDV35” and is shown in Figure 4. 26. It must be noted that all of the hardness values shown in these figures are expressed in Vickers scale.

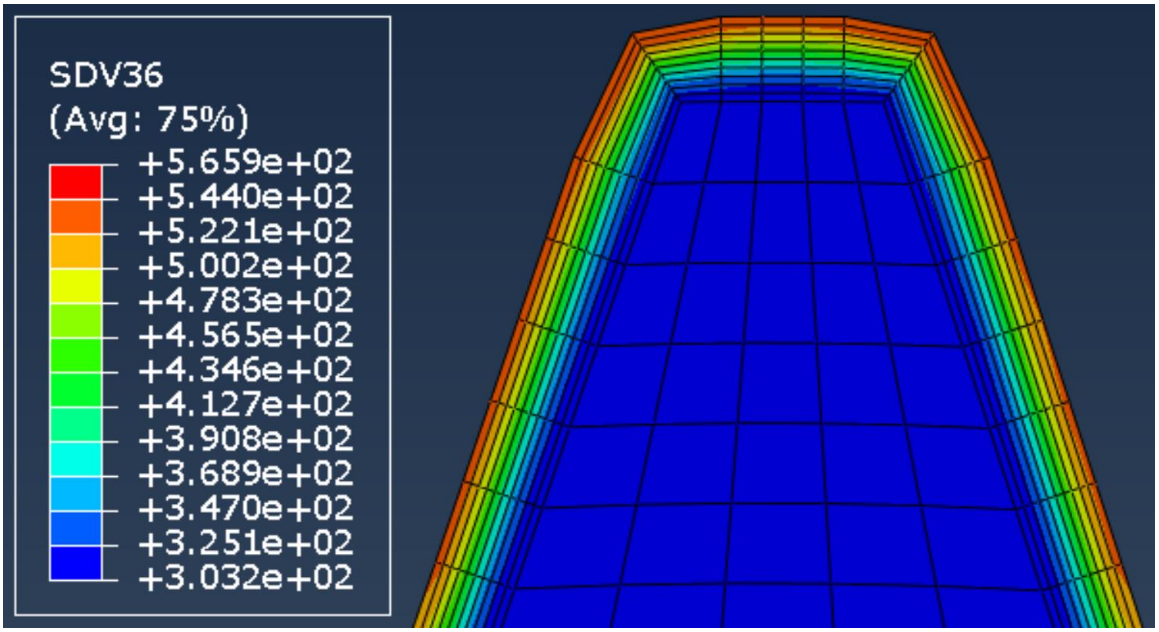

Figure 4. 24: Hardness of bainite at gear tooth surface expressed in Vickers scale.

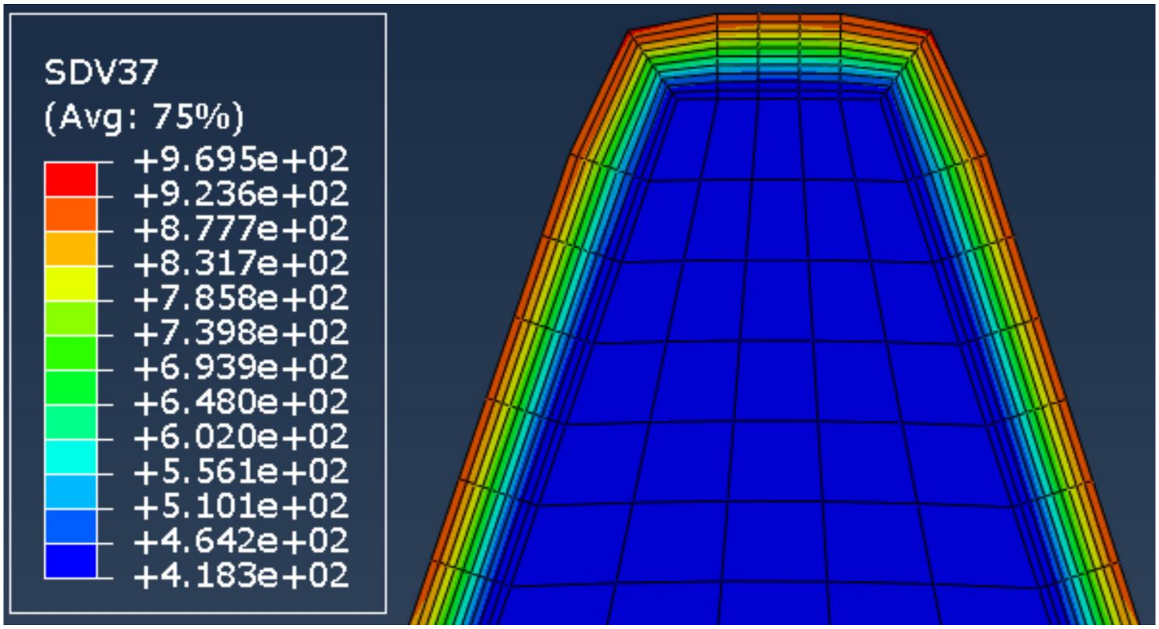

Figure 4. 25: Hardness of martensite at gear tooth surface expressed in Vickers scale.

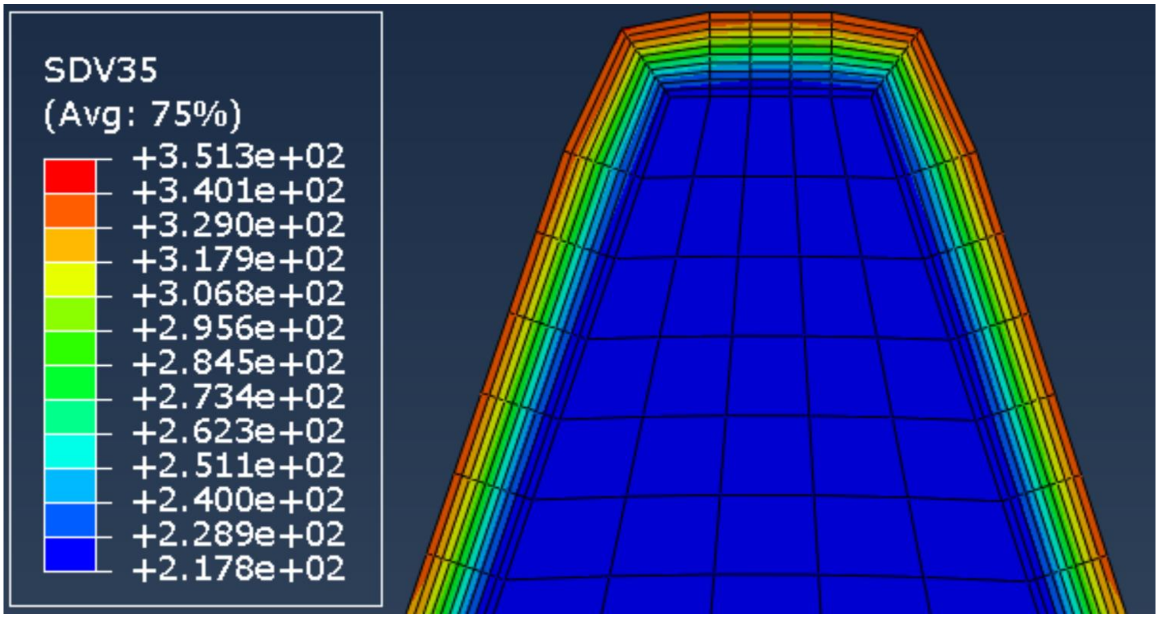

Figure 4. 26: Hardness of austenite at gear tooth surface expressed in Vickers scale.

What can be understood from these images, is that the hardness for all three steel phases is greater at the surface of the component where the carbon concentration is higher, and then decreases inside the component where the carbon content decreases. It is also confirmed that the hardness of martensite is the greatest between the three.

The overall hardness after quenching is therefore then evaluated with equation 71, as shown in the methodology chapter. This is done by knowing the microstructure, that is shown as a function of depth in Figure 4. 18, and by knowing the hardness values for each steel phase and at each location, that are displayed in the above images.

The overall hardness found after quenching is shown in Figure 4. 27.

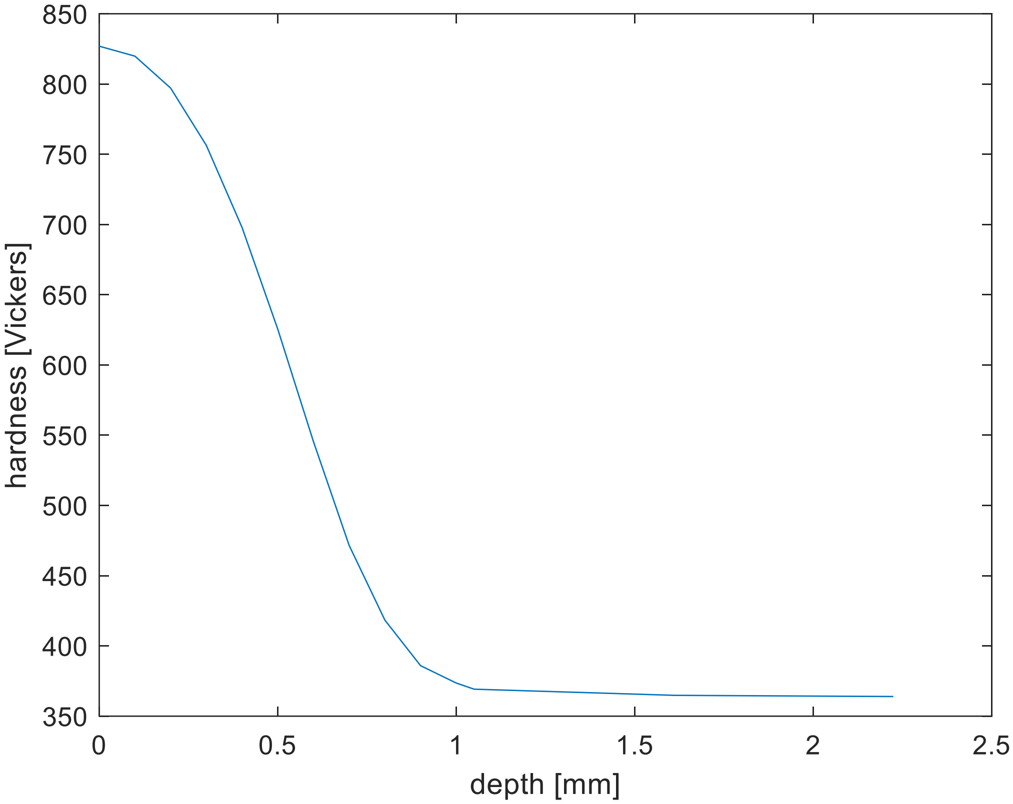

Figure 4. 27: Overall hardness found after quenching at the gear tooth surface.

As expected, the hardness evaluated is greatest at the surface, and then decreases quite rapidly when moving from the surface towards the interior of the component. This decrease in hardness is due both to the decrease in carbon concentration, that, as seen in equations 68 to 70, is a very important factor for the hardness value, and also to the fact that martensite, that has the highest hardness between the three phases that are present in the component, reaches its maximum very close to the surface and then decreases quite rapidly leaving the field to bainite, that is less hard. In fact, it is possible to see that the hardness value after about 1 mm of depth stabilizes and remains quite constant. This constant area region is due to the fact that, after a certain depth, the two factors that affect the microhardness the most: alloying composition and microstructure, do not change anymore or change very little in value, as it is possible to see from both Figure 4. 18 and Figure 4. 6. In fact, from Figure 4. 6, it is possible to see that the carbon content decreases from the high value at the surface, to the 0.165% found in the starting steel, in less than 1mm of depth. Since the rest of the alloying composition is considered to be constant and uniform, the hardness after the depth at which the carbon reaches the value that was present in the starting steel, will not change anymore due to the alloying composition. On the other hand, it is also possible to see from Figure 4. 28, that plots the as-quenched hardness along with the values of the different steel phases percentages as a function of depth, that, after about 1mm of depth, the microstructure starts to vary less and remains composed of about 51% bainite and 48% martensite, with also very little presence of retained austenite. Therefore, after about 1mm, both the microstructure and the alloying compositions show very little variation, and this is the reason why the hardness remains quite constant after about 1mm of depth. In Figure 4. 28, the blue lines refer to the steel phases percentage and to the scale shown on the left of the figure. On the other hand, the red curve shows the trend in hardness after quenching as a function of depth and refers to the axis shown on the right.

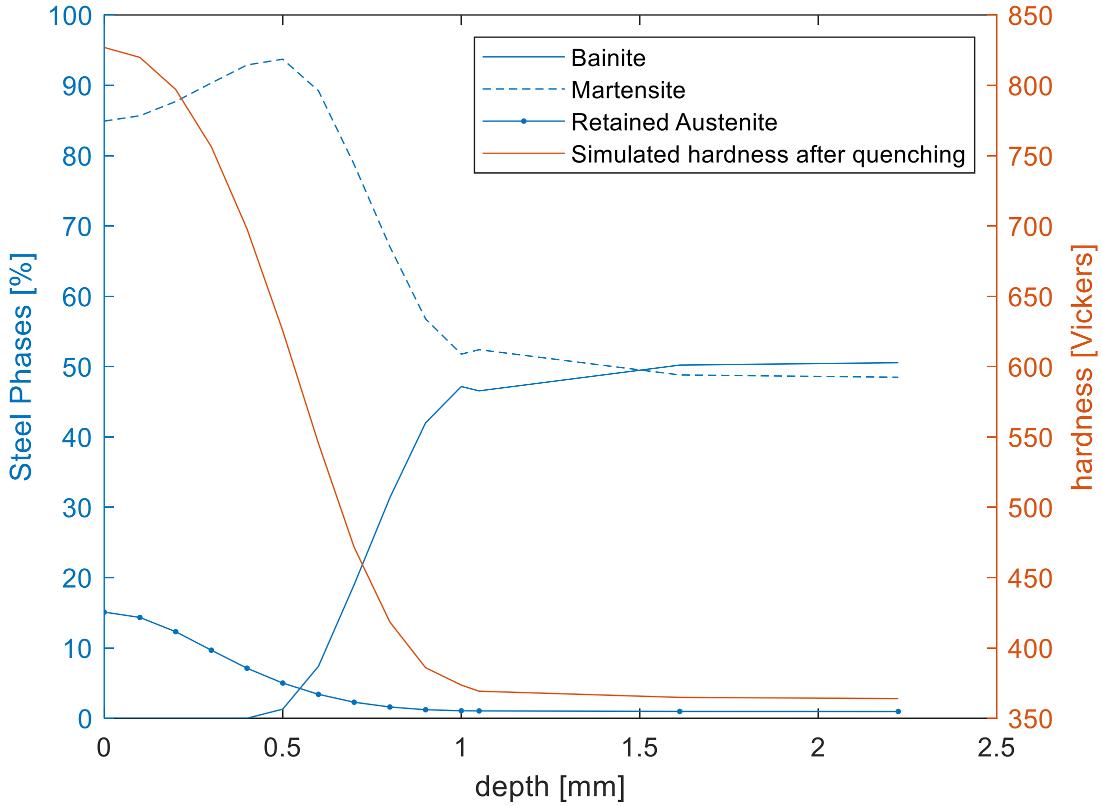

Figure 4. 28: Steel phases percentage at gear tooth surface (blue scale) along with simulated as-quenched hardness (red scale).

The values just presented are referring to the hardness after quenching. However, as seen in the literature review and methodology chapter, this hardness is then reduced during the tempering process, where the carbon atoms are allowed to diffuse away from the deformed martensite crystal structure. The tempering effect, as described in the methodology section, is taken into account by considering the reduction in hardness that it determines in the martensite phase. The method with which this is done, is explained in the methodology chapter. The tempering temperature and time cannot be disclosed because proprietary information of the OEM. However, these values are in the range that was discussed in the methodology section, so below 200°C and for a time frame of up to two hours.

The overall hardness, found at the gear tooth location after tempering, as a function of depth, is shown in Figure 4. 29.

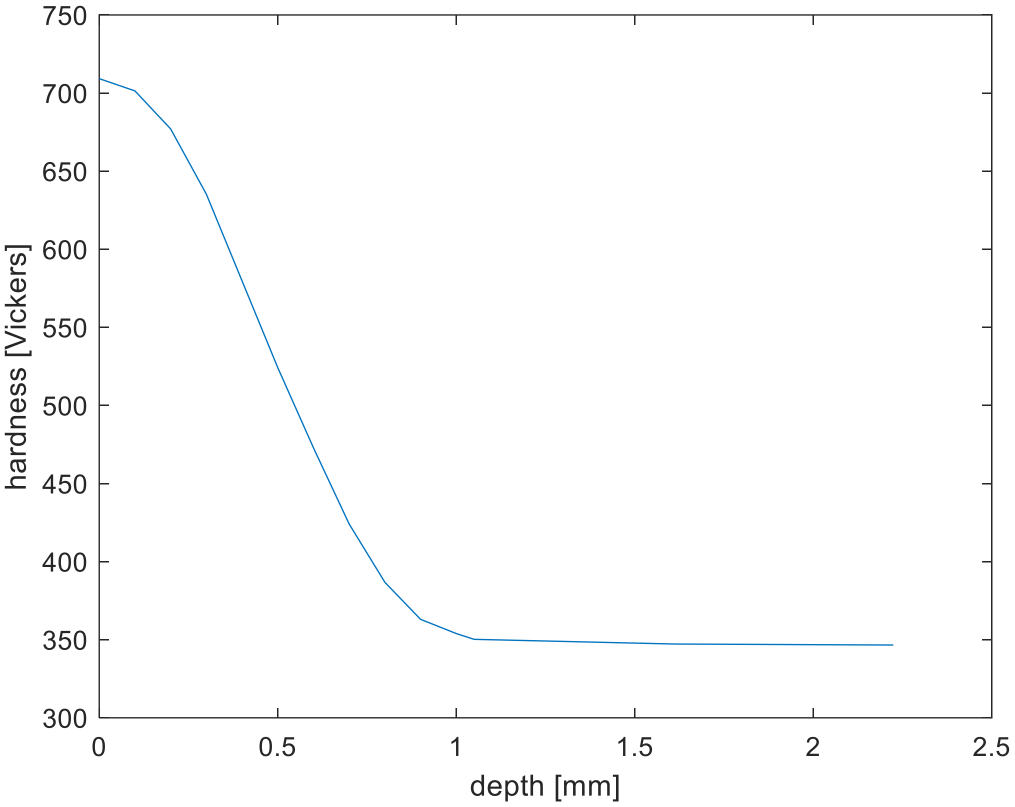

Figure 4. 29: Overall hardness found in the gear tooth after tempering.

A graph comparing the hardness before and after tempering is shown in Figure 4. 30.

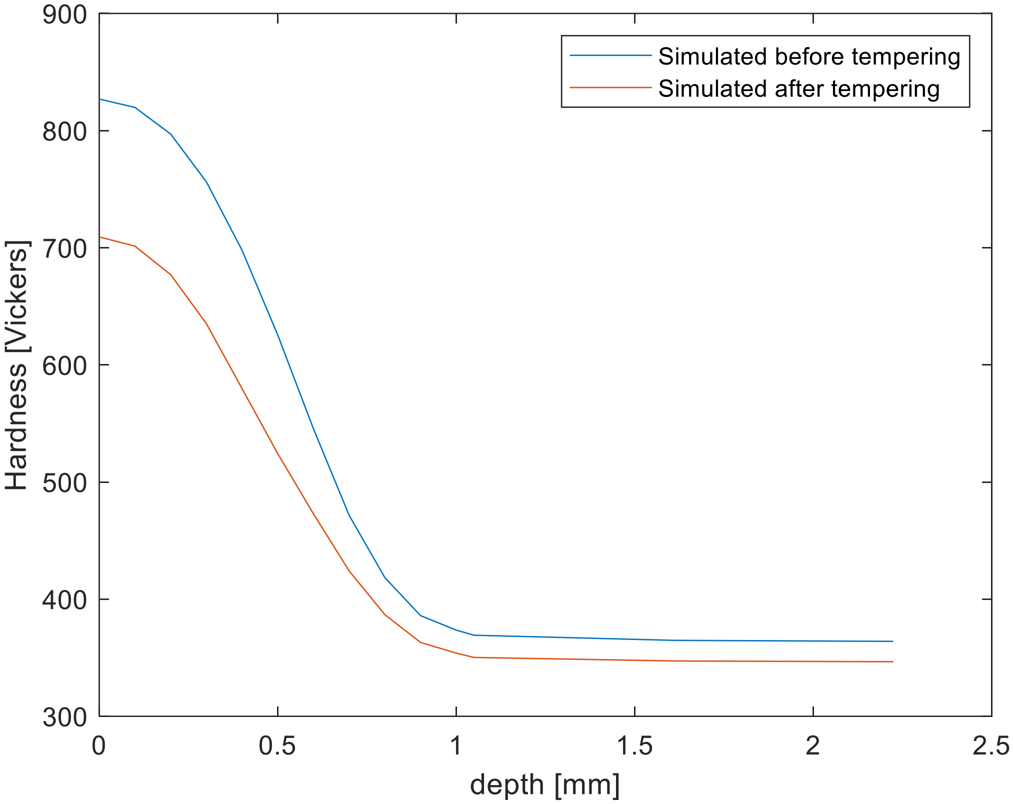

Figure 4. 30: Comparison between hardness found at the gear tooth before and after tempering.

What can be seen from Figure 4. 30 is that the hardness after tempering is generally lower, as expected, with respect to that found after quenching. However, the difference between the two hardness values is not uniform along the depth. In fact, it is possible to see that the biggest decrease in hardness is seen at the surface of the tooth. The hardness deep inside of the tooth, on the other hand, is not so affected by tempering. This is due to the fact that, as seen in the methodology, the only phase that is considered to be affected by tempering, is martensite. Therefore, since the hardness of martensite is the only one to be modified and reduced, the greatest difference between the as-quenched hardness and the tempered-hardness is seen in the regions that have the greatest amount of martensite. This explains why the hardness decrease at the surface, where more martensite is present, is much greater with respect to that that occurs deeper inside the component, where the amount of martensite is much lower.

These values of microhardness where then compared to experimental measurements taken on the real component by some operators at the well-known OEM. The experimental microhardness measurements are shown in Figure 4. 31, where they are plotted as a function of the depth at which they were measured.

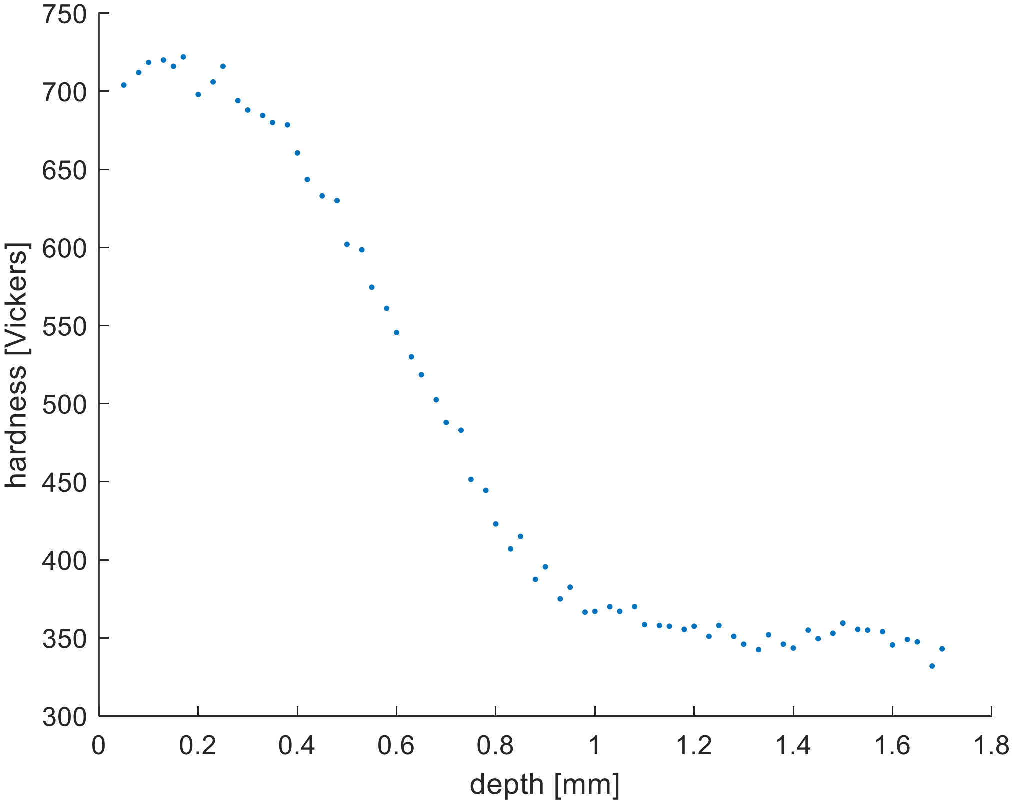

Figure 4. 31: Experimental microhardness measurements on real gear component after tempering at tooth region.

In order to grasp the general trend of the experimental microhardness measurements as a function of depth, an interpolation function was used. This interpolation function is shown in Figure 4. 32.

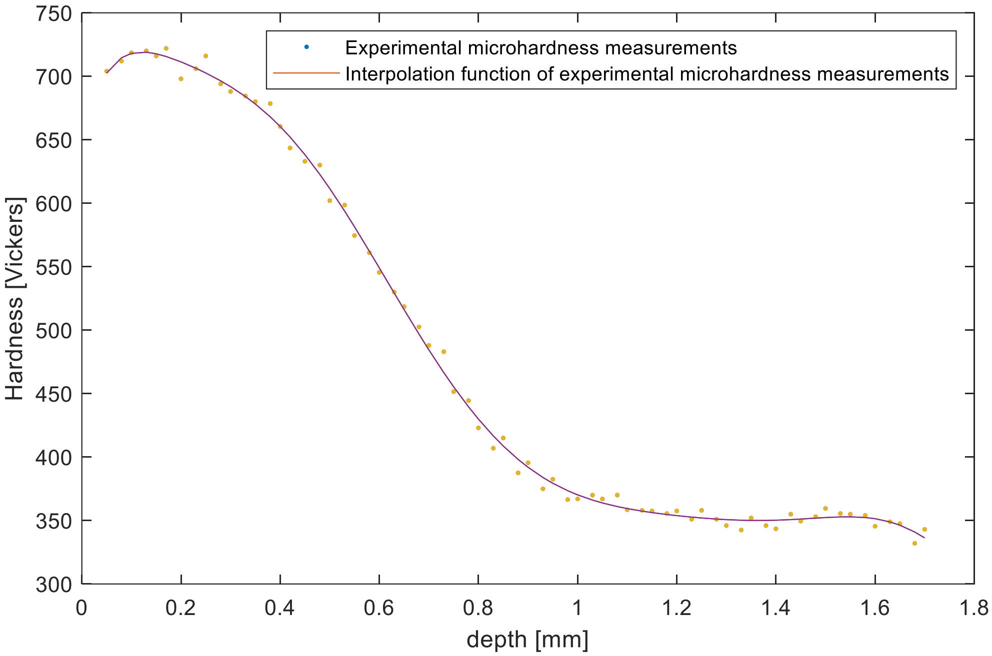

Figure 4. 32: Interpolation function of the experimental hardness at the surface of the gear tooth after tempering.

The hardness after tempering obtained with the simulation is now compared to these experimental results to see how close the two set of values are. The comparison between the simulated and experimental microhardness values is shown in Figure 4. 33.

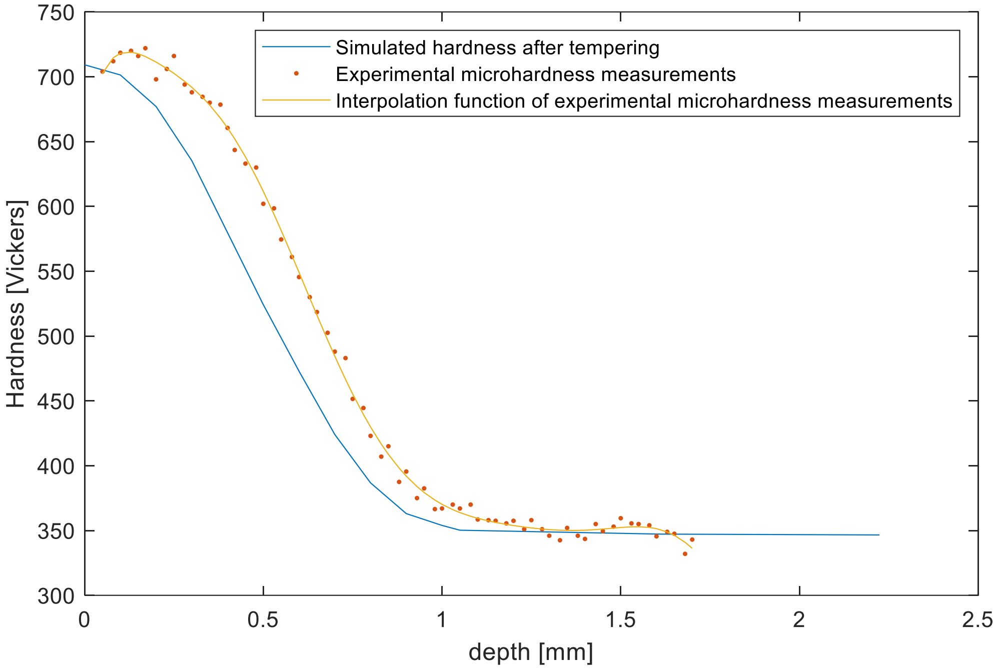

Figure 4. 33: Comparison between simulated and experimental hardness results at the surface of the gear tooth.

What can be seen from Figure 4. 33, is that the simulated microhardness has a value at the surface that is quite similar to that seen with the experimental microhardness measurements. The difference in hardness between the simulated and experimental curves is then minimal in the region starting right below the surface and reaching a depth of about 1 mm, where the simulated microhardness assumes values that are slightly lower with respect to the simulated ones. After 1 mm in depth, finally, both the experimental microhardness and the simulated one obtain hardness values that are quite similar and remain nearly constant.

This comparison shows, for the gear tooth region, that the simulation tool can give to the user the correct idea on the trend of the hardness of the component as a function of depth. In fact, the simulated and experimental values seem to be in reasonably good agreement. The simulation, however, shows slightly lower hardness values in the region from the surface to the depth value after which the hardness remains quite constant.

4.1.2.2 Gear Hub Location

4.1.2.2.1 Steel Microstructure found at gear hub and qualitative comparison with microstructure images

The gear hub region, as it can be seen from Figure 4. 12, is a bulkier region of the gear with respect to the gear tooth. The presence of a larger quantity of material implies a lower cooling rate at that location, and so generally a lower amount of martensitic phase with respect to what was found in the tooth region that is less bulky. Furthermore, the gear hub has less surface exposed to the quenching gas with respect to the gear tooth region, and also this tends to lean towards the presence of less martensite in the gear hub with respect to the gear tooth.

The steel microstructure, that is obtained by applying the Lee et al. formulations and the Koistinen-Marburger equation in the user subroutine USDFLD, is reported below. Again, as for the gear tooth region, the cooling rate experienced in the gear hub is fast enough to prevent the formation of ferritic and pearlitic structures. In fact, the simulation shows that no formation of perlite and ferrite occurs during cooling. Therefore, again, the simulated microstructure is composed of mainly bainite, martensite, and retained austenite. Considering the outputs of the simulation taken from a location in the gear hub, the following results were obtained for what concerns the percentage of bainite, martensite and retained austenite.

In Figure 4. 34, the fraction of martensite in percentage is shown as a function of depth.

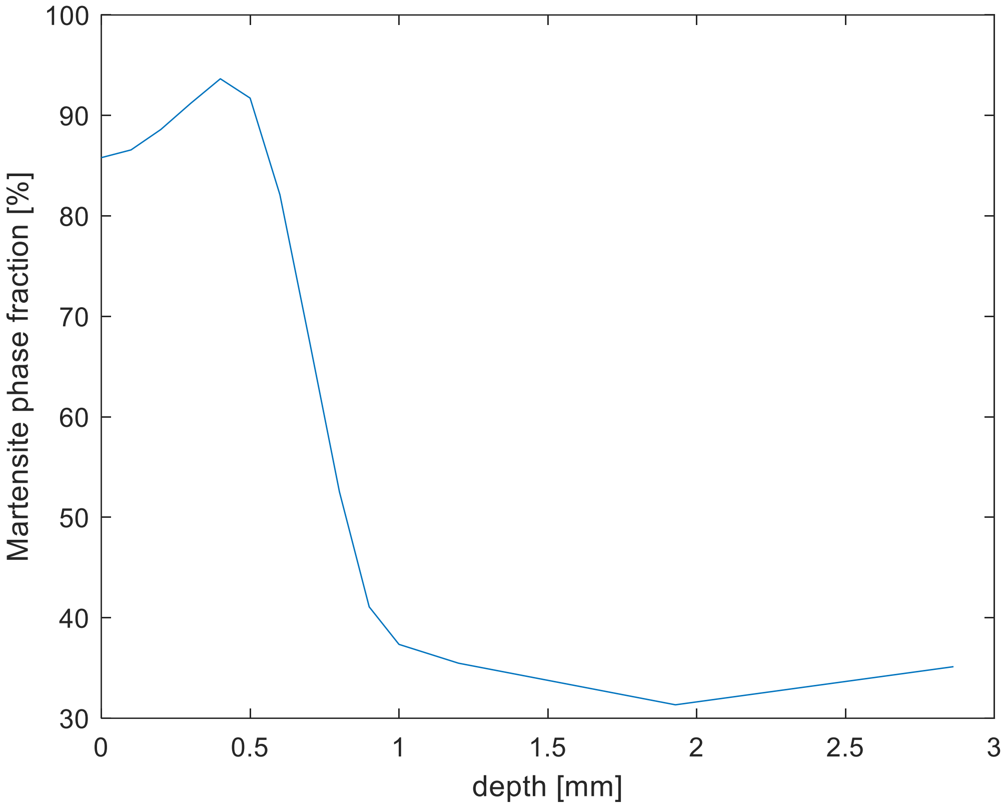

Figure 4. 34: Fraction of martensite as a function of depth at the hub surface of the gear component.

In Figure 4. 34, as done before for the tooth region, only the situation close to the surface is shown as this location is where the major changes in steel phase fractions are found.

Very similar observations to those made earlier when considering the tooth region can be made. In fact, the amount of martensite is very high close to the surface, and then decreases going deeper within the component. The amount of martensite at the surface is of about 85%, the value then slightly increases moving away from the surface, reaching the maximum value of about 93 % at 0.4mm from the surface. After this peak, the value of martensite decreases and reaches a value of about 35% in the core of the gear hub. It is possible to see that, as discussed above, the value of martensite found when distant from the surface is higher for the hub region with respect to that simulated for the tooth region. This is due to the cooling rate in the gear that is lower in the hub region with respect to that found in the tooth region, due to the inferior amount of surfaces exposed to the quenching fluid, and to the greater amount of material present in the hub region. The slower cooling rate determines a higher presence of bainite. This can be in fact seen in Figure 4. 35, that shows the percentage of bainite as a function of depth. What can be noticed, is that moving away from the surface the percentage of martensite decreases and, in turn, a greater percentage of bainite is found. At the core, the percentage of bainite found is of above 60%.

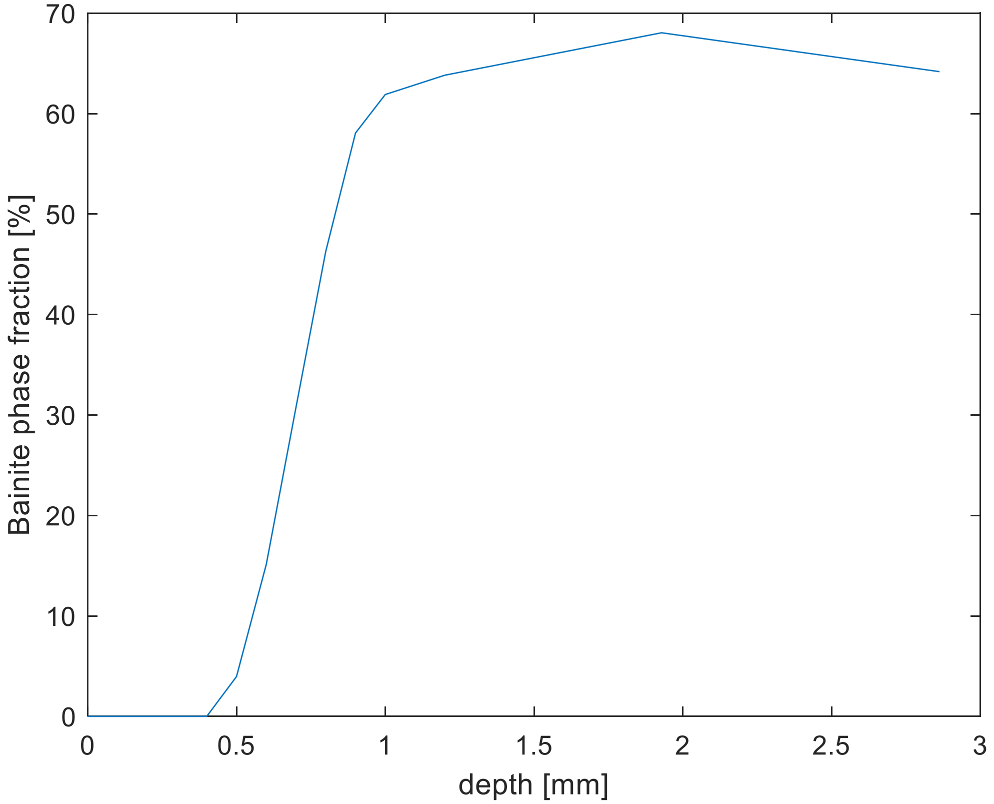

Figure 4. 35: Fraction of bainite as a function of depth at the hub surface of the gear component.

Completing the microstructure at the hub region surface, is retained austenite, accounting for about 15%. The percentage of retained austenite as a function of depth for the hub region is shown in Figure 4. 36.

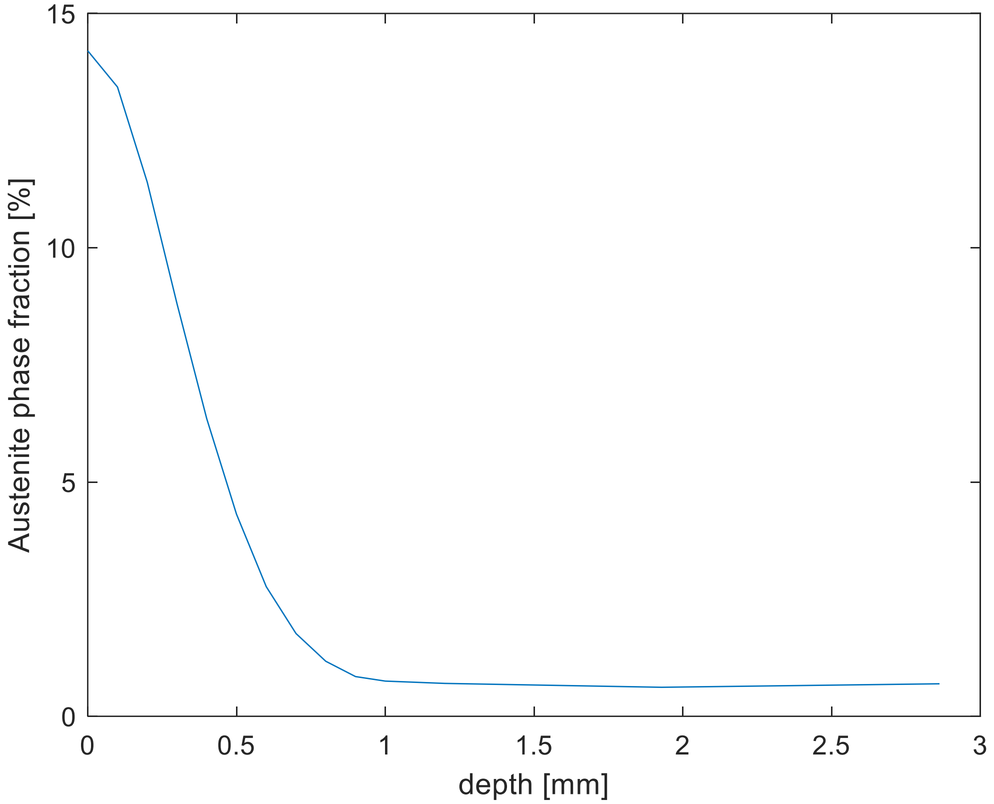

Figure 4. 36: Fraction of retained austenite as a function of depth at the hub surface of the gear component.

In Figure 4. 36, in fact, it can be seen that, at the surface, 15% of retained austenite is found. This amount then decreases quite rapidly when going deeper inside the component. The reason why this retained austenite is found at the surface, is the same as that explained earlier for the tooth region, and so it is due to the higher carbon concentration at the surface that reduces the transformation starting temperature for martensite formation.

In Figure 4. 37, a graph is included summarizing all info provided above. In this image, the percentages of retained austenite, bainite and martensite are shown together as a function of depth.

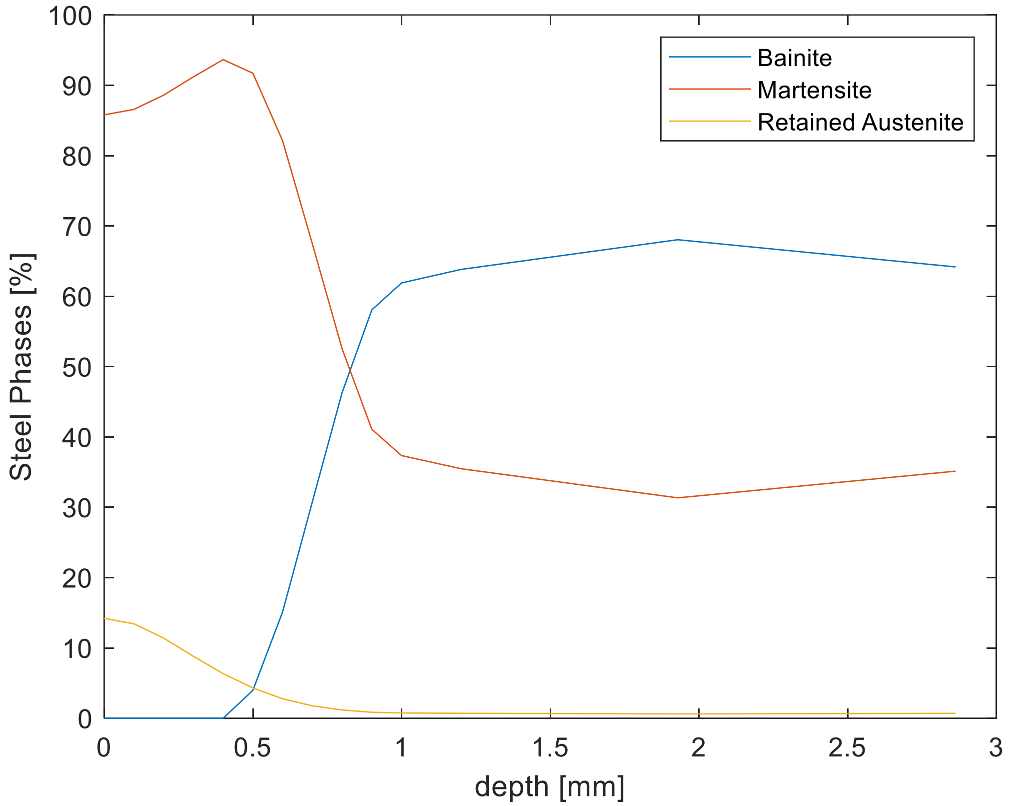

Figure 4. 37: Percentage of different steel phases as a function of the depth at the hub surface of the gear component.

In this image, what was described above can be seen in its entirety. In this image it is very clear to see that, when moving away from the surface, the microstructure shifts from becoming composed of mostly martensite to becoming composed of mostly bainite.

As done for the gear component, in order to qualitatively test the validity of the results, these steel phase predictions are compared to the microstructural images that were taken using an optical microscope with a 500X magnification by the operators at the well-known OEM. Again, five images, looking at the microstructure at five different depths within the gear hub, were taken. As for the tooth sample, also the hub sample on which the microstructure images were taken, was polished and etched with Nital.

The microstructure images taken at the depths of 0.05 mm, 0.23mm, 0.4 mm, 0.58 mm and 0.75 mm from the surface are shown in Figure 4. 38, Figure 4. 39, Figure 4. 40, Figure 4.

41 and Figure 4. 42. Very similar observations to those made above for the tooth region can be applied also for this component. Therefore, the residual austenite is identified by very bright white features, the martensite is identified by brownish colored zones such as those shown in the blue circle in Figure 4. 21, and finally the bainite can be seen when looking at areas resembling what is enclosed in the yellow circle in Figure 4. 21. Again, in all of the images taken at different depths, the presence of some black dots that are remnants of imbedded polishing grit due to the sample preparation, can be seen.

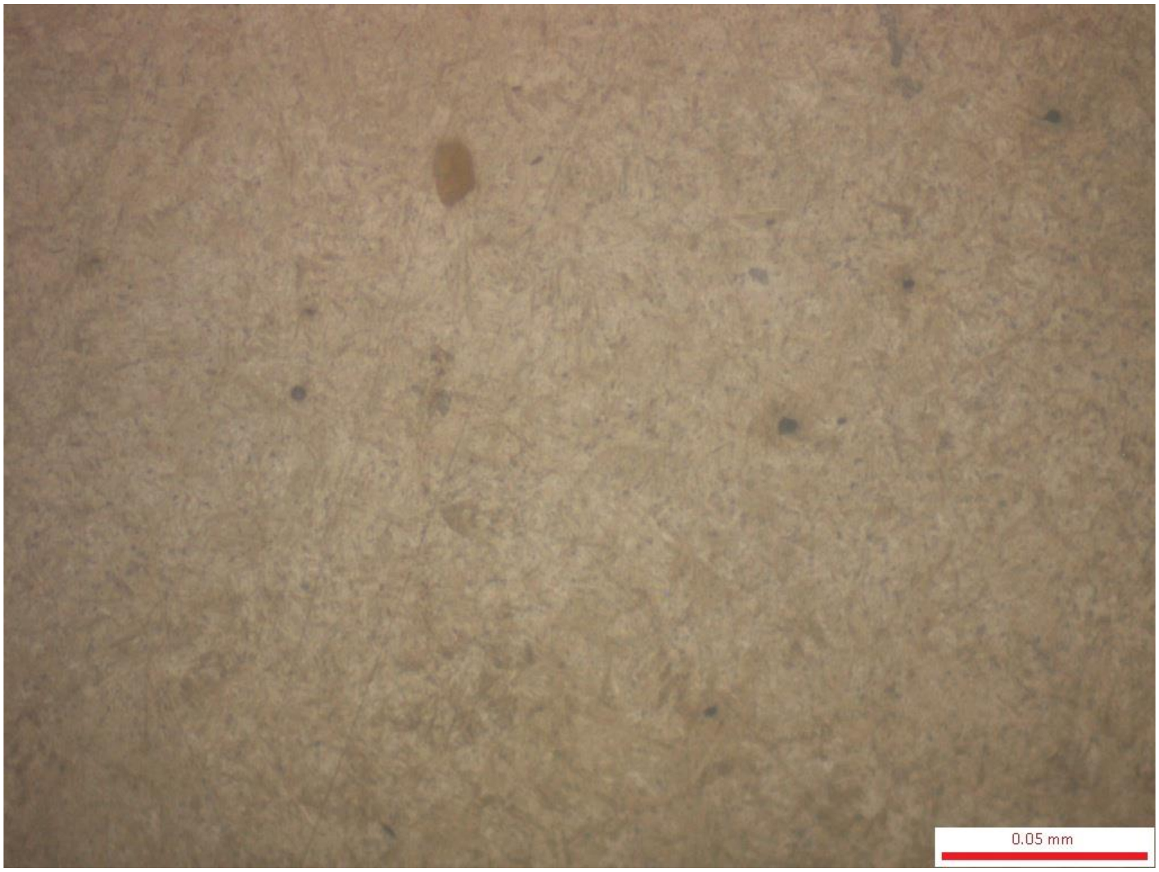

Figure 4. 38: Optical microscopy image at 0.05 mm from the gear's surface at the hub region.

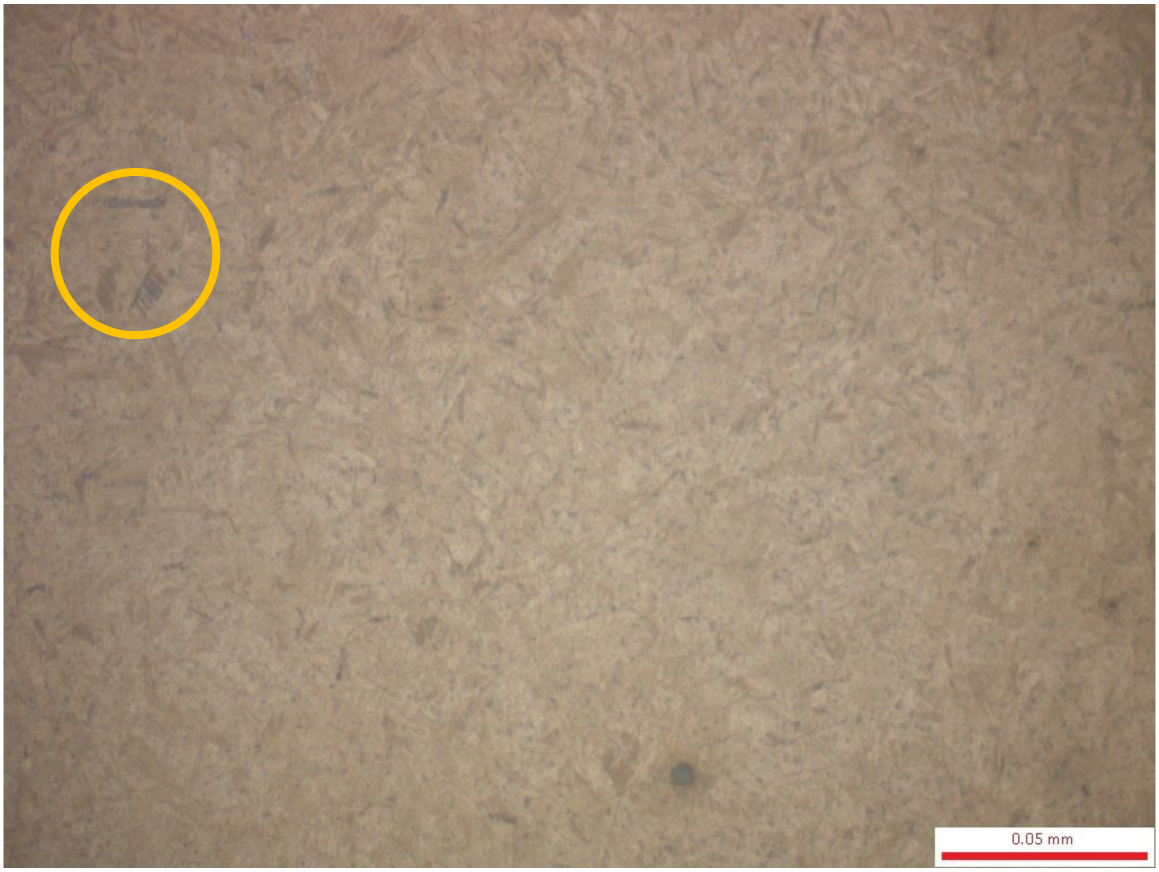

Figure 4. 39: Optical microscopy image at 0.23 mm from the gear's surface at the hub region.

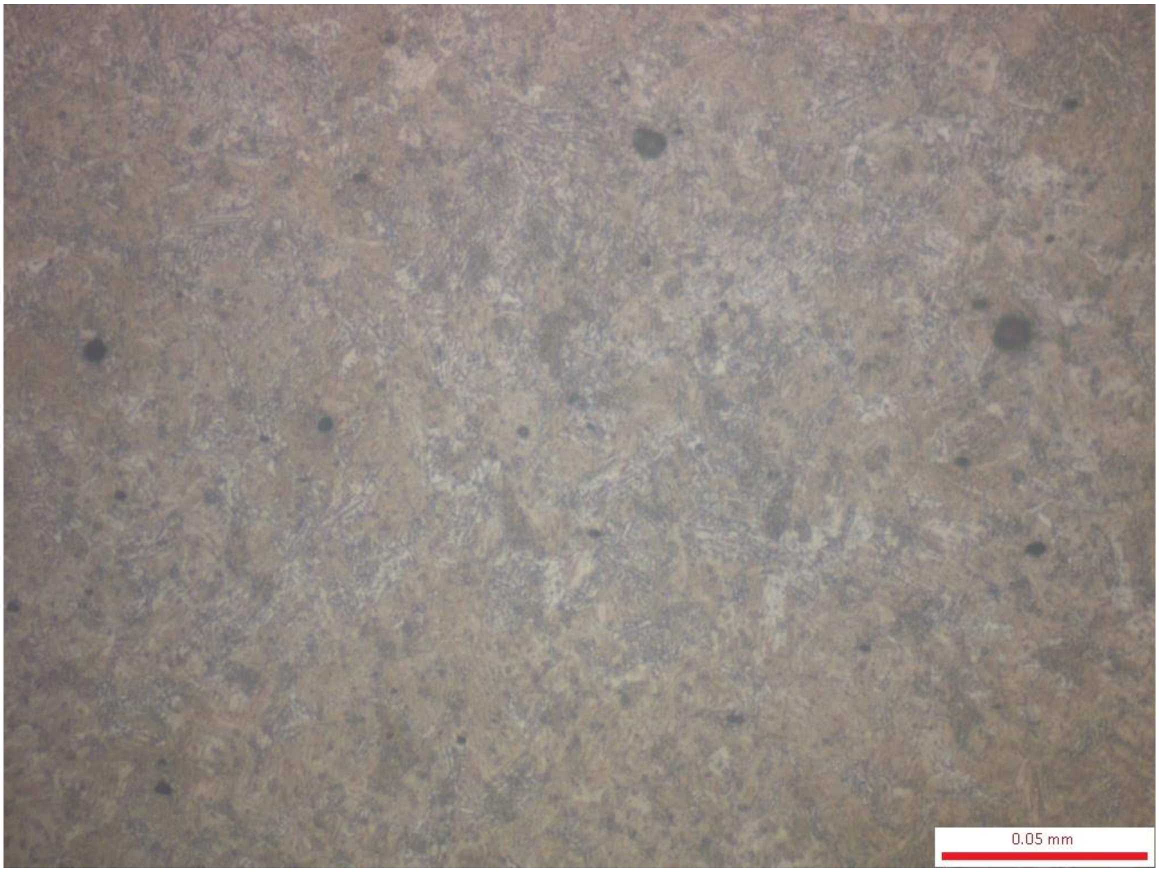

Figure 4. 40: Optical microscopy image at 0.4 mm from the gear's surface at the hub region.

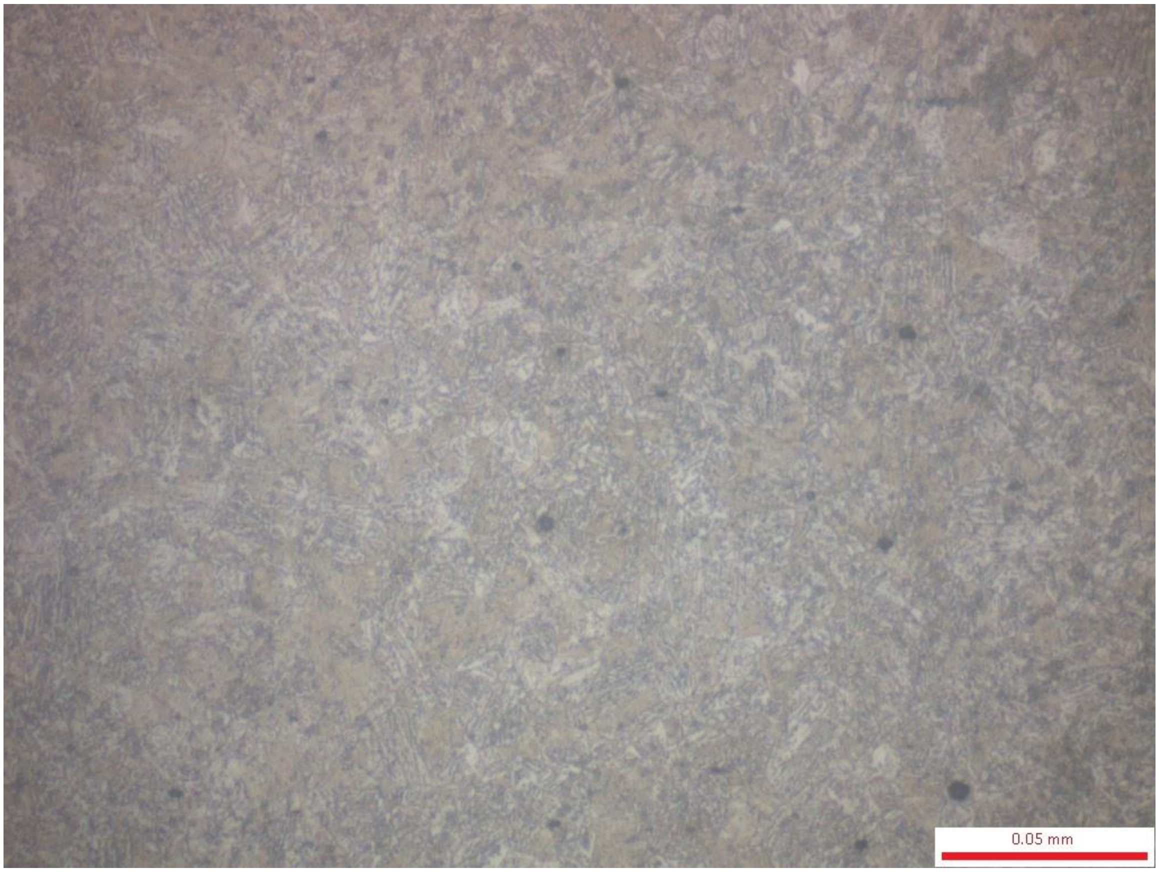

Figure 4. 41: Optical microscopy image at 0.58 mm from the gear's surface at the hub region.

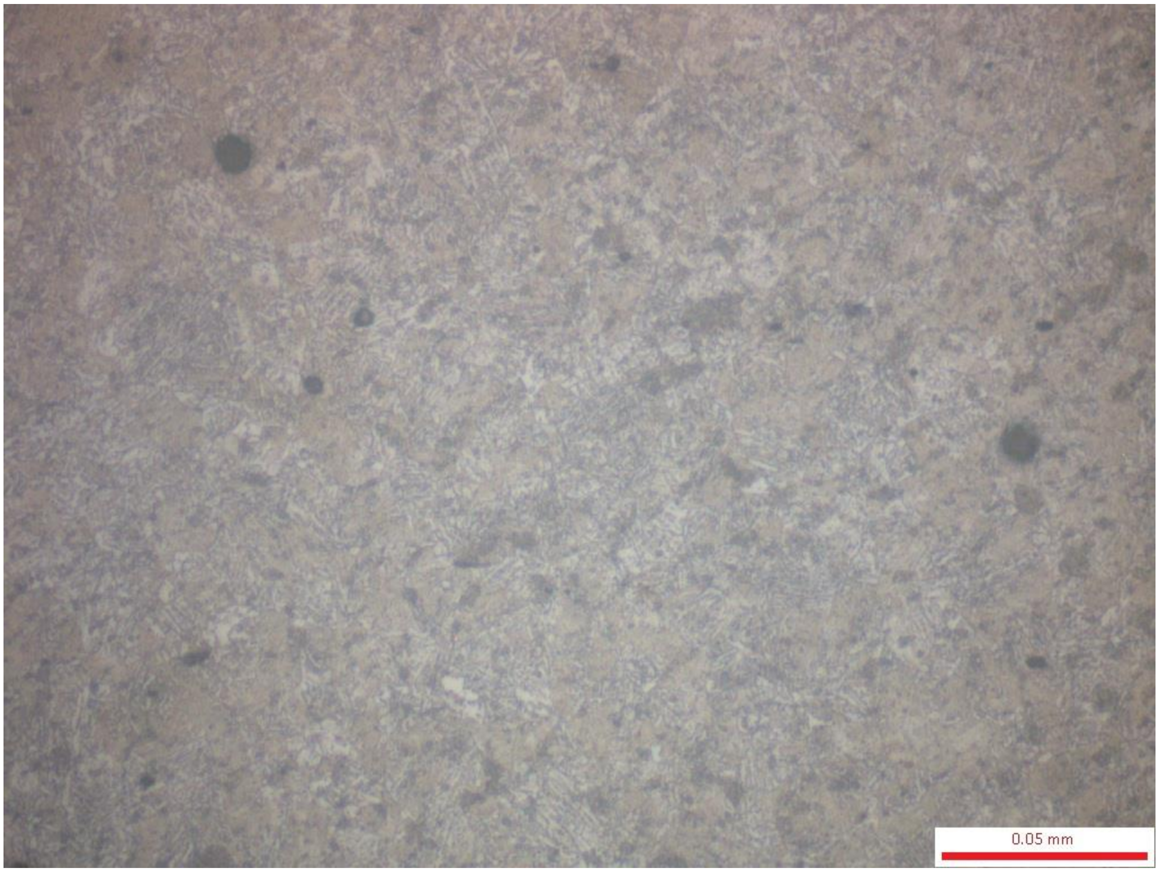

Figure 4. 42: Optical microscopy image at 0.75 mm from the gear's surface at the hub region.

In Figure 4. 38 and Figure 4. 39, the microstructures that are seen are composed of mostly martensite, with negligible presence of residual austenite. Again, as seen before for the tooth region, there could be some austenite in the images that is not visible at this magnification but that could become visible at higher magnifications. There could also be some austenite that transformed to martensite during the preparation of the sample. However, both of these facts cannot be known for sure and may not apply to this situation. In Figure 4. 38, no bainitic structure seem to be present. In Figure 4. 39, on the other hand, the structures included in the yellow circle, present features that have a feathery appearance. In fact, they do not have an elongated and pointy appearance, but rather a bulkier one, with the edges also appearing more rounded. This structure could be identified as bainite. It must be noted, however, that these bainitic regions are minimal when considering the entire Figure 4. 39 and so, as seen for the surface, also at 0.23 mm from the surface the microstructure is composed of mainly martensitic phase. The presence of mostly martensitic phase is predicted also from the simulation tool, that at these locations finds that the microstructure is made up of mostly martensite with decreasing traces of residual austenite. Therefore, in these locations, apart for the residual austenite, of which traces are predicted by the simulation tool and that are not visible in the images, the general microstructure composition seems to have been correctly predicted by the simulation tool.

Considering the images: Figure 4. 40, Figure 4. 41 and Figure 4. 42, that were taken at depths of 0.4mm, 0.58mm and 0.75mm respectively, very similar observations can be made in these micrography images. In all three images, in fact, the bainite phase starts appearing in considerable amounts. The bainite, as explained earlier, has an appearance similar to that shown inside the yellow circle in Figure 4. 21, where more bulkier and feathery looking features can be recognized. In these figures, the amount of bainite increases when looking at the images taken at greater distances from the surface. The increase in bainite in the images at larger depth, is of course coupled with a decrease in the brownish areas that represent the martensitic structure. Overall, at these locations, the phases that are found when looking at the microstructure are mostly bainitic and martensitic, where the amount of martensite is greater in the images taken closer to the surface and the amount of bainite is greater in the images taken further away from the surface. The simulation tool, at the location of 0.40mm from the surface, predicts that no amount of bainite is found. This is a very similar situation as that discussed previously when considering the results at the gear geometry, in fact, the amount of bainite starts increasing immediately after the 0.40 mm depth. Therefore, also in this case, the absence of bainite at 0.40mm from the surface in the simulation could be due to a mesh refinement issue. For the situation at 0.58mm and 0.75mm from the surface, the simulation tool predicts the presence of bainite and its increase as a function of depth.

Overall, the simulation tool seems to reasonably predict the trend of the different steel phases as a function of depth. The main differences between what is predicted with the simulation tool, and what is observed in the experimental microstructure images, are regarding the retained austenite at, and immediately below, the surface, and the bainite percentage at the depth of 0.4mm. The first difference could be due to the magnification of the image that does not allow the vision of the retained austenite zones or perhaps also due to the transformation that could have happened from austenite to martensite during the sample preparation. The second difference could be due to the mesh found at the surface. In fact, perhaps a finer mesh at the surface could show a smoother bainite variation with depth, and could also predict the presence of bainite at that depth. The simulation tool, therefore, from a qualitative point of view seems to correctly grasp and predict the trends of the different steel phases as a function of depth, showing accordance with what is seen from the microstructure images. As explained above when considering the images taken in the tooth region, it is very difficult to perform a quantitative analysis starting from the images shown above, where the bainitic and martensitic features can bare a significant resemblance, therefore only a qualitative analysis of the images, as done above, is provided.

Now that the microstructure has been described, in the following paragraph the simulated microhardness for a location in the gear hub will be presented. The simulated microhardness, as done also previously for the tooth geometry, will then be compared to the experimental results obtained in the gear hub region.

4.1.2.2.2 Microhardness simulation results and comparison with experimental microhardness measurements at gear hub

As explained earlier, the microstructure has a great influence on the microhardness values. In fact, as seen earlier in the images: Figure 4. 24, Figure 4. 25, and Figure 4. 26, when considering the gear tooth, the different steel phases have different hardness values. In particular, the martensitic phase displays the greatest hardness values. In all steel phases, the hardness is much higher at the surface with respect to regions more distant from it, due to the presence of carbon atoms at the surface because of the carburizing process.

As explained in the methodology chapter, the hardness after quenching is evaluated by applying equation 71. The overall hardness found after quenching for the gear hub region is shown in Figure 4. 43.

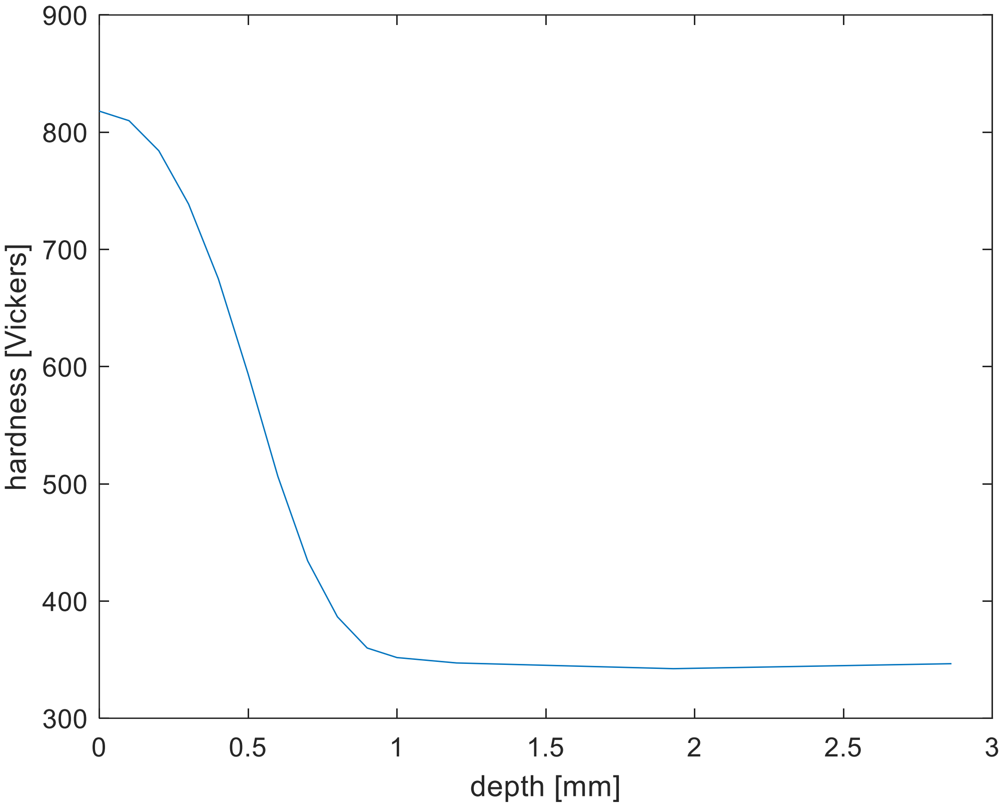

Figure 4. 43: Overall hardness found after quenching close to gear's surface at the hub region.

As seen also in Figure 4. 26 for the as-quenched hardness close to the gear's tooth surface, the as-quenched hardness predicted for the gear hub, that is shown in Figure 4. 43, is highest at the surface and then decreases whilst moving away from the surface. The hardness, after a depth of about 1mm stops varying and remains quite constant. This trend was observed also in the gear tooth region. As explained before, this trend is due to the fact that at around 1 mm, both the factors that greatly affect the microhardness stop to variate in a significant manner. In fact, the carbon content at the gear hub, that is not an edge region and so still has a carbon concentration as that shown in Figure 4. 6, starting from the high value found close to the surface, reaches the value of the alloying composition that was present in the starting steel at about 1 mm depth, after which it stops varying. At the same time, also the microstructure, as shown in Figure 4. 37, stops to vary in a significant way after about 1 mm of depth. For this reason, the hardness after about 1 mm of depth remains quite constant.

In Figure 4. 44, on the other hand, the hardness after tempering is found. A graph comparing the hardness before and after tempering is then shown in Figure 4. 45.

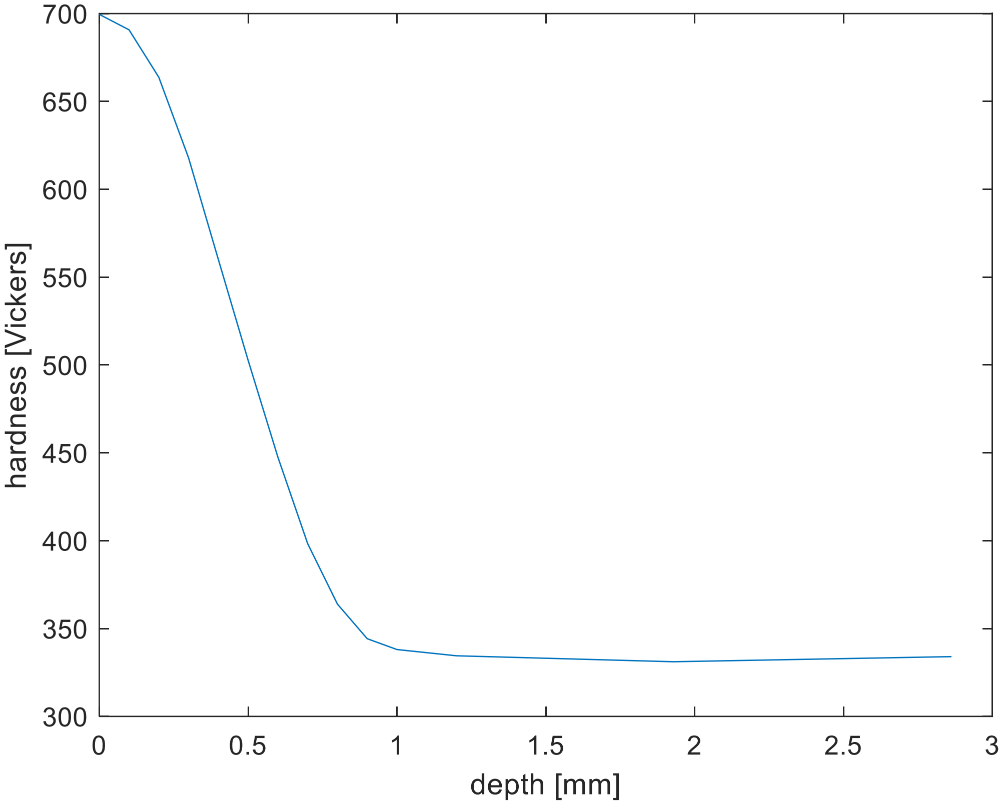

Figure 4. 44: Overall hardness found in the gear component after tempering in the hub region.

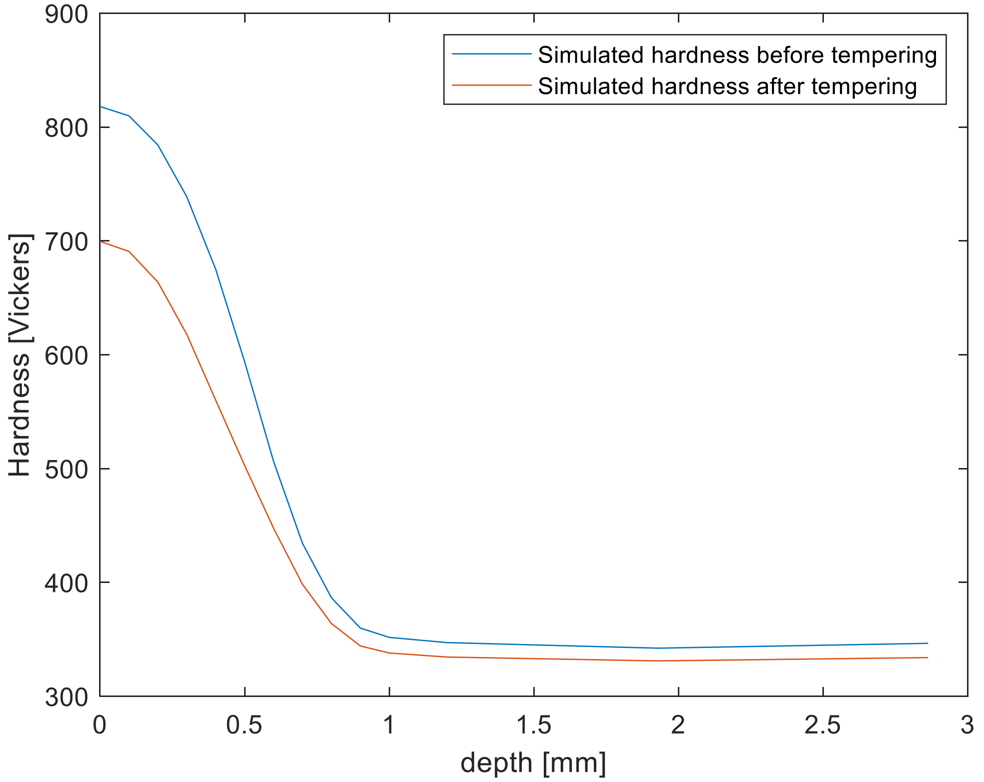

Figure 4. 45: Comparison between hardness found in the gear component at the hub region before and after tempering.

From Figure 4. 45, as it was previously observed when considering the gear geometry, it can be seen that the hardness found after tempering is lower with respect to the as-quenched one. Furthermore, it is possible to notice again that the greatest variation in hardness after tempering is found at the surface. This happens for the same reason as explained earlier when considering the gear's tooth region. In fact, the assumption is made, as explained in the methodology chapter, that the martensite hardness is the only one affected by the tempering. Therefore, only the martensite hardness will be decreased during tempering. For this reason, regions where a greater amount of martensite is present, like the surface, will show a greater difference in hardness before and after tempering, as they present more martensite for which the hardness is reduced. In fact, the difference between the hardness before and after tempering, after about 1mm of depth, so further away from the surface, is much lower due to the lower percentage of martensite that is found.

What can be also seen when looking at the hardness values found in Figure 4. 45, is that the hardness values found far from the surface, so after about 1mm of depth, are lower with respect to those that were found at the same depth for the gear tooth. This is because at greater depths, the hub region shows a greater amount of bainite with respect to that that was found in the gear tooth region, and, as discussed earlier, the hardness of bainite is lower with respect to that of martensite.

The experimental microhardness measurements obtained in the gear hub region of the real component by some operators at the well-known OEM are displayed in Figure 4. 46 as a function of the depth at which they were measured.

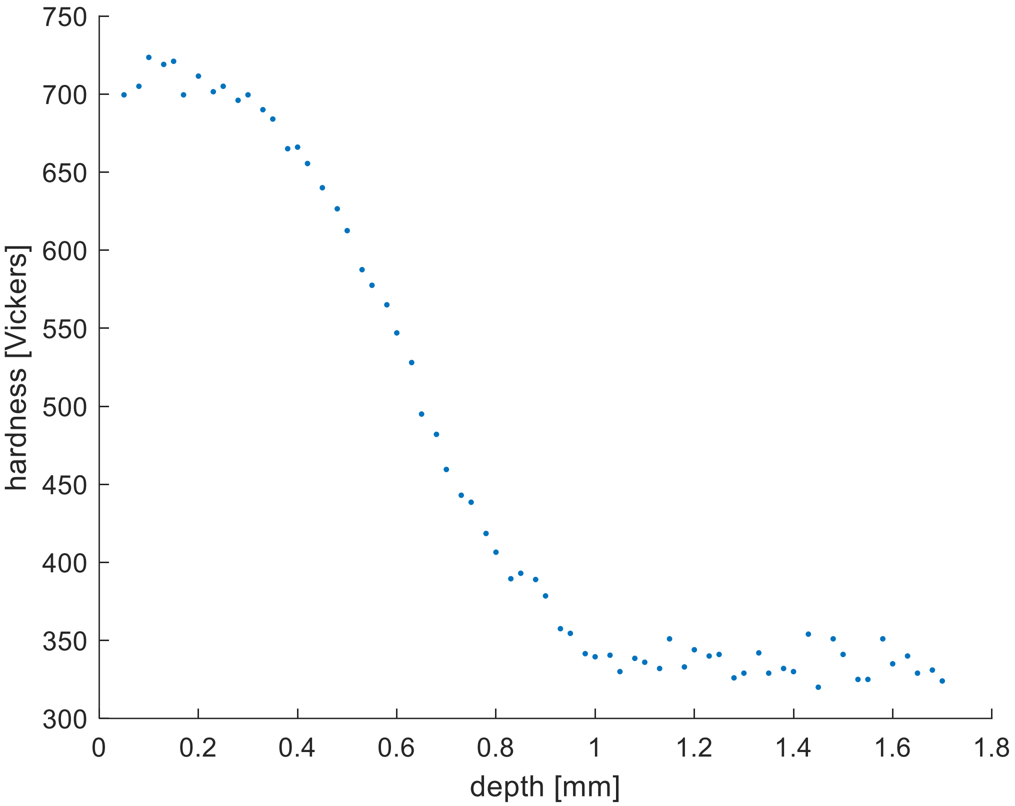

Figure 4. 46: Experimental microhardness measurements performed on gear component at the hub region after tempering.

What can be seen when looking at these values, is that also these experimental values present lower microhardness values going deeper inside the component with respect to those found at the same depth in the gear's tooth region, that are shown in Figure 4. 31. In fact, whilst the values of hardness that are found deeper inside the gear geometry are of around 350 Vickers in the tooth region, in the hub region they vary around the value of about 330 Vickers.

As done previously for the gear tooth, in order to better understand the behavior of these experimental points, a graph interpolating them is included. This graph is shown in Figure 4. 47.

Finally, in Figure 4. 48 a comparison between the experimental microhardness measurements found on the real component at the gear hub region, and the simulated microhardness results after tempering in the same region, is shown in Figure 4. 48.

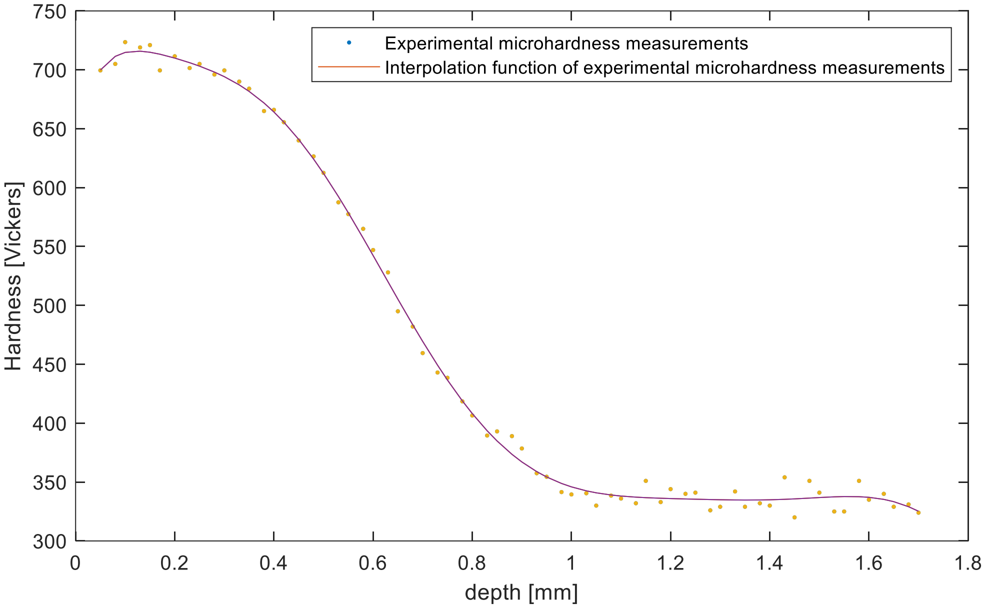

Figure 4. 47: Interpolation function of experimental microhardness measurements performed on gear component at the hub region after tempering.

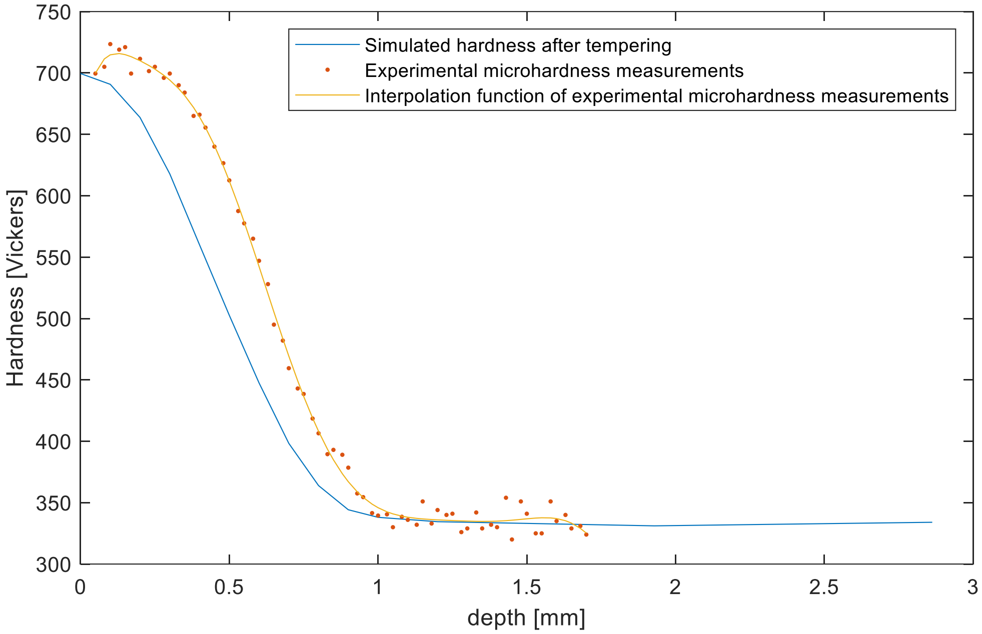

Figure 4. 48: Comparison between simulated and experimental hardness results at the surface of the gear in the hub region.

What can be seen from Figure 4. 48, is that again, as seen for the tooth region, the microhardness profile found with the simulation is in reasonably good agreement with the one that is obtained experimentally. It is possible to see that the simulated microhardness values at the surface and at the core of the gear hub, are very similar to those obtained experimentally. In the depth interval going from the surface and towards the 1mm depth, the two microhardness profiles show some variations. The simulated microhardness seems to slightly underestimate the experimental microhardness values.

Overall, considering both results at the tooth and at the core, the simulation tool seems to be able to correctly identify and predict the trend of the different microstructures present. Furthermore, the simulation tool is able to correctly identify the microhardness trend as a function of depth for both of the gear's regions.

In the following paragraph, the carburizing and quenching-tempering simulations for the transmission shaft component, introduced in the methodology chapter, will be introduced and discussed. Furthermore, a comparison between the experimentally obtained microhardness measurements and microscopy images, and the simulation results, will also be carried out.

4.2 Transmission Shaft Geometry

In order to present the simulation results obtained when considering the transmission shaft component, in this sub-chapter, two paragraphs are present: one dealing with the carburizing study results, and the other one dealing with the quenching-tempering results and comparison with experimental measurements.

4.2.1 Transmission Shaft Carburizing Simulation

This component, as also the gear component, is carburized by vacuum carburizing using Acetylene gas as carbon carrier. Therefore, again the methodology described in the vacuum carburizing section of the methodology chapter is used to evaluate the carbon diffusivity, mass transfer coefficient, and carbon potential. The carbon diffusivity values, to be inserted in ABAQUS as inputs, are evaluated with equation 5 and using the alloying composition reported in Table 3. 7 for 27MnCr5. The mass transfer coefficient, since acetylene is again used, is evaluated with equations 12 and 13, as explained in the methodology chapter and also done for the gear component. Again, the values of the carburizing pressure and temperature to be used in equations 12 and 13, are the same as those used in the real vacuum carburizing process with which the component, on which the experimental test were conducted, was treated. These values, however, cannot be reported because considered confidential information of the OEM. What can be said, however, is that, whilst the carburizing temperature used for the treatment of this component is higher with respect to that used for the treatment of the gear component analyzed previously, the carburizing pressure used for the two components is the same. For what regards the carbon potential, as done also previously for the gear component, since the carburizing temperature is not exactly 950°C, for which the carbon potential of 1.39 was found in [5], the value used in the simulation is adjusted to reflect the actual carburizing temperature of the transmission shaft component, by considering the variation between the values of the carbon potential at 920°C and 950°C.

As mentioned previously in the methodology chapter, the surface of the component that is exposed to the vacuum carburizing treatment is the external surface of the hollow cylinder.

In the following paragraph, the mesh utilized for the carburizing study will be discussed.

4.2.1.1 Description of mesh used in transmission shaft geometry

For the carburizing simulation, the mesh utilized is displayed in Figure 4. 49.

This mesh was designed following a similar reasoning to that described above for the gear component. In fact, this kind of mesh was used because, since the carburizing process is localized at the components surface and affects only a very small portion in depth of the component, by using a mesh that is very refined only at 2 mm from the surface and leaving the rest of the component with a coarse mesh, ensures that the results will be accurate because of the refined mesh at the surface and, at the same time, not to time-consuming and computational expensive to obtain, thanks to the lower amount of elements. A close-up image of the refined mesh at the surface is shown in Figure 4. 50.

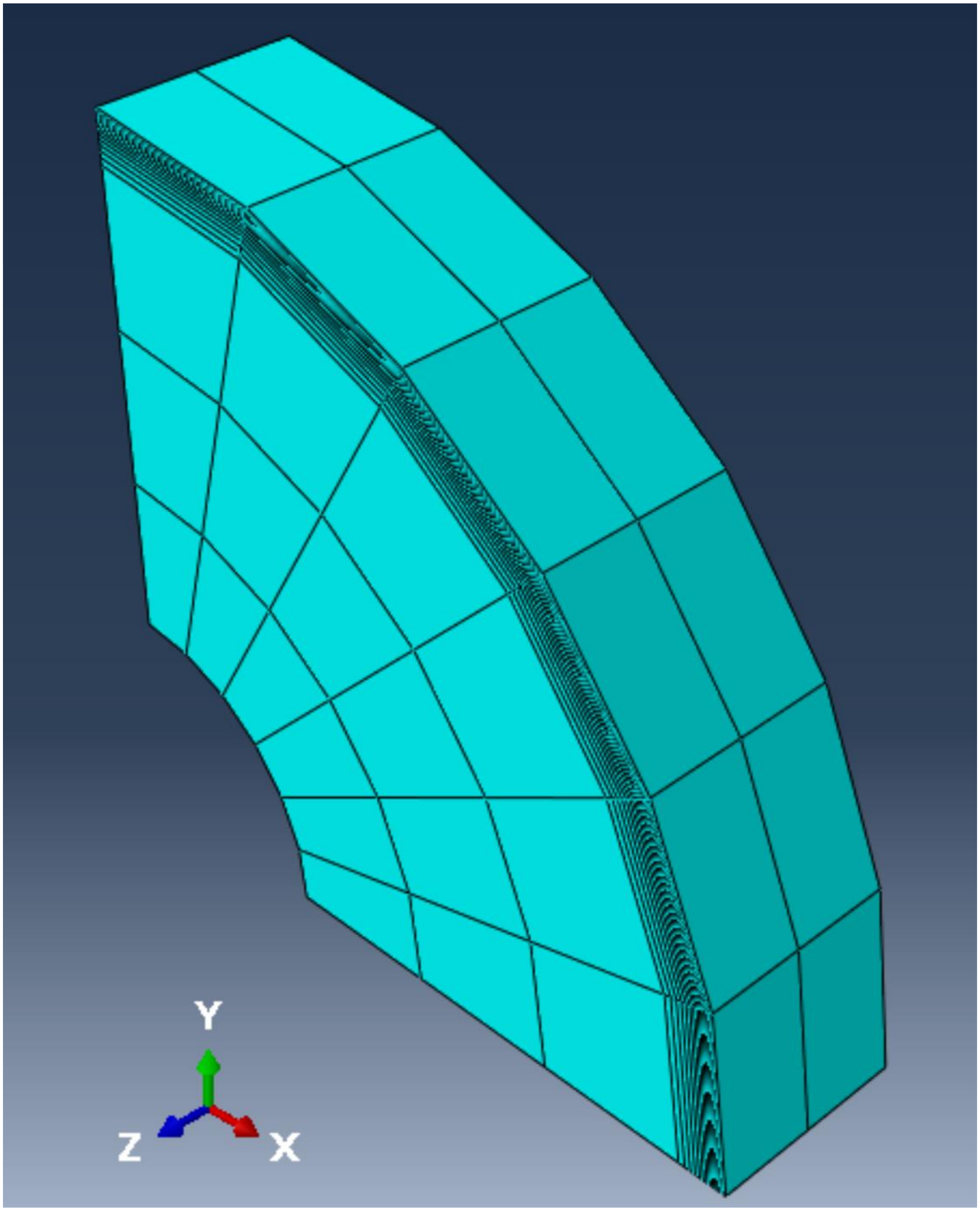

Figure 4. 49: Mesh utilized in transmission shaft component.

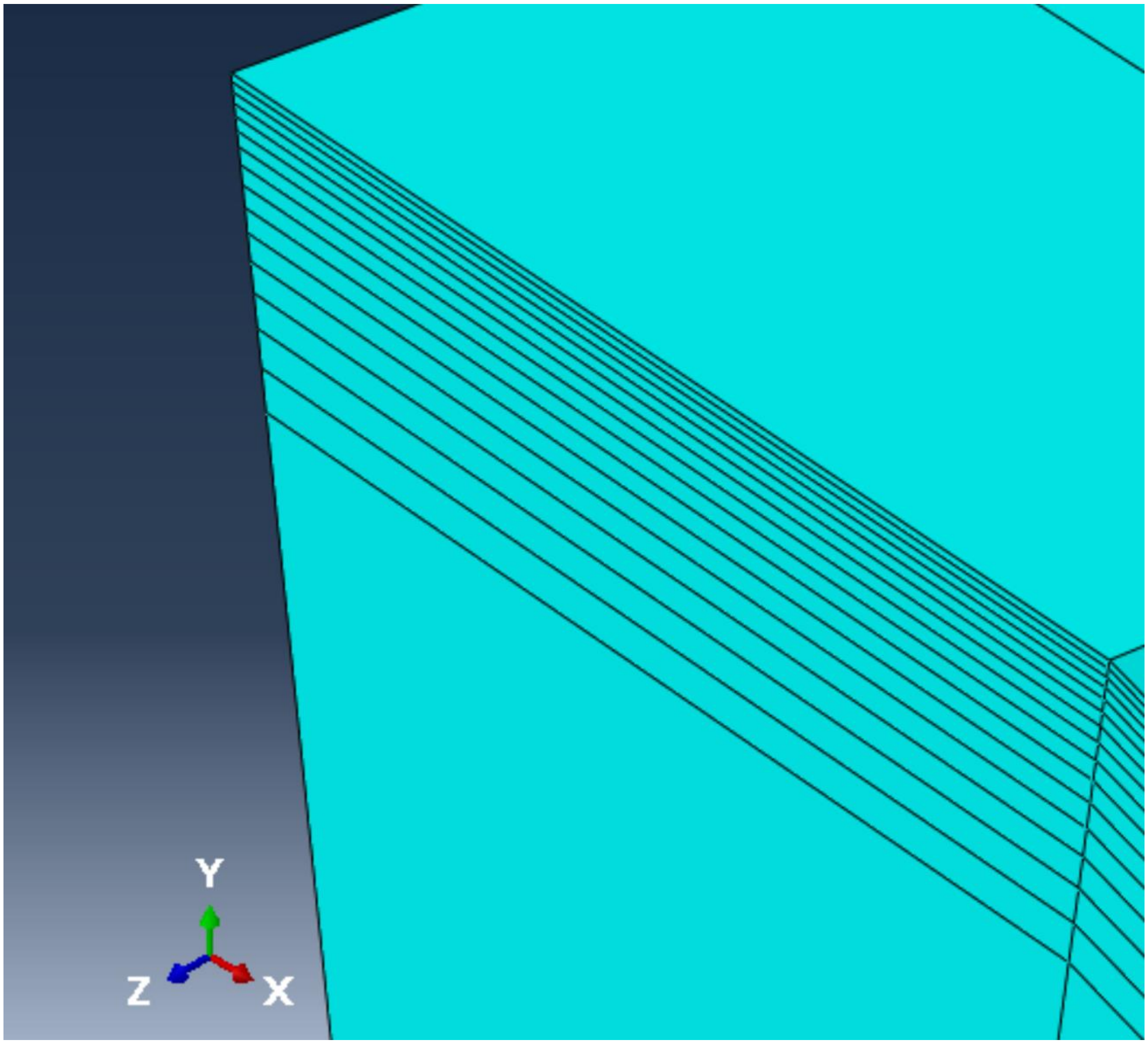

Figure 4. 50: Mesh refinement at the transmission shaft surface.

As for the gear mesh, also the mesh of the transmission shaft component is made up of “tetra” elements.

Now that the mesh used in the carburization process, the carburization study outputs will be displayed.

4.2.1.2 Carbon content simulated in transmission shaft geometry

The output of the carburizing study in terms of carbon concentration distribution is shown in Figure 4. 51

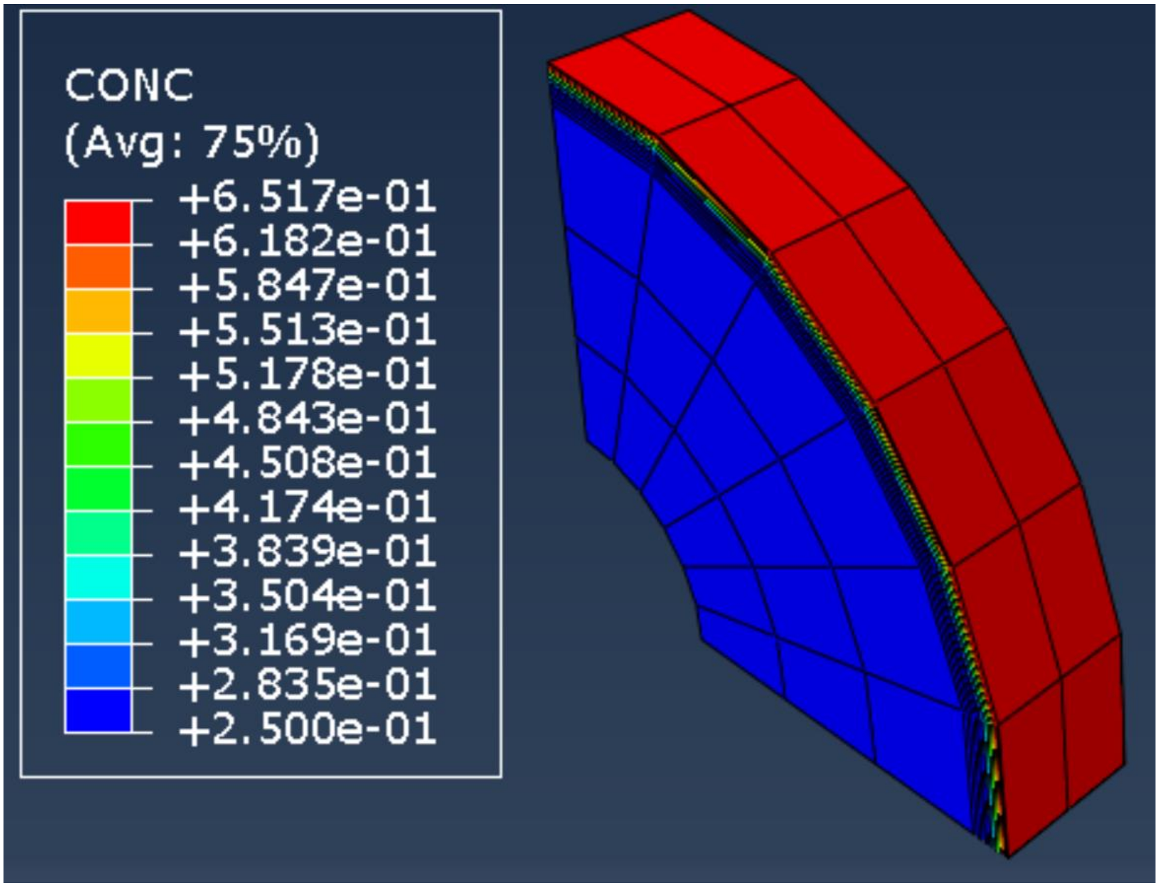

Figure 4. 51: Carbon distribution within transmission shaft component.

What can be seen is that the carbon concentration, as expected, has the highest value at the component's surface. The carbon concentration than decreases towards the interior of the component and reaches the value of the carbon content of the original steel in the component's core. In this case, the starting carbon concentration was of 0.25%.

A zoom-in of Figure 4. 51, that better shows the situation at the component's surface, is shown in Figure 4. 52.

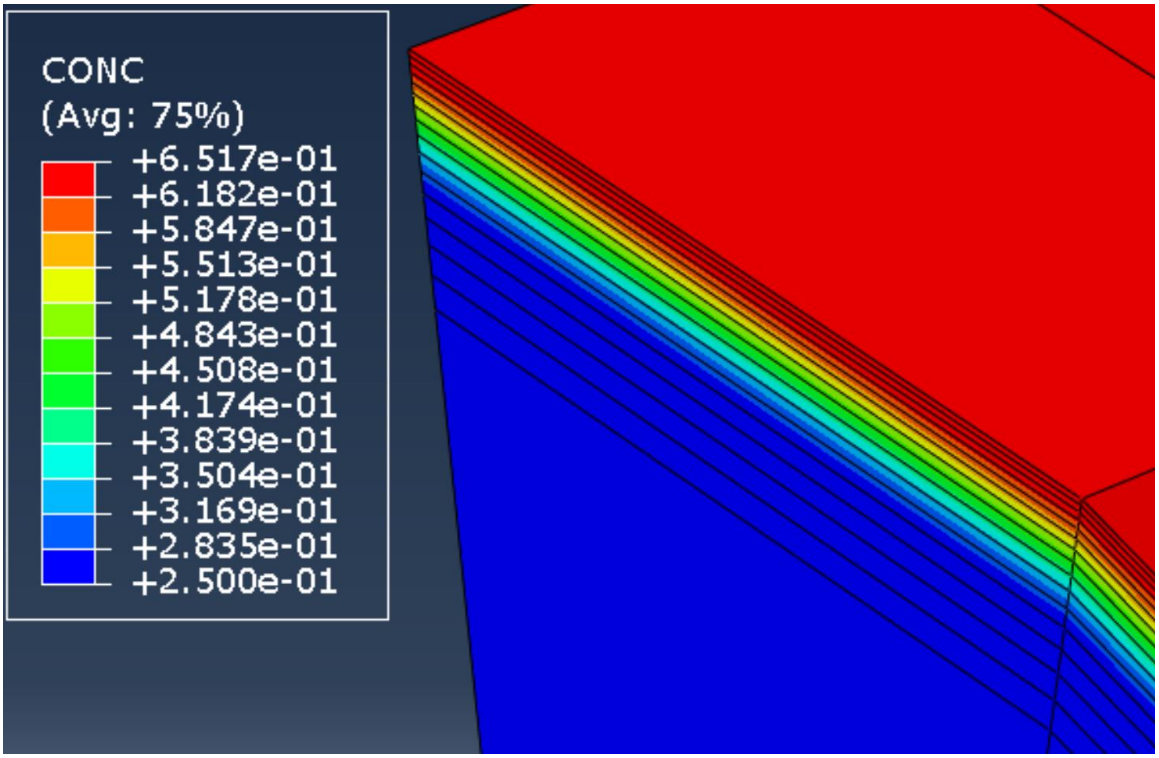

Figure 4. 52: Carbon concentration at the transmission shaft external surface.

What can be seen in Figure 4. 52, is that the mesh refinement at the surface covers the depth where the carbon concentration varies. This means that the coarser mesh should not have influence on the accuracy of the results. It is possible to see, as also seen previously for the gear component, that the carbon variation affects only a very small portion of the depth of the component. To better see this, a plot showing the variation of carbon along the component depth is shown in Figure 4. 53.

From Figure 4. 53 it is possible to see that at the surface the carbon concentration is a little above 0.65%. From that point, the concentration quickly decreases and reaches a value of 0.25%.

As also done previously for the gear geometry, in Figure 4. 54, the carbon concentration variation during the vacuum carburizing operation is shown for three points at three different depths from the surface. The location of the three different points: A, B and C, is shown in Figure 4. 55. Point A is right at the surface, point B is at the 0.4 mm from the surface and finally point C is at a depth of 0.96 mm. These three points were chosen in order to show different trends in carbon content over the carburization duration. Figure 4. 54 shows the same behavior that was previously discussed for the gear component when looking at Figure 4. 7. Therefore, the explanation behind the behavior of the trends for point A, B, and C, will not be discussed again.

Again, as for the gear component, the duration of each pulse and diffusion phase cannot be disclosed. However, what can be seen when comparing Figure 4. 54, to Figure 4. 7 that was obtained for the gear component, is that different values of the carbon potential, that is the carbon content that the surface reaches during each pulse phase, are used for the two components. This reflects the different carburizing temperatures used in the two processes for the two components. Furthermore, comparing Figure 4. 54 and Figure 4. 7, it is possible to see that the two processes used for the shaft and gear geometries are different also in the duration and number of the different pulse and diffusion phases. The number and duration of the different pulse and diffusion phases are usually designed to obtain the wanted final properties in the component.

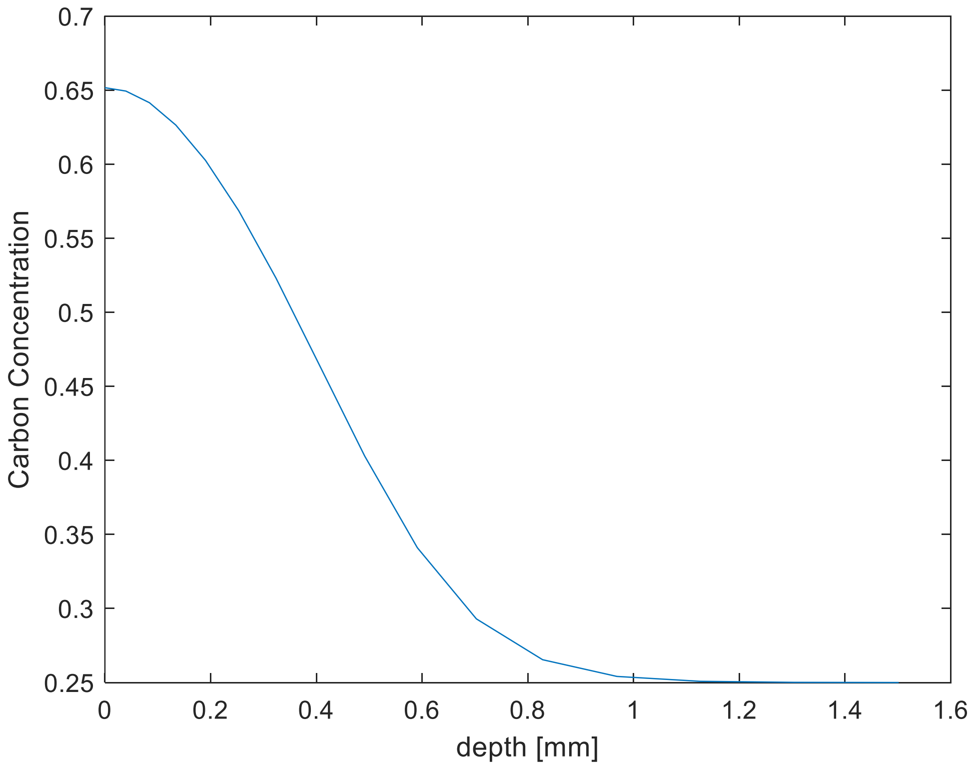

Figure 4. 53: Carbon profile as a function of depth at transmission shaft component surface

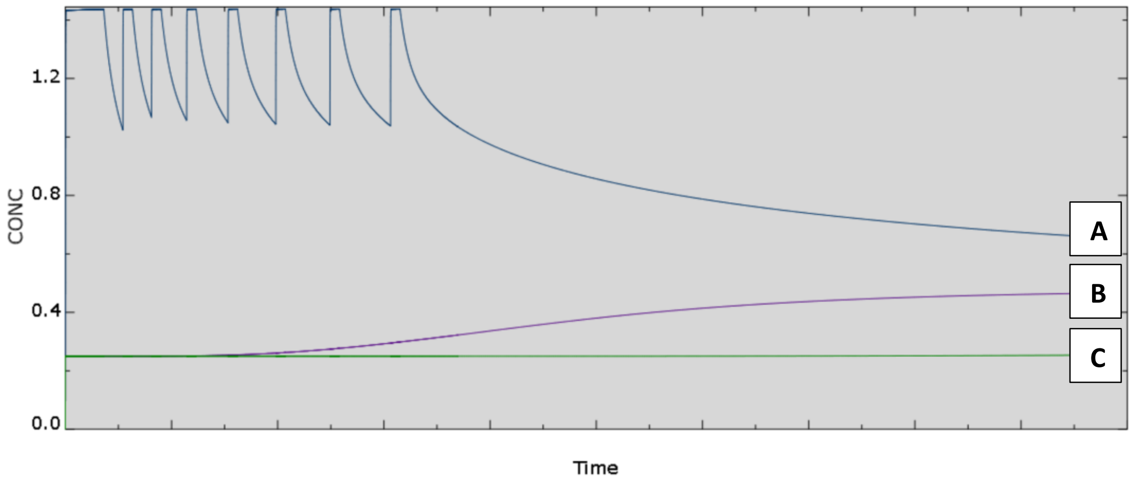

Figure 4. 54: Carbon variation over time during vacuum carburizing, for three different locations at, and close to the surface, of the transmission shaft component.

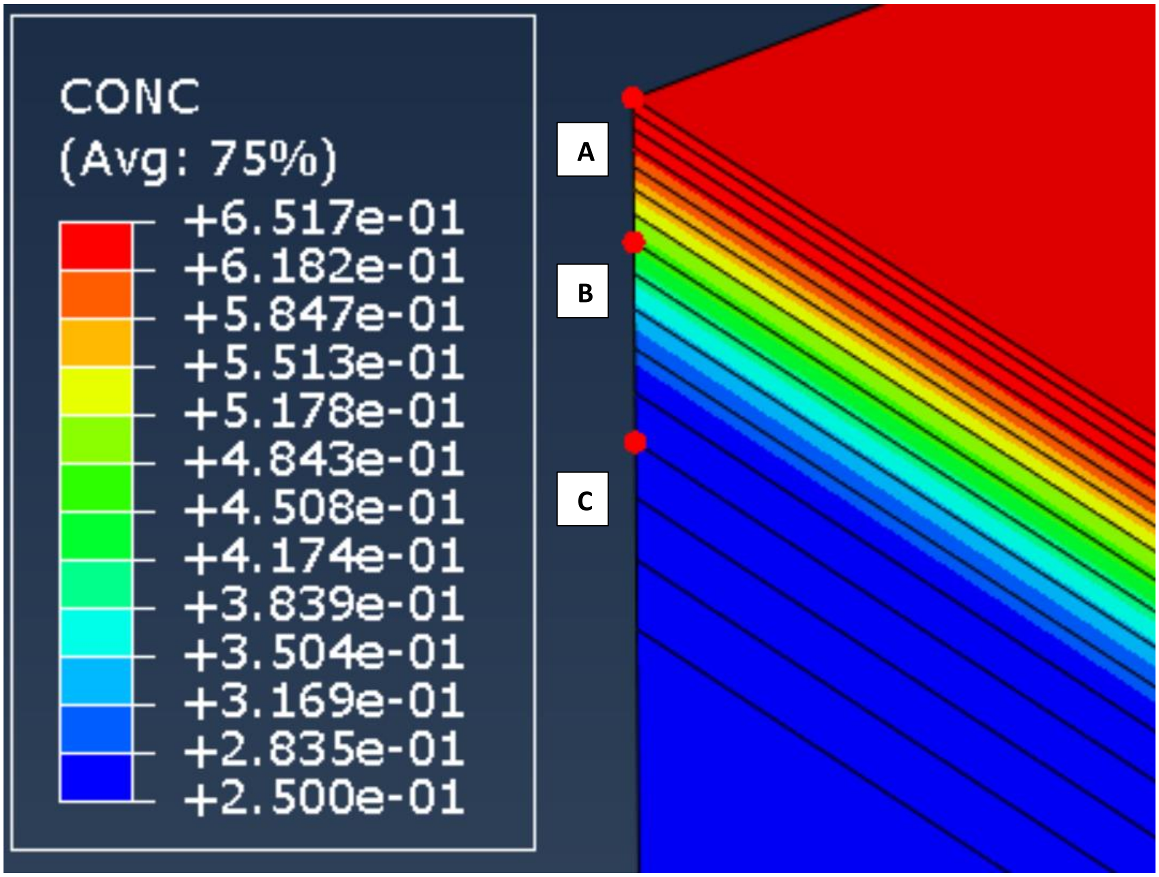

Figure 4. 55: Location of the three locations for which the carbon content is plotted against the carburizing time in Figure 4. 54

4.2.1.3 Austenite grain size found at the end of transmission shaft component carburization

The austenite grain size, expressed in ASTM standard, that is found at the end of the carburization process for the transmission shaft component, is reported in Figure 4. 56.

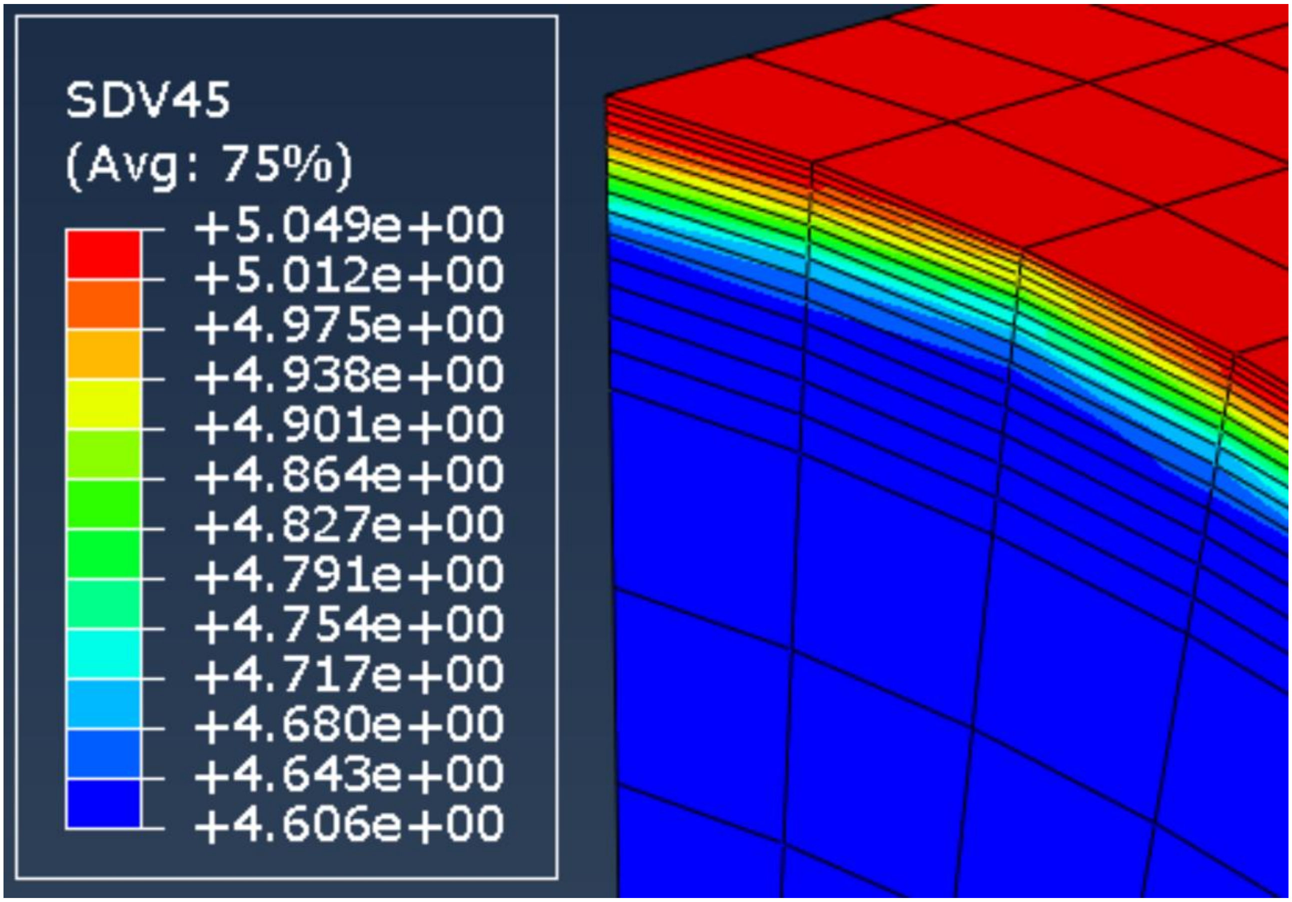

Figure 4. 56: ASTM Austenite grain size at the end of the carburization process at the surface of the transmission shaft.

In Figure 4. 56, as seen earlier for the gear component, the variable "SDV45" is the user-defined variable that is used to describe the austenite grain size expressed in the ASTM standard. Again, it is possible to see that this value is greater at the surface and then tends to decrease in value when going deeper within the component. This happens for the same reason as previously explained for the gear component. In fact, due to the different, higher, carbon concentration at the surface, at that location the austenite grains found are smaller in dimension with respect to those found in the interior of the component, where the carbon concentration is lower. Smaller austenite grain dimensions indicate greater values of the

ASTM austenite grain size value. In this case, a final ASTM austenite grain size of just above five is found at the surface. This value is lower with respect to that that was found at the surface of the gear component. This reflects the fact that the transmission shaft component was carburized for a shorter amount of time and at a higher temperature with respect to the gear component. As seen in equation 14, the combination of these two factors determines a greater austenite grain size, and so a lower value of the ASTM standard number.

In the following section, the results from the quenching and tempering study will be displayed for the transmission shaft component.

4.2.2 Quenching and tempering simulation and comparison with experimental findings for transmission shaft geometry

In the quenching and tempering simulation of the gear shaft geometry, a different mesh with respect to that shown in Figure 4. 49 and used for the carburization study, is utilized. In fact, unlike what seen for the carburization operation where only the component surface is heavily affected by the process, in quenching, the quick drop in temperature and the consequent phase transformations affects the entire component. For this reason, the mesh that is adopted still displays a mesh refinement at the surface, as seen for that used for the carburizing study, however, in this case, exhibits a fine mesh also at the component's core. The same mesh refinement at the surface used in the carburizing simulation is kept also for the quenching-tempering one. This is done in order to correctly convey from the carburization study the information regarding the carbon variation at the surface, that has a huge effect on both the component microstructure and microhardness. The mesh used is shown in Figure 4. 57. A close up look to the mesh at the surface is shown in Figure 4. 58. It is possible to see that the mesh refinement at the surface is the same as that seen for the carburization study.

The transmission shaft component is quenched using nitrogen as quenching medium, instead of the helium that was used for the gear geometry. As seen for the gear component, also for the transmission shaft geometry the interaction between the component and the quenching fluid is simulated by using a surface film condition at the surface that is coming in contact with the fluid. This surface, as mentioned in the methodology chapter, is the external cylindrical surface. This interaction is again implemented with the use of the subroutine FILM, where the value of the nitrogen temperature and the value of the heat transfer coefficient, evaluated by looking at the tables in [16] and knowing the nitrogen pressure and velocity, are varied during the quenching procedure. The nitrogen temperature and pressure during the quenching operation were provided by the OEM owner of the component being treated. The nitrogen speed was instead taken from the catalogue of the equipment that was used to perform the quenching operation. These values are not reported as considered proprietary information of the OEM.

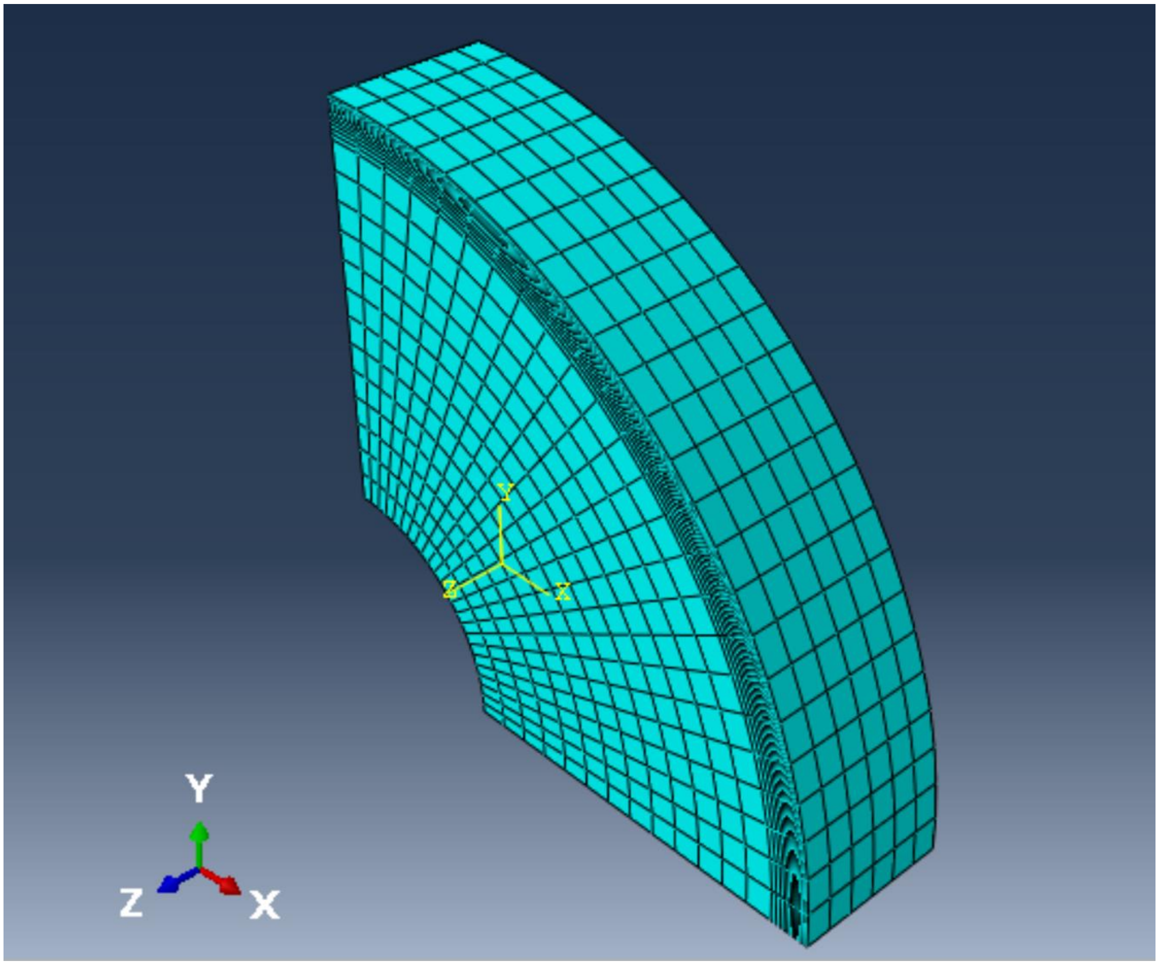

Figure 4. 57: Mesh used in quenching-tempering simulation of transmission shaft component.

As seen for the gear component, since only a small part of the component is simulated and not the entire one, different boundary conditions must be utilized in order to account for the presence of the rest of the object that is not simulated. These boundary conditions are applied to all surfaces displayed in red in Figure 3. 20, that are the surfaces where the real component would continue with respect to the simulated one. These boundary conditions are displayed as the blue and orange arrows in Figure 4. 59.

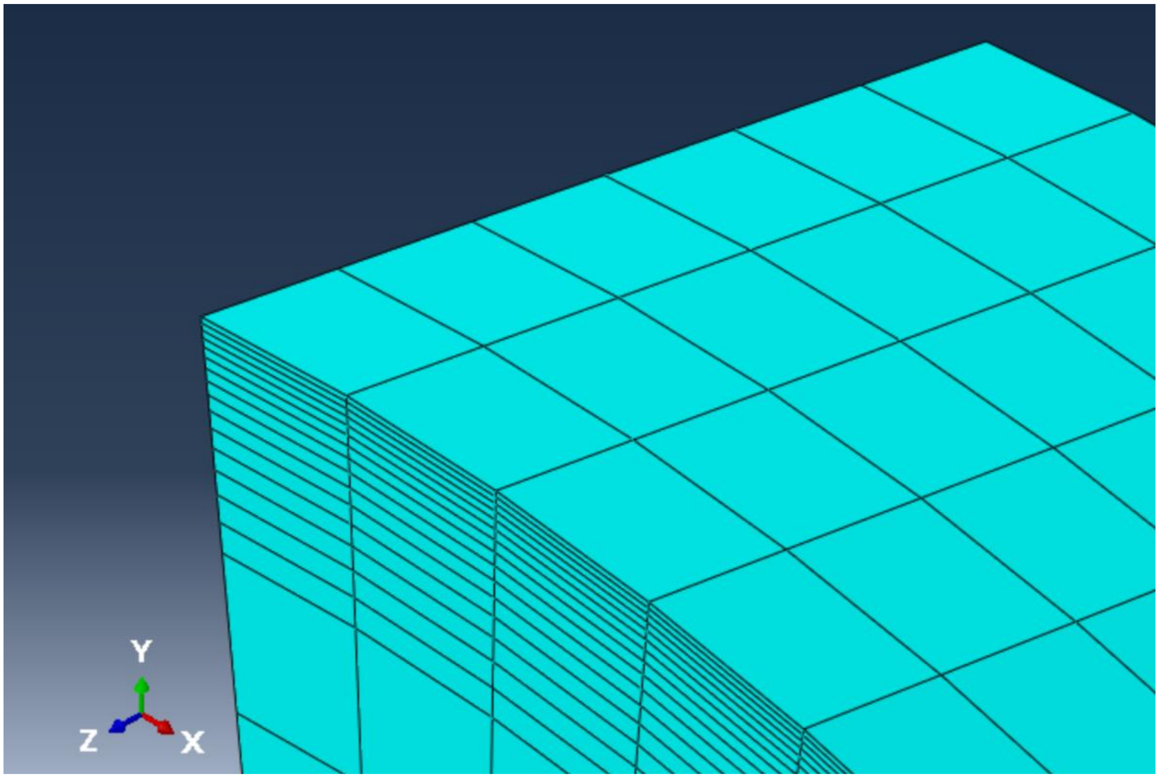

Figure 4. 58: Close-up look at mesh refinement at the surface of the transmission shaft.

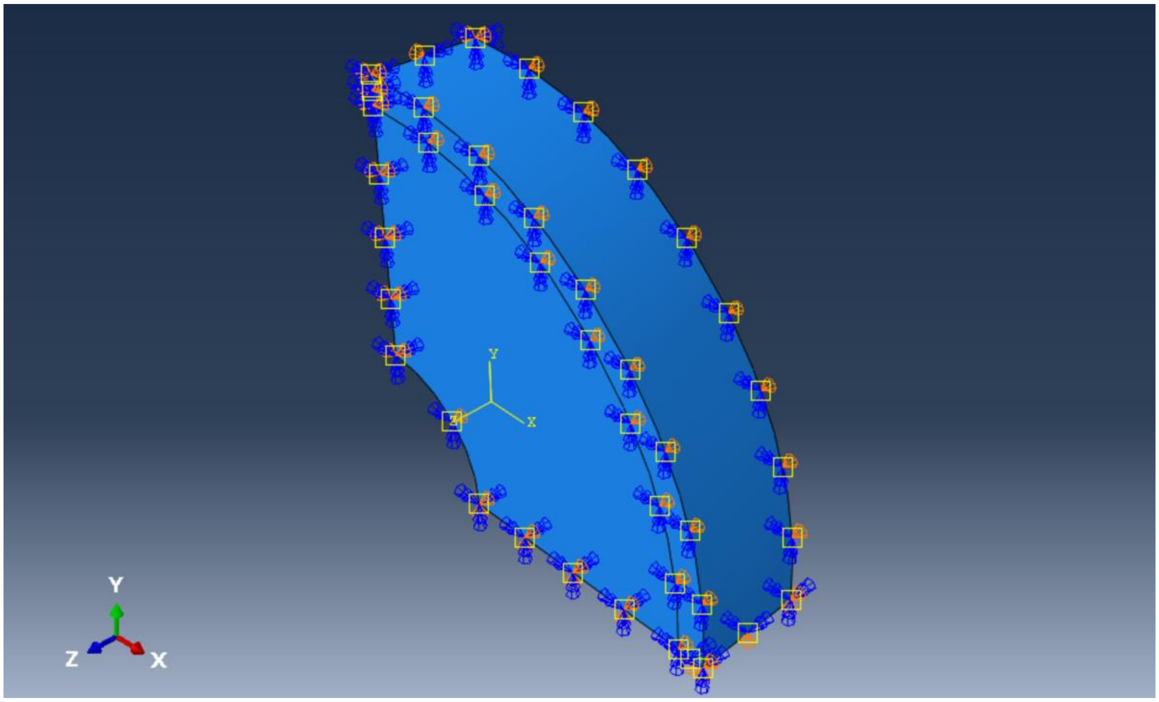

Figure 4. 59: Symmetry boundary conditions applied to the shaft component being simulated.

Now that the mesh and loads used in ABAQUS to simulate the quenching-tempering process have been reported, in the following paragraph, the simulation results in terms of steel microstructure will be displayed and compared qualitatively to experimentally obtained microscopy images.

4.2.2.1.1 Steel Microstructure found in transmission component and qualitative comparison with microstructure images

The steel microstructure, as seen for the gear component, was simulated in the simulation tool by using the Li et al. equations for the diffusive phase transformation and with the Koistinen-Marburger equation for the transformation from austenite to martensite. The application of these equations was implemented in the USDFLD subroutine.

Since the component that is simulated is a hollow cylinder, in this case, the microstructure composition found at one location at the external surface, should be the same as that found at another location always found at the surface of the shaft. In fact, no complex regions, as for example the tooth region found for the gear component, that had more surfaces exposed to the quenching fluid and so was subjected to a higher cooling rate, are present. Therefore, for the transmission shaft component, the simulated trends in microstructure and microhardness as a function of depth are the same at all external surface locations of the hollow cylinder that are simulated.

The percentage of martensite found at different locations within the component are shown in Figure 4. 60.

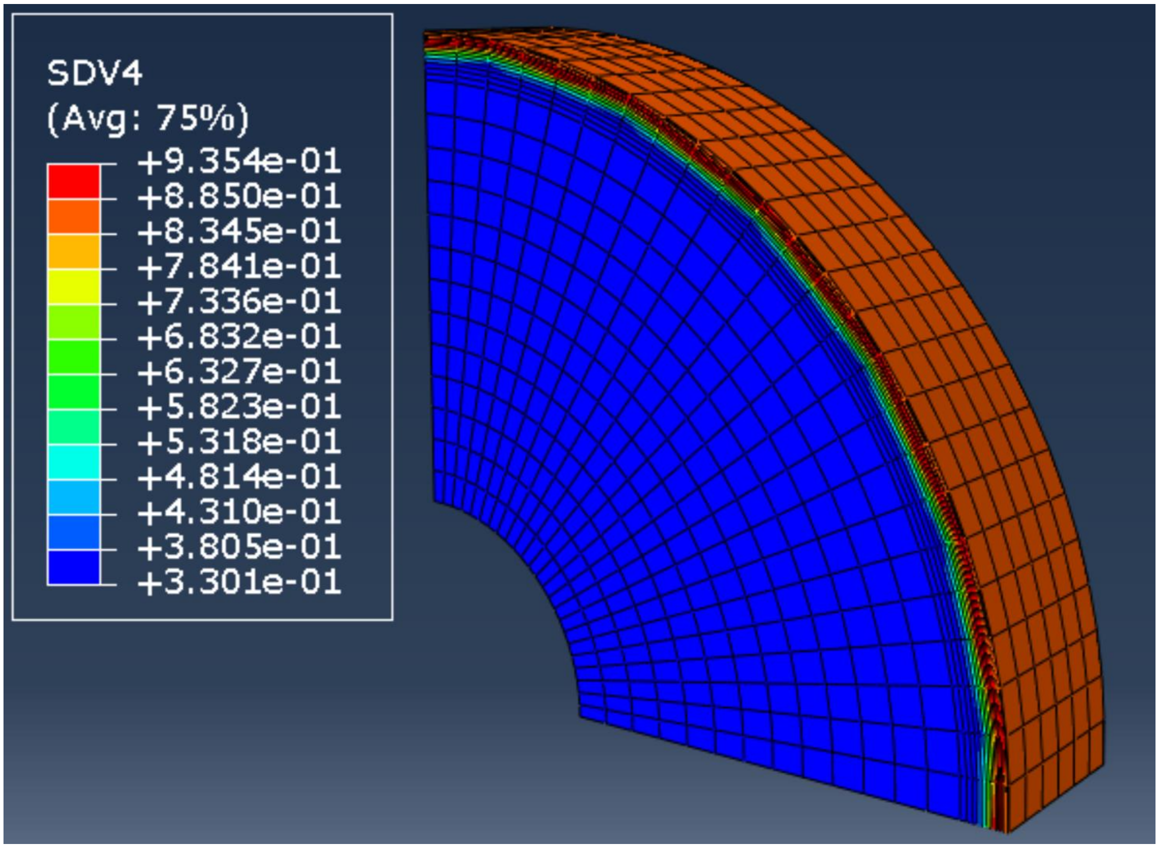

Figure 4. 60: Percentage of martensite found in the transmission shaft component after quenching.

What can be seen from Figure 4. 60, is that the highest amount of martensite is found close to the shaft's surface. The martensite percentage then decreases when going deeper within the component. In Figure 4. 61, that provides a closer look at the martensite concentration at the surface of the shaft, it can be seen that, as already seen in the tooth and hub regions of the gear geometry, the maximum amount of martensite is not found at the component's surface but rather a little below that. In fact, right at the surface, martensite is present, according to the simulation, at about 85%. The remaining 15% is therefore composed of retained austenite. The percentage of the retained austenite that is present at the component's surface, defined in the simulation as the user-defined variable SDV1, is shown in Figure 4. 62.

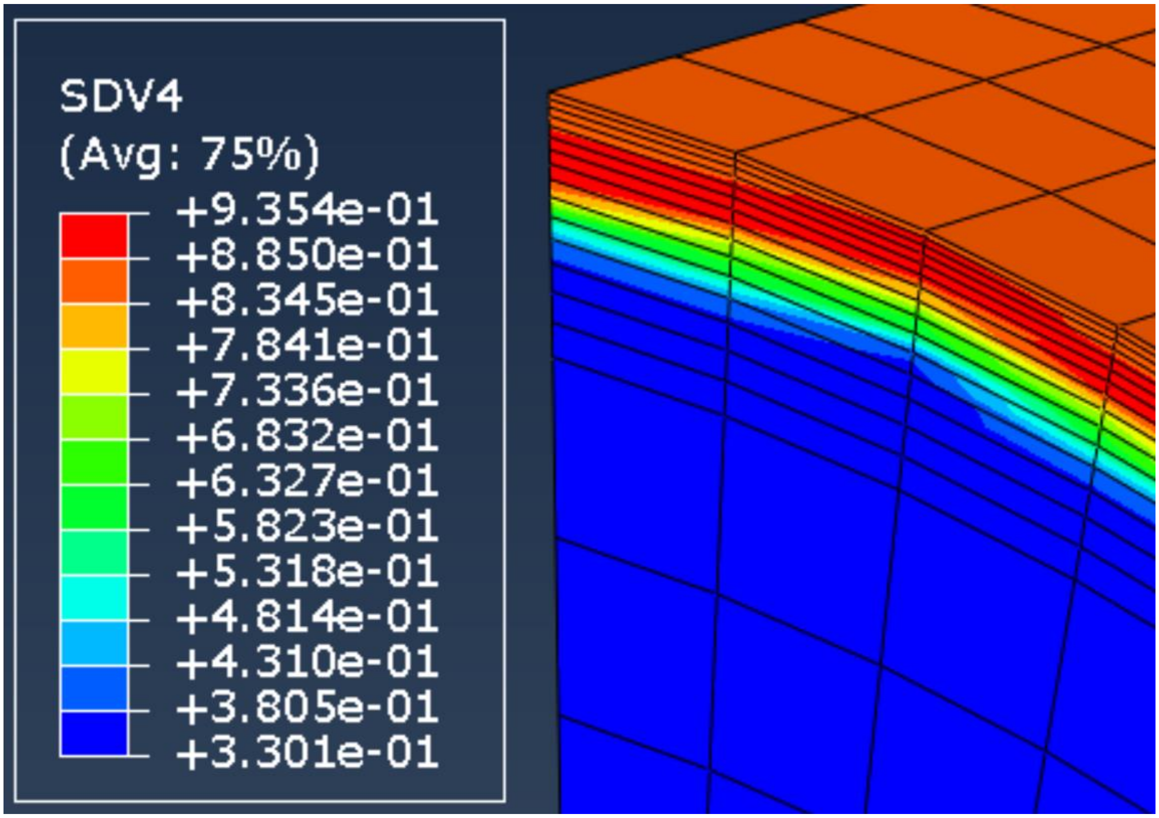

Figure 4. 61: Amount of martensite at transmission shaft's surface after quenching.

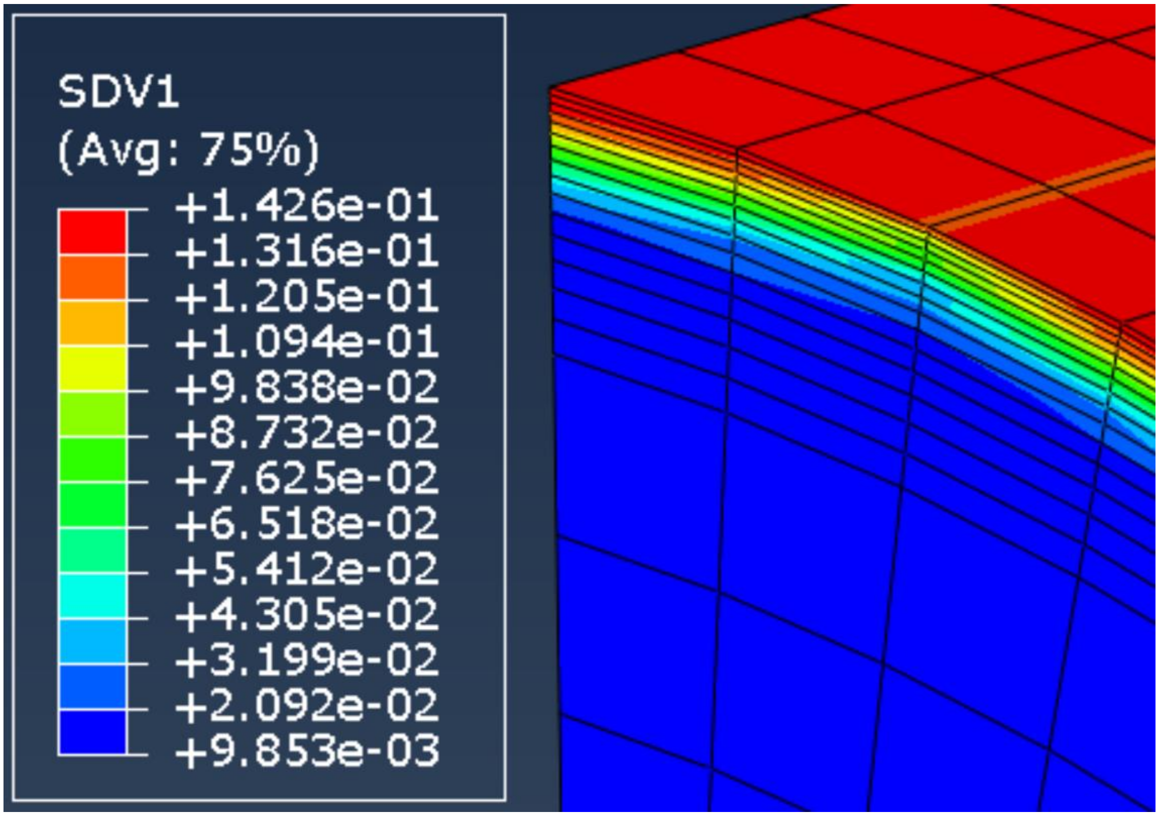

Figure 4. 62: Percentage of retained austenite at transmission shaft's surface after quenching.

What can be seen in Figure 4. 62, in fact, is that the amount of retained austenite at the surface completes the phase composition at the surface of the component. The retained austenite is greatest at the surface and then decreases quite rapidly when going deeper within the component and becomes almost negligible at the shaft's core. The presence of a greater amount of retained austenite at the surface, as explained for the gear geometry, is due to the starting transformation temperature for martensite M_s,that is lowered at that location due to the higher amount of carbon atoms. A comprehensive explanation on this subject was performed when considering the gears' tooth component in the previous paragraph. For this reason, the explanation will not be reported again here. The trend of M_s as a function of depth is shown in Figure 4. 63. In this figure, it can be seen is that the M_s value at the surface is of around 220°C, that is much lower with respect to the value of around 360°C that is found at the shaft's core.

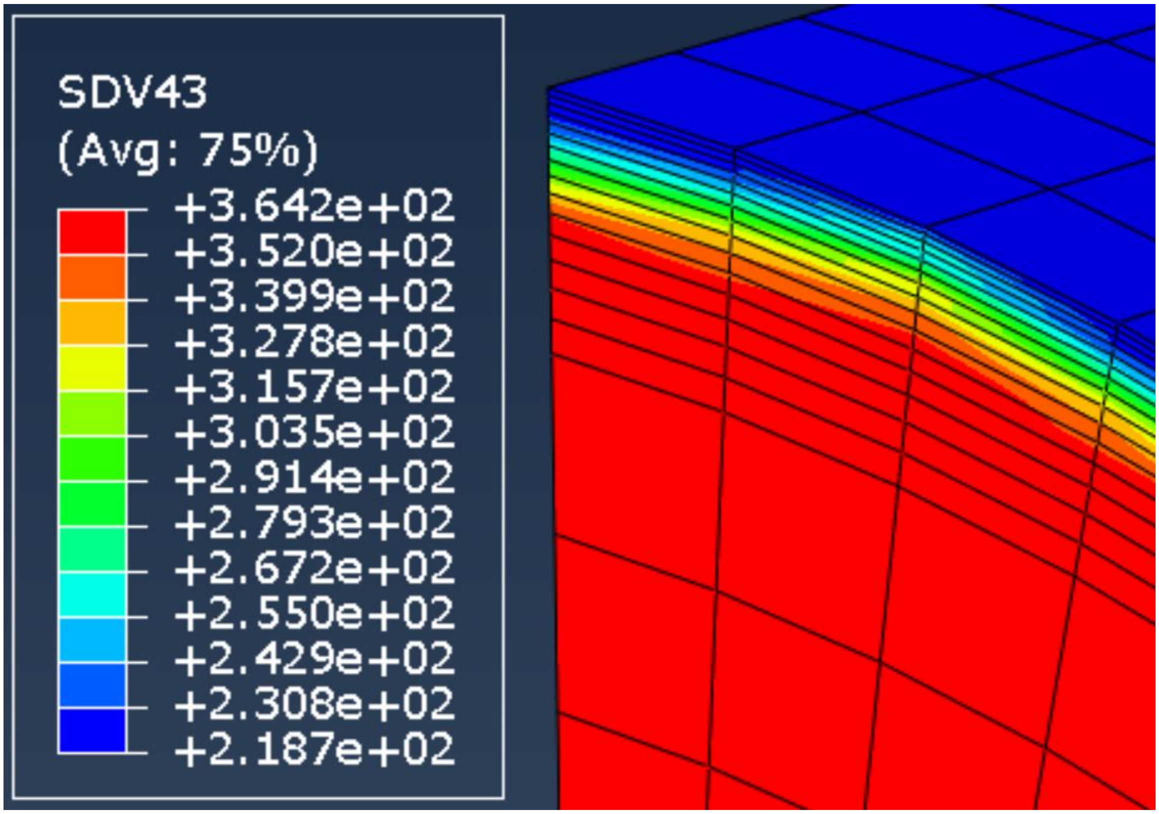

Figure 4. 63: Variation in transformation starting temperature for martensite M_s, expressed in °C, at the transmission shaft's surface.

In Figure 4. 61 and Figure 4. 60, it is possible to see also that the martensite percentage decreases very much from the surface when going towards the component's core. This is due to the fact that, going further away from the surface where the cooling gas is applied, the cooling rate experienced will decrease. A lower cooling rate can lead to the formation of bainite. That is exactly what is predicted by the simulation tool, that shows the trend of bainite growing when moving further away from the component's surface.

To summarize, the amount of bainite, martensite and retained austenite, present at different depths within the shaft geometry are shown in Figure 4. 64.

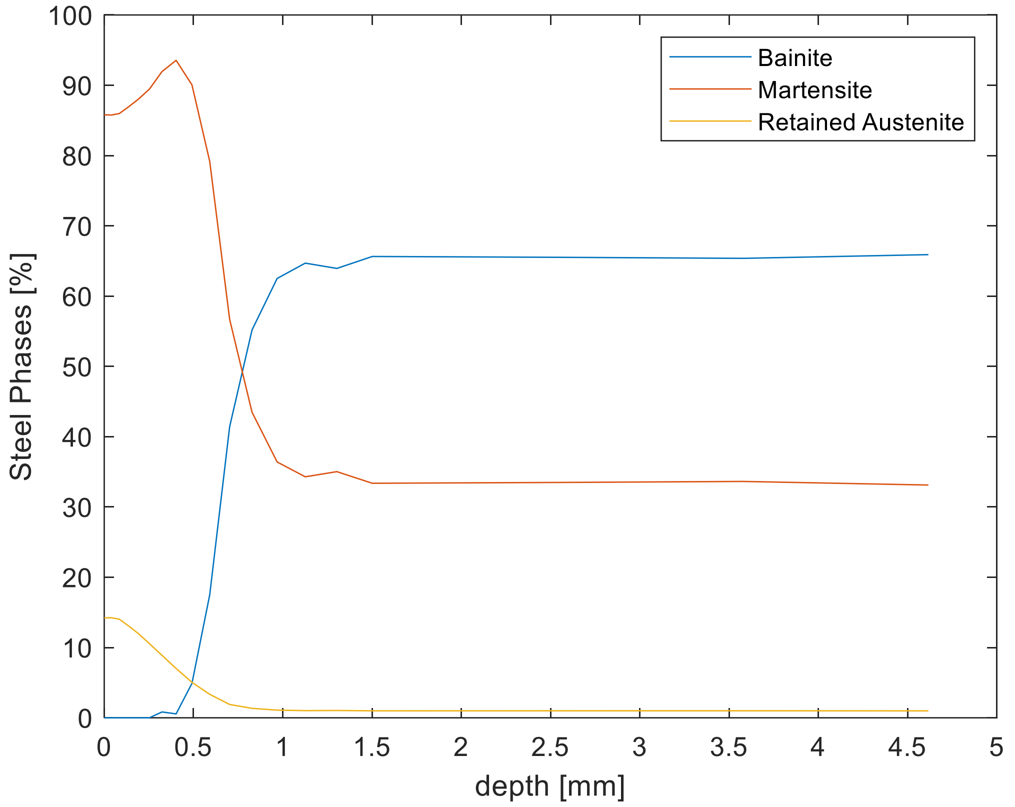

Figure 4. 64: Percentage of bainite, martensite and residual austenite as a function of the depth, found at the at transmission shaft's surface after quenching.

From this image it is clearly visible that the greatest amount of retained austenite is found at the surface. Close below the surface, the amount of austenite decreases, and the amount of martensite reaches its peak value, where a value of around 93% is reached. After the peak, the amount of martensite decreases and settles at a value of about 34%, therefore leaving space for bainite, that accounts for more than 60% of the microstructure at the shaft's core.

What can also be seen in this image is that a greater amount of bainite is found with respect to that that was found in the gear component analyzed before. This is mainly due to the lower heat transfer coefficient values used to simulate the quenching of the transmission shaft component with respect to those used for the gear component. These lower heat transfer coefficients are due to the lower speed of nitrogen inside the quenching chamber with respect to the speed of the helium that is used in the gear component quenching. The speed of the quenching gas has great weight on the values of the heat transfer coefficients, as seen in [16]. Lower heat transfer coefficients, finally, determine a slower cooling rate and so more time for bainite formation.

As done previously for the gear component, the simulation predicted results will now be compared to what is seen in experimental microscopy images taken on the real component. The microscopy images taken for this component were taken with an optical microscope at a magnification of 500X.

The sample was prepared by etching it with an etchant called Lepera. This etchant is composed of sodium metabisulfite and picral, that was left on the component for a prolonged amount of time in order to obtain a greater distinction in color between the different steel phases. Picral is composed of picric acid in an alcohol solution. This etchant was used in order to facilitate the distinction between the different steel phases. Figure 4. 65 shows the microstructure found at the surface of the transmission shaft.

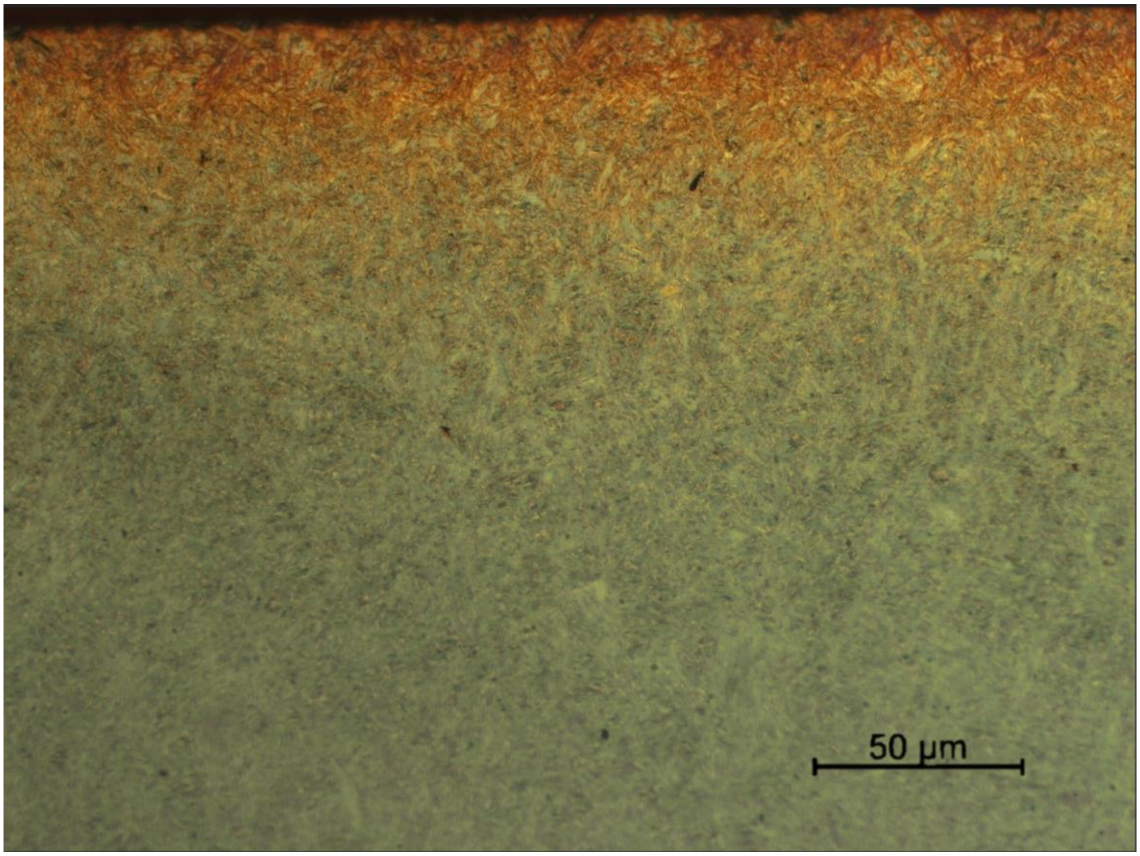

Figure 4. 65: Optical microscopy image at the transmission shaft’s surface.

In Figure 4. 65, the only microstructure that can be distinguished is martensite. This means that a similar situation to that seen in the gear component is found. In fact, the simulation tool at this point predicts a microstructure composition where a great majority of martensite is found coupled with a small presence of retained austenite. As seen with the gear component, the simulation tool correctly predicts the presence of a great amount of martensite. However, the simulation tool also predicts the presence of retained austenite that does not seem to be present in the image. This could be for the same reasons as those mentioned earlier when discussing the retained austenite condition in the gear component, although it is not possible to know with certainty.

Figure 4. 66 shows the microstructure found at a depth of 0.50mm from the surface of the transmission shaft. At this depth, traces of bainite can be found in the microstructural images. These can be recognized by the "golden looking" features circled in yellow in Figure 4. 66. These observations are in agreement with what is found in the simulation tool that, at 0.50mm depth, finds that the amount of bainite is of about 5%, with the rest of the microstructure being mostly martensite. Overall, it can be seen that the simulation tool seems to be in good agreement as it is correctly identifying the vast presence of martensite and the smaller amount of bainite.

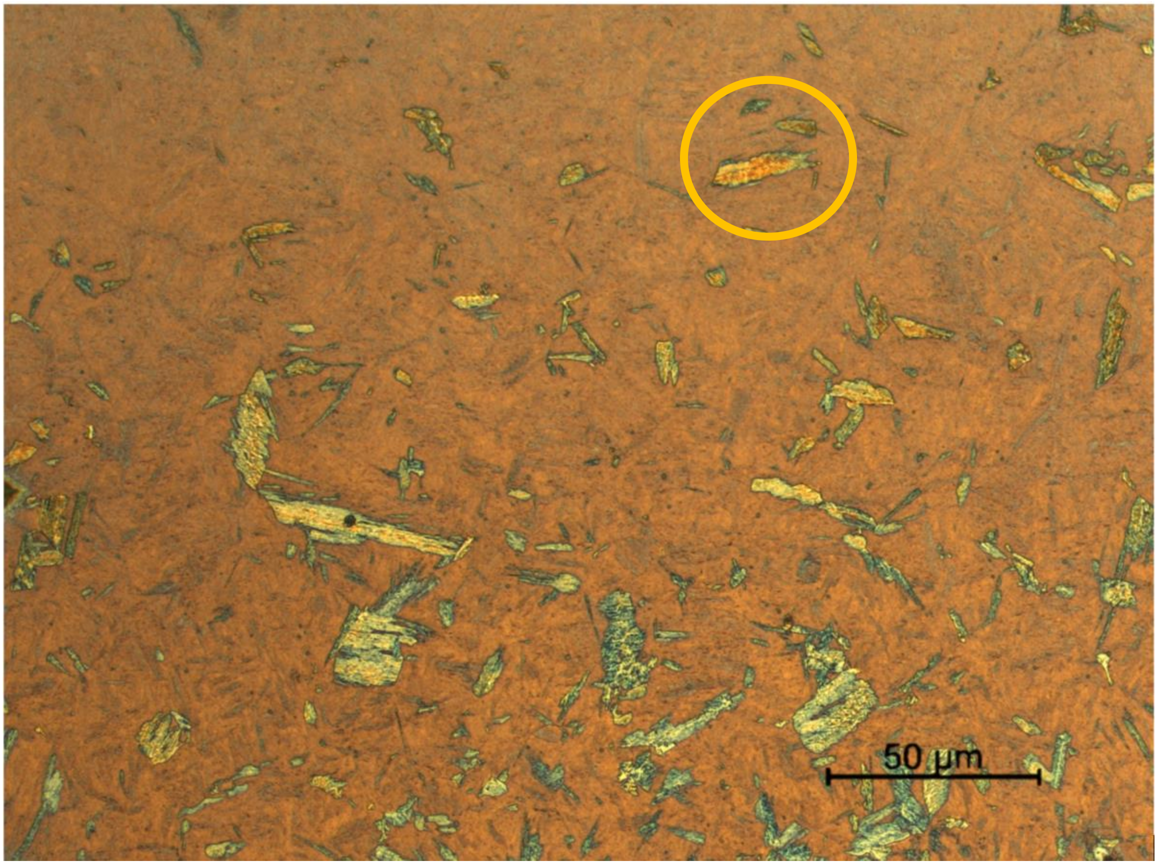

Figure 4. 66: Optical microscopy image at 0.50mm depth from the transmission shaft's surface.

Similar features are also found in the images: Figure 4. 67, Figure 4. 68, Figure 4. 69, Figure 4. 70, and Figure 4. 71. These images were taken at depths of 0.60mm, 0.70mm, 0.80mm, 0.95mm, and 1.50mm respectively.

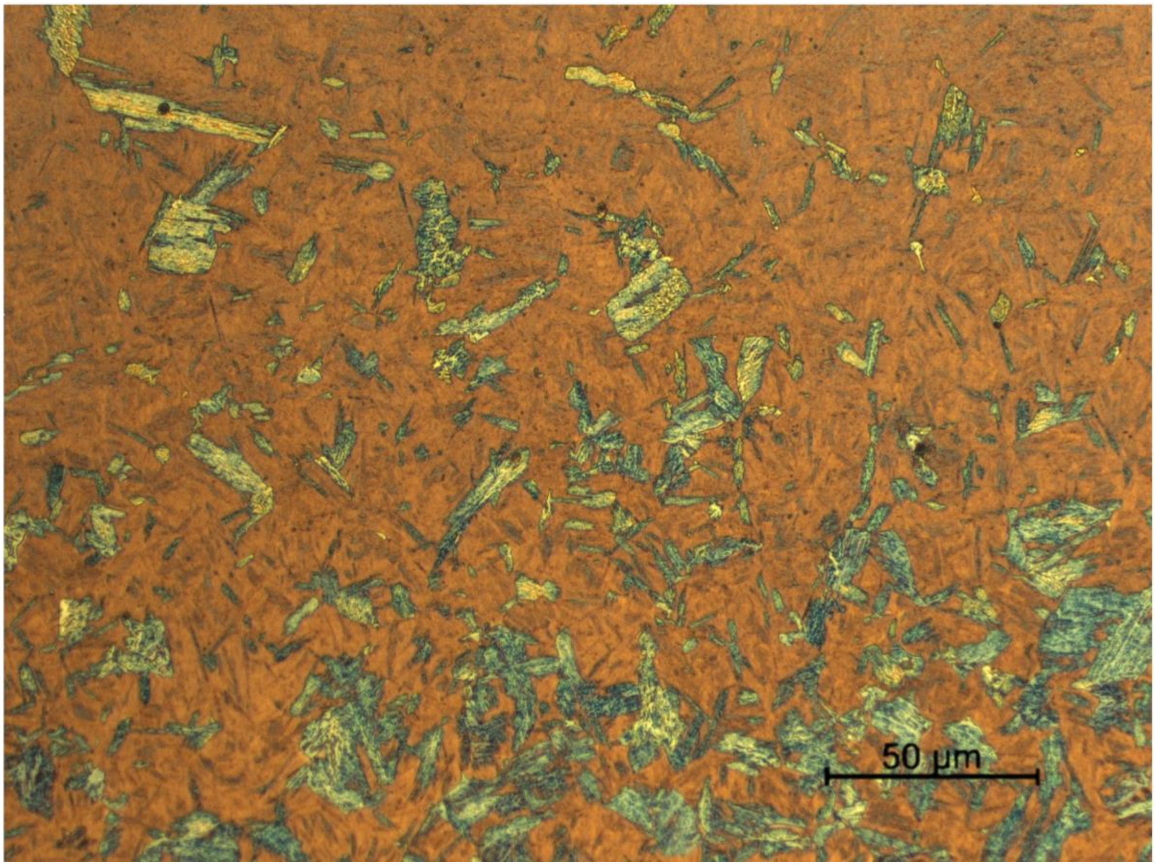

Figure 4. 67: Optical microscopy image at 0.60mm depth from the transmission shaft's surface.

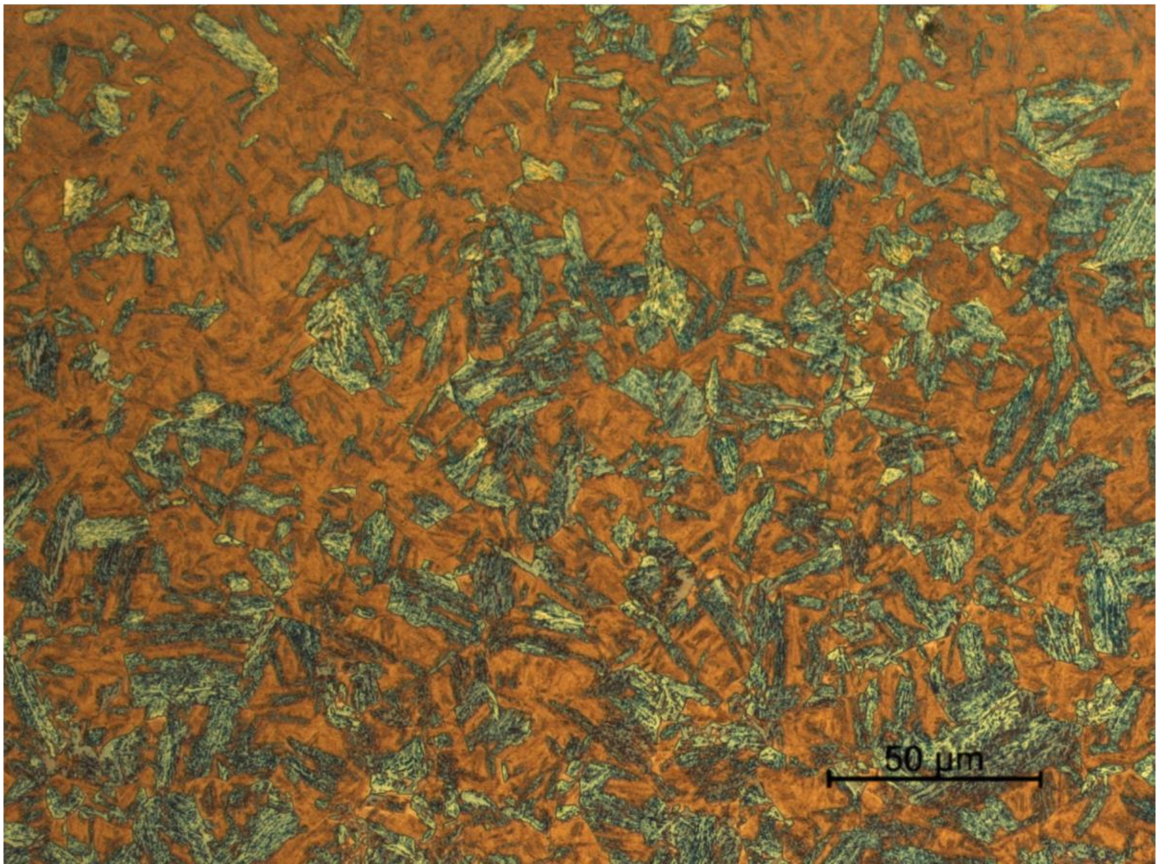

Figure 4. 68: Optical microscopy image at 0.70mm depth from the transmission shaft's surface.

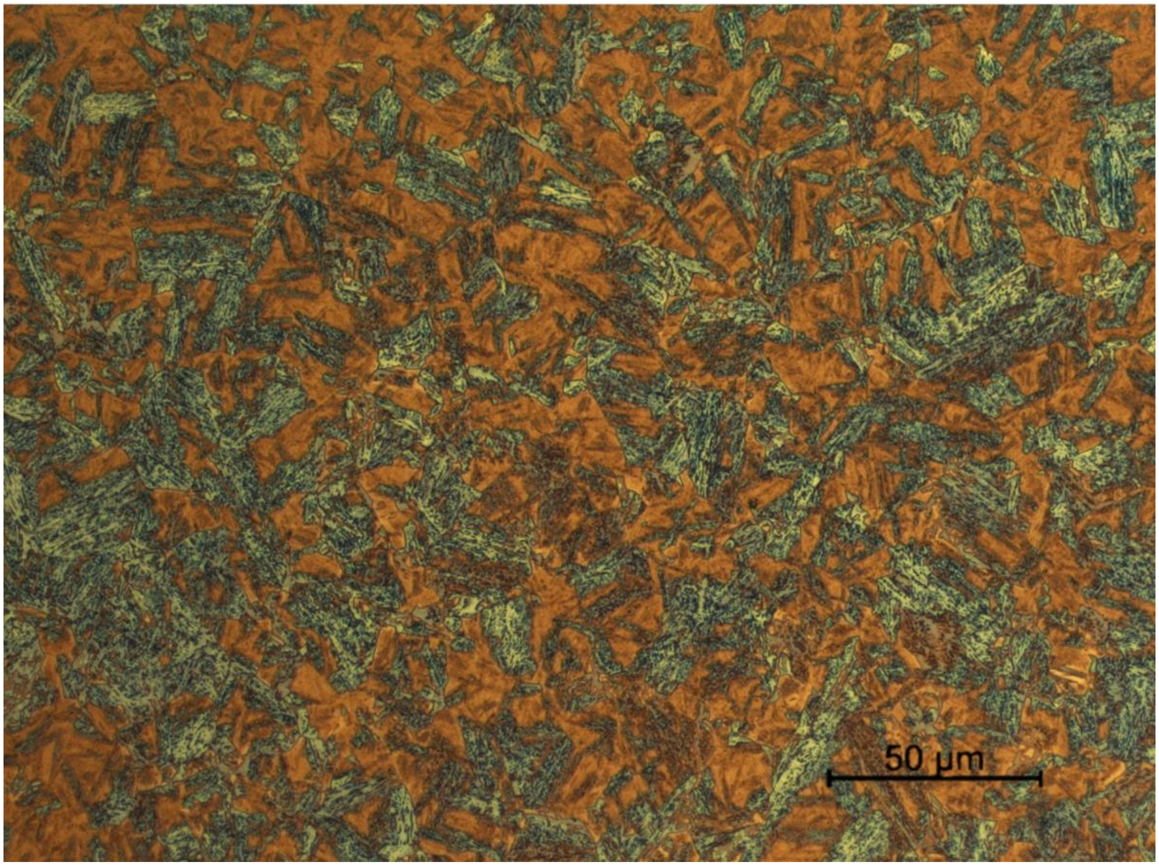

Figure 4. 69: Optical microscopy image at 0.80mm depth from the transmission shaft's surface.

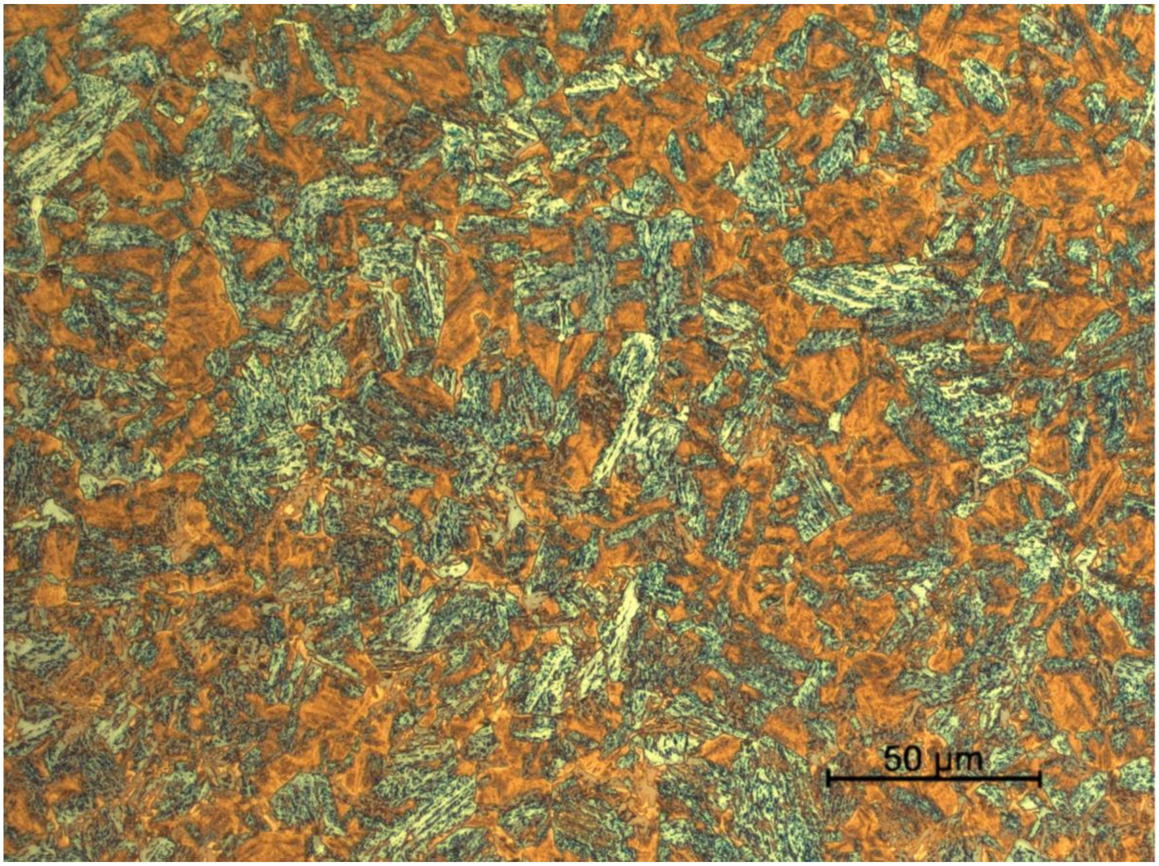

Figure 4. 70: Optical microscopy image at 0.95mm depth from the transmission shaft's surface.

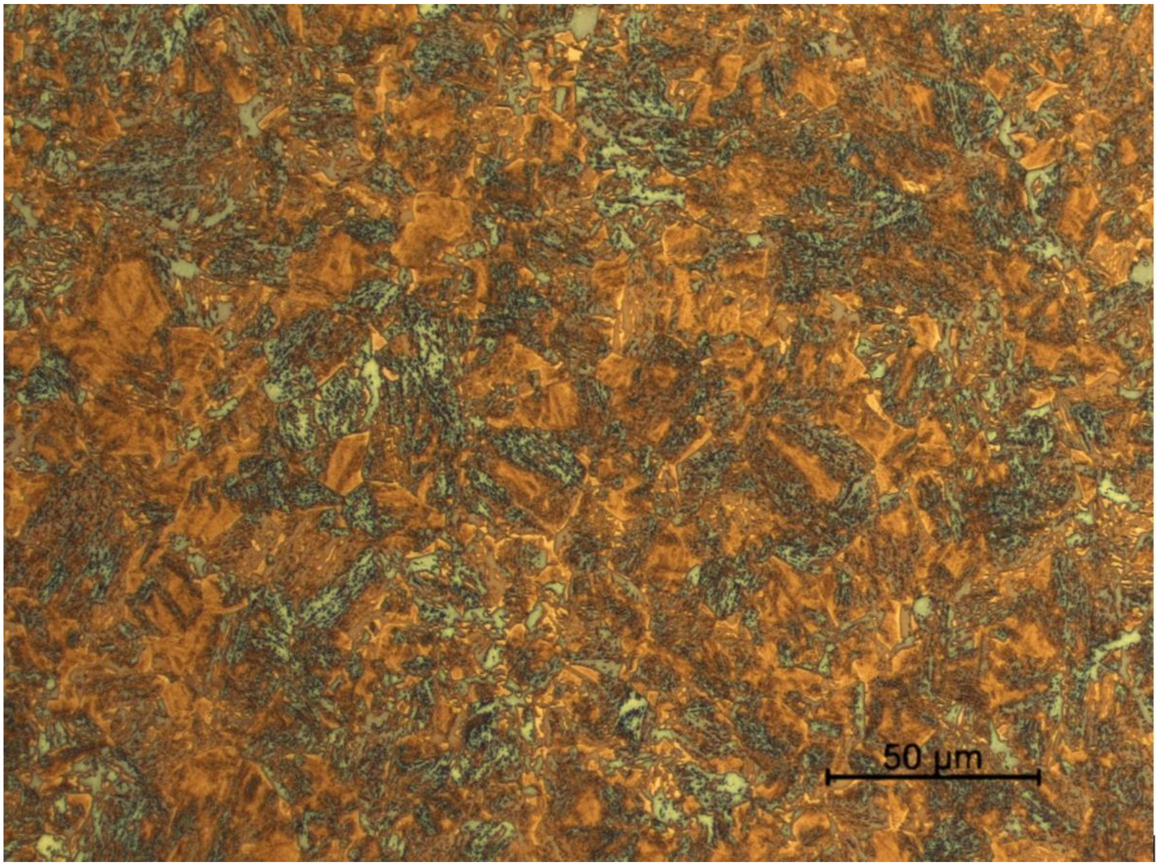

Figure 4. 71: Optical microscopy image at 1.50mm depth from the transmission shaft's surface.

What can be seen in all of these images is that the only phases that are visible are bainite and martensite.

In Figure 4. 67, the amount of bainite that can be recognized is greater with respect to that that is seen in the images taken closer to the surface, however, it is still smaller than the amount of martensite present. These observations are in agreement with what found when looking at the simulated results. In these, in fact, at a depth of 0.60mm from the surface, the amount of bainite is of about 18%, with the rest being mainly martensite.

The same can be said for what regards Figure 4. 68. In this figure, in fact, it can be seen that the amount of bainite is even greater than that found at 0.60mm depth, but it still seems to be slightly less than 50%. This situation is replicated also when looking at the simulation tool results where a percentage of bainite of about 40% is found, with the rest of the microstructure consisting of mainly martensite.

The situation changes when looking at Figure 4. 69. At the depth of 0.8mm, in fact, the amount of bainite visible seems to be greater than the amount of martensite. This is the case also in the simulation tool where a bainite phase fraction of 55% is found, with the rest of the simulated microstructure being mainly martensite.

Finally, the images: Figure 4. 70 and Figure 4. 71, show a similar condition where the amount of bainite seems to be very similar in the two images, one taken at 0.95mm from the surface and the other taken at 1.50mm from the surface. This seems to confirm the trend seen also from the simulation tool where, after about 1mm of depth, the microstructure composition remains nearly unchanged. The amount of bainite predicted by the simulation tool for these two depths is of about 65%.

These qualitative comparisons between the simulation tool predictions and the microstructure seen in the microstructural images, seem to indicate a good agreement between the two, with the simulation tool being able to correctly indicate the steel phases present and their distribution as a function of the distance from the surface.

The microstructure just defined, along with the carbon content, are now used to predict the microhardness. The simulation results in terms of microhardness will be shown in the following paragraph where they will be compared to the experimental microhardness values evaluated at the component's surface.

4.2.2.1.2 Microhardness simulation results and comparison with experimental microhardness measurements found in transmission shaft component

The microstructure shown above, as seen for the gear geometry, clearly influences the hardness values found in the shaft component. As seen when considering the gear geometry, the microhardness values are evaluated by considering the set of equations developed by Mayner et al. The outputs of such equations, in terms of the hardness of the bainite, martensite, and retained austenite steel phases, are shown in the images: Figure 4. 72, Figure 4. 73 and Figure 4. 74. It is reminded that the hardness of bainite is expressed as the user-defined variable "SDV36", the hardness of martensite is expressed as the user-defined variable "SDV37", and finally the hardness of austenite is expressed as the user-defined variable "SDV35".

What can be seen from these images, is that the hardness for all three steel phases, as seen also at the gear's tooth, is greater at the surface of the component where the carbon concentration is higher, and then decreases inside the component where the carbon content decreases. The hardest phase between the three is martensite, that has Vickers hardness values that, at the surface where the carbon concentration is higher, reach values just shy of 900 Vickers.

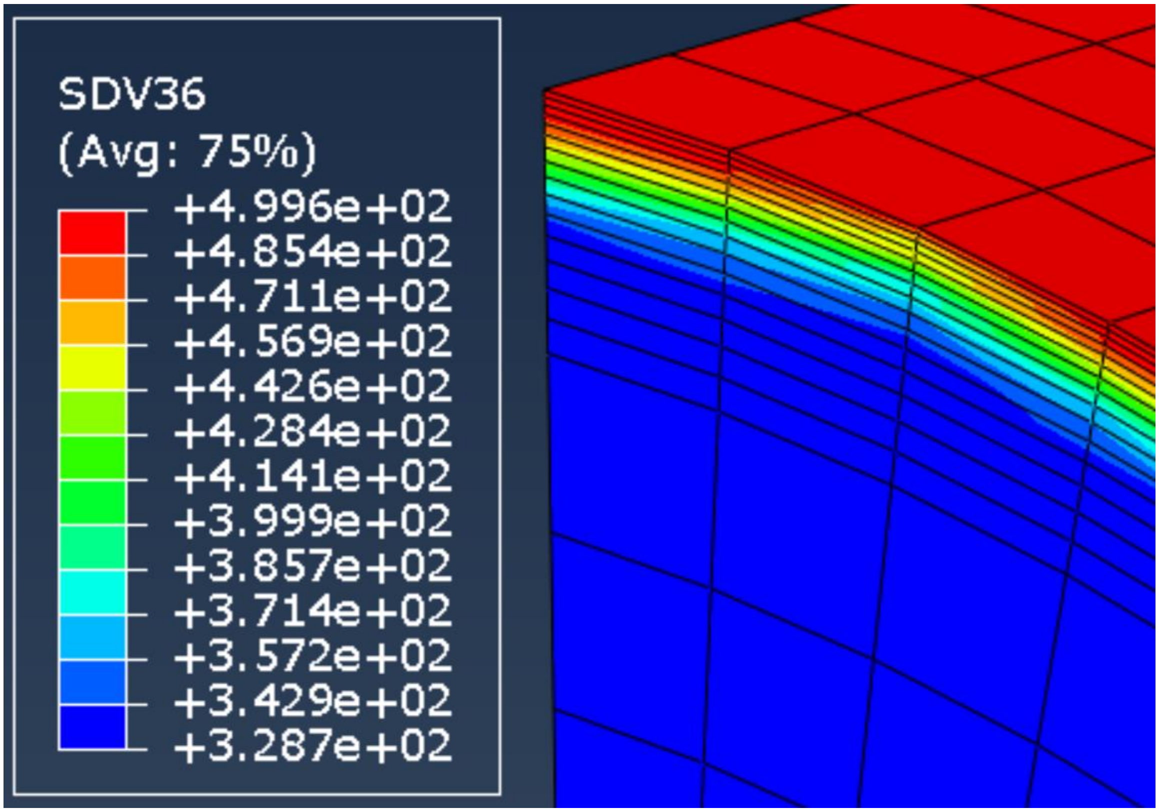

Figure 4. 72: Hardness of bainite as a function of transmission shaft's depth.

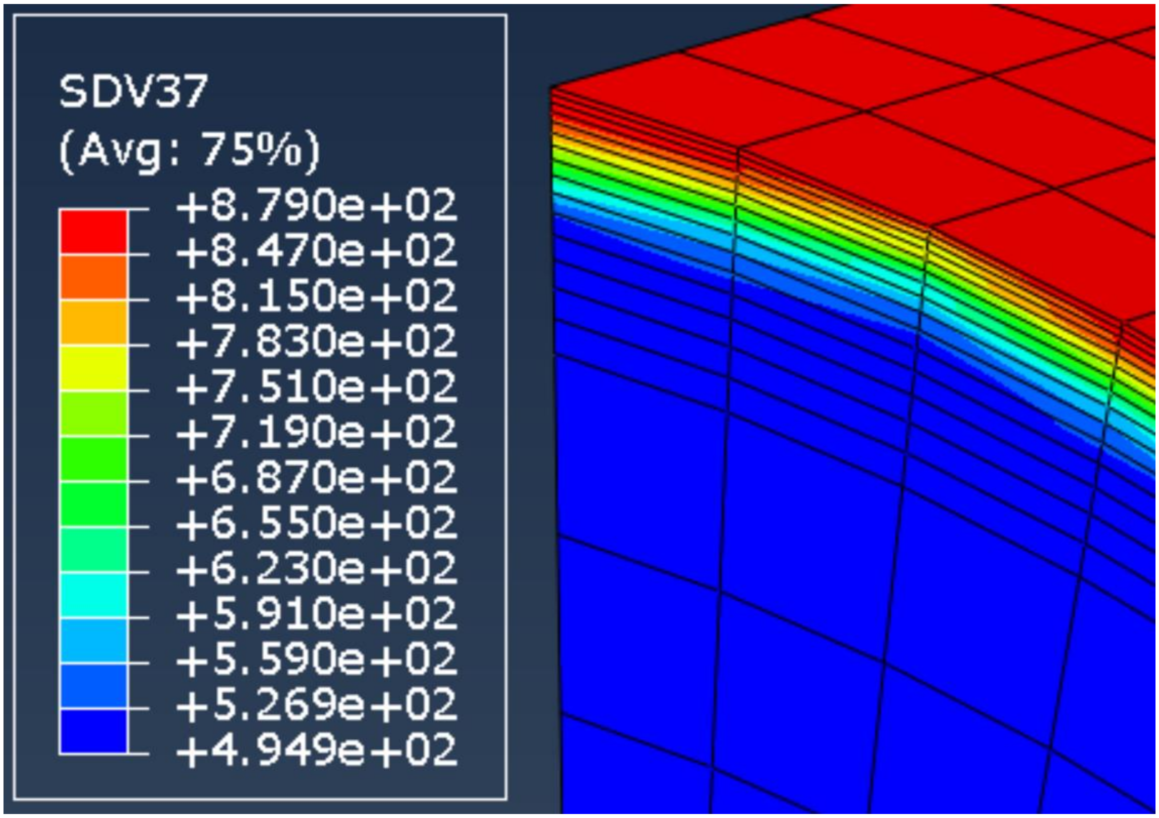

Figure 4. 73: Hardness of martensite as a function of transmission shaft’s depth.

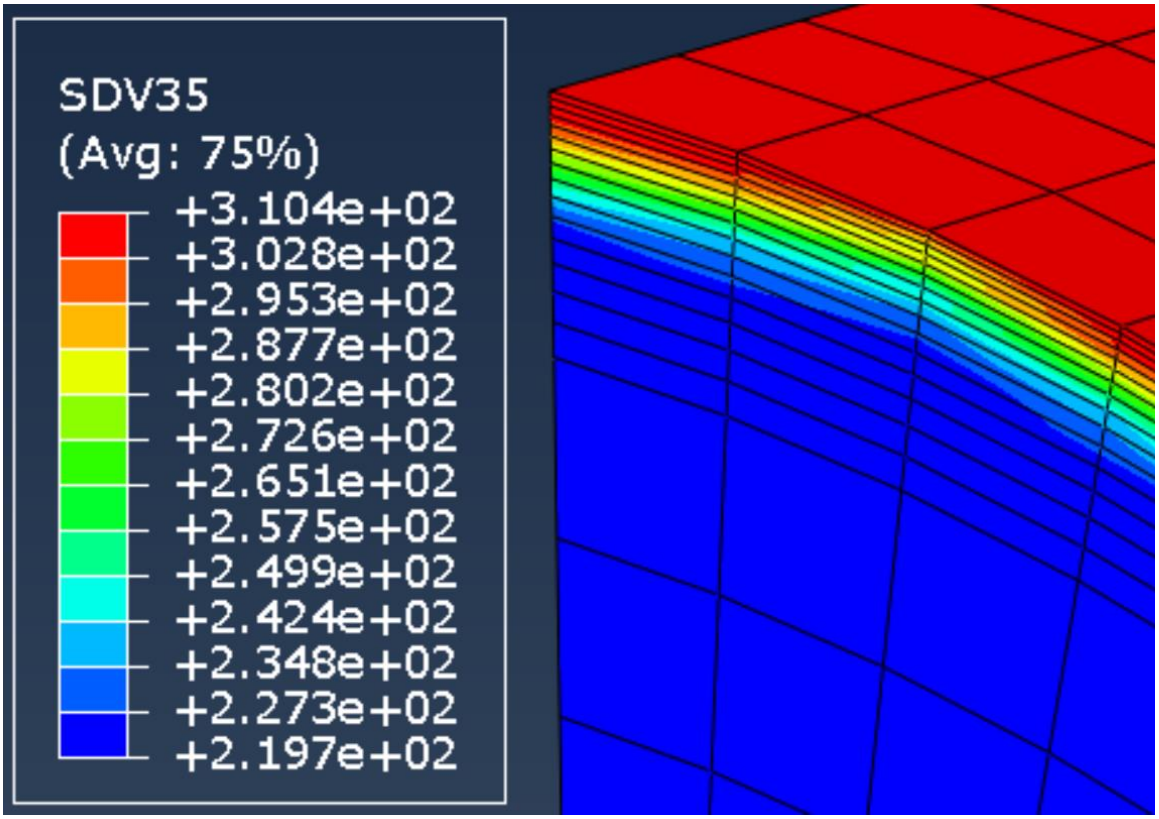

Figure 4. 74: Hardness of austenite as a function of transmission shaft's depth.

The overall hardness is therefore again evaluated with equation 71, as done with the gear component, by knowing the microstructure, that is shown as a function of depth in Figure 4. 64, and by knowing the hardness values for each phase and at each location, that are shown in Figure 4. 72, Figure 4. 73, and Figure 4. 74.

The outcome of equation 71 is defined as the user defied variable "SDV17" and is shown in Figure 4. 75. This hardness is still expressed in Vickers scale and represents the overall hardness after quenching. For sake of explanation, this hardness is also reported in graphical form in Figure 4. 76.

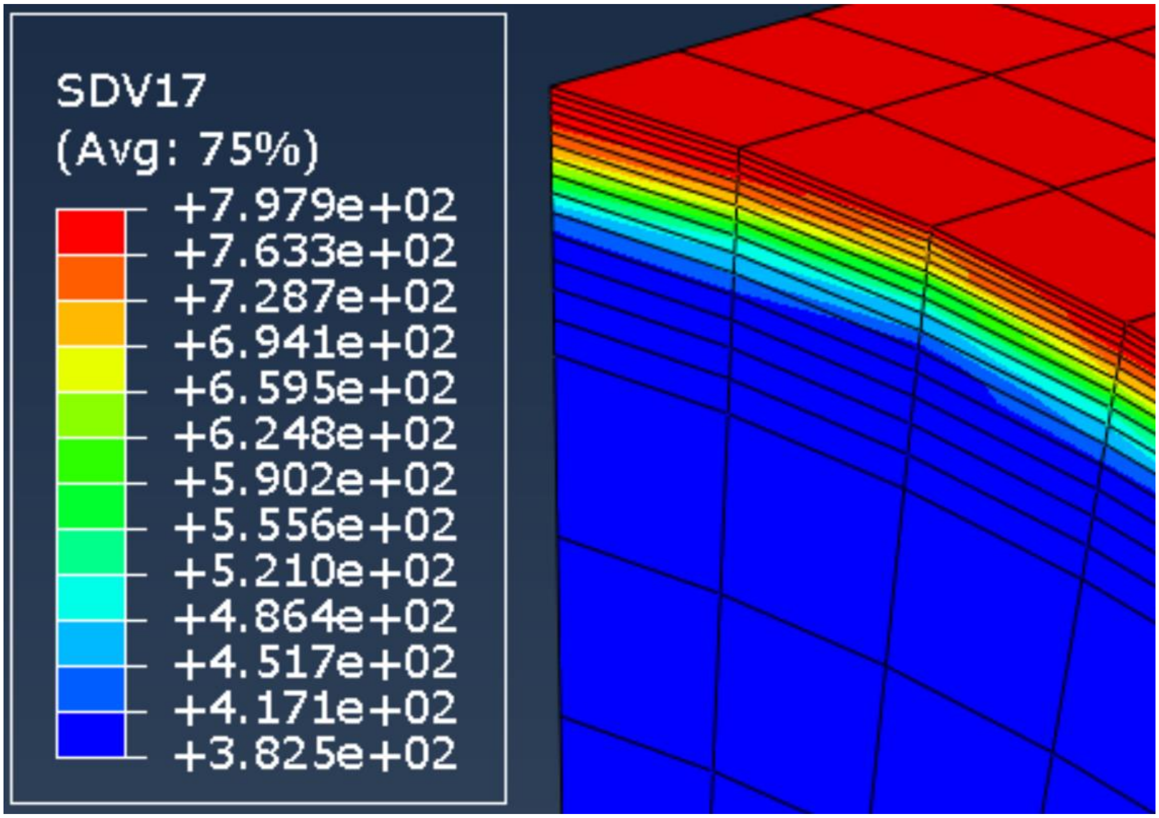

Figure 4. 75: Overall hardness found after quenching at the transmission shaft's surface.

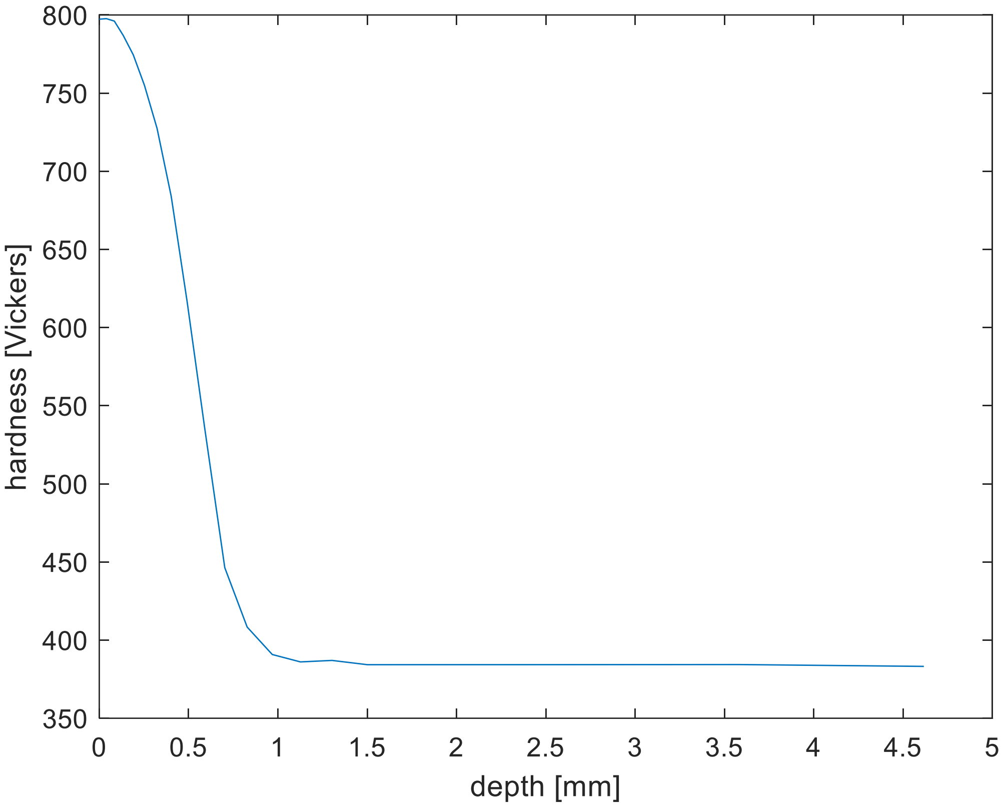

Figure 4. 76: Hardness after quenching process found in transmission shaft component as a function of depth.

As expected, and seen previously for the gear component, the hardness evaluated is greatest at the surface, and then decreases quite rapidly when moving from the surface towards the interior of the component. The reason for this decrease in value is due both the effect of the carbon concentration that decreases in value from the surface towards the shaft's core, and due to the fact that the percentage of martensite, that is the hardest phase between the three that are present, is also decreasing with increasing depth. The hardness, as seen also previously when considering the gear component, after a certain depth that is of about 1mm, reaches a value that than remains quite constant when going even deeper inside the component. This constant hardness value, as explained earlier when considering the gear component, is due to the fact that the two major factors that affect the microhardness: the carbon content and the microstructure, stop varying significantly after that certain depth. In fact, as it is possible to see from Figure 4. 53, the carbon content inside the component, starting from the high value found at the surface reaches the value of the starting steel after a depth of about 1 mm, after which it remains constant. The microstructure composition shown in Figure 4. 64, on the other hand, show that also the microstructure, shortly after about 1.5 mm depth, stops to vary in a significant manner. Therefore, since the two factors that affect the microhardness the most, stop varying after about 1mm, the constant hardness value found in Figure 4. 76 after about 1mm of depth is found.

In Figure 4. 77, that plots the as-quenched hardness along with the percentages of the different steel phases present as a function of depth, the relation between the microhardness and microstructure can be seen. In fact, it is possible to see that the hardness starts to obtain an almost constant value right about where the microstructure starts varying and becomes composed of mostly bainite, about 65%, with also martensite present in a lower amount, 35%.

In Figure 4. 77, the blue lines refer to the steel phases content and to the scale shown on the left of the figure, whilst the red curve shows the trend in hardness after quenching as a function of depth and refers to the axis shown on the right.

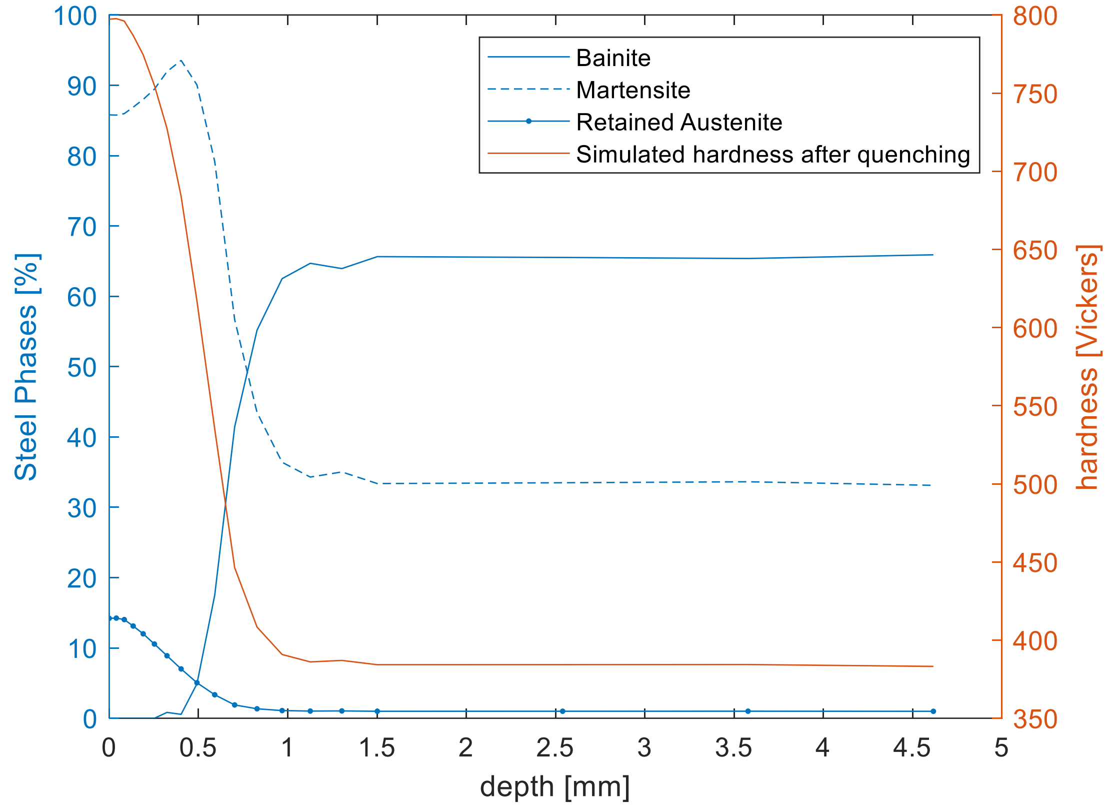

Figure 4. 77: Steel phases percentages found after quenching (left axis) and simulated as-quenched hardness (right axis) for transmission shaft component.

Now that the hardness after quenching has been described, the value found after tempering is presented.

As for the gear process, the tempering temperature and time used for the treatment of the shaft component cannot be disclosed as considered proprietary information of the OEM that is owner of the component. However, also in this case, these values are in the range that was discussed in the methodology section, so below 200°C and for a time frame of up to two hours.

The overall hardness found in the component after tempering is expressed in the simulation as the user-defined variable “SDV18” and is shown in Figure 4. 78 where it is expressed in Vickers scale. A graph showing these hardness values as a function of depth is shown in Figure 4. 79.

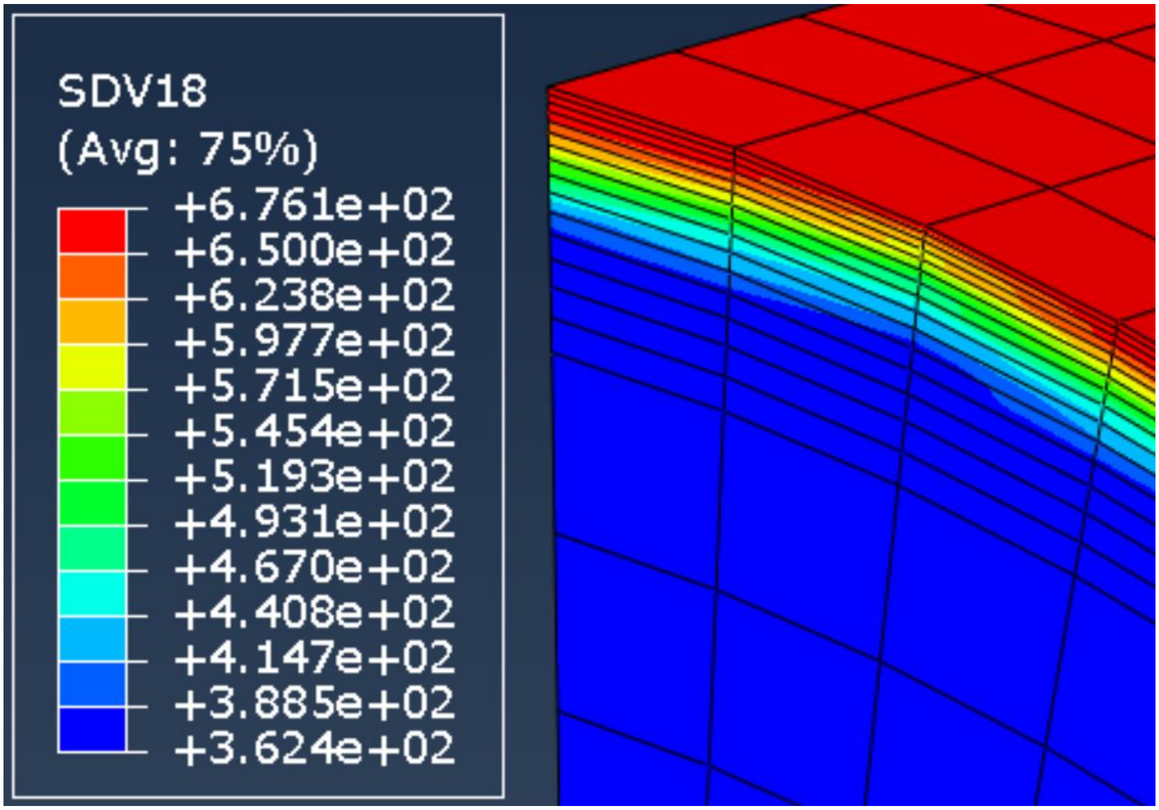

Figure 4. 78: Tempered hardness at transmission shaft's surface.

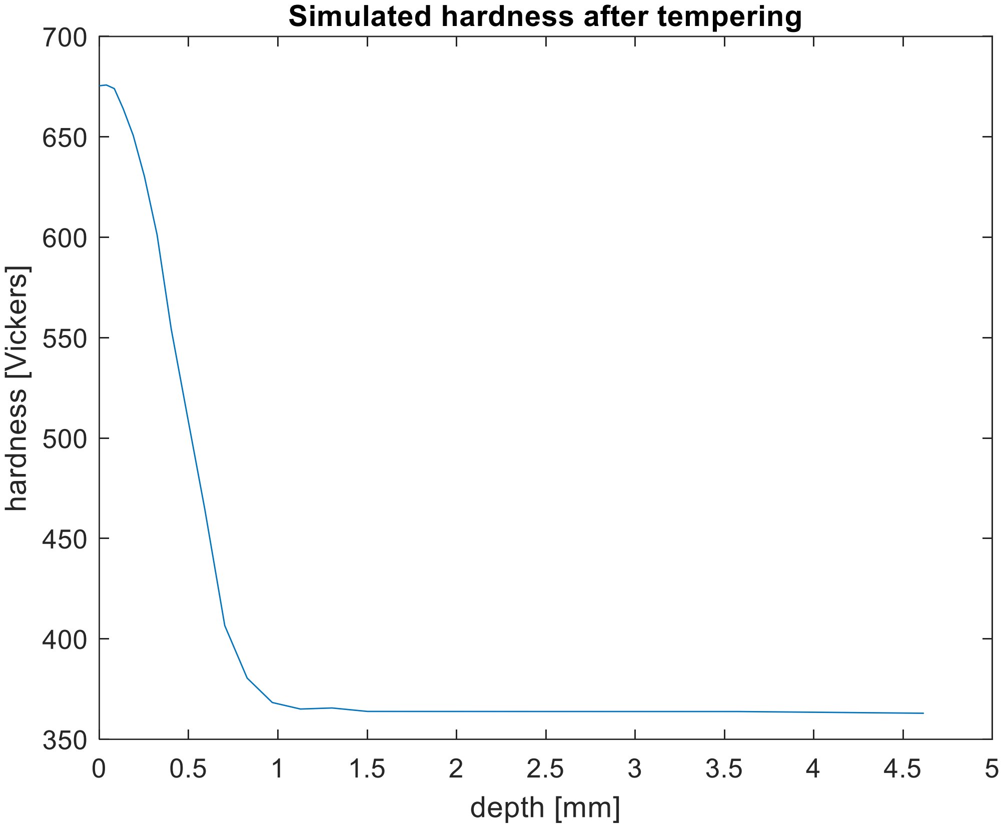

Figure 4. 79: Overall hardness found in the transmission shaft after tempering.

In order to compare the hardness values found before and after tempering, as done for the gear geometry in the previous section, the hardness values before and after tempering for the shaft component are shown in Figure 4. 80.

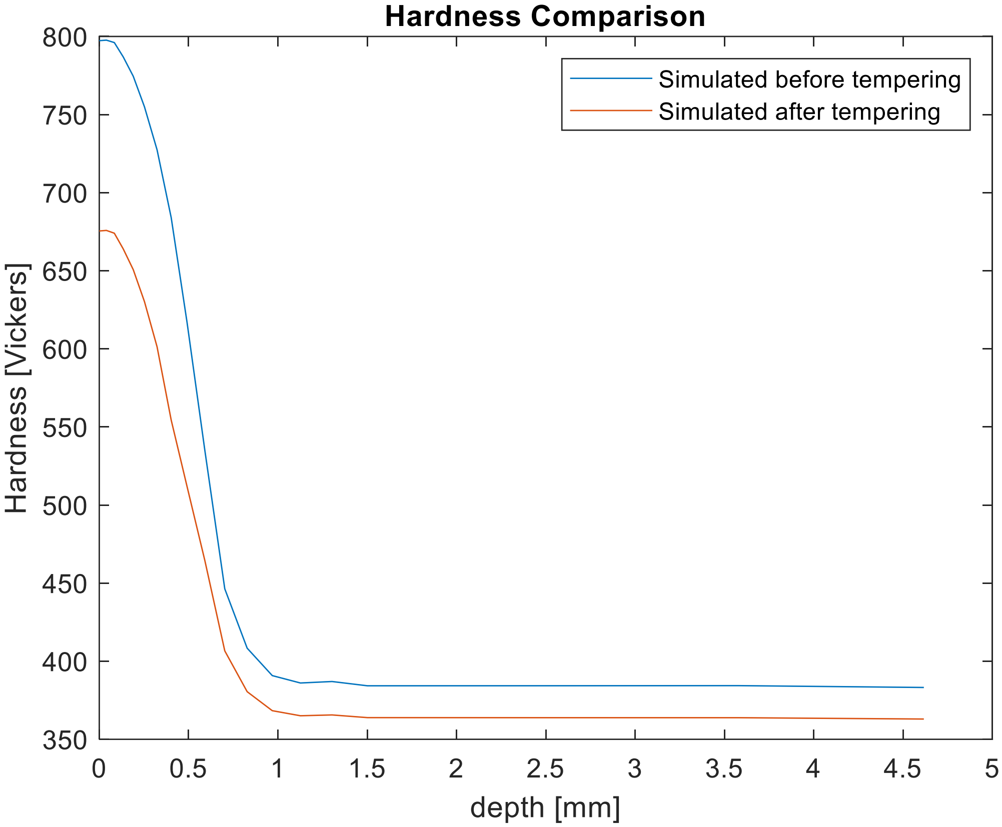

Figure 4. 80: Comparison between hardness found in the transmission shaft before and after tempering.

The results found for the shaft component are qualitatively similar to those found in the gear tooth and gear hub. In fact, the hardness values found after tempering are generally lower than those found after quenching, and the biggest difference between the hardness values found before and after tempering is found in proximity of the surface where the martensite percentage is higher. This is due to the same reasoning that was explained earlier when considering the gear geometry, and so will not be explained again here.

The values of experimental microhardness measurements taken on the real component by some operators at the well-known OEM are reported in Figure 4. 81 as a function of the depth at which they were evaluated.

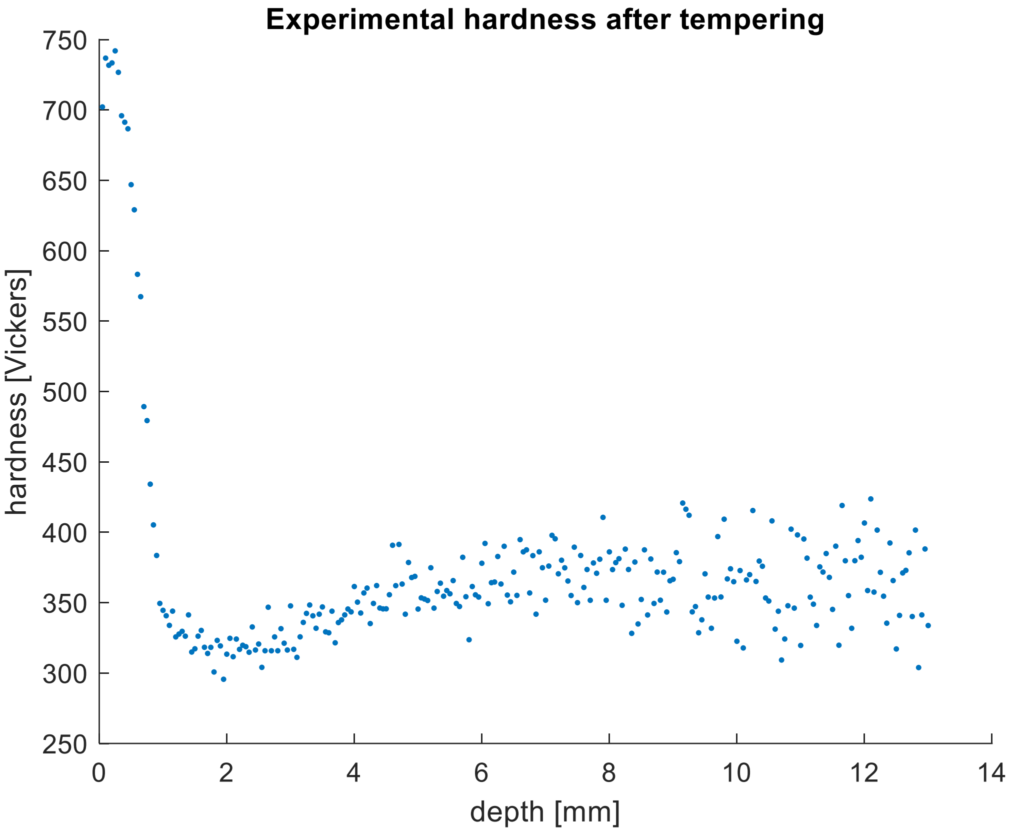

Figure 4. 81: Experimental microhardness measurements on real transmission shaft component after tempering.

What can be seen is that the measurements are quite scattered an show quite a lot of variability. In order to obtain a value of the general trend of the microhardness as a function of depth, an interpolation function was used. This interpolation function is shown in Figure 4. 82.

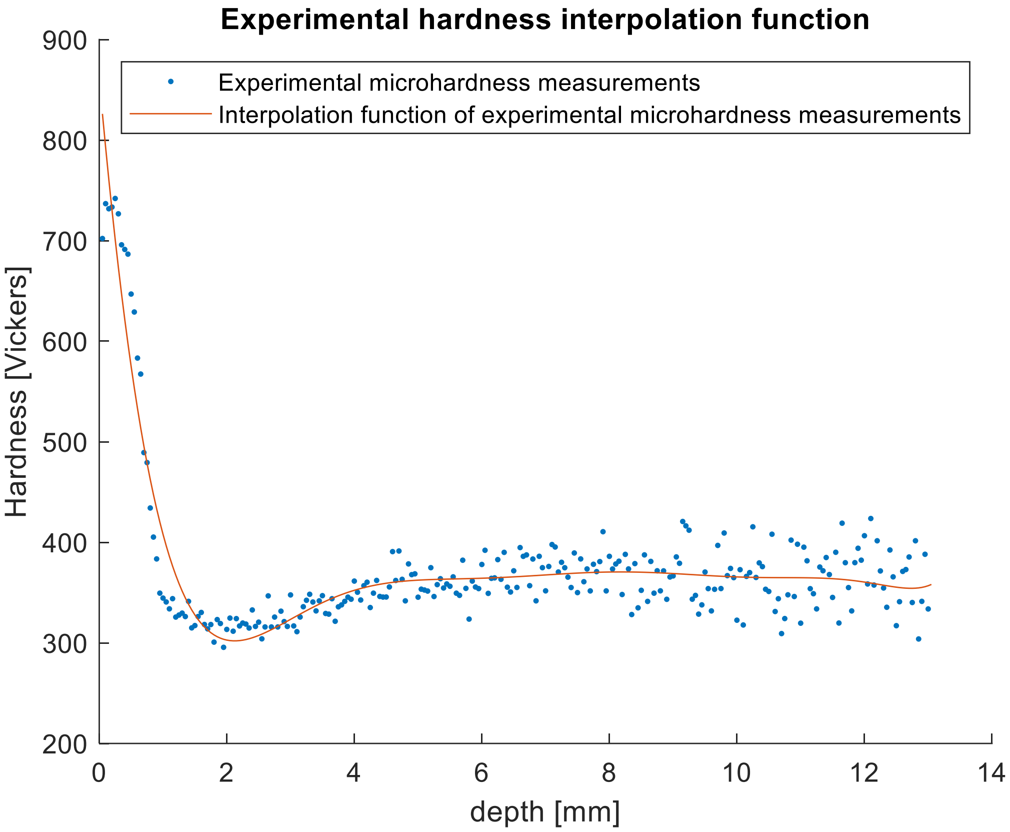

Figure 4. 82: Interpolation function of experimental microhardness measurements on real transmission shaft component after tempering.

The hardness after tempering obtained with the simulation is now compared to these experimental results to see how close the two set of values are. The comparison between the simulated and experimental microhardness values is shown in Figure 4. 83.

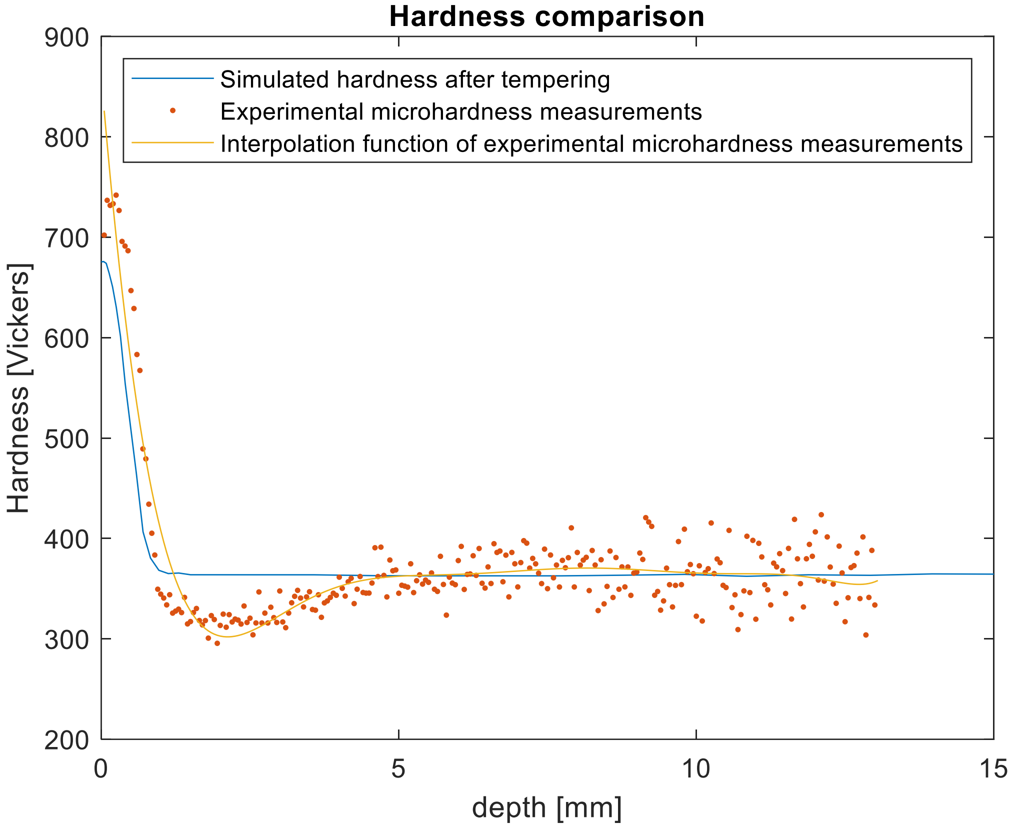

Figure 4. 83: Comparison between simulated and experimental hardness results found in shaft component.

What can be seen from Figure 4. 83, is that the simulated microhardness has a value at the surface that is slightly lower with respect to that seen with the experimental microhardness measurements. The difference in hardness between the two simulated and experimental curves is then very low in the region starting right below the surface and reaching a depth of 2 mm.

After the 2 mm in depth, the experimental microhardness shows un unusual trend as it decreases a little, reaching values of 300 Vickers at the depth between 2 mm and 4 mm. This is an unexpected behavior because the hardness is expected to become constant after the case depth, as seen in literature, and as seen for example in the experimental microhardness measurements found in the tooth and hub region of the gear component. After the strange behavior of the experimental results between around 2 mm and 4 mm depth, the experimental measurements stabilize at a value of about 360 Vickers. The simulation results after about 4mm depth seem to be in very good agreement with the experimental ones.

This hardness comparison shows that the simulation tool can give to the user the correct idea on the trend of the hardness of the component as a function of depth. In fact, although the hardness close to the surface seems to be slightly underestimated by the simulation tool, if the experimental microhardness measurements taken in the depth region between 2mm and 4mm are not considered, the graph produced by the simulation tool seems to correctly follow the experimental microhardness trend and be in good agreement with the experimental measurements. The region between 2mm and 4mm, in fact, shows an experimental hardness behavior that is following an unusual path with respect to that usually seen in literature and seen for the gear component. This, because usually the hardness decreases from the surface towards the interior of the component and then, after a certain depth, it reaches a constant value. However, this is not seen in the set of experimental measurements seen in Figure 4. 83, where in the region between 2 mm and 4 mm of depth, a strange decrease and increases in hardness values is found. Therefore, not considering this area, the simulated microhardness trend seems to be in good agreement with the experimental measurements.

Now that the results have been described and compared to experimental finding for both the shaft and the gear geometry, a discussion on the microhardness trends and their difference with respect to the experimental measurements will be made.

4.3 Error Analysis

What can be seen when looking at the images: Figure 4. 33, Figure 4. 48, and Figure 4. 83, that show the plots comparing the experimental and simulated microhardness profiles for the transmission shaft component and for the gear component in both the tooth and hub region, is that, although the hardness trends seem to be in reasonably good agreement, the simulation tool seems to provide a slight underestimation of the hardness measurements in the region going from the surface towards the core of the component. In order to analyze this difference, a graph representing the percentage of error between simulated and experimental measurements is plotted. This graph is only created for the gear component in the tooth region, however similar results are expected also for the gear component in the hub region and for the transmission shaft component, since a similar microhardness underestimation is found in all three cases. This graph is reported in Figure 4. 84.

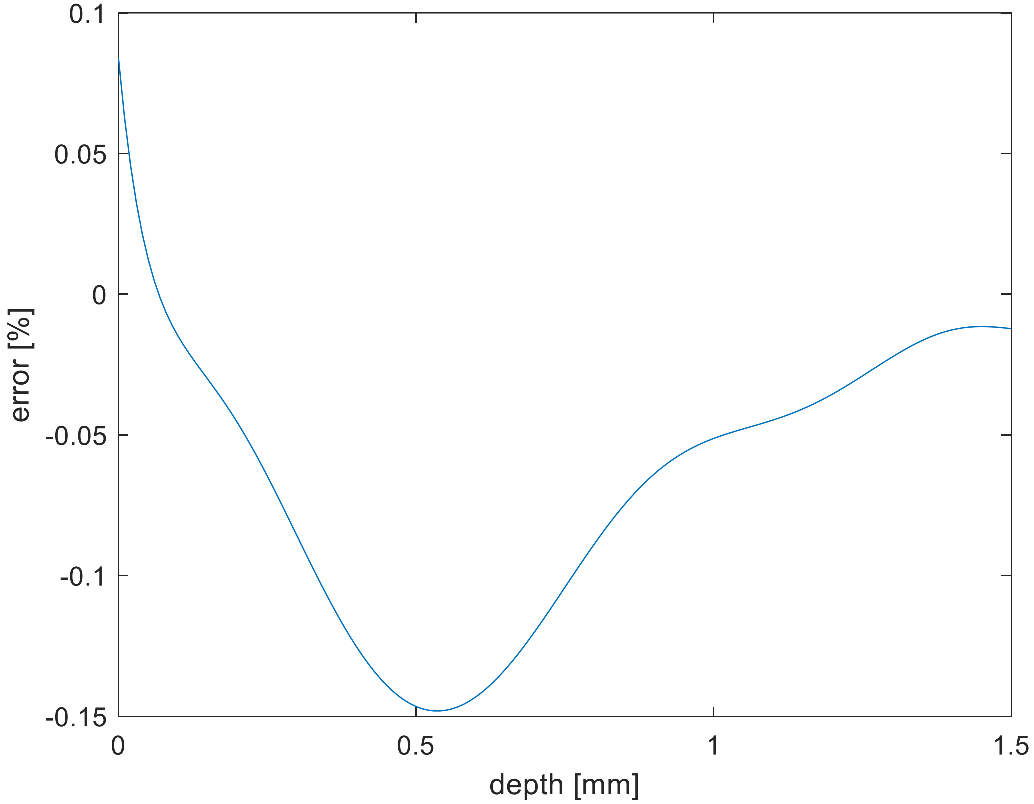

Figure 4. 84: Error percentage between simulated and experimental measurements for gear component in the tooth region.

This error was calculated numerically using equation 78.

$$percentage\ of\ error = \frac{(simulated\ hardness - experimental\ hardness)}{experimental\ hardness} \tag{78}$$

For the evaluation of this error, the interpolation curve of the experimental measurements was considered. What can be seen from this graph is that the hardness prediction is quite accurate at the surface and in the component's core. However, in the region going from the surface towards the interior of the component, the error curve increases in magnitude and assumes negative values. This means that the prediction in those locations is underestimating the microhardness values. This confirms what was seen graphically.

However, what can also be seen from the images: Figure 4. 33, Figure 4. 48, and Figure 4. 83, is that it seems like there is an offset in the abscissa direction between the simulated microhardness and the experimentally measured one. With this in mind, Figure 4. 85 is plotted, where the simulated microhardness evaluated for the gear component in the tooth region is plotted against the experimental microhardness measurements in that location, considering however a positive shift of the simulated microhardness curve of 0.13 mm towards the interior of the component.

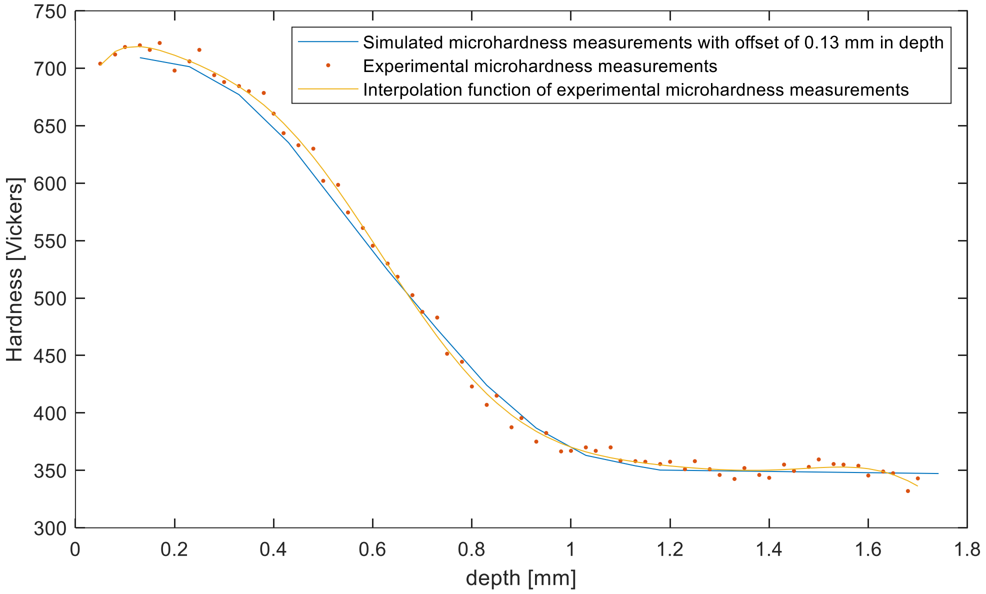

Figure 4. 85: Simulated microhardness with offset of 0.13mm in depth and experimental microhardness measurements and interpolation curve.

What can be seen is that in this case the two curves seem to be in better agreement with respect to what is seen in Figure 4. 33 where the simulated microhardness profile was not shifted. The error graph, evaluated with equation 78, for this situation where the simulated hardness values were "shifted" of 0.13mm towards the core of the component, is shown in Figure 4. 86.

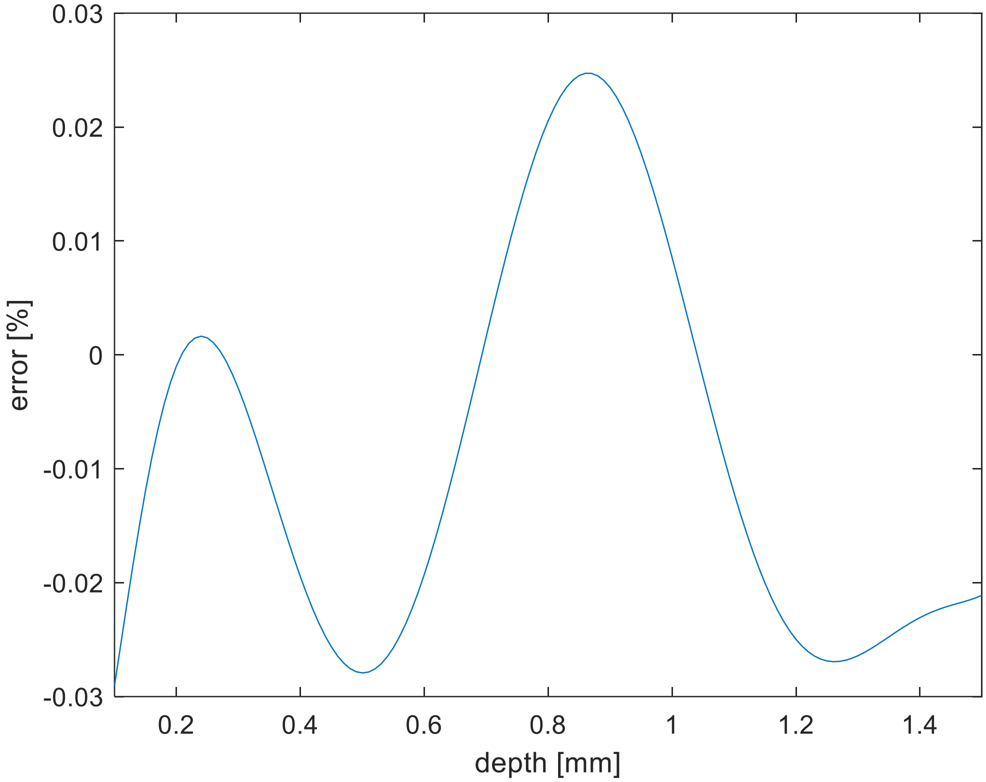

Figure 4. 86: Error percentage between simulated and experimental measurements where simulated results were offset of 0.13mm towards the interior of the component.

What can be seen when looking at Figure 4. 86, is that the amount of error found in this case is much lower with respect to that seen in Figure 4. 84, which is shown by the lower magnitudes found on the ordinate scale.

The microhardness in the simulation tool was evaluated with the Mayner et al [69] formulations reported the methodology chapter in equations 68 to 71. What can be seen when looking at these equations, is that the microhardness is greatly dependent on the carbon content and on the microstructure. Furthermore, also the microstructure is dependent on the carbon content as the latter heavily affects the transformation temperatures. Considering the fact that the simulated microhardness trend seems to better represent the experimental microhardness when it is shifted fractions of millimeters to the right, it is a reasonable to believe that the carbon profile could be the source of the microhardness underestimation in the simulation. In fact, a higher carbon content along the depth of the component from the surface towards the core, would determine greater hardness values and so would probably solve the hardness underestimation issue. Going deeper in this concept, if the carbon profile had to be the source of the hardness underestimation error, this could be due to the values of the carbon diffusivity. In fact, a higher carbon diffusivity would mean that the carbon would be able to diffuse further inside the component. This would determine a higher carbon content along the path from the surface towards the core of the component and could therefore solve the hardness underestimation issue in this region. This could be the object of further studies, where different carbon diffusivity theories could be applied to the simulation tool to check if the hardness underestimation issue can be solved by using different formulations available in literature and providing greater carbon diffusivity values.

As mentioned earlier, the previous discussion was done considering the gear tooth, however, similar observations could most probably be made also for the gear hub and for the transmission shaft as they show a similar microhardness behavior.

Now that the simulation results have been presented and commented, in the following chapter a summary of the thesis research will be presented, and the main conclusions will be drawn.

CHAPTER 5:
CONCLUSIONS

5.1 Summary and conclusions drawn

In this thesis, a simulation tool is developed with the aim of predicting properties found in steels after a carburizing-quenching-tempering heat treatment sequence. The prediction of properties of the steel after heat treatments can lead to a great number of advantages from both a timing point of view and also from a monetary standpoint. The main objective when developing the simulation tool was to correctly predict the microstructure and microhardness properties of components heat-treated by carburizing-quenching-tempering, and to display them to the user in a clear and understandable manner.

In order to do so, it was decided to create the simulation tool using a powerful general purpose such as ABAQUS, to which a set of additional codes were added to simulate all the metallurgical phenomena not already present in ABAQUS. This being the case, a set of different additional codes were prepared and linked to ABAQUS in order to perform the simulations. Each user code provided a different helpful function to the simulation. The simulation tool that was produced shows two main modules: one concerning the simulation of the carburizing process and so the addition of carbon atoms at the surface of the component; and the other module concerning the simulation of the quenching- tempering processes.

Both modules, when provided with the required inputs, provide to the user some results that can be clearly visible in the ABAQUS post processing by over-imposing the results directly on the geometry of the component, therefore allowing for a fast understanding of the overall situation. The results can also be probed from the geometry on which the simulation is conducted and plotted as a graph function. Therefore, the results obtained from the simulation tool are quite clear and can be easily understood. The simulation provides many outputs to the user such as the temperature field, the transformation starting temperatures for the different steel phase, the cooling rates, and other interesting results. However, the most important outputs of the simulation tool are regarding the information on the amount of different steel phases present at any location inside the component, and the prediction of the microhardness found in the component before and after tempering.

In order to validate these results obtained by the simulation tool, the outputs obtained from the simulation when considering two automotive powertrain components, were compared to a set of experimental microstructure images and microhardness measurements taken on the real components. In particular, the two components that were simulated and on which the experimental measurements were taken were a gear geometry and a transmission shaft. The comparison between experimental and simulated results showed that the simulation tool is generally capable of correctly predicting the nature of the different steel phases that originate inside a component. In fact, in both components the simulation tool managed to predict the significant presence of martensitic and bainitic microstructures, and also the general variation of these two phases as a function of the distance from the surface.

Both the simulation tool and the microstructure images showed a great amount of martensite at the surface. Also, both the simulation and the experimental results revealed the gradual decrease in martensite percentage when moving further away from the surface, coupled in turn with an increase in the bainitic microstructure. A point of difference, however, concerns the presence of retained austenite. In fact, the simulation tool seems to predict a higher amount of retained austenite close to the surface with respect to that that is actually seen in the microstructure images. It could be due to the fact that the magnifications of the microstructure images preclude the recognition of the austenite phase. In addition, it could also be due to the fact that retained austenite, if stressed, could transform into martensite due to the effect of the transformation induced plasticity. Therefore, the residual austenite could have transformed into martensite during the sample preparation, and therefore not be visible anymore in the micrograph images. These hypotheses, however, cannot be known with certainty.

In terms of the comparison between the simulated and experimental microhardness measurements, the simulation tool again seems to correctly simulate the microhardness trend and seems to provide results that are in reasonably good agreement with the experimental microhardness measurements. The simulated tool however seems to slightly underestimate the microhardness values ranging from the surface towards the component's core. This last problem could be due to the carbon diffusivity values used during the carburization study; however further studies are required to confirm this hypothesis.

The main conclusions are listed as follow:

- The simulation tool correctly identifies qualitatively the steel phases present after the surface treatment;
- The simulation tool correctly identifies the microhardness trend as a function of depth from the component's surface;
- A slight microhardness underestimation in the simulation was observed, that could be due to the carbon diffusivity values used in the simulation. Further studies could be done to analyze this hypothesis;
- The simulation tool being an FEA analysis, and having been built on top of many different formulations that account for the different metallurgical phenomena, has also some limitations:
    - Firstly, the simulation necessitates of a very fine mesh at the surface, in order to obtain accurate predictions for all simulated phenomena occurring at that location, as carburizing for example. This mesh refinement, coupled with a complex geometry, can lead the simulation to become very computational expensive and long.
    - A second limitation of this simulation tool is due to the different assumptions/limits that were introduced when utilizing some formulations or reasonings. For example, the tempering process is simulated by assuming that the low tempering time and temperature do not lead to major changes in all steel phases, but rather only to a decrease in the hardness of the martensite steel phase. This, as mentioned in the paper [33], can be considered as a reasonable assumption only if the tempering time and temperature are low. In the two components that were simulated and of which the simulated results were compared to the experimental ones, the tempering time and temperatures were low and so there was no issue in applying this methodology. However, this fact could become a limitation if

a process showing higher values of tempering time and temperature had to be simulated.

- Further studies considering different heat treatment parameters and different steels, and comparing with experimental measurements, are required in order to correctly validate the simulation tool.

5.2 Future works

Although the simulation shows reasonably good qualitative agreement for both microstructure and microhardness predictions, before the usage of this simulation tool for more serious applications, a few more studies are recommended:

- Additional microstructural investigation at higher magnifications at the component's surface is recommended, in order to identify if the amount of residual austenite found by the simulation tool is an overestimation or if it is an accurate result. Furthermore, an X-Ray diffraction analysis could be performed on the component in order to study the presence of austenite at different depths. ASTM E975 is the standard practice for the X-Ray determination of residual austenite.

- More simulations and comparisons with experimentally derived values should be conducted, considering perhaps diverse components and with differing heat treatment parameters, in order to validate the simulation tool.

- Further studies could be done in order to study influence of the carbon diffusivity values on the simulated microhardness and microstructure. This could possibly lead to solving the slight microhardness underestimation issue.

Another interesting continuation of this work could concern the prediction of the stress field and of the deformations at the end of quenching. In the methodology section of this thesis, a method was shown to simulate the strain, and therefore deformation during quenching. However, no experimental measurements were performed on the real components to evaluate these deformations. For this reason, these results of the simulation were not taken into any consideration in this thesis research. However, a comparison between the simulated deformations and those experienced on a real component and evaluated experimentally, could be material for a future study. This would permit the evaluation of the simulation tool also from another point of view. This being the case, also the residual stresses simulated could be compared to experimentally obtained measurements, perhaps obtained using the X-Ray diffraction method.

REFERENCES/BIBLIOGRAPHY

[1] Elmi Hosseini, Seyed Reza & Li, ZhuGuo. (2016). Pack Carburizing: Properties, Microstructure and Modeling.

[2] Yaakoubi, M., Kchaou, M., & Dammak, F. (2013). Simulation of the thermomechanical and metallurgical behavior of steels by using ABAQUS software. Computational Materials Science, 68, 297–306.

[3] Bortoleto, E., G. Sarmiento, Anselmo Fioranelli and A. Gastón. "Using Abaqus User Subroutines to Develop a New Finite Element Modeling Tool for Heat Treatment Simulation." (2009).

[4] Gur, Hakan & Simsir, Caner. (2012). Simulation of Quenching: A Review. Materials Performance and Characterization.

[5] Zhang, Lei. 2017. Modeling and Verification of Simulation Tools for Carburizing and Carbonitriding. : Worcester Polytechnic Institute.

[6] S.J. Lee, D.K. Matlock, C.J. Van Tyne, ISIJ Int. 51 (2011) 1903–1911

[7] Arttu Laitinen, Two-Dimensional Simulation Of Thermal Cutting Of Low-Alloyed Steels, Master of Science Thesis

[8] Krauss, George. (2015). Steels - Processing, Structure, and Performance (2nd Edition) - 5. Martensite. ASM International.

[9] Lee, Seok-Jae & Matlock, David & Vantyne, Chester. (2013). Comparison of two finite element simulation codes used to model the carburizing of steel. Computational Materials Science. 68. 47–54.

[10] Michael J. Schneider, Madhu S. Chatterjee, Introduction to Surface Hardening of Steels, Steel Heat Treating Fundamentals and Processes, Vol 4A, ASM Handbook, Edited By Jon L. Dossett, George E. Totten, ASM International, 2013, p 389–398

[11] Phạm, Dương & Hoang, Anh & Nguyen, Duong & Le, Van Vang. (2017). Effect of factors on the hydrogen composition in the carburizing process. International Journal of Applied Engineering Research

[12] Hasan, M. Z., Hussein, A. A., Hasan, A. S., & Ali, O. M. (2020). Improvement of AISI 1018 Carbon Steel Gr 1018 mechanical properties by liquid carburizing in salt bath. Materials Today: Proceedings, 20, 512–516. p

[13] Smirnov, A. & Ryzhova, M. & Semenov, Michael. (2017). Choice of Boundary Condition for Solving the Diffusion Problem in Simulation of the Process of Vacuum Carburizing. Metal Science and Heat Treatment.

[14] Qin, M. "Vacuum Carburising and High Pressure Gas Quenching Technology in Automotive Industry." International Heat Treatment and Surface Engineering 2, no. 3-4 (2008): 116–120.

[15] CARTER, G. C. "Optimizing Gas Quenching." Advanced materials & processes 149, no. 2 (1996)

[16] Narazaki, Michiharu & Kogawara, Minoru & Qin, Ming & Watanabe, Youichi. (2009). Measurement and Database Construction of Heat Transfer Coefficients of Gas Quenching. Strojniski Vestnik. 55. 167-173.

[17] Errera, Marcelo Risso, and Luiz Fernando Milanez. "Thermodynamic Analysis of a Coke Dry Quenching Unit." Energy conversion and management 41, no. 2 (2000): 109–127.

[18] Krauss, George. (2015). Steels - Processing, Structure, and Performance (2nd Edition) – 4 Perlite, Ferrite, and Cementite. ASM International

[19] Krauss, George. (2015). Steels - Processing, Structure, and Performance (2nd Edition) – 3 Phases and Structures. ASM International

[20] Steel-Carbon diagram: https://practicalmaintenance.net/?p=1315 ; Retrieved: 20/09/2021

[21] Zoom-In Iron-Carbon diagram: https://nanopdf.com/download/applications-of-fe-c-phase-diagram_pdf ; Retrieved: 20/09/2021

[22] Krauss, George. (2015). Steels - Processing, Structure, and Performance (2nd Edition) - 8. Austenite in Steel. ASM International.

[23] Krauss, George. (2015). Steels - Processing, Structure, and Performance (2nd Edition) - 6. Bainite. ASM International.

[24] D.P. Koistinen and R.E. Marburger, A General Equation Prescribing the Extent of the Austenite-Martensite Transformation in Pure Iron- Carbon Alloys and Plain Carbon Steels, Acta Metall., Vol 7, 1959, p 59–60

[25] Krauss, George. (2015). Steels - Processing, Structure, and Performance (2nd Edition) - 17 Tempering of Steel. ASM International.

[26] FILM documentation: https://abaqus-docs.mit.edu/2017/English/SIMACAESUBRefMap/simasub-c-film.htm; Retrieved: 20/09/2021

[27] UMAT documentation:https://abaqus-docs.mit.edu/2017/English/SIMACAESUBRefMap/simasub-c-umat.htm ; Retrieved: 20/09/2021

[28] HETVAL documentation:https://abaqus-docs.mit.edu/2017/English/SIMACAESUBRefMap/simasub-c-hetval.htm ; Retrieved: 20/09/2021

[29] USDFLD documentation: https://abaqus-docs.mit.edu/2017/English/SIMACAESUBRefMap/simasub-c-usdfld.htm; Retrieved: 20/09/2021

[30] Eser, Atilim & Bezold, Alexander & Simsir, Caner & Broeckmann, Christoph. (2013). Simulation of Hardening and Tempering of Tool Steels.

[31] UHARD documentation:https://abaqus-docs.mit.edu/2017/English/SIMACAESUBRefMap/simasub-c-uhard.htm; Retrieved: 20/09/2021

[32] UEXPAN documentation: https://abaqus-docs.mit.edu/2017/English/SIMACAESUBRefMap/simasub-c-uexpan.htm ; Retrieved: 20/09/2021

[33] Khan, D., Gautham, B. Integrated Modeling of Carburizing-Quenching-Tempering of Steel Gears for an ICME Framework. Integr Mater Manuf Innov 7, 28–41 (2018).

[34] DFLUX documentation: https://abaqus-docs.mit.edu/2017/English/SIMACAESUBRefMap/simasub-c-dflux.htm; Retrieved: 20/09/2021

[35] Kula, P., R. Pietrasik, and K. Dybowski. "Vacuum carburizing—process optimization." Journal of Materials Processing Technology 164 (2005): 876-881.

[36] Li, M.V., Niebuhr, D.V., Meekisho, L.L. et al. A computational model for the prediction of steel hardenability. Metall Mater Trans B 29, 661–672 (1998).

[37] Lyassami, Mountadar & Shahriari, Davood & Ben FREDJ, Emna & Morin, Jean-Benoit & Jahazi, Mohammad. (2018). Numerical Simulation of Water Quenching of Large Size Steel Forgings: Effects of Macrosegregation and Grain Size on Phase Distribution. Journal of Manufacturing and Materials Processing.

[38] Song, D.-L & Gu, Jianfeng & Pan, J.-S & Hu, M.-J. (2004). Numerical simulation of quenching of large sized blocks of 718 steel used for plastic dies. Materials Science and Technology.

[39] Braz Fernandes, Francisco & Denis, Sabine & Simon, A.. (1985). Mathematical model coupling phase transformation and temperature evolution during quenching of steel. Materials Science and Technology.

[40] Huiping, Li & Zhao, Guoqun & Shanting, Niu & Chuanzhen, Huang. (2007). FEM simulation of quenching process and experimental verification of simulation results. Materials Science and Engineering: A. 452. 705-714.

[41] BUCHMAYR, B., & KIRKALDY, J. (1990). Modeling of the temperature field, transformation behavior, hardness and mechanical response of low alloy steels during cooling from the austenite region. Journal of Heat Treating,(2), 127–136.

[42] Koohi Esfahani, Ali & Babaei, Mahdi & Sarrami, Saeid. (2020). A numerical model coupling phase transformation to predict microstructure evolution and residual stress during quenching of 1045 steel. Mathematics and Computers in Simulation.

[43] Huiping, L., Zhao Guoqun and He Lian-fang. "Research on key technologies of FEM simulation of temperature field in the process of quenching." Frontiers of Materials Science 1 (2007): 359-365.

[44] Wei, Y., Zhang, L. & Sisson, R.D. Modeling of Carbon Concentration Profile Development During Both Atmosphere and Low Pressure Carburizing Processes. J. of Materi Eng and Perform 22, 1886–1891 (2013). https://doi.org/10.1007/s11665-012-0353-6

[45] COMSOL documentation: https://www.comsol.it/model/carburization-and-quenching-of-a-steel-gear-78061; Retrieved: 20/09/2021

[46] Munts VA, Baskakov AP (1980) Rate of carburizing of steel. Met Sci Heat Treat 22(5):358–360.

[47] Tibbetts GG (1980) Diffusivity of carbon in iron and steels at high temperatures. J Appl Phys 51(9):4813–4816.

[48] Karabelchtchikova, Olga. 2007. Fundamentals of Mass Transfer In Gas Carburizing.: Worcester Polytechnic Institute.

[49] Wang, Haojie & Liu, Jing & Tian, Yong & Wang, Zhaodong & An, Xiaoxue. (2020). Mathematical Modeling of Carbon Flux Parameters for Low-Pressure Vacuum Carburizing with Medium-High Alloy Steel. Coatings.

[50] Kim, DW., Cho, YG., Cho, HH. et al. A numerical model for vacuum carburization of an automotive gear ring. Met. Mater. Int. 17, 885–890 (2011).

[51] Zajusz, Marek & Tkacz-Śmiech, Katarzyna & Marek, Danielewski. (2015). Modeling of vacuum pulse carburizing of steel. Surface and Coatings Technology.

[52] Seok-Jae Lee, Young-Kook Lee, Prediction of austenite grain growth during austenitization of low alloy steels, Materials & Design, Volume 29, Issue 9, 2008, Pages 1840-1844,

[53] ABAQUS Documentation for coupled temp-displacement step: https://classes.engineering.wustl.edu/2009/spring/mase5513/abaqus/docs/v6.6/books/usb/default.htm?startat=pt03ch06s05at19.html ; Retrieved: 20/09/2021

[54] AZOM MATERIAL AISI 4140 information: https://www.azom.com/article.aspx?ArticleID=6769 ; Retrieved: 20/09/2021

[55] TTT Diagram:https://www.metallurgyfordummies.com/time-temperature-transformation-ttt-diagram.html ; Retrieved: 20/09/2021

[56] Kang, S.-H. & Im, Y.-T. (2007) Three-dimensional thermo-elastic–plastic finite element modeling of quenching process of plain-carbon steel in couple with phase transformation. International journal of mechanical sciences.

[57] Johnson WA, Mehl RF. Reaction kinetics in processes of nucleation

and growth. Transactions of AIME 1939;

[58] Avrami M. Kinetics of phase change I. Journal of Chemical Physics 1939;

[59] Avrami M. Kinetics of phase change II. Journal of Chemical Physics 1940;

[60] Lyassami, Mountadar & Shahriari, Davood & Ben FREDJ, Emna & Morin, Jean-Benoit & Jahazi, Mohammad. (2018). Numerical Simulation of Water Quenching of Large Size Steel Forgings: Effects of Macrosegregation and Grain Size on Phase Distribution. Journal of Manufacturing and Materials Processing.

[61] J.S. Kirkaldy and D. Venugopalan: Phase Transformation in Ferrous Alloys, A.R. Marder and J.I. Goldenstein, ed., Am. Inst. Min. Engrs., Philadelphia, PA, 1984, pp. 125-48.

[62] SLIDESHOW on ASTM grain size number:https://www.georgevandervoort.com/images/Quantitative-metallography/IntroToStereologyGrainSize.pdf ; Retrieved: 20/09/2021

[63] Nguyen, T.C., Weckman, D.C. A thermal and microstructure evolution model of direct-drive friction welding of plain carbon steel. Metall Mater Trans B 37, 275–292 (2006).

[64] G.E. Linnert: Welding Metallurgy, 4th ed., American Welding Society, Miami, FL, 1994, vol. 1, p. 837.

[65] Hamelin, Cory & Muránsky, Ondrej & Smith, Mike & Holden, Thomas & Luzin, Vladimir & Bendeich, Philip & Edwards, Lyndon. (2014). Validation of a numerical model used to predict phase distribution and residual stress in ferritic steel weldments. Acta Materialia. 75. 1–19. 10.1016/j.actamat.2014.04.045.

[66] Obasi, G., Pickering, E.J., Vasileiou, A.N. et al. Measurement and Prediction of Phase Transformation Kinetics in a Nuclear Steel During Rapid Thermal Cycles. Metall Mater Trans A 50, 1715–1731 (2019).

[67] Chipalkatti, J. (1999). Modeling of austenite decomposition in an AISI 4140 steel (T). University of British Columbia.

[68] Li, H., Zhao, G. & He, L. Research on key technologies of FEM simulation of temperature field in the process of quenching. Front. Mater. Sci. China 1, 359–365 (2007).

[69] P. Maynier, J. Dollet, and P. Bastien: Hardenability Concepts with Applications to Steels, D.V. Doane and J.S. Kirkaldy, eds., AIME, New York, NY, 1978, pp. 518-44.

[70] Rakhit, A.. "Heat Treatment of Gears: A Practical Guide for Engineers.", Chapter 5, (2000).

[71] Gear typical tempering temperatures: https://gearsolutions.com/features/heat-treating-heavy-duty-gears/ ; Retrieved: 20/09/2021

[72] Parrish G (1999) Carburizing: microstructures and properties. ASM International, Materials Park

[73] Hollomon JH, Jaffe LD (1945) Time-temperature relations in tempering steel. Trans AIME 162(223–249)

[74] Judge, V K, J G Speer, K D Clarke, K O Findley, and A J Clarke. "Rapid Thermal Processing to Enhance Steel Toughness." Scientific reports 8, no. 1 (2018): 445–445.

[75] Grange RA, Hribal CR, Porter LF (1977) Hardness of tempered martensite in carbon and low-alloy steels. Metall Trans A 8(11): 1775–1785.

[76] Transmission Shaft Image:https://www.terraintamer.com/en/4wd-products/transmission-driveline-cat/transmission-shafts ; Retrieved: 20/09/2021

[77] D.P. Koistinen, The Distribution of Residual Stresses in Carburized Cases and Their Origin, Trans. ASM, Vol 50, 1958, p 227–241

[78] https://www.britannica.com/technology/surface-hardening ; Retrieved: 20/09/2021

VITA AUCTORIS

NAME: Filippo Jones

PLACE OF BIRTH: Torino, TO, Italy

YEAR OF BIRTH: 1998

EDUCATION: Politecnico di Torino, B.Sc., Torino, TO, 2019